NTNU – Trondheim
Norwegian University of
Science and Technology

Deformation, Phyllonitization and Associated Element Mobilization of Granitoid Rocks:

A geochemical study of the Fagervika granitoid, Norway.

Anette Utgården Granseth

Geology
Submission date: May 2015
Supervisor: Bjørn Eske Sørensen, IGB
Co-supervisor: Trond Slagstad, NGU

Norwegian University of Science and Technology
Department of Geology and Mineral Resources Engineering

Abstract

The Fagervika granitoid is a felsic, peraluminous intrusion that was emplaced in oceanic crust at 481 Ma, now represented as the Bymarka ophiolite in Trondheim, Norway. It belongs to the Støren Group in the Upper Allochthon within the Scandinavian Caledonides. The emplacement onto the Baltican margin during the Caledonian orogeny occurred around 420 Ma, with following collapse in 400 - 380 Ma. Regionally, the rocks have been subjected to greenschist to lower amphibolite facies metamorphic conditions.

Detailed mapping at centimetre to decimetre scale of the Gråkallen area reveals the complex distribution of phyllonitic shear zones hosted by a granodiorite, with transport direction interpreted as a top-to-the-west movement. Field observations and petrographic studies were performed for mineral identification and textural descriptions. Comparison of the modal mineralogy with whole-rock data including trace elements is used to show chemical variation between the different lithologies. Mineral chemistry was examined with element mapping by Scanning Electron Microscopy (SEM), Electron Microprobe Analysis (EMPA) and Laser Ablation Inductively Coupled Mass Spectrometry (LA-ICP-MS). These methods report the major and trace element distribution along with the Rare Earth Elements (REE) distribution in each mineral phase. Isocon analysis of paired granodiorite-phyllonite samples enabled for quantification of the gains and losses in the system.

The rocks at Gråkallen are granodioritic, with only minor variations in modal mineralogy across all samples. The granodiorite is hypidiomorphic, show no preferred mineral orientation with early growth of mica and dynamic recrystallization of quartz. Phyllonitic shear zones have developed locally in the granodiorite and signs of widespread fluid interaction and metasomatism is evident throughout the rocks. The granodioritic assemblage is represented by Qtz + Pl + Kfs + Ms ± Py, with secondary accessories Ep + Aln + Ttn, which has been identified as the main REE-carriers. Allanite is enriched in the LREE, while epidote contains LREE to a lesser degree and titanite holds the HREEs, reflecting each minerals' preferential affinity for the REEs. The feldspars are altered, with alkali feldspar neocrystallized to albite, and plagioclase is seritized and saussuritized, with widespread muscovite and epidote. Major elements Na and K have been mobilized and Ca to a lesser degree, while the REEs has only been mobilized at micro scale in the granodiorite.

The phyllonitic shear zones trend approximately N-S and consist of elongated quartz grains in a muscovite matrix, defining the assemblage of Qtz + Ms ± Py ± feldspar porphyroclasts. The formation of the muscovite indicates the presence of water-rich fluid. The Ca-bearing accessories Ep + Aln + Ttn has been destabilized, along with most of the feldspar due to deformation and high fluid/rock ratio, though some titanite is remnant. In addition, the fluid composition enabled for mobilization of trace elements and REEs. This resulted in depletion of the REE, with a greater loss of LREE compared to HREE. An epidote-rich shear zone shows a high modality of epidote, along with Ms + Py + Qtz + Ttn, with subsequent REE enrichment in comparison to the granodiorite. The REE pattern of the epidote-rich shear zone appeared as an enriched version of the granodiorite REE pattern, suggesting that stabilization of epidote and titanite prevented loss of the REEs.

This study shows that metasomatism triggered mineralogical changes and grain size reduction, especially for the feldspars in the undeformed granodiorite, enabling increased fluid flow. The heightened fluid/rock ratio allows muscovite to form, and thus promoting strain weakening and further strain partitioning. Deformation and fluid-rock interaction completely changed the mineralogy by destabilizing feldspar and the REE-bearing phases and by forming muscovite, which promoted mobilization of K, Na, Ca and the REEs during phyllonitization of the granodiorite.

Sammendrag

Fagervika granitoiden er en felsisk, peraluminøs bergart som intruderte havskorpen for 481 millioner år siden, og er nå representert som Bymarka ofiolitten i Trondheim, Norge. Bymarka tilhører Støren Gruppen i Øvre Allokton i de Skandinaviske Kaledonidene. Granitoidens og dens omkringliggende bergarter har blitt obdusert opp på den baltiske marginen under den Kaledonske fjellkjededannelsen omkring 420 Ma, med etterfølgende orogenkollaps i perioden 400 – 380 Ma. Regionalt har bergartene gjennomgått metamorfose i grønnskifer til nedre amfibolitt facies.

Detaljert kartlegging, på centimeter-desimeter skala, av Gråkallen-området viser en kompleks forekomst av fyllonittiske skjærsoner i granodioritt. Transportretningen på skjærsonene er tolket som en topp-mot-vest bevegelse. Feltobservasjoner og petrografiske studier ble utført for mineralidentifikasjon og teksturelle beskrivelser. Sammenligning av modalmineralogien med bulkkjemi samt sporelement er brukt til å vise den kjemiske variasjonen mellom de ulike litologiene. Mineralkjemi ble undersøkt ved bruk av *element mapping* med elektronmikroskop (SEM), elektronmikrosonde (EMPA) and laserablasjon (LA-ICP-MS). Disse metodene viser fordelingen av hoved- og sporelement og sjeldne jordartselementer (REE) mellom de ulike mineralfasene. Isokonanalyse utført på parede granodioritt-fyllonittprøver muliggjorde for kvantifisering av massetransport i systemet.

Bergartene på Gråkallen har en granodiorittisk sammensetning som viser små variasjoner i modalmineralogien på tvers av alle prøver. Granodioritten er hypidiomorfisk og det er ingen foretrukket mineralorientering, med begynnende vekst av glimmer og dynamisk rekrystallisering av kvarts. De fyllonittiske skjærsonene er utviklet lokalt i granodioritten. Granodioritten viser tegn på utbredt væskepåvirkning og metasomatose. Mineralselskapet består av Qtz + Pl + Kfs + Ms ± Py, med sekundære aksessoriske mineralene Ep + Aln + Ttn, som har blitt identifisert som de REE-bærende mineralene i granodioritten. Allanitt er anriket på LREE, epidot inneholder LREE i mindre grad, mens titanitt er anriket på HREE. REE-fordelingen reflekterer tilgjengeligheten og mineralenes affinitet til å oppta REE. Feltspatene er omvandlet, der alkalifeltspat er neokrystallisert til albitt, og primær plagioklas har blitt serittisert og saussurittisert, med utbredt muskovitt- og epidotdannelse. Hovedelementene Na og K har blitt mobilisert, Ca i mindre grad, mens REE kun har blitt mobilisert på mikroskala i granodioritten.

De fyllonittiske skjærsonene har en omtrentlig N-S retning og består av elongerte kvartskorn i muskovittmatriks. Mineralselskapet består av Qtz + Ms ± Py ± feltspat porfyroklaster, og dannelsen av muskovitten i fyllonitten indikerer at gjennomstrømning av vannholdige væsker har funnet sted. De Ca-bærende mineralene Ep + Aln + Ttn har blitt destabilisert sammen med mesteparten av feltspatene pga. deformasjon og høyt fluid/bergartsforhold, men allikvel har titanitt blitt bevart i fyllonitten. I tillegg har væskesammensetningen mest sannsynlig spilt en rolle i mobiliseringen av sporelementene og REE, som førte til utarming av REE, med et større tap av LREE sammenlignet med HREE. En epidot-rik skjærsone viser et høyt innhold av epidot, i tillegg til Ms + Py + Qtz + Ttn. Denne prøven viser anrikning av REE og har samme REE trend som granodioritten, hvilket tyder på at stabiliseringen av epidot og titanitt hindret tap av REE.

Denne studien viser at metasomatose forårsaket mineralogiske endringer og kornstørrelsesreduksjon, spesielt for feltspatene i den udeformerte granodioritten som muliggjorde for økt væskestrøm. Deformasjon og økt væskepåvirkning endret mineralogien totalt ved å destabilisere feltspat og de REE-bærende mineralene, etterfulgt av dannelse av muskovitt, som fremmer *strain weakening* og etterfølgende *strain partitioning*. Destabiliseringen av mineralene fremmet mobilisering av K, Na, Ca og REE under fyllonittisering av granodioritten.

Acknowledgements

This master thesis has been carried out at the Department of Geology and Mineral Resources Engineering (IGB) at the Norwegian University of Science and Technology (NTNU), Trondheim, and it was written in collaboration with the Geological Survey of Norway (NGU). Associate professor Bjørn Eske Sørensen (NTNU) and Dr. Trond Slagstad (NGU) have been the main supervisors for this project.

First and foremost, I would like to thank my supervisors, Bjørn and Trond, for their guidance and help throughout this project, and for always having an open door policy. In addition, I would also like to thank Dr. Nolwenn Coint at NGU. Their encouragement and expertise has truly benefitted my project. Moreover, I am grateful for the opportunity I was given to present my own poster at the Joint Assembly conference in Montréal, Canada, which can be found in the appendix. It was a truly inspiring experience. Finally, I would like to thank my dear classmates that I have travelled halfway around the world with in the last five years. Your friendship and support means a lot to me, and grøt-fredag will never be the same without you.

Anette Utgården Granseth

15.05.15, Trondheim

Note to reader: digital appendix of geochemical data is available for download at http://daim.idi.ntnu.no, and it contains 1) whole-rock data represented by major and trace elements and XRD results; 2) mineral chemistry data: a) EMPA results including spot locations; b) Laser results including spot locations; c) SEM maps for the 8 thin sections scanned and d) calculated mineral formulas for the muscovite and the epidote and allanite.

Front page: Brown allanite surrounded by high-relief titanite and transparent epidote (Thin section photo, Figure 25*).*

Contents

Abstract ..... **iii**

Sammendrag ..... **v**

Acknowledgements ..... **vii**

Introduction **1**

Regional geology **3**

Caledonides 3

Bymarka Ophiolite 4

Fagervika granitoid 5

Previous studies 6

Mining history and mineralizations 7

Theory **9**

Elements and geochemistry 9

Metasomatism and element mobilization 12

Cation metasomatism 17

Methods **21**

Field work preparation and mapping 21

Sampling 21

Sample preparation 22

Petrography 23

Geochemical analysis 23

Whole-rock geochemistry 24

Mineral chemistry 25

Sources of error 28

Results **33**

Field observations 34

Geochemical analysis 45

Whole-rock geochemistry 45

Mineral chemistry 50

Isocon diagrams 66

Discussion **73**

Granodiorite....73
The epidote-rich shear zone....77
Formation of the phyllonite....78
Metamorphic conditions recorded....79
Element mobility related to deformation in greenschist facies conditions....83
Timing of alteration and deformation....86
Fluid behaviour....86
Implications of element mobility....88
Conclusion....89
Further work....90
References....91
Appendix....97

List of figures

Figure 1: Regional tectonostratigraphic map 4
Figure 2: Geological map of the Bymarka ophiolite. 5
Figure 3: Ionic charge versus ionic radius diagram. 11
Figure 4: Schematic overview of the work flow during sample preparation 23
Figure 5: Geological map constructed based on the fieldwork done in 2013 and 2014. 33
Figure 6: Field observations of the granodiorite 35
Figure 7: Mineralogical and textural observations in the granodiorite 36
Figure 8: Field observations of the phyllonite 37
Figure 9: Mineralogical and textural observations in the phyllonite 39
Figure 11: Field observations of the aplite and the epidote-rich shear zone 40
Figure 12: Mineralogical and textural observations in the aplite and hydrothermal quartz 42
Figure 13: Field observations of the location at the steep cliff 44
Figure 14: Summary of all methods applied to the collected samples. 45
Figure 15: The granodiorite and phyllonite samples normalized. 48
Figure 16: Relative enrichment/depletion diagram 49
Figure 17: Montage showing a scan of the granodiorite thin section (P20) 52
Figure 18: Montage showing a scan transitional phyllonite thin section (P18B) 53
Figure 19: Montage showing a scan of the phyllonite thin section (P28) in PPL and XPL 54
Figure 20: Montage showing a scan of the epidote-rich shear zone thin section (P31-d). 55
Figure 21: Ternary feldspar diagram 56
Figure 22: Element map reveals that there is no internal zonation within the garnet. 58
Figure 23: Total REE vs. Al plot after Petrík et al. (1995). 59
Figure 24: Chondrite-normalized REE patterns of allanite and titanite 60
Figure 25: Chondrite-normalized REE patterns of allanite, epidote and titanite 60
Figure 26: Chondrite-normalized REE patterns of allanite, epidote and titanite 61
Figure 27: Chondrite-normalized REE patterns of epidote measured by LA-ICP-MS. 61
Figure 28: Chondrite-normalized REE patterns of epidote measured by LA-ICP-MS. 62
Figure 29: Chondrite-normalized REE patterns of epidote measured by LA-ICP-MS.. 63
Figure 30: Chondrite-normalized REE patterns of allanite and epidote 65
Figure 32: TiO_2 and Zr variation diagram. 68
Figure 33: It was assumed that Zr and TiO_2 were immobile 71

Figure 34: Schematic summary of the different lithologies and associated mineral assemblages. 83

List of tables

Table 1: Overview of the different elements in each element list used for microprobe 27
Table 2: XRD-results showing the modal mineralogy of each sample. 47
Table 3: Volume and mass changes calculated from the Isocon analysis 72

List of equations

Equation 1: Partition Coefficient 9
Equation 2: Alkali feldspar to Albite 17
Equation 3: Oligoclase to Albite 18
Equation 4: Alkali feldspar to Muscovite 19
Equation 5: Calculated Muscovite formula 57
Equation 6: Calculated Muscovite formula in contact with Garnet 57
Equation 7: Plagioclase alteration 73
Equation 8: Epidote formation 74
Equation 9: Albite to Muscovite 79

Introduction

The Fagervika granitoid is the largest felsic intrusion in the Bymarka ophiolite and from emplacement in oceanic crust at 481 Ma (Slagstad et al., 2014) and to present day, the granitoid has experienced greenschist to lower amphibolite facies metamorphism, but also a significant amount of deformation has been accommodated during this time interval.

The aim of this study is to look at the link between the element mobility and deformation in granitoid rocks. Detailed geological mapping of Gråkallen, petrographic studies, with emphasis on the mineralogical and textural features, and comprehensive sets of geochemical data were combined in order to explain the element mobility. An in-depth examination of the granodiorite will define the mineralogical starting point of the rocks prior to deformation. Description of the granodiorite-phyllonite transitions in the Fagervika granitoid will be addressed in order to relate the deformation, metamorphism and element mobilization. In addition, a single cm-thick epidote-rich shear zone, which is different from the phyllonites, will also be discussed. In conclusion, the mobilization path of the major and trace elements will be clarified, and the causes for the mobilization will be explained. Microstructural analysis of the deformation processes dominating in the formation of the phyllonite is addressed, though it is not highlighted.

Regional geology

Caledonides

The Scandinavian Caledonides are divided into four distinctive tectonostratigraphic units, the Lower, Middle, Upper and Uppermost allochthon (Roberts and Gee, 1985) (Figure 1). The Uppermost Allochthon is considered to have an origin at the Laurentian margin of the Iapetus Ocean, while the Upper Allochthon straddles the transition of the Iapetus and the Baltican continent and the Middle and Lower Allochthons have affinities to the Baltican continent (Stephens et al., 1985, Roberts et al., 2002a). The allochthons are represented by thrust sheets translated approximately east to south-eastwards during the Caledonian orogeny, when the Iapetus ocean closed and the continents of Laurentia and Baltica collided during the Late Silurian – Early Devonian (Gee, 1975, Robinson et al., 2014). The tectonostratigraphic system has a designated layer-cake configuration saying that the lower allochthons have had a shorter transporting distance than the higher-lying allochthons, however, several of the allochthons contain segments of crystalline basement (Gee and Roberts, 1983). These subdivisions of the allochthons have been the framework for the research that has been done in the Scandinavian Caledonides for the last 30 to 40 years. Corfu et al. (2014) review the traditional tectonostratigraphic model of the allochthons and its inadequacies and rigid structure and introduce the Caledonides without the genetic implication to a tectonic level. Newfound understanding of the palaeogeographical reconstructions based on faunal and palaeomagnetic data (Torsvik et al., 1996, Torsvik and Cocks, 2005) along with better age-constraints reveal a more complex geological history that do not fit into the tectono-genetic model that imply either a Laurentian, Iapetus or Baltican origin (Corfu et al., 2014). A project currently in work, examines the Umbukta gabbro that currently is designated to Rödingsfjäll Nappe Complex in the Uppermost Allochthon (Roberts and Gee, 1985). New evidence indicates that the Seiland Igneous Province situated in the Middle Allochthon and the Umbukta gabbro in the Uppermost Allochthon has the same magmatic source and same age (570 – 560 Ma). If these rocks derive from the same magmatic source, it implies that todays tectonostratigraphic division of these units are questionable, as they should be designated to the same tectonostratigraphic unit (Høyen, In Prep.).

Some features can be found throughout the Caledonides, whereas other, usually higher-laying sections are restricted to a specific part. By that, Corfu et al. (2014) divide the Scandinavian

Caledonides into three distinct segments: Southern, Central and Northern segment. Moreover, they hope with this new approach the true nature of the Scandinavian Caledonides will be revealed as the deformational history through time can be taken into consideration.

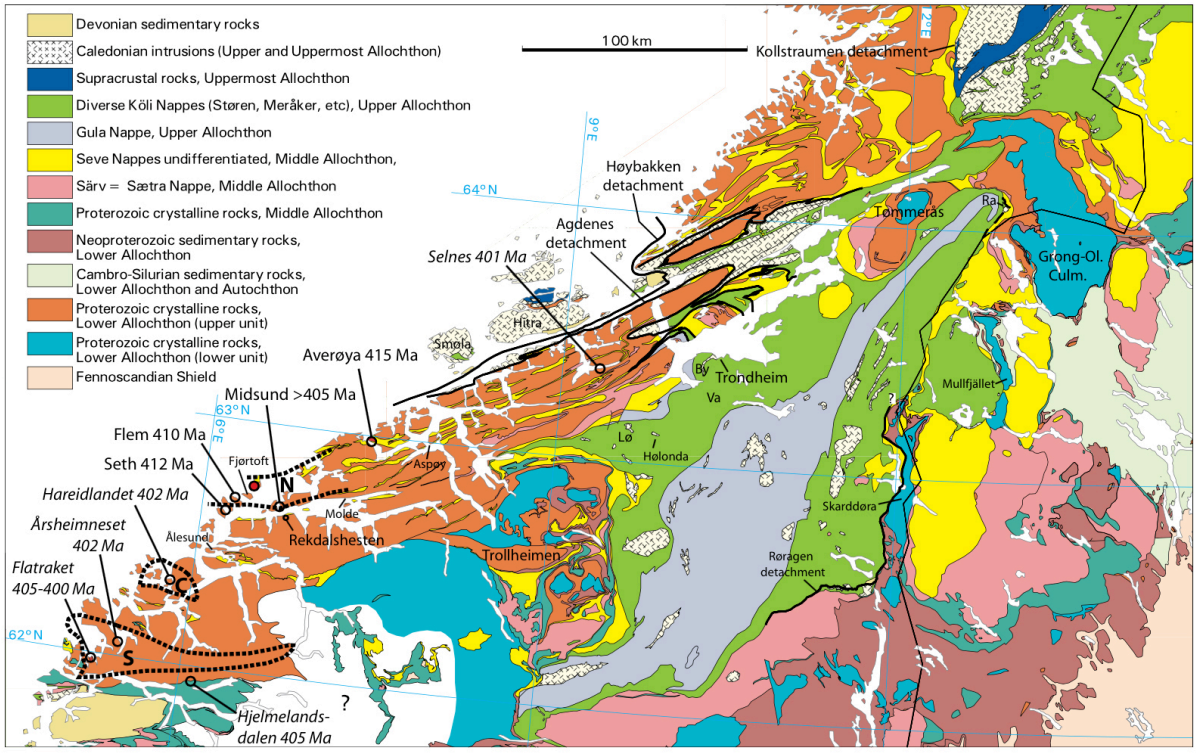

Figure 1: Regional tectonostratigraphic map showing the complexity of the geology in the Caledonides. The legend shows the Nappes and their respective Allochthons. Trondheim and the Fagervika granitoid shown on the map as a Caledonian intrusion located in the Støren nappe, in the diverse Köli Nappes. After Robinson et al. (2014).

Bymarka Ophiolite

Ophiolitic sections ranging from gabbros, sheeted dykes, plagiogranites to pillow lavas and volcaniclastic sediments can be observed at Løkken, Vassfjellet and Bymarka, which is found within the Støren Nappe of the Upper Allochthon (Grenne et al., 1980, Grenne, 1989, Roberts et al., 2002b, Slagstad et al., 2014). The ophiolites are interpreted to have been obducted onto a microcontinent, as represented by the Gula complex that today is located underneath of the Støren Nappe (Gale and Roberts, 1974, Roberts et al., 2002b, Hollocher et al., 2012, Hollocher et al., 2014).

High-precision dating and correlation of the meta-volcanic and –sedimentary units, along with geochemical data, puts the formation of the ophiolites at around 500 – 480 Ma and the obduction of the ophiolites followed shortly after at ~480-475 Ma (Eide and Lardeaux, 2002,

Roberts et al., 2002b, Hollocher et al., 2012). Grenne (1989) and other authors put the ophiolites of the Caledonides in in a supra-subduction setting, positioned in a back-arc spreading or arc rifting regime (Grenne et al., 1999, and references therein).

The ophiolites of the Støren Nappe have undergone metamorphism in greenschist to lower amphibolite facies, due to seafloor alteration, obduction of the ophiolites and later continent-continent collision and final emplacement during the Scandian phase in the Silurian to Early Devonian (Roberts and Sturt, 1980, Eide and Lardeaux, 2002, Slagstad et al., 2014, Hollocher et al., 2014). Today, the pseudostratigraphy of the ophiolites in Bymarka is only locally preserved, with a pervasively overprinted mineral fabric and retrograde metamorphism (Slagstad, 1998, Slagstad, 2003)

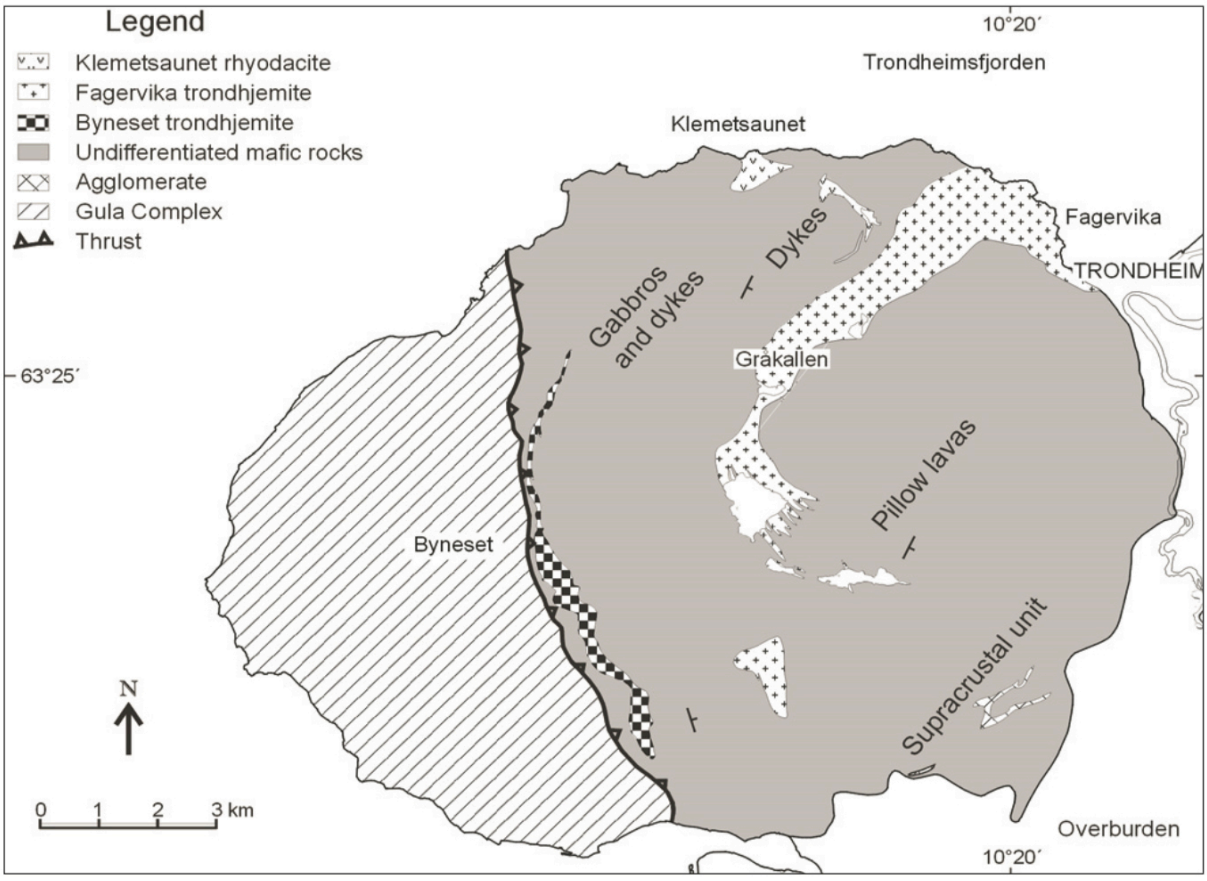

Figure 2: Geological map of the Bymarka ophiolite, with the Fagervika granitoid situated in the middle of the ophiolite complex. It stretches from the Trondheimsfjord and fingers out around the lake of Skjelbreia. Gråkallen is also depicted on this map. After Slagstad (2003).

Fagervika granitoid

The Fagervika granitoid is one of three felsic intrusives in the Bymarka ophiolite, the other two being the Klemetsaunet rhyodacite and Byneset trondhjemite (Slagstad, 2003, Slagstad et

al., 2014) (Figure 2). Klemetsaunet rhyodacite is described as a fine-grained felsic layers occurring in close proximity to the transition between the gabbro and sheeted dykes, and is interpreted as plagiogranites formed by fractional crystallization of a basaltic magma with a MORB-like composition in an ocean-floor setting (Slagstad, 2003). The Byneset trondhjemite occurs as a sheet-like intrusive, and at one locality, crosscutting the Klemetsaunet rhyodacite, indicating a younger age (Slagstad et al., 2014). The Byneset trondhjemite has been interpreted as melting of a thick pile of basaltic rocks that formed during obduction onto a continental margin (Slagstad, 2003, Slagstad et al., 2014). However, the Fagervika granitoid is by far the largest, showing variable degree of deformation and composition ranging from granitic to granodioritic and trondhjemitic (Watne, 1991, Slagstad et al., 2014). The granitoid was formed in an island arc coeval to slightly younger than the oceanic crust (Slagstad, 2003, Slagstad et al., 2014). It is inferred that the source material for the Fagervika granitoid contains a considerable contribution from a continental source based on Sm-Nd isotopic data (Slagstad et al., 2014). U-Pb zircon dating of the Fagervika granitoid has been done at two occasions: Roberts et al. (2002b) yielded an approximate age of 481 Ma, while Slagstad et al. (2014) reported an age of 481 ± 3 Ma, which represents the crystallization age of the intrusion.

The Fagervika granitoid has been mapped numerous times and been given equally many different names over the years: The Ilsvik granodiorite (Watne, 1991, and references therein), quartz tuff (Banks, 1992), Bymarka or Fagervika trondhjemite (Slagstad, 1998, Slagstad, 2003) and most recently Fagervika granitoid (Roberts et al., 2002b, Slagstad et al., 2014). I find the term granitoid most fitting when referring to the entire intrusion, as it is a collective term for alkali feldspar granite, granite, granodiorite and tonalite (therein trondhjemite) (Streckeisen, 1976), as the composition of the intrusive is highly dependent on the location (Watne, 1991, Slagstad et al., 2014). When referring to the Gråkallen locality that has been mapped during the work on this thesis, granodiorite is used, as it is the dominating composition (See Figure 6).

Previous studies

Geochemical and geochronological work has been done in Bymarka previously, related to the ophiolitic sections and plagiogranites by Slagstad and others (Slagstad, 2003, Slagstad et al., 2014, and references therein), as well a several diplomas and master theses (Watne, 1991, Slagstad, 1998, Vedeler, 2013). The quite extensive project done by Watne (1991) describes

the rocks in the map sheet of Trondheim, Norway, in terms of Caledonian allochthons and stratigraphy. He discusses the relationships between the different groups of the Støren Nappe and Gula Nappe and their spatial evolution through time. Detailed descriptions and field photos of the different lithologies is accompanied by structural investigations along with discussions regarding the metamorphic history, age determination and economic geology of the area. The aim of the study by Slagstad (1998) was to map and investigate the rocks in Bymarka, especially the leucocratic rocks and their relationship to the surrounding greenstones, using geochemical, petrological and structural investigations that later were put in a regional geological context. He showed that greenstones most likely originated at a mid-ocean ridge and along with the intrusives that later underwent greenschist metamorphism along with dismemberment of the ophiolite fragment (Slagstad, 1998). Vedeler (2013) looked at the petrology and geochemistry of the Klemetsaunet plagiogranites, with emphasis put on the metamorphic alteration the rocks have undergone. His results inferred that the regional metamorphism played a greater role than the ocean floor metamorphism, as no conclusive evidence could be found supporting the latter (Vedeler, 2013).

Mining history and mineralizations

Bymarka and Trondheim has a history of prospecting and small-scale mining, mainly for copper. The first record of prospecting in Bymarka dates back to 1736, where as today, there is no mining activity in Bymarka. However, the history of mining in the area is acknowledged by the names of local areas and lakes, such as Kopperdammen, Blyberget, Brennan and Kolbotnan (Rø and Midtsian, 1995). They were prospecting for pyrite and chalcopyrite in Bymarka, as pyrite could be utilized in the production of sulphuric acid (Rø and Midtsian, 1995). Some of the ores in the area are found as sulphide-impregnated greenstones and lenses, not far from the intrusive contact to the granitoid (Rø and Midtsian, 1995). In the Løkken—Hølonda area lies Løkken Verk, which is a volcanogenic massive sulphide (VMS) deposit hosting pyritic Cu-Zn and is one of the worlds largest ophiolite-hosted deposits in the world that also resides in the Støren Nappe (Grenne et al., 1999, and references therein). These mineralizations are linked to the ocean ridge spreading centres where cold sea water circulate through and interact with the oceanic crust (Robb, 2005).

South of Gråkallen and Vintervatnet, a quartz vein is exposed along a road cut where ore mineralizations has been found, consisting mainly of pyrite (FeS_2) with numerous, but small inclusions of chalcopyrite ($CuFeS_2$), bornite (Cu_5FeS_4), covelline (CuS), cubanite ($CuFe_2S_3$)

and digenite (Cu_9S_5). The minor phases represent different mineral phases that carry Fe, Cu, Zn, Bi, Te, Ti, Ag and Au, in which some still remain unidentified (Størseth, pers. comment). In 1990, the locality south of Vintervatnet hit the local media, as minor amounts of gold were reported among these minerals. However, there was unfortunately no commercial or economic value of this finding and it was soon forgotten (Rø and Midtsian, 1995).

Theory

Elements and geochemistry

A *major element* constitutes of more than 0.1 wt. % in a rock and is usually presented as an oxide. SiO_2, Al_2O_3, FeO (sometimes given as Fe_2O_3), MgO, CaO, Na_2O, and K_2O as typical examples, and these major elements are the main mineral- and rock-building constituents (Best, 2009, Winter, 2010). The *trace elements* represent less than 0.1 wt. % of the concentration and is usually given as a single element and in ppm (1000 ppm is 0.1 wt. %) (Rollinson, 1993, Best, 2009, Winter, 2010). These low-abundance elements can form their own mineral phases when they reach saturation level, such as Zr, P and Ca that can form minerals like zircon, apatite and titanite, but for the most part, these elements substitute into other major minerals (Rollinson, 1993, Winter, 2010). Some petrologists designate the interval between 1.0 and 0.1 wt. % to *minor elements*, such as TiO_2, P_2O_5 and MnO. These elements are commonly substituted with the major elements, but depending on the setting they are located in, it can either act as a major or trace element (Winter, 2010). These differences for the major and trace elements in behaviour is useful in discriminating magmatic and petrological processes, which is especially true for trace elements (Rollinson, 1993, Winter, 2010).

The concentration of a trace element in a rock or mineral depends on whether the elements preference is to a solid or melt/fluid phase. This relationship can be described by a *partition coefficient*, D:

Equation 1: Partition Coefficient

$$D = \frac{Concentration\ in\ solid}{Concentration\ in\ melt/fluid}$$

After Henderson (1984). Thus, an element with a D-value >1 seems to prefer the solid phase and is characterized as *compatible*, where as an element that has a D-value <1 prefers the melt/fluid phase and is termed as *incompatible* (Henderson, 1984, Rollinson, 1993, Winter, 2010). Partition coefficients are commonly applied to solid/melt relationships, though it is fully applicable when the melt phase is exchanged with a fluid phase. The partition coefficient is not the only controlling factor, as it is also influenced by the pressure, temperature and mineral composition. Onuma et al. (1968) and Jensen (1973) showed that the charge and ionic

radii contribute considerably in trace element partitioning in a mineral/melt system, as it is a significant relationship between the partition coefficient and the ionic radii of the REEs (Henderson, 1984). However, at crustal pressures, a partition coefficient may be insignificant as an elements concentration in a fluid is also given by the ligand content in the fluid (Yardley, 2009).

Based on their ionic potential (charge/radius ratio) the incompatible elements can be further separated into: *Large Ion Lithophile Elements* (LILE), comprise of Cs, Rb, K, Ba, Sr, Eu^{2+} and Pb^{2+}; *High Field Strength Elements* (HFSE) with U, Nb, Ta, Ti, Hf, Zr, Pb^{4+}, Th, Sc; and the *Rare Earth Elements* (REE) (described below) (Pearce, 1983, Best, 2009). Among these incompatible element groups, the LILEs with their small valence and high ionic radius are regarded as the more mobile and "compatible" (they are not compatible, they are just less incompatible), while the HFSEs have a smaller ionic radius and higher valence, which are qualities that have shown to have a higher priority during crystallization of a mineral (Figure 3) (Best, 2009, Winter, 2010). Goldschmidt (1937) stated three simple for rules in order to predict the trace element behaviour, based solely in the valence and the ionic radii of an element.

1. Ions with similar ionic radii and ionic charge would show no preferential incorporation of either ion into a crystal lattice, which is the case for element pairs such as Zr-Hf and Y-Ho.
2. Ions with the same valence, but with different ionic radii, the smaller ion shows preference to the solid phase.
3. Ions with similar radius, but different valence state, the higher-charged ion is preferred into to the solid phase.

The rare earth elements are series of 15 metallic elements with atomic number 57 to 71 and includes of La, Ce, Pr, Nd, Pm, Sm, Eu, Gd, Tb, Dy, Ho, Er, Tm, Yb and Lu. REEs are regarded as a single consistent group because they have similar chemical and physical properties due to their decreasing ionic radii and increasing atomic number (Rollinson, 1993). They are all trivalent, though some species can have a different oxidation state (e.g. Ce^{4+} and Eu^{2+}) in which may produce Eu anomalies as Eu^{2+} may substitute for Ca^{2+} in Ca-bearing phases, such as plagioclase and epidote (Rollinson, 1993, Best, 2009). The REEs have also been subdivided into LREE (La - Sm) and HREE (Gd – Lu) in order to distinguish the light and the heavy REEs (Henderson, 1984). REEs usually have high partition coefficient for

accessory minerals, as these minerals have the ability to incorporate the REEs into their crystal lattice (Henderson, 1984).

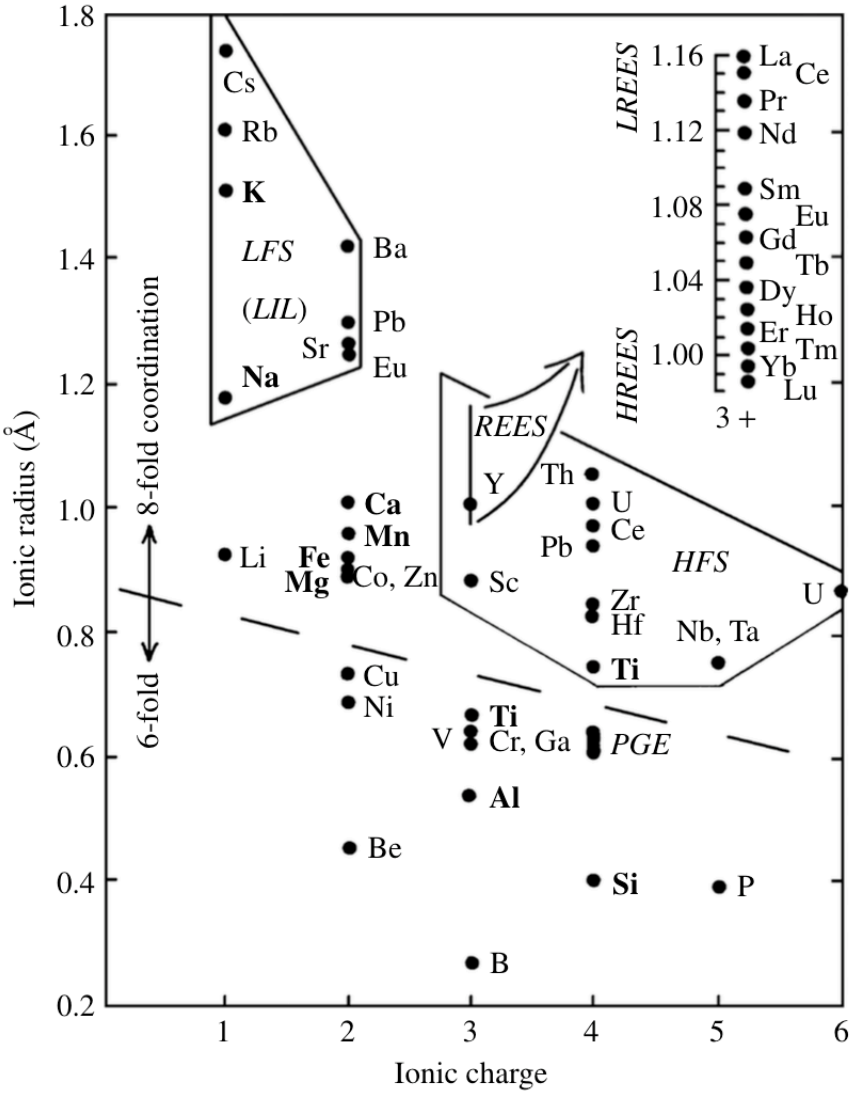

Figure 3: Ionic charge versus ionic radius diagram. Based on their ionic potential, two groups are evident: the LILEs and the HFSEs, with the REEs plotting amongst the latter. After Best (2009).

When concluding his study of REE mobility during granite alteration in southwest England, Alderton et al. (1980) listed several important factors that can control the mobility of the REEs:

1. The REE content of the reacting minerals;
2. The mineral stability towards the hydrothermal fluid;
3. Availability of sites within the secondary minerals that can accommodate REEs;
4. REE concentration in the hydrothermal fluid;
5. The transport ability of the fluid to carry REEs out of the system.

For example, in high fluorine fluids, Zr can be mobilized by forming complexes such as ZrF_6^{2-} and with zircons ability to hold REEs a phase decomposition would possibly effect the mobility of REE (Alderton et al., 1980). Rubin et al. (1993) proposes that the mineralogical host controls the mobility of different trace elements. As zircon is not very susceptible to decomposition compared to other Zr-bearing minerals, e.g. sodium pyroxenes and amphiboles, which have shown to contain 7.0 wt.% ZrO_2 in some cases. These minerals are more easily changed during hydrothermal alteration, so during alteration the Zr is released and potentially mobilized (Rubin et al., 1993).

Metasomatism and element mobilization

According to the International Union of Geological Sciences (IUGS) Subcommission on the Systematics of Metamorphic Rocks, *metasomatism* is defined as ”a metamorphic process by which the chemical composition of a rock or rock portion is altered in a pervasive manner and which involves the introduction and/or removal of chemical components as a result of the interaction of the rock with aqueous fluids (solutions). During the metamorphism the rock remains in a solid state” (Fettes et al., 2007).

A hydrothermal fluid has the ability change over time as material is dissolved and precipitated in solution due to changes in temperature, pressure and density, and it can reach supercritical fluid conditions (Pirajno, 2009). Hydrothermal fluids can be subdivided into several major types based on the fluid origin: *Sea water* or the oceans is recognized for the salinity, which can originate from different sources: hydrothermal discharges, e.g. from black smokers and weathering of the continental crust (Pirajno, 2009). Dominating components found in seawater today is Na^+, K^+, Ca^{2+}, and Mg^{2+} and anions Cl^-, HCO_3^-, and SO_4^{2-}, which adds up to a total typical oceanic salinity of 3.5 wt. % (Robb, 2005). The circulation of seawater in the oceanic crust is highly responsible for the seafloor alteration along mid-ocean ridges and the metal redistribution in these parts, especially in areas with high heat and fluid flow (Robb, 2005, Bach et al., 2013). *Meteoric water*, which includes lakes, rivers and groundwater originates as rainfall and infiltrating the crust along fractures and zones of high permeability (Robb, 2005, Pirajno, 2009). It has the largest contribution to weathering and erosion and generally has a lower salinity than sea water, about 100 ppm and Ca^{2+} and HCO_3^- is the dominant ions, but also minor CO_2 (Pirajno, 2009). Groundwater contain alkali metals, sulphates, chlorides, bicarbonates, in which the concentration relies on the amount of time in contact with the host rock and the host rock composition (Pirajno, 2009). If a fluid is trapped

in the interstitial pore spaces during diagenesis of sedimentary rocks, it is termed *connate* or *formational water* (Robb, 2005, Pirajno, 2009). Connate waters are released during burial and diagenetic processes as a result of pore space reduction and will carry an isotopic fingerprint that will differentiate between a meteoric water or sea water origin (Pirajno, 2009). In temperatures in excess of 200°C, diagenesis turns into metamorphism, and where *metamorphic fluids* originate from devolatilisation and decarbonation reactions during prograde metamorphism (Robb, 2005). Hydrous mineral assemblages are transformed into mineral assemblages with lower volatile content (Yardley, 2013), and the fluids are usually dominated by H_2O, CO_2 and CH_4 and commonly with low salinity and low content of reduced sulphur (Robb, 2005). With the low porosity and high fluid pressure of the metamorphic rocks coupled with the slow rate of fluid release and endothermic character of the reactions, indicate that metamorphic fluids is not a major contributor to metasomatism (Yardley, 2005, Yardley, 2013). *Magmatic fluids* are released during magma cooling and crystallization and these fluids commonly, along with water, contain H_2S, CO_2, SO_2, SO_4^{2-}, HCl, B, F and H_2 (Yardley, 2013). The composition of magma-derived fluids is dependent on the initial magma composition, where mafic rocks contain CO_2-rich fluids, while the more felsic can be CO_2-containing waters with low salinities (Yardley, 2013, and references therein).

Any fluid can be responsible for metasomatic alteration and it commonly occurs along shear zones, fractures, faults and permeable lithologies (Harlov and Austrheim, 2013, Yardley, 2013). The newly introduced and non-equilibrated fluid can exchange material with the host rock in attempt to reach equilibrium and if a suite of rocks has been subjected alteration and metamorphism, it is highly likely that some elements has been mobilized (Winter, 2010). The mobilization is dependent on the mineralogical changes the rock undergoes and the true nature of the fluid that flushes through (Rollinson, 1993). Along with any change in pressure, temperature and/or chemical environment could induce a large-scale metamorphic or a small-scale metasomatic reactions, involving a re-equilibration of the mineral assemblages and possibly mass transport (Putnis and Austrheim, 2013). The study group on metasomatic rocks of Zharikov et al. (2007) subdivided the metasomatic processes into:

1) Ion-by-ion replacement in minerals by simultaneous dissolving and precipitating minerals and thus maintaining a constant volume;
2) Replacement of rocks during solid state;
3) Significant changes in the chemical composition either by adding or removing chemical components, besides from the perfectly mobile H_2O and CO_2.

4) Formation of chemical zones representing the equilibrium between the rocks and the fluids. Occurrence of complete sequence of zones constitutes a metasomatic column.

Fluid pathways and mass transport

As defined by Korzhinskii (1959) there are two main types of metasomatism: Diffusional and infiltrational, that is independent of their environment. The diffusion of solutes in a stationary system, either through a solid or fluid is termed *diffusional metasomatism*, and it is driven by the chemical potential of the solutes over a long period of time and at high temperatures (Zharikov et al., 2007, Vernon and Clarke, 2008, Pirajno, 2013). Metasomatic rocks resulted from diffusion often show rims along cracks and other contact surfaces, as well as mineral composition can vary across a metasomatic zone and it generally occurs on a local scale between rocks that show different composition (Zharikov et al., 2007) .

During *infiltrational metasomatism*, the fluid flow is driven by a pressure gradient that causes the fluid derived from an external source to move through a host rock (Zharikov et al., 2007, Pirajno, 2013). Metasomatic rocks caused by infiltration show a more homogenous mineral composition through a metasomatic zone and generally occupy larger volumes than diffusion as it is a more effective transport mechanism (Zharikov et al., 2007, Yardley, 2013).

Such advection of, or diffusion through, a fluid is said to be controlled by the permeability of the surrounding rocks, which have been proposed at small-scale grain-boundaries, cleavage folia and deformation-induced permeability to cracks and fracture networks, faults, shear zones, or by creating new flow paths by hydraulic fracturing due to overpressure from devolatilisation (Vernon and Clarke, 2008, Putnis and Austrheim, 2013). In low-permeability rocks, the fluid pathways have been ascribed to the pre-existing porosity at the grain boundaries or dilatancy (permeability formed by deformation) (Putnis, 2002, Putnis and Austrheim, 2010, Putnis and Austrheim, 2013).

The general view of mass transport is that chemical components occur by solid state-diffusion at the grain scale (Vernon and Clarke, 2008). However, such a model is inadequate in explaining regional-scale metasomatic alteration, as solid state diffusion is a very slow process, except at very high temperatures (Putnis, 2002). Though the creation of new fluid pathways does not reveal how fluids can flow through entire crystals. A coupled dissolution-precipitation mechanism has been proposed, where a fluid moves through a mineral from the

grain boundaries and inwards by continuously dissolving and precipitating minerals (Putnis, 2002, Putnis and Austrheim, 2010).

Fluids can carry distinctive chemical signatures which reflect its pathway from the original source, such as hydrogen and oxygen isotopes, salinity and isotopic ratios (Yardley, 2009). However, there is also the possibility that fluids will mix and consequently show features that are valid to more than one source region (Robb, 2005). Under normal crustal pressures, the hydrothermal fluids is regarded as a fluid dominated by dissolved salts, where the Na^+, Ca^{2+}, K^+ and Fe^{2+}/Fe^{3+} are the predominant cations and Cl^- as the dominant anion, while at higher crustal pressures, between 10 – 20 kbar, more silica and alumina-silicates are dissolved into the fluid (Yardley, 2009, and references therein, Yardley, 2013). With increasing Cl^- concentration and/or temperature in a fluid, it has shown that the solubility of several transition metals, such as Fe, Mn, Pb and Zn, will also increase (Holland, 1972, Yardley, 2005, Yardley, 2013). The definition of solubility is the maximum limit of how much material a hydrothermal solution can carry under any given condition (Wood and Samson, 1998), and the increasing solubility of metals is a very important factor for ore-forming conditions (Yardley, 2013).

The work of Holland (1972) showed that in order to increase the metal solubility and transport in a fluid requires addition of components that can act as a carrier for the metal, called ligands, as pure water cannot carry a significant amount of dissolved species. The most common ligands found in fluids in addition to H_2O are NH_3, Cl^-, OH^- and HS^- (Pirajno, 2009). However, there is a many other important ligands, such as F^-, NO_3^-, CO_3^{2-}, SO_4^{2-}, PO_4^{3-}, Br^-, I^-, CN^- and H_2S, where different ligands show affinity to different metals (Robb, 2005, Pirajno, 2009). The complexes CO_3^{2-}, F^- and SO_4^{2-} and also Cl^- has shown the ability to carry REE over a significant distance and the complexing ability between the ligand and REE was also correlational to the alkali content in the fluid (Humphris, 1984).

Fluid-rock interactions

The most evident course when a fluid is not in equilibrium with a mineral, is to react and dissolve the mineral until equilibrium has been reached between the fluid and mineral (Putnis and Austrheim, 2013). With every re-equilibration between a mineral and fluid phase, there is dissolution, transport and precipitation. And this new mineral assemblage will be determined by the temperature, pressure, host-rock composition, fluid composition and fluid-rock ratio

(Robb, 2005). The temperature and pressure largely defines the most stabile mineral assemblage, the host-rock composition states the available species for the re-equilibrated mineral assemblage, and the fluid composition controls mainly to which extent the host rock is dissolved. The fluid/rock ratio is defined as the mass of solvent water in the initial aqueous phase divided on the mass of rock the fluid passes by (Reed, 1997), and the intensity of alteration is dependant on the fluid/rock ratio, as it concerns whether if a reaction will go to completion or not (Robb, 2005, Pirajno, 2009).

Importance of fluids

Field examples from the anorthositic granulites from the Bergen Arcs (Austrheim and Griffin, 1985, Jamtveit et al., 1990), with P-T conditions consistent with eclogite facies showed that metamorphic reactions was inhibited by the lack of fluids. Eclogites or eclogitized granulites could only be found where fluid infiltrating shear zones were crosscutting the granulites. This exemplified the importance of fluids during metamorphism in that the changes were not entirely controlled by the P-T conditions, but also by the fluid access.

In the St. Anthony Complex, a mylonitic biotite-amphibolite shear zone is hosted in a ophiolite aureole, formed during tectonic emplacement (Dostal et al., 1980). The study showed that the mylonite acted as a pathway so fluids could flow through and metasomatic reactions altered the chemistry of the mylonite extensively. Also the elements that are normally considered to immobile were affected, such as Ti, Zr, Nb, Y and P, and the REEs, though, each element had different degree of immobility.

Extent of metasomatism

The extent of metasomatism is controlled by the concentration of the dissolved material in the fluid and the total volume of fluid available to pass through (Yardley, 2013). The higher load of dissolved solids and higher amount of fluid available will results in increasing metasomatic conditions. However, in shallow settings there might be metasomatising conditions with low concentration of dissolved load but with high fluid flux, where as in the deeper crust there might be a small fluid flux, but with a large concentration of dissolved load in the fluid will also trigger metasomatism. (Yardley, 2013)

Cation metasomatism

Trying to structure alteration types is a rather extensive task, as many different names has been proposed based on which species is introduced, what kind of process has been performed, or what is the end result. The extensive work *Hydrothermal Processes and Mineral Systems* by Pirajno (2009) results in more than 1000 pages regarding hydrothermal processes linked to mineral resources and ore deposits, but not all hydrothermal processes leads to the formation of ore deposits. *Metasomatism and the Chemical Transformation of Rock* edited by Harlov and Austrheim (2013), does not only govern the alteration linked to mineral systems in the crust, but also small scale-dissolution-precipitation mechanisms, fluid transport and interaction, fluid composition, as well as metasomatic alteration in different tectonic settings from crust to mantle. Hydrothermal alteration seem to be the most commonly used term relating to ore deposits and is being stated as a sub-type of metasomatism (Pirajno, 2009), while metasomatism also includes the non-ore-forming settings (Harlov and Austrheim, 2013), though the terms have been used interchangeably. At places, the descriptions are overlapping, but efforts have been given in presenting relevant theory for this thesis. The following metasomatism types are described based on the species that is added and exchanged and deals with Na, Ca and K, which is the predominant exchanges in alumina- and silica-rich rocks, such as granitoids, though it is worth mentioning that also Mg metasomatism is a common reaction found in shallow marine rocks by swapping Fe and Mg (Barton et al., 1991).

Sodium and Sodium-Calcium metasomatism

Na exchange with K is the typical substitution for the Na metasomatism as they a have similar valence state, while Na can exchange with the divalent Ca, implying a coupled substitution with Na-Si for Ca-Al. The Na metasomatism with the exchange of Na for K occurs within the feldspar, by a simple base cation reaction (Pirajno, 2009):

Equation 2: Alkali feldspar to Albite

$$\underset{Alkali\ feldspar}{KAlSi_3O_8} + Na^+ \longrightarrow \underset{Albite}{NaAlSi_3\,O_8} + K^+$$

The Na-Ca metasomatism is commonly found where igneous plagioclase is replaced by albite-rich plagioclase, which can be given as:

Equation 3: Oligoclase to Albite

$$\underset{Oligoclase}{NaAlSi_3\,O_8 \cdot CaAl_2Si_2O_8} + Na^+ + H_4SiO_4 \longrightarrow \underset{Albite}{2NaAlSi_3\,O_8} + Ca^{2+} + Al^{3+} + 4OH^-$$

After Putnis and Austrheim (2013). Mafic minerals are replaced with Ca-bearing minerals, such as epidote and actinolite (Barton et al., 1991). Unfortunately, this kind of metasomatism and mineral assemblage is very difficult to separate from the greenschist facies metamorphism, which is isochemical (Vernon and Clarke, 2008).

Calcium metasomatism

Ca metasomatism is commonly seen in mafic rocks in sea floor settings, thus the name sea water alteration by Pirajno (2013). Ca is added and substituted for Mg, K and Na, where e.g. anorthite-rich plagioclase is altered to epidote, often yielding albite-rich, epidosites and quartz-epidote-chlorite mineral assemblages (Barton et al., 1991, Pirajno, 2009). Experimental studies show substantial mass transfer, where Mg^{2+} is consumed during the reaction and H+ is released, which lowers the pH of the fluid (Pirajno, 2013). Further, the H^+ can react by consumption and subsequent release of e.g. Ca and K (Pirajno, 2009). The change in alteration comes to show that metasomatic fluid evolves over time and distance.

Potassium metasomatism

K metasomatism occur when added K exchanges with Na or Ca, with either forming alkali feldspar and/or muscovite (Barton et al., 1991). Orville (1962) proposed that an equilibrated fluid phase in two-feldspar granite would become poorer in alkali feldspar and richer in albite as the temperature is lowered. When a fluid that is equilibrated with the hot two-feldspar granite (high K/Na ratio) flows into cooler parts of rock the fluid must lower its own K/Na ratio in order to reach equilibrium, which can be achieved in two ways: One, replacing the albite with alkali feldspar, and thus increase of the Na content and reduction of the K content in the fluid; and two, seritization of the plagioclase, which will lower the K content in the fluid by crystallizing K-bearing sericite (Orville, 1962).

Hydrogen ion metasomatism

H^+ metasomatism is defined by the exchange of H^+ with K, Na or Ca, yielding either a hydrated mineral assemblage or the release of water and cations (Vernon and Clarke, 2008, Pirajno, 2009). The extent of alteration is controlled by the fluid acidity and the neutralizing

abilities of the reacting minerals (Barton et al., 1991). An example is seritization of the alkali feldspar is where H^+ is consumed and K^+ is released, enabling the alkali feldspar to react and form sericite (Hemley and Jones, 1964).

Equation 4: Alkali feldspar to Muscovite

$$\underset{Alkali\ feldspar}{3\,KAlSi_3O_8} + 2\,H^+ \longrightarrow \underset{Muscovite}{KAl_3Si_3\,O_{10}(OH)_2} + 2\,K^+ + \underset{Quartz}{6\,SiO_2}$$

Mineral alterations are reactions where one mineral can react to form a new mineral with a different composition, which can be visually identified by their texture and structure. The next two paragraphs briefly present the most abundant metasomatic alterations found at Gråkallen.

Seritization

Seritization is the process where Al-rich minerals, such as alkali feldspar and plagioclase, are replaced by sericite, a fine-grained variety of muscovite (Fettes et al., 2007). The growth of sericite requires access to water-rich fluid and a source of K^+ in order for the alteration to occur, either from the alkali feldspar or externally. In sericitization of the plagioclase, the K^+ interacts with the plagioclase so the Ca-component in the plagioclase can release the Ca^{2+} into solution while K^+ remains to form sericite (Equation 7) (Shelley, 1993). The feldspar minerals are prone to alteration and are commonly found to have a rather dusty appearance in thin sections.

Saussuritization

Calcic plagioclase is replaced by a saussurite mineral assemblage, which constitute of epidote minerals, sericite and calcium-silicates, as the available Ca^{2+} in the solution resulted from the seritization are free to form epidote while the altered plagioclase is left as more albite-rich than initially (Equation 8) (Shelley, 1993, Fettes et al., 2007).

Methods

Field work preparation and mapping

A total of 30 days were spent in the field mapping out Gråkallen, the central parts of the Fagervika granitoid. The public map service ”Norge i Bilder” (www.norgeibilder.no) offers high-resolution aerial photos of large parts of Norway and carry with them geographical coordinates in their metadata, in which can be used to georeference aerial photos. With this, a method was developed based on the aerial photos and making it possible to map outcrops directly on the same scale as the photo, approximately 1:300. An overview map was downloaded and divided into rectangles based on an appropriate section of the area. (The maps downloaded in 2013 were printed with a datum and geographical coordinates, but that service was removed sometime in 2013/2014. However, the coordinates of the maps could be found in the map metadata.) The maps were imported into Inkscape, an Open-Source vector graphics editor for Windows, Mac OS X and Linux (Harrington et al., 2003). Based on the colour and shape contrast given by different features in the field (e.g. vegetation, outcrops, lakes, man-made structures, etc.) one could execute auto-contouring which digitally created contour lines around the different features.

When in the field, you bring a white map with contour lines to draw on, together with the associated aerial photo. These two maps together made it easier to determine your exact position by being able to identify the contrast of different shapes, sizes and colours of structures and features as they are both represented on the map and in the field (Sørensen and Granseth, 2014).

Sampling

32 samples were collected during fieldwork in 2013 and 2014. Some of these samples were split into several individual ones, making it a total sample number of 38. This thesis addresses 26 of the collected samples, with 22 polished thin sections representing 9 granodioritic samples, 8 phyllonitic including the epidote-rich shear zone, 2 aplites, 3 hydrothermal quartz with sulphides. Three sets of paired samples were taken: P18A - P18B, P26B-u - P26B-d and P31-u - P31-d. These six samples represent the local transition between granodiorite and altered phyllonite and epidote-rich shear zone. The four samples that are not represented in the thin section selection consists of three granodioritic that were not prioritized due to close

proximity to other similar samples, along with one massive sulphide sample sent to geochemistry and that is associated with one of the hydrothermal quartz samples. And also, the selection and number of samples were based on their geographical distribution within the field area, the lithology these rocks represent and how easy it was to obtain an unweathered and fresh sample. For full overview of all samples and methods, see Figure 14.

Sample preparation

Thin Section

The thin section laboratory at the Department of Geology and Mineral Resources Engineering at the Norwegian University of Science and Technology (NTNU) prepared the polished thin sections with a size of 28×48 mm and thickness of 30 μm.

Crushing, milling and micronization

The main part of crushing and milling were executed at the Mineral Processing Lab at the Department of Geology and Mineral Resources Engineering, where the crushing and milling steps are depicted in the preparation column in Figure 4. First, the samples were crushed in the Retsch Jaw Crusher, where the size of the samples was reduced from several centimetres and down to approximately 0.5 cm grain size. Second, further crushing of the samples in the Disc Crusher reduced the grain size further down to a powdery material. After the first two steps, the material was split up in two fractions, 20 to 30 g going to preparation for X-Ray Diffraction (XRD) and 70 to 120 g to be shipped off to ALS Chemex for whole-rock analyses. Third, the 20-30 g fraction were milled in a Siebtechnik Disc Mill for 4 minutes with agate grinding set, to reduce the grain size prior to using the McCrone Micronizing Mill, in step four. The micronization were performed by stacking 42 agate pellets in a plastic container along with two heaped spoons of sample material and 10 mL of ethanol. The mill ran for 4 minutes and the container was later flushed with more ethanol to collect the milled material. The sample was dried at 100°C, collected and pressed in a standard Bruker PNMA XRD sample holder, set for XRD analysis. The fractions that were shipped off to ALS Chemex for whole-rock geochemistry and trace element analysis went through the sample preparation procedure PREP-31, where the sample was weighed and logged in at arrival, crushed to where at least 70% of the sample passed a 2mm sieve, then split and pulverized to where 85% passes 75 micron sieve.

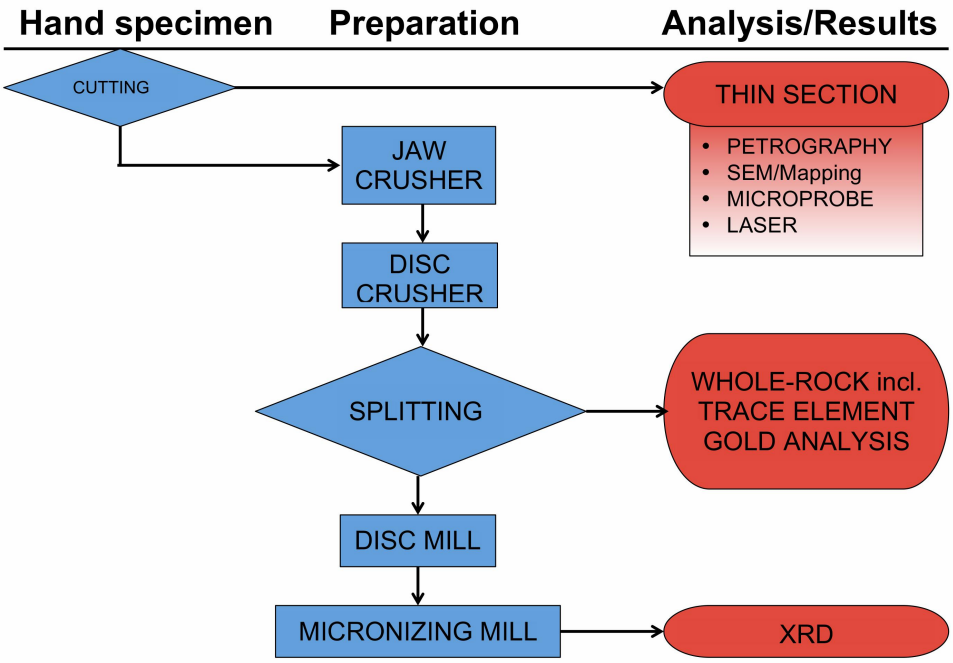

Figure 4: Schematic overview of the work flow during sample preparation. The work flow starts in the upper left corner with cutting of the hand specimen, with one part going to thin section preparation and one part going to preparation for geochemical analysis. For the geochemical analyses, two crushing steps are required for the material that is going to whole-rock incl. trace element and gold analysis. Four crushing and milling steps were necessary for the material going to XRD analysis.

Petrography

Polarized light microscopy was performed for a first-hand identification of the different mineral phases in thin sections. Images of the thin sections were captured by camera mounted on the microscope and with Epson Perfection V600 Photo Scanner with added linear polarized filters.

Geochemical analysis

Modal mineralogy was performed by XRD analysis at the Department of Geology and Mineral Resources Engineering, NTNU. Mineral chemistry analysis was achieved by Electron Microprobe Analysis (EMPA) at the Department of Materials Science and Engineering, NTNU and by Laser Ablation Inductively Coupled Mass Spectrometry (LA-ICP-MS) performed at the Texas Tech University in Lubbock, USA. Scanning Electron Microscopy (SEM) work was performed at the facilities of The Geological Survey of Norway (NGU) and

the Department of Materials Science and Engineering, NTNU. The external company ALS Chemex performed the analyses for the whole-rock geochemistry including trace element and gold analyses. All descriptions of the methods used by ALS Chemex are based on the description pamphlet that is available and can be downloaded from their website (www.alsglobal.com).

Whole-rock geochemistry

X-ray diffraction (XRD)

X-ray powder diffraction is a fast, but powerful and versatile analytical method that can determine the physical and chemical characteristics of crystalline minerals. The diffraction utilizes the interaction between electrons and x-rays and the resulting interference from the unique atomic arrangement of a material (Will, 2006). To ensure proper counting statistics and to minimize the effects of large grains and preferred orientation, the XRD samples were milled in ethanol in order to obtain an equal grain size distribution and with d_{50} below 15 µm. 20 samples were analysed in a Bruker X-ray Diffractor D8 Advance at the Department of Geology and Mineral Resources Engineering, NTNU. Settings were adjusted to 40 kV, 40 mA and CuKα radiation of wavelength Kα1 = 1.5406 Å and Kα2 = 1.54439 Å and a Kα1/ Kα2 ratio of 0.5. Diffractograms were recorded from 3-65 °2θ, in 0.009 °2θ increments with 0.6 s counting time per increment and with a total analysis time was 71 minutes per sample (Cepuritis et al., In review). The interpretation of each sample was done in the EVA software and is based on the results from the petrography. The quantification was performed in the Rietveld refinement software TOPAS 4.2.

Whole-rock geochemistry, by method ME-ICP06

The whole-rock analyses were preformed on the fractions sent to ALS Chemex. 0.200 g of the prepared sample were mixed together with lithium metaborate/lithium tetraborate flux (0.90 g) and fused at 1000°C. The melt is then cooled and combined with 100 mL of 4% nitric acid/2% hydrochloric acid. This solution is analysed by inductively coupled plasma – atomic emission spectroscopy (ICP-AES), and the major elements were reported in weight percentage of the oxide.

Loss on Ignition (LOI), by method OA-GRA05

1.0 g of sample material were heated in an oven at 1000°C for one hour, then cooled and weighed. The loss on ignition percentage was calculated based on the mass difference and it reveals the loss of any remaining volatiles (e.g. H_2O and CO_2) in the sample.

Trace element analysis, by method ME-MS81

0.200 g of prepared samples were added to lithium metaborate flux (0.90 g), mixed and fused at 1000°C. The melt is cooled and dissolved in 100 mL of 4% nitric acid/2% hydrochloric acid. This solution is analysed by inductively coupled plasma - mass spectrometry (ICP-MS), and the results are reported in parts per million (ppm).

Gold analysis, by method Au-ICP21

A sample is fused together with lead oxide, sodium carbonate, borax, silica and other required reagents, mixed with gold-free silver and then yielding a precious metal bead. The bead is submerged in 0.5 mL diluted nitric acid and heated in a microwave oven. Then 0.5 mL of hydrochloric acid is added to the mixture and run again in the microwave. The resultant solution is cooled, diluted to 4 mL and analysed by ICP-AES against known standards.

Mineral chemistry

Scanning Electron Microscope (SEM)

SEM work was preformed at two different locations. At NGU, a 1450 Variable Pressure (VP) SEM manufactured by LEO Electron Microscopy Ltd was used. It has an X-ray analytical system and accompanying INCA software, suite version 4.09 by Oxford Instruments. A Hitachi Analytical Variable Pressure SU6600 SEM with Bruker Quantax 800 Espirit software was used at the Department of Materials Science and Engineering, NTNU. The objective for these investigations was to identify different mineral phases by using SEM in addition to petrographic investigations. The investigations performed at NGU did not have carbon-coated thin sections, as opposed to the analyses run at NTNU, which were coated with an Agar Turbo Carbon Coater. As most geological samples are non-conductive, a conductive coating (e.g. carbon) is necessary to prevent charging of the sample (Reed, 2005). But by running the SEM in variable pressure mode creates a neutralizing environment for the sample by injecting gas into the specimen chamber and making the carbon-coating redundant (Reed, 2005). At NGU, the beam current and acceleration voltage were set to 70 μA and 15 kV, respectively.

The probe current and working distance were set to 1.2 nA and 15.0 mm. At NTNU, the working distance was set to 15 mm and the acceleration voltage was 15 kV. A method was set up for visualizing the distribution of elements at thin section scale, especially for the major phases such as quartz, feldspar, mica and epidote. By setting up an "AutoMate" session within the INCA software at NGU, the software captures backscatter images and element maps at specific coordinates, in which it scans entire thin sections. After the finished session, the INCA software stitched the backscatter images and element maps together to a larger image with larger overview of the thin section. The adjusted variables in the INCA software were image resolution of 1024x768, medium speed, data of 8 bits and one frame. The smart map setup were determined to a map resolution of 1024x768 (same as the image resolution), process time 3, spectrum range of 0-10 kV, number of frames 3, dwell time 200 and channels 2K.

Electron microprobe analysis (EMPA)

The EMPA is an analytical technique used to quantitatively determine the chemical composition of selected samples, compared to standards of known composition (Reed, 2005). A total of 93 points were analysed, distributed on seven polished thin sections that were prepared and carbon-coated, in order to create a conductive surface on the samples. The analyses were conducted on a JEOL JXA-8500F thermal field emission electron probe micro analyser with wavelength dispersive detectors (WDS) at the Department of Materials Science and Engineering at NTNU. The analyses were performed with a defocused beam at 2 μm, beam current at 20 nA with acceleration voltage at 15 kV.

The microprobe analysis sessions were divided into two lists based on which minerals/elements that were scheduled for examination (Table 1). The two lists had eight elements in common (Si, O, Ca, Al, Fe, Mg, Mn, Ti) in addition to other elements specific for the mineral phases they were aimed to analyse. List one was designed for analysing epidote, allanite, apatite, titanite and zircon, and included nine elements (Ce, La, Y, Zr, Hf, P, F, Cl, Nd) in addition to the eight common elements. List two was set up for analysing the feldspars, micas and garnet and had five extra elements (K, Na, Ba, Cr, S).

A total of twenty-two reference standards were used for different elements, which included apatite (F, P, Ca), barite (Ba), benitoite (Ti), chromium oxide (Cr), molybdenite (S), monazite (La, Ce), olivine (Mg, Fe), plagioclase with An_{65} (Na, Al, Si), rhodonite (Mn), sanidine (K),

tugtupite (Cl) and cubic zirconia (O, Zr), which came from Astimex Scientific Limited. NdF_3, pure Yttrium and an Hf-wire consisting of hafnium and zirconium referenced the elements neodymium (Nd), yttrium (Y) and hafnium (Hf). Counting times for Mn, Mg, Fe, Al and Hf were 20 seconds and the rest of elements were counted for 10 seconds.

Table 1: Overview of the different elements in each element list used for microprobe analysis. The first eight elements are the same in each list, while the remaining nine and five elements differ based on the mineral phases that was analysed. Note the difference for the detection limits of the first eight elements that are common for both lists.

Element list 1	Detection limit (ppm)	Element list 2	Detection limit (ppm)
Epidote, Allanite, Apatite, Titanite, Zircon		Feldspar, Mica, Garnet	
O	763	O	473
Mg	68	Mg	101
Al	68	Al	95
Si	176	Si	159
Ca	134	Ca	119
Ti	118	Ti	111
Mn	117	Mn	157
Fe	141	Fe	187
P	121	K	125
F	493	Na	146
Cl	113	Ba	176
Y	391	Cr	144
Zr	298	S	300
La	453		
Ce	468		
Nd	884		
Hf	500		

For the epidote and allanite formula calculations, the standards for Si, Al and Ca changed to diopside for the Si and Ca, and almandine garnet for Al, due to resolution issues with the microprobe data.

Laser Ablation

Epidote, allanite and titanite grains in four samples (P01, P28, P31-u and P31-d) were selected for LA-ICP-MS, as these minerals have the ability to hold REE. The LA-ICP-MS analyses were performed at the GeoAnalytical Laboratory at Texas Tech University using their New Wave UP213 Nd:YAG laser system, with an Agilent 7500CS ICP quadrupole MS. Spot diameter of 25 – 30 microns were selected for the allanite, and 40 microns for the epidote and titanite grains, with a laser pulse rate of 5 Hz and fluence of 10 – 14 J cm^{-2}. The precision and accuracy were determined for LA-ICP-MS system by reanalysing basaltic glass BHVO-2 standard, and most of data were reduced using NIST 612 glass with 10 allanite analyses were reduced using the NIST 610 glass standard. An internal standard of 30 wt. % SiO_2 for all three minerals were applied. Professor Calvin Barnes performed the analyses along with senior research associate Melanie Barnes at the Texas Tech University.

Sources of error

Construction of maps

"Norge i Bilder" is based on several layers of aerial photos where the newest photo is the top layer. 23 of the maps used were produced in 2013 based on aerial photos from 2010, where as the 5 maps produced in 2014 were based on photos from 2013. New aerial photos of Gråkallen were taken in 2013, which were not available at the time of the production of the first set of maps. This age difference could create a slight variation in how the graphics editor sets the contours on the maps. Comparison of aerial photos from 2010 and 2013 show a difference in image resolution and the colour of the vegetation in the area. The vector graphics editor detected the differences between the two maps, and thus, the contours were displayed differently. When georeferencing the finished maps, the overlapping parts between the maps had correct coordinates, but because the aerial photos had displaced the contour lines, it seemed like the maps are not correctly referenced, as shown by a slight displacement of contour lines between maps.

In order to keep it clear and organized, a systematic grid parallel to compass orientation should have been constructed for the entire area and all the maps should have been constructed at the same time, and by doing so would have minimized the contour line and georeferencing issues mentioned previously.

Sample preparation

The first step after the sample collection was to divide a sample into smaller pieces and select parts for thin section preparation and geochemical analysis. The selected samples and pieces are considered to be quite homogenous and representative, and therefore any separation of the samples should not create a distortion of the data. In order to minimize contamination during sample preparation, the equipment was vacuumed and blown with compressed air and then dried with alcohol after each sample. An agate grinding set was preferred in the Disc Mill, as the tungsten carbide (WC) could contaminate the samples. The sulphide-rich samples were staining the milling equipment due to the small grain size and by crushing quartz in between each sample in both the Disc Mill and micronizing mill resolved this issue as the quartz acted as a cleaning agent. Performing XRD analysis on the epidote-rich shear zone alone was desired, so all other parts were removed from the sample manually. When analysing the XRD results of the shear zone, it raises some doubt about the success of the analysis. At least one mineral appears in such a substantial proportion that cannot be supported petrographically, unless it was viewed as contamination from the removed parts. XRD results reveal plagioclase modals of 21.3 % (Table 2), but no plagioclase is observed in the shear zone and Na-map from the SEM mapping of the shear zone reveals a depletion of the Na component (Figure 20), where as albite is well represented in the white leached zone and in the granodiorite.

Mass loss during preparation

During preparation for the geochemical analysis every sample was weighed between every crushing and milling step. In that way, it was easy to keep track of the mass loss in the process. The average for all samples from start to end, going through the jaw crusher, disc crusher, sample splitting and disc mill were a mass loss of approximately 8%, ranging between 5 and 15 %. The greatest contributor of mass loss was the disc crusher that could leave behind piles of uncrushed material within the crusher, resulting in an average loss of 6.5 %. The smallest contribution came equally from the jaw crusher and the disc mill with an average of 0.8 % and 0.6 %, respectively. The splitter revealed a surprising loss of 1.6 % even though splitting does not involve any grain size reduction, but a separation of the material. However, there is no reason to assume the loss of material created a misrepresentation of the modal mineralogy by e.g. loss of only one mineral phase. In the instances where the sulphide were staining the equipment came from samples that contained one or two mineral phases,

and those were not considered to be homogenous or representative for the whole-rock to begin with.

XRD

The XRD method is based upon that the surface of the sample shows a mineral grain orientation distribution representative of the rock sampled. Exaggerating the XRD sample preparation could create a preferred orientation of the grains along with sample compaction, which makes the results deviate from the true random distribution of the crystals (Will, 2006). This is most likely not an issue as spending too much time preparing the XRD moulds were avoided. The overlapping of diffraction peak intensities can make the identification of the minerals problematic. However, the samples show a very simple and distinct mineralogy, so no obvious problems were encountered. XRD is a quantitative method for the major elements and modal percentages of the minerals has an uncertainty that should be accounted for, hence all the quantified results should be rounded to the nearest percentage and the results reporting less than 1% should be described as such. When the interpretation is done in conjunction with petrographic or similar data, XRD is a very reliable and robust method.

SEM

One must also take into consideration that some elements do have overlapping peak intensity, shown in the SEM spectra. The SEM software will be able to deconvolute and separate the peaks, but not always, so it could be a smart move to consider which element that would give the most sense in the given context of your sample (Goldstein et al., 2003). This was the case when both Ag (2.983 keV) and Th (2.996 keV) showed up on the spectra interchangeably. This was resolved later when analysing at the EMPA with the WDS detector and the results came back positive for Th.

External analyses

ALS Chemex is a globally acclaimed company that provides geochemical analytical data to the industry. They proudly announce their consistency and reliable service to their clients and all their methods and descriptions are available online for download to any user. The ALS Chemex laboratory follows strict regulations, certifications and requirements of international standards. Along with the results when the analyses are completed, they attach a quality control certificate that compare the analyses to a reference standard range in which the measurement should fall in between.

EMPA

The microprobe performs quantitative measurements by using known standards with known compositions and it is considered as a reliable and accurate method. Any result should give a total of 100, but that is hardly ever the case. The analysis reports totals commonly in the range of the 90 to 103, but also as low as 76.3 in the barium sulphate and as high as 108.8 in quartz. The low total could be that an unknown element also present but was not in the element list, thus not counted for. The analyses regarding the more complex minerals of epidote and allanite show an overall high total ranging between 102 to 104 %, but very low totals when converted to the oxide version of the element. The high numbers could be the results of overestimating the counting in a simple mineral, such as quartz, which normally does not hold any other elements. Charging of the sample could give a total above 100 % if the beam has been stationary for too long or if the carbon coating has a non-uniform thickness or other structures (Reed, 2005).

LA-ICP-MS

Some of the ablation spectra were quite rough, which may be due to internal zoning of the mineral or the presence of the more than one phase in the ablation zone. To take that into consideration, P (apatite), Ti (rutile, ilmenite, magnetite), Ba and Sr (for muscovite and feldspar) were carefully monitored. During the ablation, the laser drilled through and into the glass slide in which the thin section is attached to. Drill-through are usually seen as enrichment in Zr and possibly Ba, and my section appear to be enriched in Zr. In order to prevent contamination, the laser signal was cut off prior to the contamination in the signal.

Results

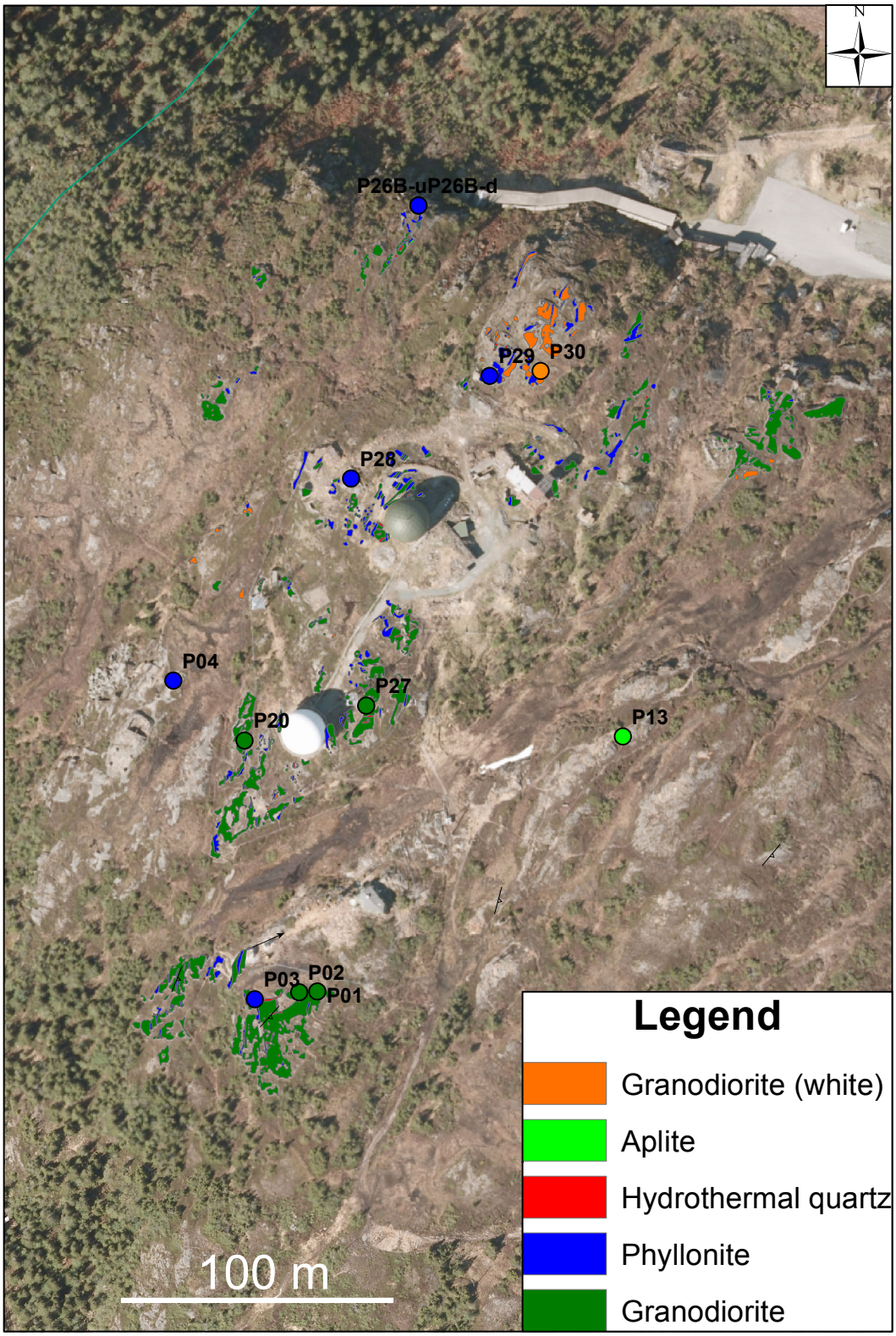

Figure 5: Geological map constructed based on the fieldwork done in 2013 and 2014. Magnified areas of the map are available in the appendix, as most of the details are lost in this overview map. The granodiorite shown by the orange and green colour in the legend represent the same mineralogy, but were separated due to of their colour differences in the field.

Field observations

The landscape at Gråkallen is dominated by good rock exposure and on either side of the peak of Gråkallen; the lithologies have a strike going N-S to NE-SW (Figure 5). Bogs and marshes are located between the outcrops, which appear to be parallel to the strike of the different lithologies. The depressions of the bogs may be a result of weaker zones in the rock.

Fagervika granodiorite

The granodiorite is holocrystalline and hypidiomorphic to allotriomorphic, with a colour variability ranging from green-white (Figure 6b) to white-pink (Figure 6c) and pink-green. It is peraluminous with A/CNK >1 and classifies as a granodiorite in the Gråkallen area (Figure 6d), by having quartz and plagioclase as the major constituents in the rock (Streckeisen, 1976, Le Maitre et al., 2002). The granodiorite is weakly foliated and shows a dip ranging between 22 and 42 degrees with an average of 30 degrees towards the southeast. At outcrop, the surfaces of the granodiorite are rounded and massive (Figure 6a), with crosscutting phyllonitic shear zones, quartz veins and aplite dykes. Xenoliths of greenstone material have also been found within the granodiorite (Figure 6b). The white-pink colour variation could be the result of a different colour variety of microcline, as it can be colourless, pink, white and even yellow, red and green (Deer et al., 1992).

The *quartz* show a dominant grain boundary migration texture with long wavelength bulges that has been overprinted later shown by bulging at grain boundaries and an inequigranular grain size distribution. The *plagioclase* is anhedral to subhedral with typical tabular habit. The grains exhibit polysynthetic twinning with occasional kinking. Seritization of the plagioclase with an occasional unaltered rim, which indicate a different composition of the rim. Infrequent saussuritization gives a disordered appearance with inclusions of both sericite and epidote. *Alkali feldspar* is anhedral, displaying albite exsolution lamellae and microcline twinning, with small polygonal albite grains crosscutting the alkali feldspar and swapped-rim development. The recrystallized quartz and neocrystallized albite from alkali feldspar are distinguishable by the size and grain shape: the quartz has bulging grain boundaries, amoeboid shape and sweeping undulose extinction and subgrains, whereas the albite has an averagely smaller and equant size with Carlsbad twinning. *Epidote* is found along grain boundaries and in aggregates, both as fine-grained and more euhedral and frequently along with platy *muscovite*, anhedral *titanite* and cubic *pyrite*. A distinct grain boundary between

the core and rim has been observed (Figure 27). Brown pleochroic *allanite* is occasionally observed, often as a gradational transition from allanite to epidote.

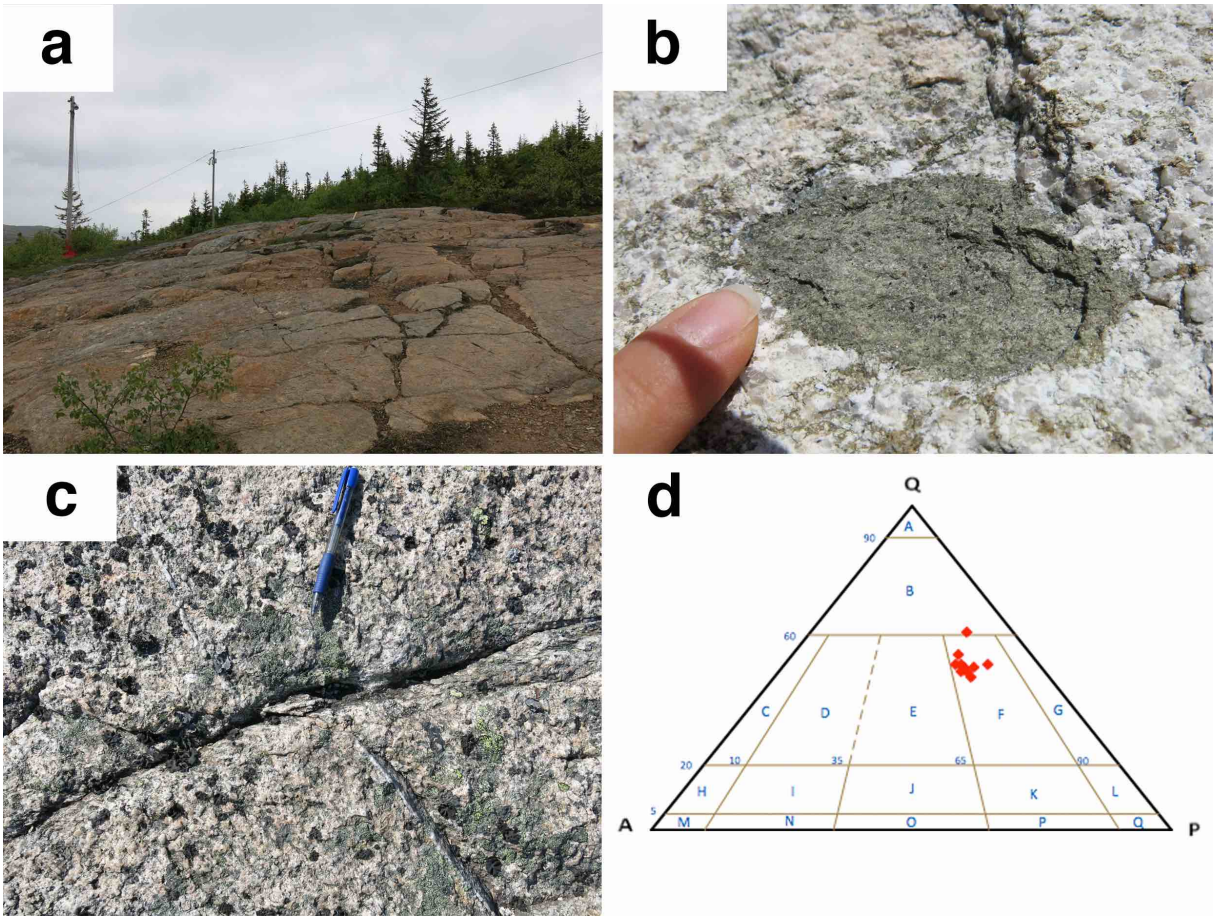

Figure 6: Field observations of the granodiorite: a – The surface rocks at Gråkallen are usually massive and very rounded, with a very weathered appearance shown by the reddish colour evident at some places. View towards the SW. b – Small xenoliths of greenstone material within the green-white granodiorite, but only a few have been found. c – A typical appearance of the white-pink granodiorite, along with a thin quartz vein transecting from the upper left to the lower right corner, which later were crosscut and dragged by a thin shear zone. d - QAPF diagram for plutonic rocks after Streckeisen (1976) and Le Maitre et al. (2002) shows the granodioritic composition for the rocks specifically at Gråkallen. One sample (P26B-u) has a slightly higher quartz proportion (Q = 61), putting it in the quartz-rich granitoid field.

Phyllonite

The deformed rocks at Gråkallen are a phyllosilicate-rich mylonite with a significant proportion of muscovite (Sander, 1911, Yardley, 1989, Passchier and Trouw, 1996, Fettes et al., 2007). The rocks are distinguished mainly by the white-yellow colour at outcrop scale with elongated quartz grains set in a muscovite matrix, where it defines a foliation and lineation. The lineation plunges towards the northeast with a dip of approximately 32 degrees. Rust is often present due to the weathering of pyrite, as cubic cavities can be seen at certain

locations. The phyllonite ranges from being platy and splitting up like slates to a more massive, rounded rock (Figure 8a-d).

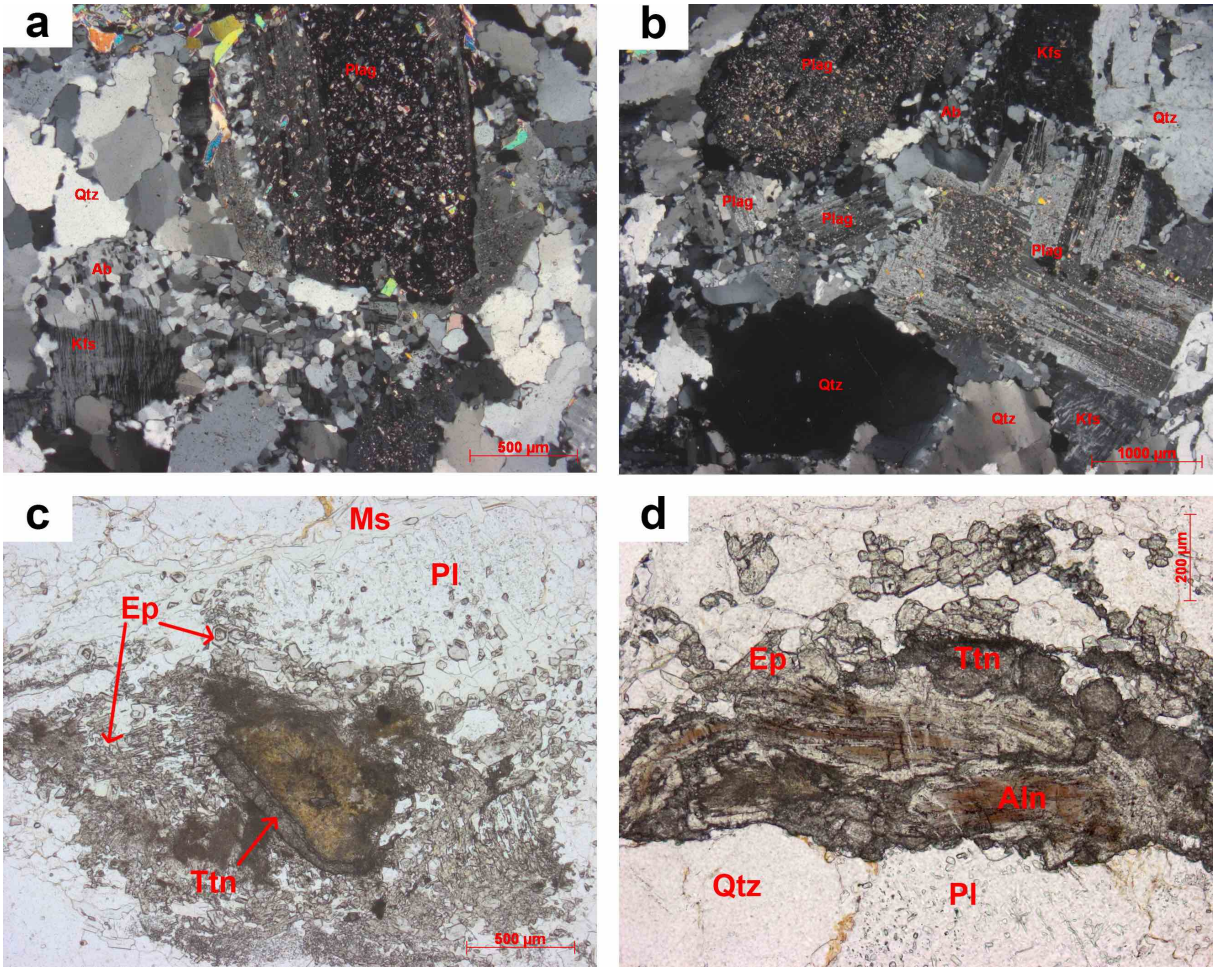

Figure 7: Mineralogical and textural observations in the granodiorite: a – Recrystallized quartz showing wavy grain boundaries and altered plagioclase with weak polysynthetic twinning, seen by the many inclusions of sericite and muscovite along the grain boundaries. The alkali feldspar is showing clear albite exsolution lamellae, which are mantled by polygonal albite grains with Carlsbad twinning. b – Image shows the least deformed sample, P20. The plagioclase has a dusty appearance due to the seritization and saussuritization. The quartz shows undulose extinction with weakly curved grain boundaries. Note the completely extinct quartz grain with the hexagonal habit in the lower left corner. c – Large clusters of subhedral epidote, along with a tail-shaped titanite and a brown mineral aggregate that contain a Th-bearing mineral. d – Anhedral mineral aggregates consisting of titanite, epidote and brown pleochroic allanite cores.

The main mineral assemblage is quartz + muscovite ± pyrite. Porphyroclasts of albite with inclusions of quartz has also been found within the muscovite foliation, but it is considered to be a transitional feature between the granodiorite and the phyllonite (see Figure 9b and d). In thin section, the *quartz* is recrystallized showing a dominant grain boundary migration that later has been overprinted by bulging, with occasional relict quartz grains that are not recrystallized (Figure 9e). Muscovite defines the foliation and the grain size varies between

the samples, as phyllonites with the finer-grained muscovite appear to be more resilient than the phyllonites with coarser-grained muscovite. Remnants of accessory minerals are found within the foliation, such as *titanite* and *zircon* (Figure 9c). This suggests that these minerals has remained immobile during alteration and deformation and can thus be used for isocon analysis. A few grains of highly fractured anhedral alkali feldspars show signs of brittle deformation.

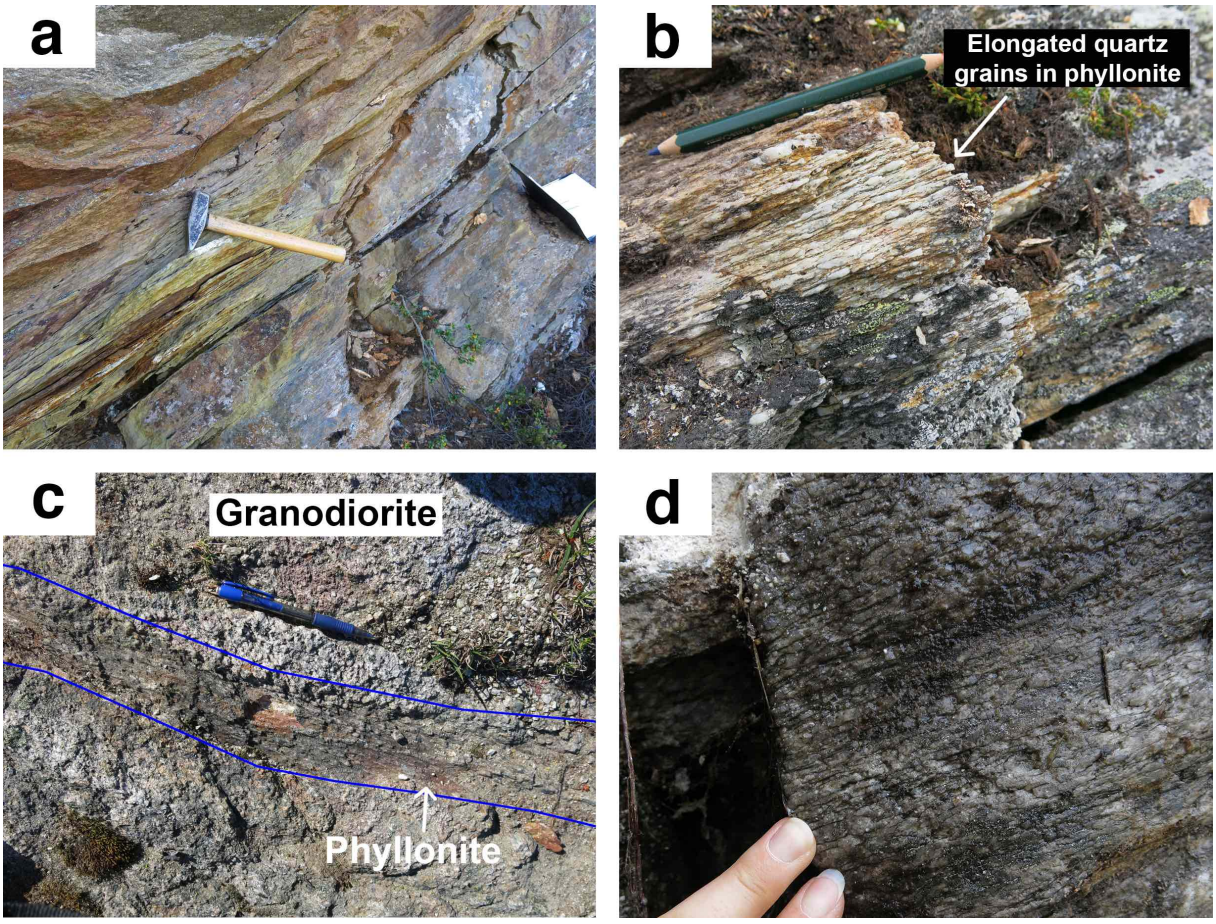

Figure 8: Field observations of the phyllonite: a – A phyllonite breaking off into slate-like sheets. This has only been found on a few localities. b – Protruding, elongated quartz grains set in the muscovite matrix. This is the most common sort at Gråkallen, being very brittle, easy-breaking and is stained by rust. c – Centimetre to decimetre thick shear zones crosscutting the granodiorite on the surface of the ground. It is very tough rock and thus very hard to sample. d – The most massive variety of the phyllonite. Trying to sample this rock with a hammer resulted in crushing the rock, as seen in the upper left corner.

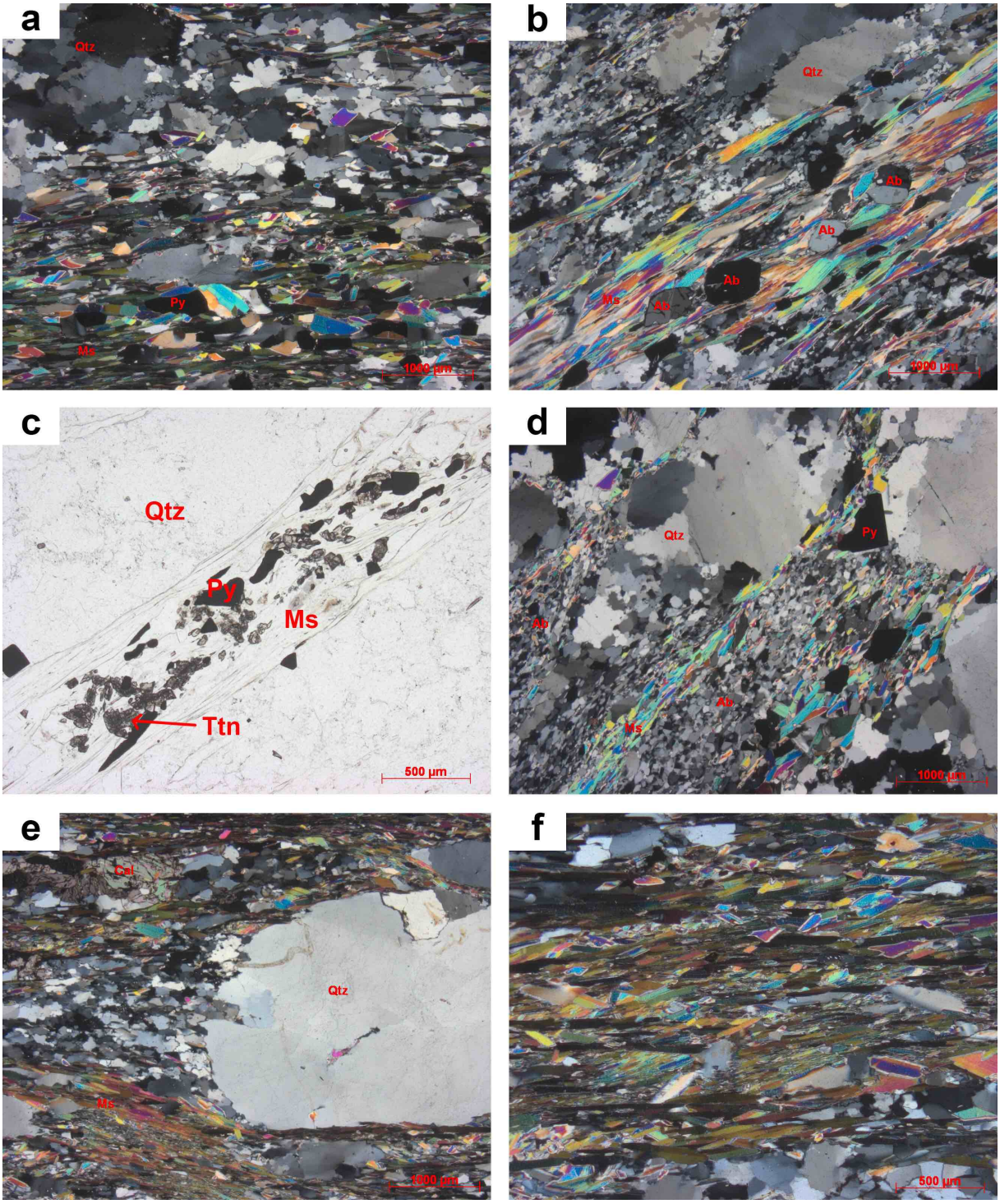

Figure 9: Mineralogical and textural observations in the phyllonite: a – A typical view for the phyllonite, with recrystallized quartz, muscovite defining the foliation of the rock and dispersed pyrite. b – Albite porphyroclasts set in the muscovite matrix, also showing Carlsbad twinning. Those clasts were also examined with the EMPA. c – Titanite grains set in the muscovite foliation in phyllonite along with pyrite, suggesting immobility during deformation. d – Sample P18-B shows what appear to be the transition between the granodiorite and phyllonite. The sample has 27 wt. % of albite that can be seen as the small polygonal grains. e –Large relict quartz with recrystallized quartz on the side edges. This sample also contains an anhedral carbonate mineral and muscovite foliation. f – Same sample as e, with a closer view of the muscovite that is sub-horizontal, smaller grains occurring at an angle to the foliation and larger grains that crosscuts the foliation.

Hydrothermal quartz

The occurrences of hydrothermal quartz are distributed fairly unsystematic throughout the area around Gråkallen, usually as veins crosscutting the granodiorite, indicating a wet hydrothermal system (Figure 10a-b). The vein thickness varies, on a centimetre to decimetre scale. The quartz mostly milky white, but also occurs as transparent, almost glassy. Within the tunnels at Gråkallen, there is a massive ten-centimetre thick quartz vein associated with massive pyrite and phyllonite that has an *approximate* strike of E-W and 45 degree dip towards the north (Figure 10c-d). Samples from the tunnels show large, subhedral to euhedral phenocrysts of *pyrite*, hosted within massive *quartz*. The quartz-domains exhibit deformation lamellae, undulose extinction and fluid inclusion trails. The quartz within the pyrite domains shows primary quartz growth extending from the pyrite grain, but also amoeboidal grain shapes. A few inclusions of *chalcopyrite* within the pyrite grains have been located.

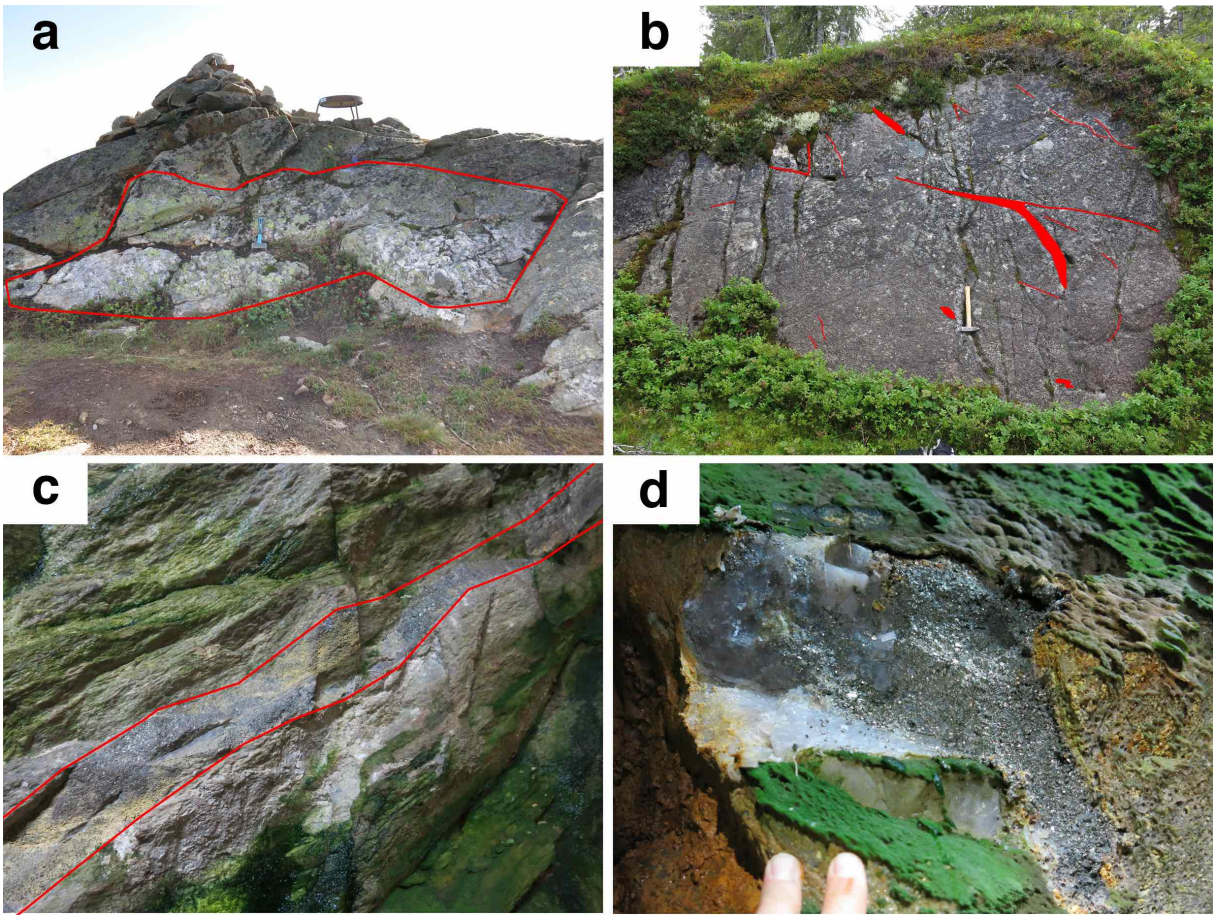

Figure 10: Field observations of the hydrothermal quartz: a – Massive hydrothermal white milky quartz, with the view facing the vein. Surrounding rocks are granodioritic. b – Quartz veins occurring as thin veins, thicker veins and rounded blobs in all directions. c – Massive hydrothermal quartz-sulphide vein in the tunnels at Gråkallen. The tunnels crosscut this particular vein, so the full length of the vein could be followed on each side of the tunnel. d – The sampling area of the massive hydrothermal quartz-sulphide vein. Most of the sulphide came off in large pieces.

South of Gråkallen and Vintervatnet, an eight-metre long quartz vein is exposed along a road cut where previous studies has shown ore mineralizations consisting mainly of pyrite with numerous inclusions, in which some still remain unidentified (Størseth, pers. comment). At this locality, the *quartz* has been recrystallized into new, amoeboidal grains, which exhibit bulging along the already wavy grain boundaries. Elongated *muscovite* occur along a small fracture, forming aggregates with subhedral to euhedral *epidote* that shows oscillatory zoning, which is common in hydrothermal epidote (Franz and Liebscher, 2004). Cubic *pyrite* up to 2 mm occurs with sporadic green *chlorite*. Subhedral *titanite* showing typical wedge-shape occurs as both isolated crystals and along with epidote and muscovite.

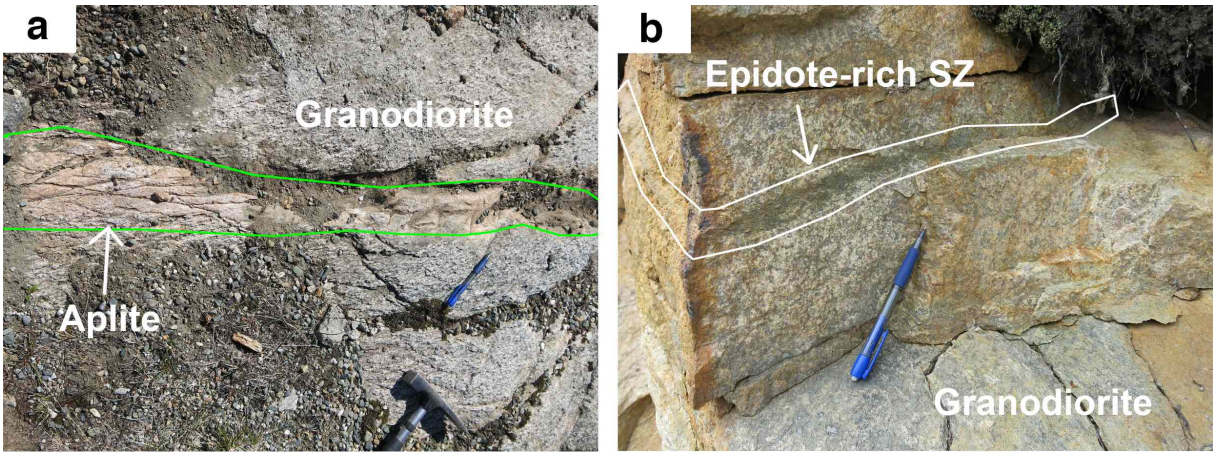

Figure 11: Field observations of the aplite and the epidote-rich shear zone: a – Thin pink aplite dyke that can only be followed for a few metres, as it pinches out and is covered in gravel. Note the pen for scale. b – 2-3 cm thick epidote-rich shear zone crosscutting the pink-green granodiorite. Note that the shear zone occurs on both sides of the block, enabling a 3D view.

Aplite dykes

At a few aplite dykes have been found within the granodiorite. The dykes are approximately 10 cm wide, pink-coloured with small porphyroclasts (Figure 11a). The dykes pinch out into the granodiorite and cannot be followed more than a few meters. Phenocrysts of *quartz*, *alkali feldspar* and *plagioclase* are set in a matrix containing the same minerals, in addition to *muscovite* and *epidote* and accessory *titanite*, *allanite* and *pyrite*. The aplite shows signs of alteration and deformation, seen by the recrystallization of quartz and seritization and saussuritization of the plagioclase and a few grains of *biotite* partially replaced by *chlorite*.

Epidote-rich shear zone

Along the road cut close to Blomstertjønna, an approximately 2 cm wide green epidote-rich shear zone in a pink-green granodiorite, with white discolouring surrounding the shear zone

(Figure 11b). Section one, the epidote-rich shear zone, consists of large euhedral crystals of *epidote*, associated with *pyrite* and aggregates of finer-grained epidote along with *quartz* and *muscovite* and occasional *titanite* (Figure 12c-d). Section two, the white leached zone; surrounding the shear zone holds mainly *quartz* and polygonal *albite*. Section three, the pink-green granodiorite, composes of *quartz*, pink *alkali feldspar* and white *plagioclase* (Appendix - Petrography) that is similar to the other granodiorites that have been sampled.

Shear zone on the steep cliff

By following the fence to the northwest end of Gråkallen, there is a spectacular shear zone locality with excellent preservation of structures. Phyllonitic shear zones crosscuts the granodiorite, with both being incredibly hard to sample, even with an electrical saw. The granodiorite at this locality is slightly richer in quartz in comparison to the other granodiorite samples and thus plots in the quartz-rich granitoid field (Figure 6d). The outcrop is continuous on the surface over several metres towards the cliff. Large fractures close to the cliff reveals a cross-section of the rocks.

The thickness of the least deformed domains ranges from 5 to 20 cm, while the thickness of the phyllonitic shear zone varies considerably, ranging between <1 cm to ~1 m. The phyllonitic shear zones with muscovite extensional shear bands at this outcrop show a dextral sense of shear, suggesting an approximate top-to-the-west transport direction, as seen in Figure 13b with the view towards S-E. The C- and S-surface is parallel to the phyllonitic shear zone boundaries with C' shear band that curves towards and transects the main foliation of the shear zone. The phyllonitic shear zone has accommodated more strain than the surrounding rocks. C' shear bands develop normally in mica-rich rocks, such as phyllonites (Passchier and Trouw, 1996). S- and C-surfaces are almost parallel and define a composite foliation and suggests a prolonged history of deformation (Fossen, 2010).

The granodiorite at this locality (P26B-u and P26B-d) is white-green and is similar to the rest of the granodioritic rocks with a mineral assemblage of quartz + alkali feldspar + plagioclase + muscovite, with accessory epidote, titanite and calcite. However, this sample has 53.3 wt. % quartz, while the other samples average at 45 % quartz.

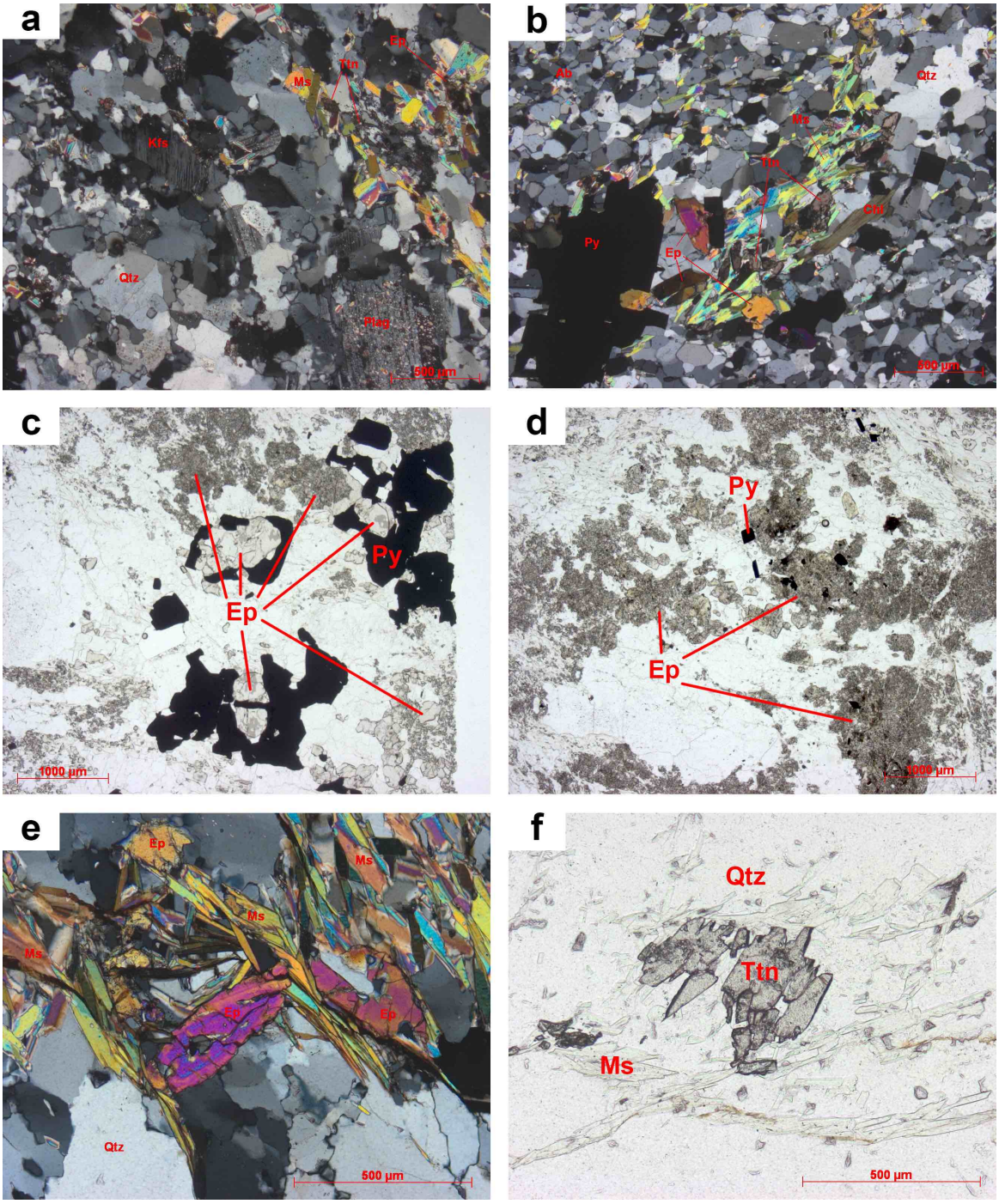

Figure 12: Mineralogical and textural observations in the aplite and hydrothermal quartz: a – b – Aplite with phenocrysts of quartz, plagioclase and alkali feldspar, in a matrix composed of the same minerals along with accessory titanite, allanite, pyrite and chlorite. c – d – Epidote-rich shear zone, showing the abundance of epidote. It occurs as coarse-grained transparent epidote along with pyrite, and as large aggregates of fine-grained epidote. The large transparent areas are quartz. e – Epidote and muscovite hosted by hydrothermal quartz, showing oscillatory zoning. f – Subhedral, wedge-shaped titanite associated with muscovite in the hydrothermal quartz.

The granodiorite at the steep cliff locality has the lowest alkali feldspar content of all the granodiorite samples with 8 wt. %, but a higher content of muscovite of 11.2 wt. % when

compared to 11.2 - 14.8 wt. % alkali feldspar and 4.7 to 7.7 wt. % muscovite of the other granodiorite samples. It also has the lowest plagioclase content with 26.1 wt. %, but the other samples ranges close by between 29 to 35.8 wt. % plagioclase (Table 2).

The phyllonitic shear zones partitions into highly deformed domains and has a main mineral assemblage of quartz (65 wt. %) and muscovite (33.9 wt. %) with the muscovite being medium grey in colour, along with accessory plagioclase, calcite and pyrite. The quartz grains are for the most part recrystallized into newer smaller grains, but some remain completely preserved in terms of original grain size, with the muscovite foliation wrapping around the quartz (Appendix - Petrography), similar to the other phyllonites.

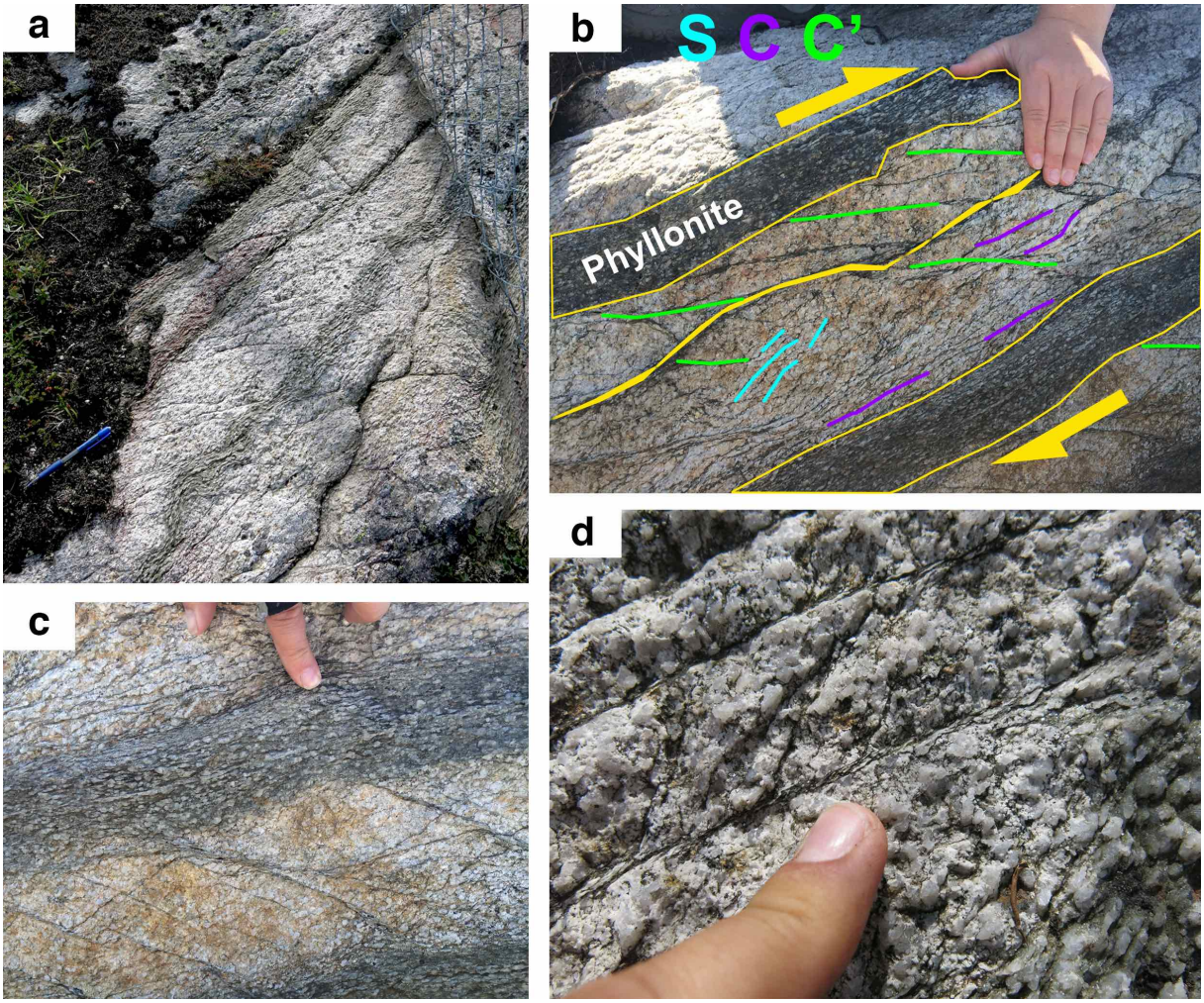

Figure 13: Field observations of the location at the steep cliff: a - A large scale view of the shear zones on the ground surface. b – The cross sectional view of the shear zones and shear bands. Note the colour difference between the white-stained granodiorite and the medium grey phyllonite. The view is approximately NE to SW from left to right in the photo. c – Close-up view with the same cross section as figure b. d – Close-up image of the thin shear bands that are oblique from the phyllonitic shear zones, that show small scale imbrication within the shear bands.

Geochemical analysis

Sample	Rock	Thin section	Whole-rock geochemistry			Mineral chemistry		
			XRD	Whole-rock, incl. trace elements	Gold analysis	SEM-map	EMPA	Laser ablation
AU1	Quartz	X	X	X	X			
AU2	Aplite	X	X	X	X			
P01	Granodiorite	X	X	X		X	X	X
P02	Granodiorite	X	X	X			X	
P03	Phyllonite	X	X	X				
P04	Phyllonite	X	X	X		X	X	
P05	Granodiorite	X	X	X				
P09	Granodiorite		X	X	X			
P13	Aplite	X	X	X	X			
P17	Granodiorite		X	X	X			
P18A	Granodiorite		X	X	X			
P18B	Phyllonite	X	X	X	X	X		
P20	Granodiorite	X	X	X	X	X		
P22-T	Granodiorite	X	X	X	X			
P23A-T	Quartz-Sulphides	X						
P23B-T	Sulphides		X	X	X			
P25A-T	Quartz-Sulphides	X	X	X	X			
P25B-T	Phyllonite	X	X	X	X			
P26B-u	Granodiorite	X	X	X	X			
P26B-d	Phyllonite	X	X	X	X			
P27	Granodiorite	X	X	X	X	X		X
P28	Phyllonite	X	X	X	X	X	X	
P29	Phyllonite	X	X	X	X			
P30	Granodiorite	X	X	X	X		X	
P31-u	Granodiorite	X	X	X	X	X	X	X
P31-d	Epidote-rich shear zone	X	X	X	X	X	X	X

Figure 14: Summary of all methods applied to the collected samples. A total of 26 samples representing the lithologies found at Gråkallen. 22 thin section were examined, 25 XRD analyses, 25 whole-rock incl. trace elements with 20 gold analyses. All mineral chemistry work were performed on the polished thin sections, where 8 SEM-maps were scanned at NGU, 7 thin section were examined with the EMPA at NTNU and 4 thin sections were sent to Texas Tech University, USA for LA-ICP-MS.

Whole-rock geochemistry

XRD

The quartz content of the granodiorite samples ranges between 44 and 49 wt. %, with an average of 45 wt. % (Table 2). One sample, P26B-u, show a slightly different mineral distribution (see Shear zone on the steep cliff). The alkali feldspar ranges from the lowest content in sample P22-T with 9 wt. % to 17 wt. % in the P30, while most of the samples lies at 14 wt. %. The plagioclase content is rather constant, ranging between 29 and 36 wt. %, with 32 wt. % as the average value. Those samples with the lowest alkali feldspar content appear to have the highest amount of plagioclase, and vice-versa. Muscovite content ranges from 5 to 8 wt. %, with the majority of the samples having 5 wt. %. Epidote shows a range between <1 and 4 wt. %. The samples that are showing <1 are known to contain the mineral, based on petrographic data. The aplite sample, P13, show the same mineral distribution as the granodioritic samples, though they are texturally different.

Phyllonites show higher quartz content than the granodioritic samples, with ranges between 62 and 72 wt. %. The P18-B sample is considered to be transitional between the granodiorite the phyllonite and show a significantly lower quartz content at 52 wt. %, but shows a notably high content of plagioclase of 27 wt. %, while the average plagioclase content of the other phyllonites is maximum of 6 wt. % with half of the samples are <1 wt. %. Even as a transitional sample, no Ca-bearing epidote is detected. Two samples show a presence of alkali feldspar (2 and 4 wt. %), but are not detected in most of the samples. The amount of muscovite ranges over a wide interval, from 18 to 38 wt. %. The lowest of 18 wt. % is the sample that has the highest amount of plagioclase (27 wt. %), and the relationship between the amounts of muscovite and plagioclase seems to be inversely proportional for the rest of the samples. The pyrite content shows no consistency, ranging from <1 to maximum 5 wt. %. The epidote-rich shear zone sample, P31-d, have the same amount of quartz, but the alkali feldspar is lowered to 1 wt. % and plagioclase to 21 wt. %, which is significantly lower than the granodiorite. The muscovite content is at 19 wt. %, which is much higher than the granodiorite (average 5 wt. %), but as high as the lowest value of phyllonite. The epidote content is 14 wt. %, but is suspected to be higher as the SEM mapping reveals the loss of Na, albite, in the shear zone (Table 2). The albite resides in the surrounding leached zone and is probably contaminating the sample, suggesting that the total amount of plagioclase of 21 wt. % in the shear zone is anomalously high and the true level is expected to be lower.

Table 2: XRD-results showing the modal mineralogy of each sample, sorted after rock type. Samples that have no data were excluded, as they were not considered to be representative. Minerals showing <1 are known to be present, but their modality is approaching the detection limit for the XRD.

Sample	Rock	Quartz	Alkali feldspar	Plagioclase	Muscovite	Epidote	Pyrite	Calcite	Titanite	Chlorite	Garnet
P01	Granodiorite	46	14	33	5	3	-	<1	<1	-	-
P02	Granodiorite	44	14	32	8	2	-	<1	<1	-	-
P05	Granodiorite	46	15	29	5	4	<1	<1	<1	-	-
P09	Granodiorite	44	15	35	5	<1	-	<1	-	-	-
P17	Granodiorite	45	11	34	5	4	-	<1	<1	-	-
P18A	Granodiorite	49	12	29	5	4	<1	<1	<1	-	-
P20	Granodiorite	44	14	36	5	2	-	<1	<1	-	-
P22-T	Granodiorite	46	9	36	7	<1	<1	2	<1	-	-
P26B-u	Granodiorite	53	8	26	11	<1	-	<1	<1	-	-
P27	Granodiorite	47	13	31	6	2	<1	<1	<1	-	-
P30	Granodiorite	45	17	31	5	<1	-	<1	<1	-	<1
P31-u	Granodiorite	45	14	33	5	2	<1	<1	<1	-	-
P03	Phyllonite	62	-	<1	38	-	<1	-	-	-	-
P04	Phyllonite	72	-	<1	26	-	1	-	-	-	-
P18B	Phyllonite	52	2	27	18	-	3	-	-	-	-
P25B-T	Phyllonite	64	4	6	21	-	5	-	-	-	-
P26B-d	Phyllonite	65	-	<1	34	-	<1	<1	-	-	-
P28	Phyllonite	68	-	3	29	-	<1	-	-	-	-
P29	Phyllonite	69	-	2	27	-	2	-	-	-	-
P31-d	Epidote-rich shear zone	42	1	21	19	14	2	<1	<1	-	-
AU1	Quartz	-	-	-	-	-	-	-	-	-	-
AU2	Aplite	-	-	-	-	-	-	-	-	-	-
P13	Aplite	44	15	35	6	<1	<1	<1	-	-	-
P23A-T	Quartz-Sulphides	-	-	-	-	-	-	-	-	-	-
P23B-T	Sulphides	-	-	-	-	-	-	-	-	-	-
P25A-T	Quartz-Sulphides	-	-	-	-	-	-	-	-	-	-

Whole-rock chemistry and trace elements

In the sulphide samples, up to 0.033 ppm of gold were detected (Appendix – Whole-rock analyses).

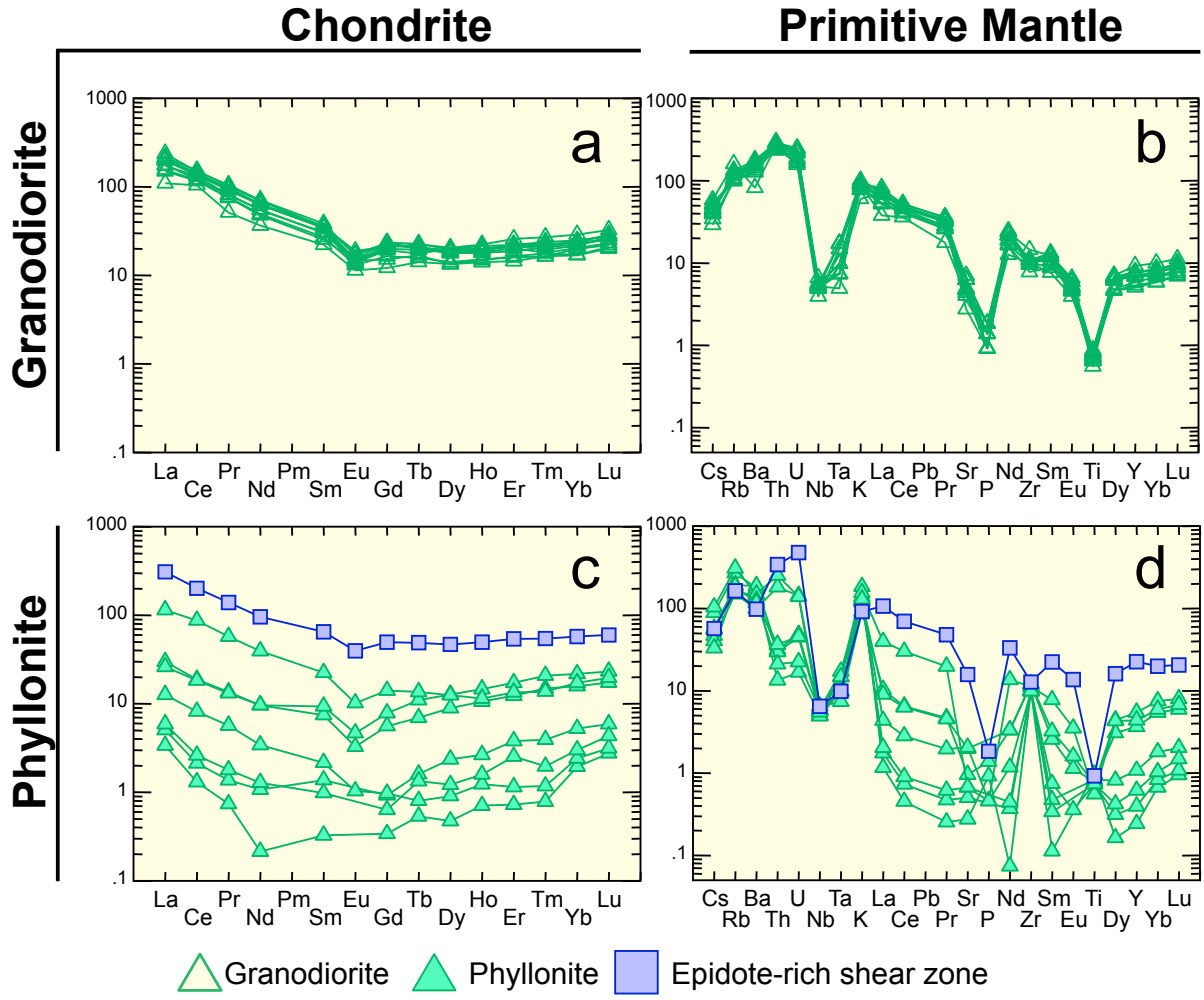

Figure 15: The granodiorite and phyllonite samples normalized to C1 chondrite and primitive mantle, after Sun and McDonough (1989). The hollow green triangles represent the granodiorite, filled green triangles are the phyllonites, while the filled blue squares represent the epidote-rich shear zone. a – Chondrite-normalized granodiorite, b – Primitive mantle-normalized granodiorite, c – Chondrite-normalized phyllonite, and d – Primitive mantle-normalized phyllonite.

The granodiorite show an enrichment up to 100 – 250 times of the chondrite for the LREE, with a steep decrease from La to Sm along with a small Eu anomaly, and relatively flat, but increasing slope for the HREE (Figure 15a). There is negative Nb, Ta, Sr, P and Ti anomalies in the primitive mantle-normalized diagram (Figure 15b). The granodioritic samples show tight clustering of their data, indicating that there is only a slight variation of the whole-rock composition.

The REE pattern for the phyllonite normalized to chondrite varies from weakly decreasing to steep negative slope for the LREE, with a small negative Eu anomaly, or Eu below detection limit. The HREE varies from being irregular and uneven with a weakly positive slope to be sub-horizontal (Figure 15c). The more enriched the phyllonite samples are, the more similar the shape of the REE pattern is to the granodiorite. The primitive-mantle diagram (Figure 15d) shows great variability in the data, and compared to the phyllonite-chondrite diagram (Figure 15c) it shows that roughly the same order of samples occur to be the most depleted and range into the more enriched rocks, with the epidote-rich shear zone being the most enriched sample in REE. Nb, Ta, Zr and Ti appear to be consistent in all the phyllonite samples seen as a clustering effect, even though that these rocks are highly altered and deformed, suggesting immobility.

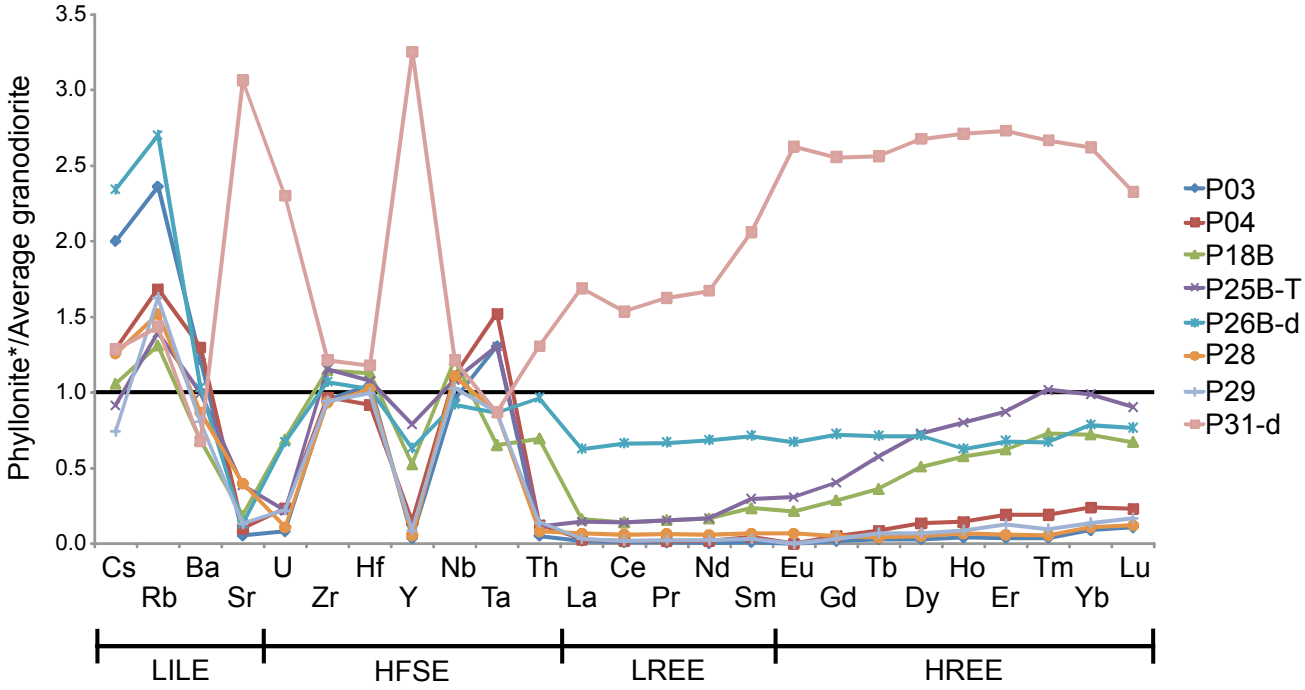

Figure 16: Relative enrichment/depletion diagram based on trace elements of the whole-rock data showing trace element behaviour when normalized to the average granodiorite values. The elements on the x-axis were subdivided into trace elements groupings based in their charge/size ratio (LILE/HFSE) and REEs (Rollinson, 1993). Some Eu (Sample P03, P04 and P29) values plot on the zero line as the measurements were below the detection limit. *Epidote-rich shear zone is also included.

The altered rocks, both the phyllonites and the epidote-rich shear zone were plotted and normalized to the average values of the granodiorite (Figure 16). All the samples show depletion to enrichment of the LILEs. Rb shows enrichment in all the samples as it can enter into the muscovite lattice (Etheridge and Cooper, 1981). Ba and Cs is straddling the 1:1 line

and Sr appear to be highly depleted in all samples except for the epidote-rich shear zone. The epidote-rich shear zone samples show enrichment of U and Y with values larger than 2 and 3 times the average granodiorite, in comparison to all other phyllonites that are depleted. Zr, Hf, Nb and Ta is scattered around the 1:1 line, which is believed to be due to the immobile tendency of these elements. Th has a higher concentration in the epidote-rich shear zone, while the phyllonites ranges from being unaffected to depleted. The epidote-rich shear zone is enriched in all the REEs, specifically the HREE that reaches 2.5 times the values of the average granodiorite. Sample P26-d is consistently depleted in all the REEs in comparison to the granodiorite while samples P03, P28, P29 and P04 are depleted to less than 0.1 of the granodiorite. P18B and P25B-T are also strongly depleted in the LREE, but the loss of HREE is less than the other phyllonitic samples, shown by the positive slopes from Sm to Tm, with a small dip towards Lu.

Mineral chemistry

SEM and element mapping

The mapping reveals the major element distribution throughout the thin sections, and a small selection of samples was chosen for mapping in the SEM, as it is a very time-consuming task. The sample representing the undeformed is the granodiorite P20 (Figure 17). On the Si map, there are at least two distinct phases, where the brightest parts reveal quartz distribution and the slightly darker is the feldspars along with muscovite. As a single phase, the quartz takes up a significant proportion of the sample. Looking at the Al, Na and K together is necessary to reveal the phases that have similar major chemistry, such as the muscovite, alkali feldspar and albite. The Al map also shows two separate phases, with the brightest part with a vein-like appearance representing the muscovite, while the darker grey is the feldspars. The Na map shows that most of the Al-bearing phases also contains Na, suggesting that it is albite. The K map shows the muscovite and alkali feldspar, but they are hard to differentiate. In combination with the Al map and XPL, it is possible to separate them by whiteness intensity. However, the K map also shows that muscovite and alkali feldspar is inferior to quartz and albite.

The mapping of the transitional sample P18B show that most of the primary alkali feldspar is lost, and the muscovite is the main K phase, while the bright Si phase indicate that around 50% of the surface of the thin section is quartz. Very little epidote is found within the sample,

but the amount does not vary significantly from the other phyllonite samples. As seen on the Na map, there is a large proportion of albite present, seen as the white dull phase on the slab (Figure 18) and the albite distinguishes the sample from the other phyllonites.

The phyllonite sample (P28) that was mapped in the SEM shows a simpler mineral distribution (Figure 19). The brightest parts of the Si map is the quartz, with a darker grey phase that curves around and in between the quartz, which is also reflected on the Al and K map as muscovite defining the foliation. There is third phase visible on the Al map, seen as the small grains set in the muscovite matrix. The same phase is visible on the Na map and it is the albite porphyroclasts, which is restricted to the lower part of the thin section. The Fe map, BSE and PPL image reveals that pyrite is occupying the upper part where the albite is not found.

The epidote-rich shear zone (P31-d) mapping can be subdivided into three parts seen on the slab photo in Figure 20: one, the epidote-rich shear zone; two, the leached white zone; and three, the pink-green granodiorite. Based on the SEM maps, the epidote-rich shear zone consists of mainly of epidote, muscovite, pyrite (seen on the Fe map) and quartz. The Na map shows that albite is completely leached out of the shear zone. The white leached zone consists mainly of albite and quartz with surrounding muscovite. The epidote and pyrite is more dispersed and not as common as in the shear zone. In the undeformed granodiorite, the K-bearing phase is alkali feldspar that occurs interstitially, whereas in the leached white zone it was muscovite. The undeformed granodiorite is dominated by quartz, albite and alkali feldspar along with Ca-bearing epidote and pyrite.

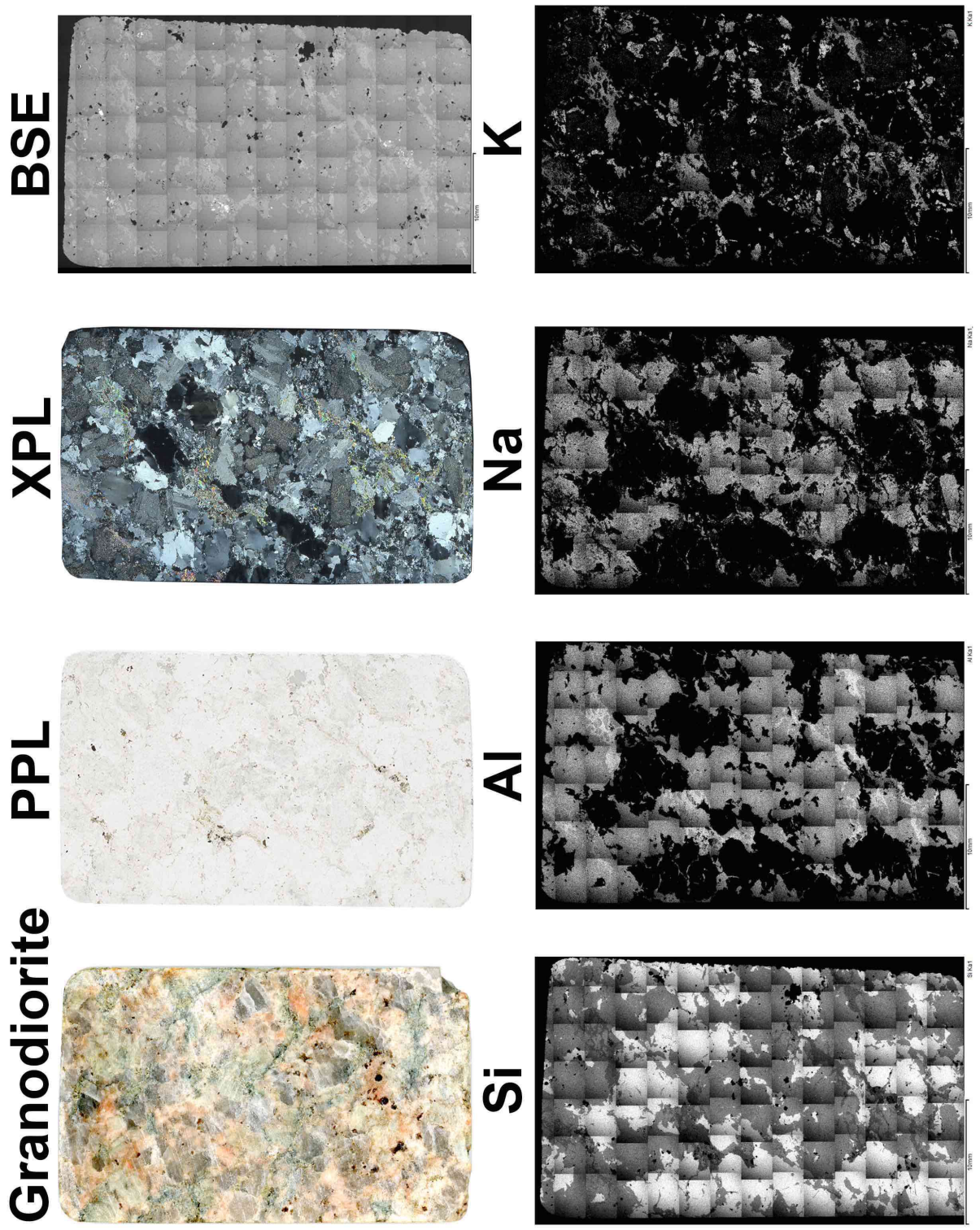

Figure 17: Montage showing a scan of the granodiorite thin section (P20) in PPL and XPL. A series of Backscatter Electron (BSE) images along with element maps were stitched together using the INCA software. Bottom row shows the Si, Al, Na and K element maps in the granodiorite. Si relates to all the phases of the sample, Al represents the feldspars and muscovite, Na is hosted by the albite and K corresponds to the alkali feldspar and muscovite. Note: The squares are a defect caused SEM instrument at low magnification and the slab is the counterpart to the actual thin section slab.

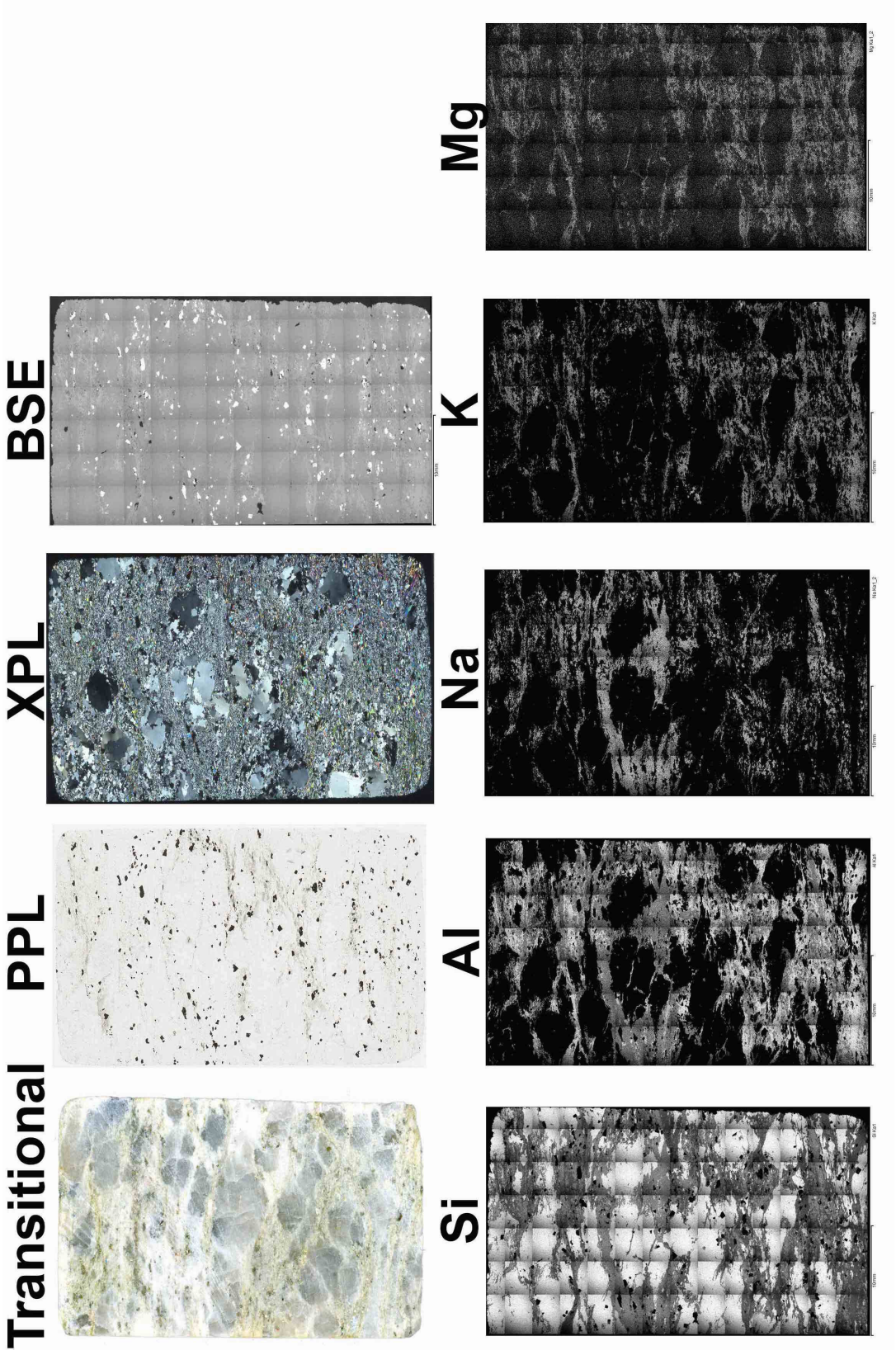

Figure 18: Montage showing a scan transitional phyllonite thin section (P18B) in PPL and XPL. Si represents all the phases in the sample, except for the pyrite shown by the black voids on the Si map. The Al map show albite and muscovite, while the Na map show the extent of the albite. The K and Mg map are coinciding and show that the muscovite have a significant proportion of Mg. Note: the slab is the counterpart to the actual thin section slab.

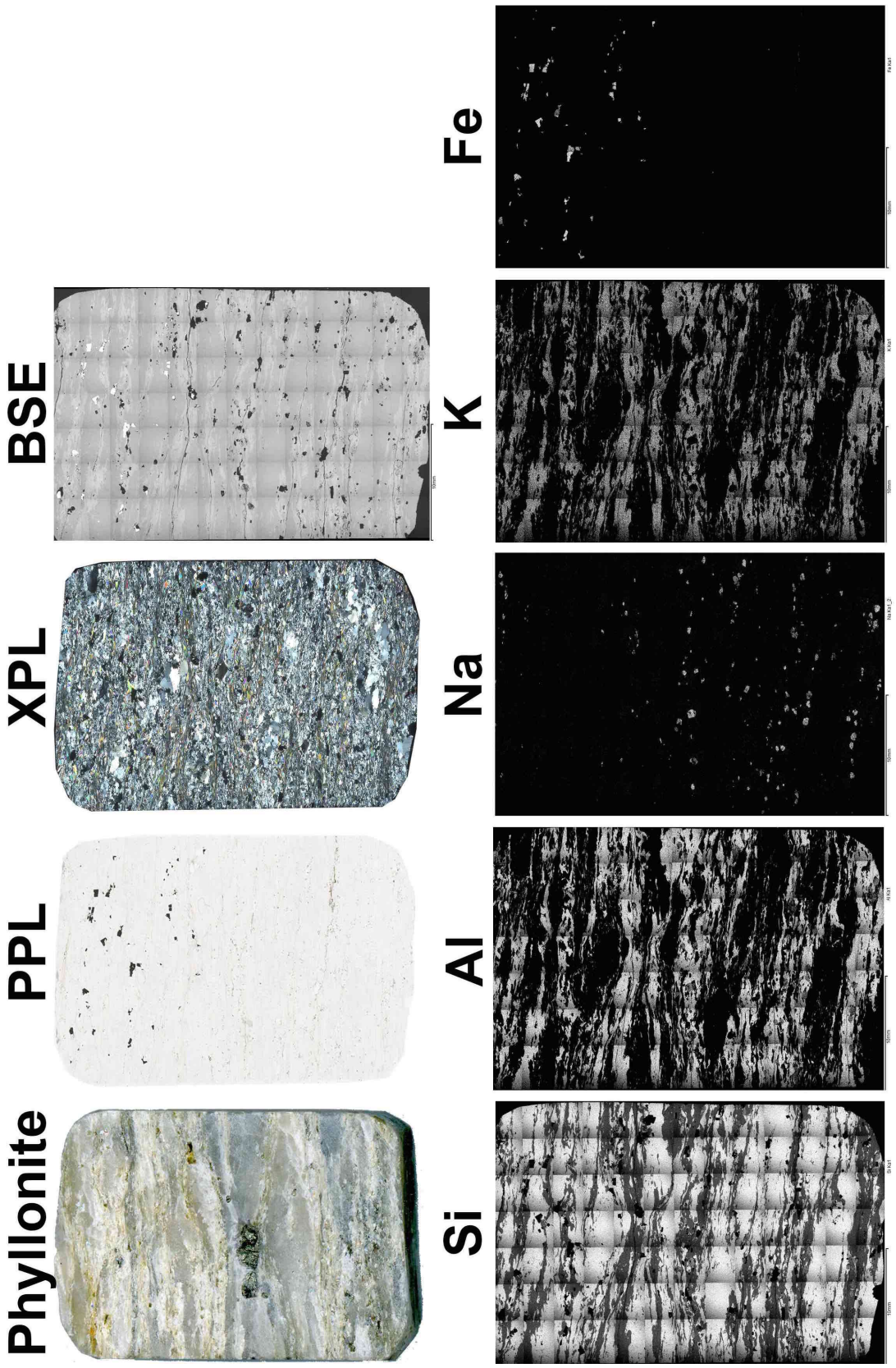

Figure 19: Montage showing a scan of the phyllonite thin section (P28) in PPL and XPL. The Si relates to the quartz and muscovite in the sample; Al also reflects the muscovite; Na is hosted by the albite porphyroclasts (as seen in Figure 9b), K reveals the muscovite and Fe is the pyrite. Compare the Na and Fe maps and note that pyrite and albite do not occur together. Note: the slab is the counterpart to the actual thin section slab.

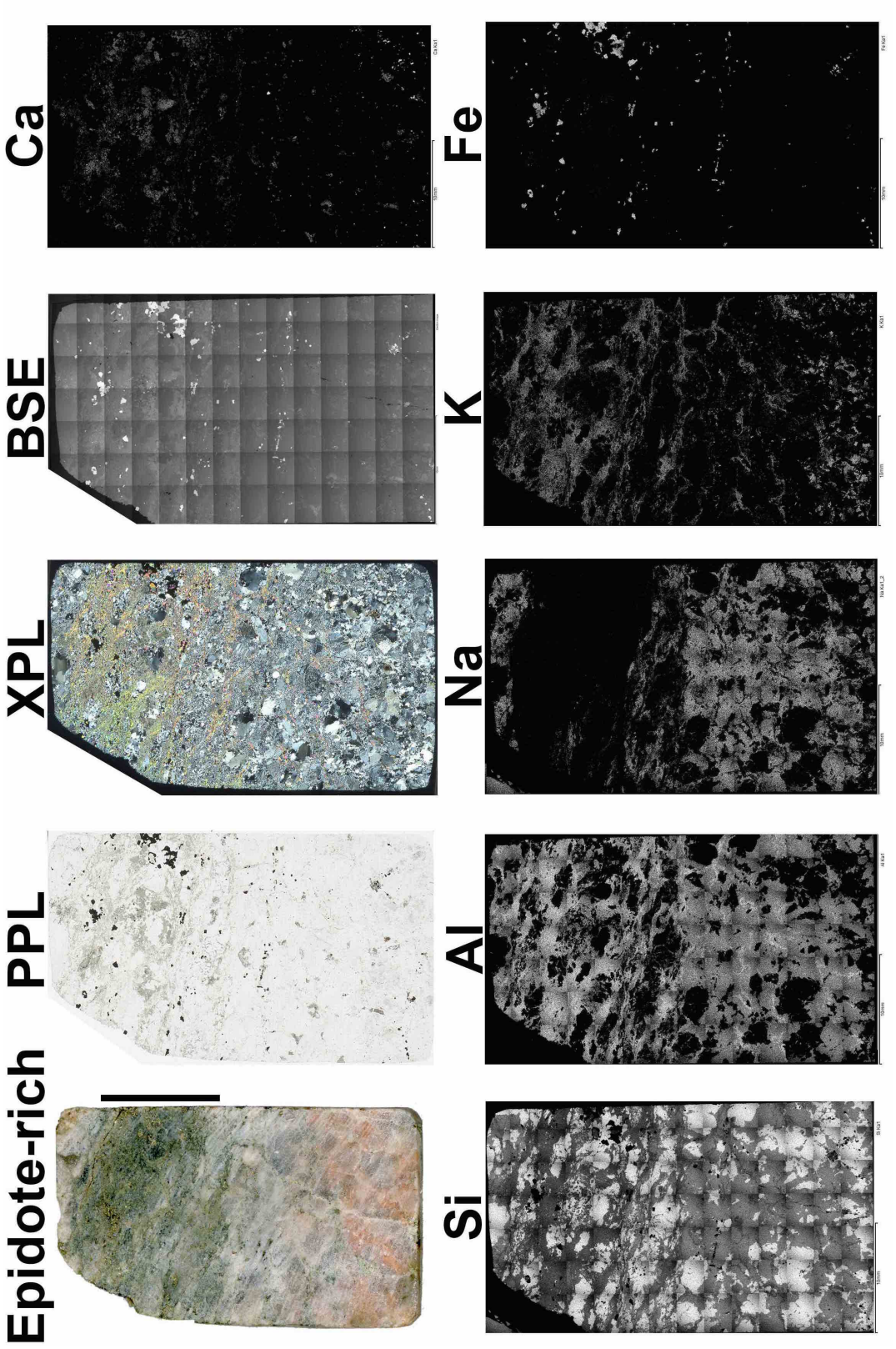

Figure 20: Montage showing a scan of the epidote-rich shear zone thin section (P31-d) in PPL and XPL. The black bar indicates extent of the shear zone. Al reflects the muscovite, the feldspars and epidote. Na is hosted by the neocrystallized albite, which is not found in the shear zone. K reveals the muscovite and the alkali feldspar in the undeformed granodiorite (bottom) part and Fe is the pyrite. The alkali feldspar and muscovite can be distinguished by their texturally different appearance. Note: the slab is the counterpart to the actual thin section slab.

Microprobe analysis

Feldspar

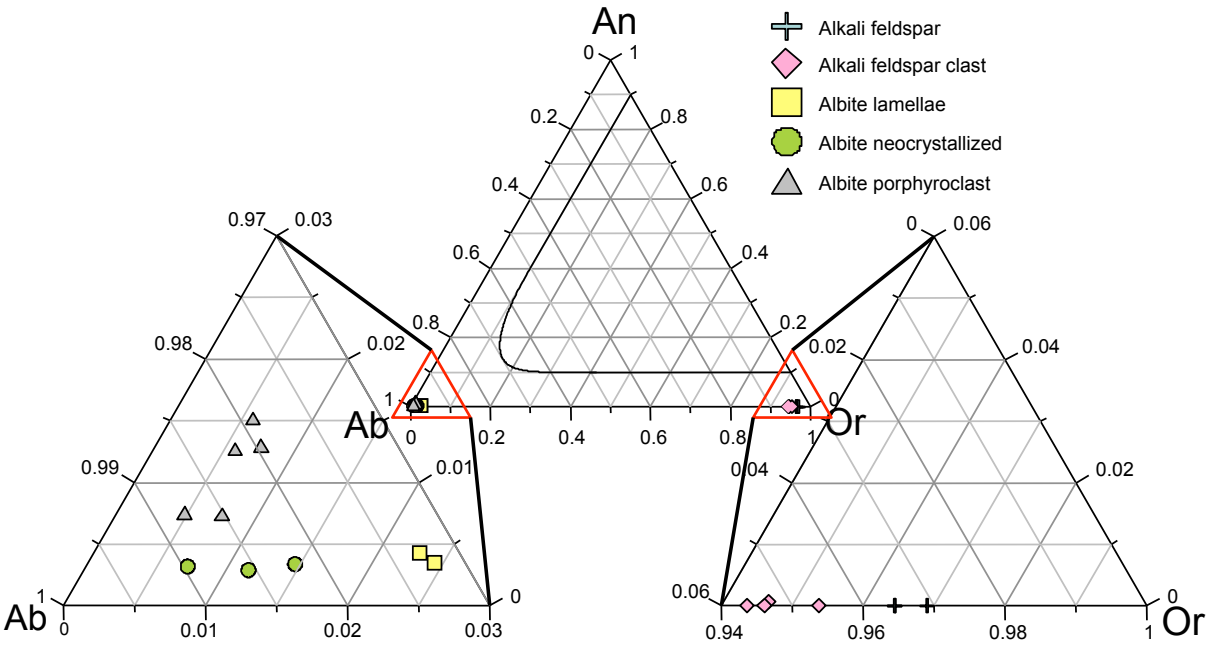

Figure 21: Ternary feldspar diagram with the compositional differences in the feldspars from the microprobe analyses. Inset from the Or-corner, showing alkali feldspar differences; with the primary feldspar from the granodiorite have a marginally higher Or-content than the alkali feldspar clast in the phyllonite. Inset from the Ab-corner showing the groupings in the albite.

The composition of the feldspars is plotted in the feldspar ternary diagram (Figure 21) and reveals the small differences of the different groups feldspars found in the samples. The alkali feldspar (grey cross) is a microcline with albite exsolution lamellae (yellow square) in the granodiorite. The neocrystallized albite (green circle) is the polygonal grains that is crosscutting and/or mantling the alkali feldspar (e.g. Figure 7a). The alkali feldspar clast (pink square) is large grain found in a phyllonite sample that showed three apparent cleavages and first order grey birefringence. The albite porphyroclasts (grey triangle) is the rounded grains showing twinning and is hosted by the muscovite matrix in the phyllonite (Figure 9b).

The primary alkali feldspar from the granodiorite has slightly higher Or-content than the alkali feldspar clast in the phyllonite (Figure 21c). All the alkali feldspar measurements show BaO content ranging between 0.5 and 0.8 wt. %. The albite lamellae, neocrystallized and porphyroclasts all plot tight in the Ab-corner. However, there appear to be initial clustering trend between the groups (Figure 21c). The albite lamellae have the lower Ab-content of the three, while the albite porphyroclasts in phyllonites has the highest An-content. Given the groupings of the different feldspar types measured, yields an average formula:

$Ab_{97.2}Or_{2.4}An_{0.4}$ representing the albite exsolution lamellae; $Ab_{98.4}Or_{0.8}An_{0.8}$, for the neocrystallized albite in the primary alkali feldspar; and $Ab_{98.3}An_{1.1}Or_{0.6}$, for the albite porphyroclasts in the phyllonite. The two groupings in the alkali feldspar yield: $Or_{96.6}Ab_{3.4}$ for the primary alkali feldspar and $Or_{94.7}Ab_{5.3}$ for the alkali feldspar clast in the phyllonite.

Muscovite

Microprobe analyses were performed on muscovite in the phyllonite and muscovite in the granodiorite in contact with garnet. The muscovite in the phyllonite represents the muscovite defining the sub-horizontal foliation and the muscovite that occurs at an angle. Mineral calculations were done based on 22 oxygen atoms in the muscovite formula. There were no significant difference between the muscovite defining the foliation and the muscovite occurring at an angle, and were thus combined into a single formula:

Equation 5: Calculated Muscovite formula

$$(K_{2.10-2.16}Na_{0.03-0.07})(Al_{3.23-3.31}Fe_{0.32-0.40}Mg_{0.25-0.30}Ti_{0.02-0.03}Mn_{0.01-0.02})$$
$$(Si_{6.59-6.62}Al_{1.37-1.41})O_{20}(OH)_4$$

The muscovite in the phyllonite has a FeO content of average 3.2 wt. % and Al_2O_3 of 29.2 wt. % through all the measured spots. The muscovite in contact with the garnet has a slightly higher FeO content 7.2 wt. % and subsequent lower Al_2O_3 content at 24.7 wt. %. The differences can be assigned to Fe and Al substitution as both can occur at the Y-site.

Equation 6: Calculated Muscovite formula in contact with Garnet

$$(K_{2.08-2.22}Na_{0.02-0.04})(Al_{2.83-2.91}Fe_{0.83-0.88}Mg_{0.29-0.31}Ti_{0.03-0.04}Mn_{0.01-0.02})$$
$$(Si_{6.69-6.74}Al_{1.29-1.31})O_{20}(OH)_4$$

Garnet

Two ~300 micron grains of euhedral unzoned garnet has been found in sample P30, mantled by muscovite. The composition of the garnet is $Alm_{36}Sps_{32}Grs_{31}$, by carrying Fe, Mn and Ca that possibly could be utilized in a garnet-phengite P-T estimation. This is the same sample that has the distinct white microcline at outcrop. Element map that were constructed reveals that garnet has no internal element zonation (Figure 22). The grey colour differentiation is due to charging of the sample.

Figure 22: Element map reveals that there is no internal zonation within the garnet. The slightly brighter grey areas within the garnet are due to charging of the sample.

Epidote and allanite

The epidote mineral formulas were calculated based on 12.5 oxygen atoms and the Fe were entered as FeO and the Fe^{2+}/Fe^{3+} ratio were recalculated according to the procedure of Droop (1987) based on the ideal number of cations and oxygen in the given formula. Microprobe analyses below the given detection limit for each element were disregarded.

The allanite plots as a loosely scattered group between the 0.8 and 0.4 Fox isolines, indicating a variable distribution between the Fe^{3+} and Fe^{2+}. The epidote analyses plot close to the Al and Epidote apex, within the epidote - clinozoisite solid solution series and all iron are assumed to be Fe^{3+}. The epidote shows a maximum REE content of 0.044 c.p.f.u, including those identified as the result of the saussuritization of plagioclase and the coarse-grained epidote from the epidote-rich shear zone. The parallel trend of coupled measurements of allanite-epidote transition, shown by the connecting line between the samples (Figure 23), indicate that the substitution was controlled by the coupled exchange of $Ca^{2+} + Al^{3+} = REE^{3+} + Fe^{2+}$, in the ferriallanite - epidote solid solution, though the path from the allanite to epidote apex indicate that Fe^{3+} also played a significant part in the substitution (Petrík et al., 1995). The two filled triangles plotting along the epidote-allanite solid solution is a dark high-relief epidote-mineral with distinct cleavage. The point on the 0.8 isoline is close to the rim of the grain, while the 0.6 is a centre spot, though most likely the relationship between the

compositions of the rim-core location is not obvious. On the backscatter image during EMPA, it showed that this specific grain hosts a small REE-rich phase located in between the cleavage planes that contained 32.9 wt. % Ce_2O_3, 17.0 wt. % La_2O_3, 9.6 wt. % Nd_2O_3, 7.3 wt. % CaO and only 3.0 wt. % SiO_2.

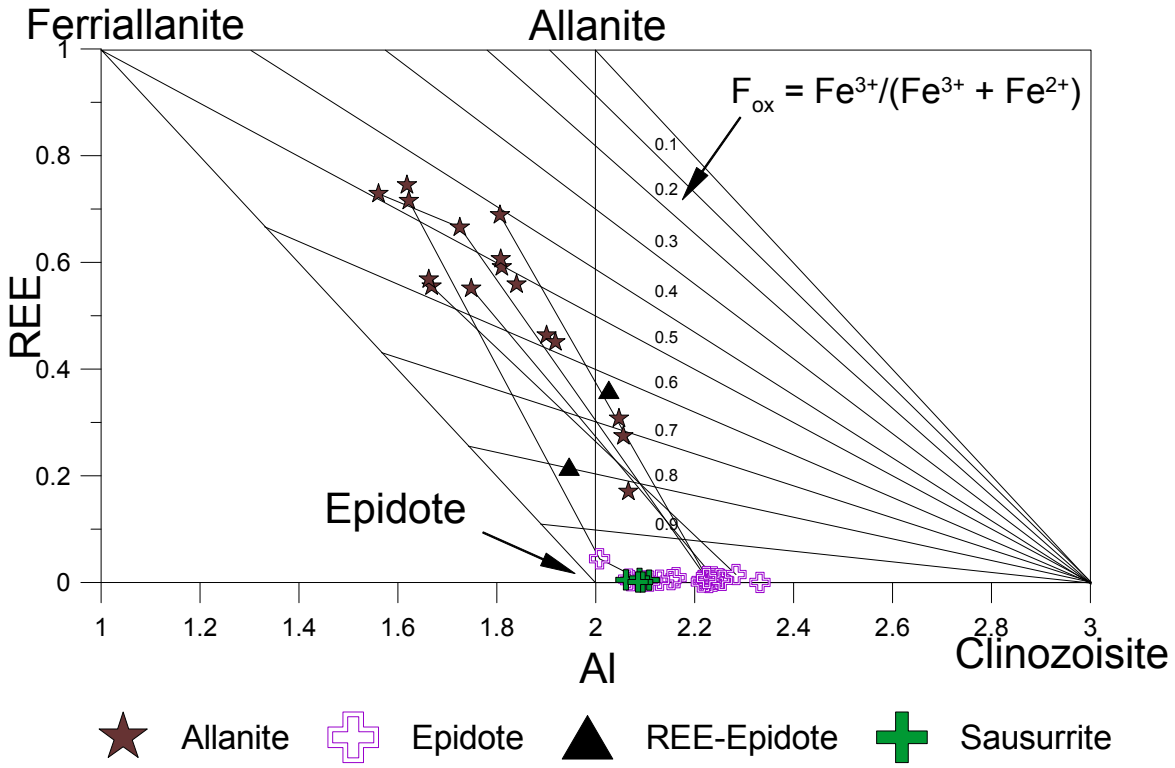

Figure 23: Total REE vs. Al plot after Petrík et al. (1995). The diagram plots cations per formula unit (c.p.f.u) values, and shows the substitution relations between Ferriallanite – Epidote: Ca + Al = REE^{3+} + Fe^{2+}; Ferriallanite and Allanite: Fe^{3+} = Al^{3+}; and Allanite – Epidote: Ca + Fe^{3+} = REE^{3+} + Fe^{2+}, with the REEs being La, Ce, Nd and Y. The lines between some of the samples are coupled analyses of allanite-epidote transitions. These lines exhibit a ferriallanite – epidote substitution trend where Ca^{2+} + Al^{3+} is exchanged with REE^{3+} + Fe^{2+}. The F_{ox} isolines estimate the amount of Fe^{2+} and Fe^{3+} in each epidote analysis (Petrík et al., 1995).

Laser ablation

The LA-ICP-MS data attained on the allanite and titanite show that all the analyses two show the same trend of all the REE patterns (Figure 24). The allanite is enriched with the LREEs with a magnitude of 10.000 to 200.000 in that of chondrite and the HREEs are in the 300 to 8.000 ranges. Allanite has a small negative Eu anomaly and a slightly decreasing slope in the HREEs. Titanite exhibits a prominent increasing slope, with a slight scattering in the LREE and enrichment in the HREE. The magnitude of the LREE is between 2 and 100 of chondrite. Some show a negative Eu anomaly while other show no anomaly. In the HREEs, the patterns are more similar and clustered and they are enriched in the order of 500 to 2.000.

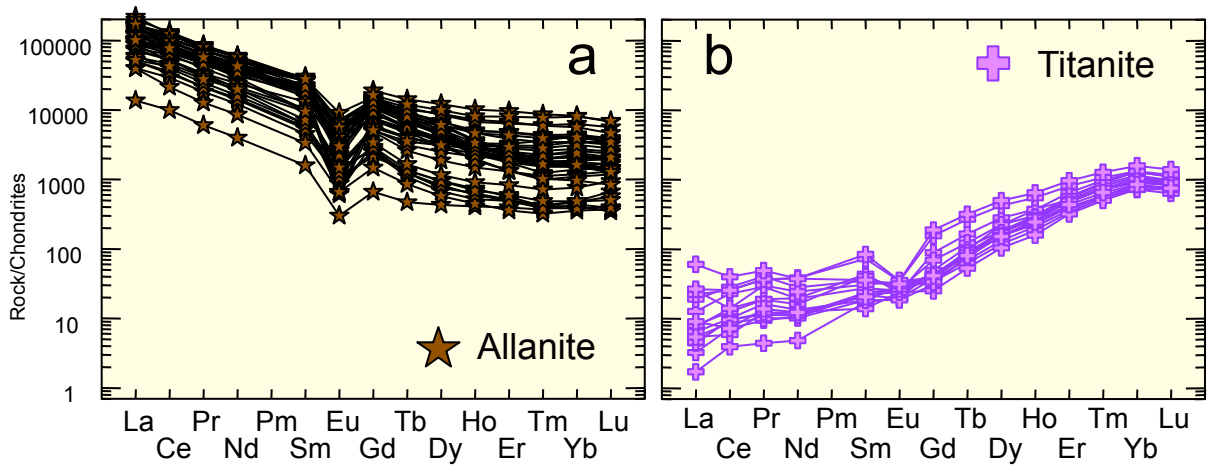

Figure 24: Chondrite-normalized REE patterns of allanite and titanite measured by LA-ICP-MS. Both the allanite and titanite show the same trend within each mineral. Samples normalized to C1 Chondrite of Sun and McDonough (1989).

The allanite in mineral assemblage Aln-Ep-Ttn (Figure 25) show an enrichment of the LREE in the order of 100.000 to chondrite and a negative Eu anomaly, as previously mentioned. Titanite shows the opposite trend, with an increasing enrichment towards the HREEs. The epidote measured the furthest away from the REE-phases show a rather flat REE pattern with Eu anomaly, while the closer measurement have a small negative Eu anomaly and increased enrichment in HREE, similar to the titanite. Both epidote analyses show a higher enrichment in the LREE than the titanite.

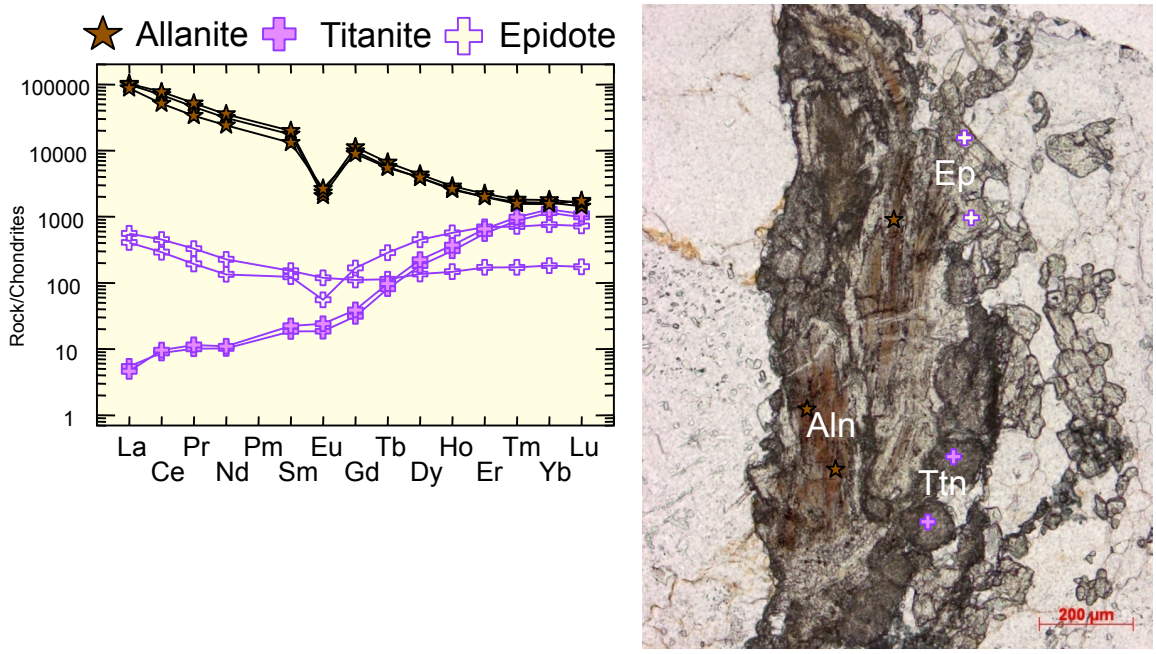

Figure 25: Chondrite-normalized REE patterns of allanite, epidote and titanite measured by LA-ICP-MS. Allanite is enriched by the factor of 200.000, epidote with 1.000 and titanite approximately 10 in the LREE, to that of chondrite. The REE patterns seem to converge towards the HREE. The epidote analysis that is the furthest away from the titanite does not

converge towards the HREE. Samples normalized to C1 Chondrite of Sun and McDonough (1989).

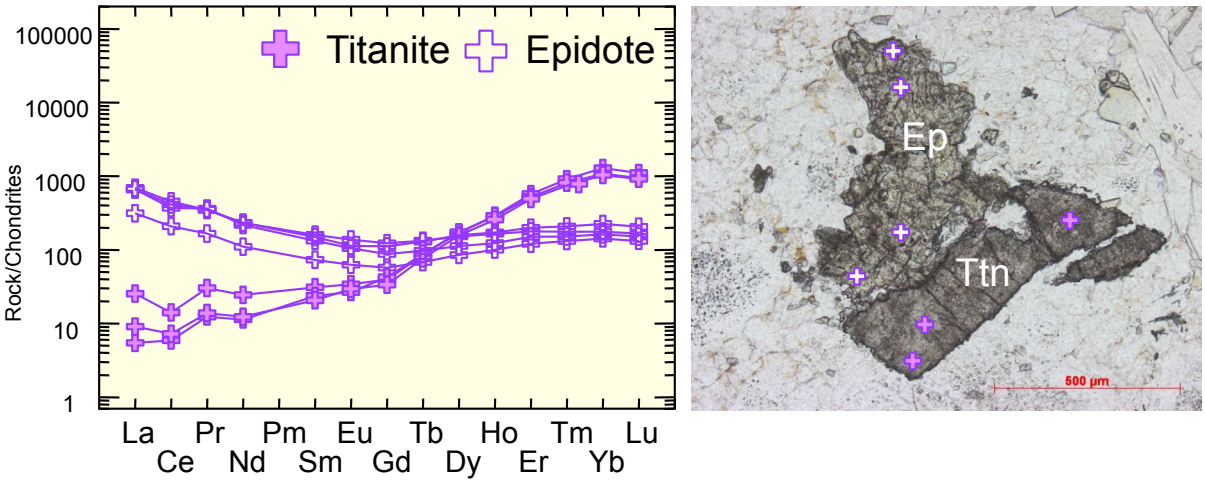

Figure 26: Chondrite-normalized REE patterns of allanite, epidote and titanite measured by LA-ICP-MS. Epidote shows an enrichment in LREE with 400 to 1.000, while the titanite is near chondrite values. Around Tb-Dy and in the HREE, titanite shows larger values than the epidote. Samples normalized to C1 Chondrite of Sun and McDonough (1989).

In the epidote-Titanite clusters (Figure 26), the titanite shows no difference from the rest of the titanite measurements, with an increasing HREE enrichment in the order of 1.000. The epidote is richer in the LREE compared to the titanite and it has a relatively flat pattern with no Eu anomaly. Close to Tb-Dy, the patterns for the two minerals intersect and titanite becomes the most enriched phase, showing that they are competing for the same REEs, with epidote incorporate the LREEs, while titanite takes the HREEs.

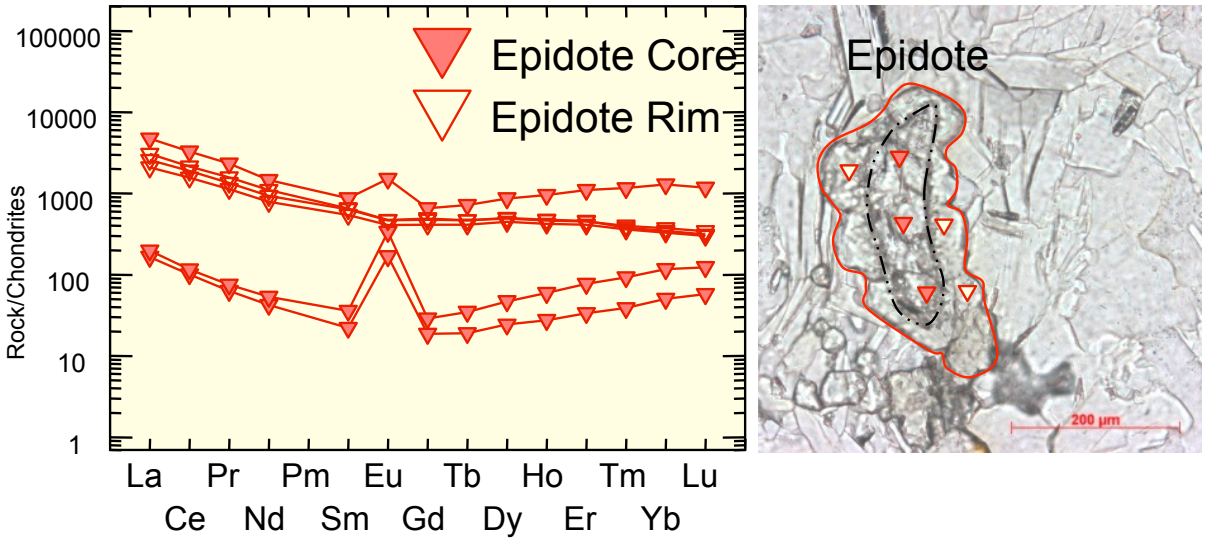

Figure 27: Chondrite-normalized REE patterns of epidote measured by LA-ICP-MS. Epidote show dissimilar REE patterns between the core and the rime in the epidote. The distinguishing feature is marked by the dotted line and the full red line outlines the entire epidote grain. The rim shows a flat REE patterns that ranges from 3.000 in LREEs to 300 in HREEs. The core shows evident positive Eu anomaly, though the top-most measurement shows a smaller anomaly

and REE enrichment similar to that of the rim. A possible explanation is that the outlier is caused by mixing of the core and rim during the laser ablation. Samples normalized to C1 Chondrite of Sun and McDonough (1989).

Measurements were taken on a single epidote grain that shows a distinct core and rim feature, marked by the dotted line (Figure 27). In the core of the grain, there is a positive Eu anomaly with a basin-shaped REE pattern with enrichment in the range of approximately 100 times of that of chondrite. The rim has a rather flat pattern and no Eu anomaly, but is more enriched in the REEs than the core, ranging from 2.000 of the LREEs to 1.000 of the HREEs. This suggests that there must have been REEs in the fluid that was incorporated during the growth of the epidote rim. Two out of three analyses of the core shows a lower REE content compared to the rim, while one measurement shows the highest REE enrichment, but with a smaller, positive Eu anomaly. It is probably due to a mixing between core and rim material during the measurement.

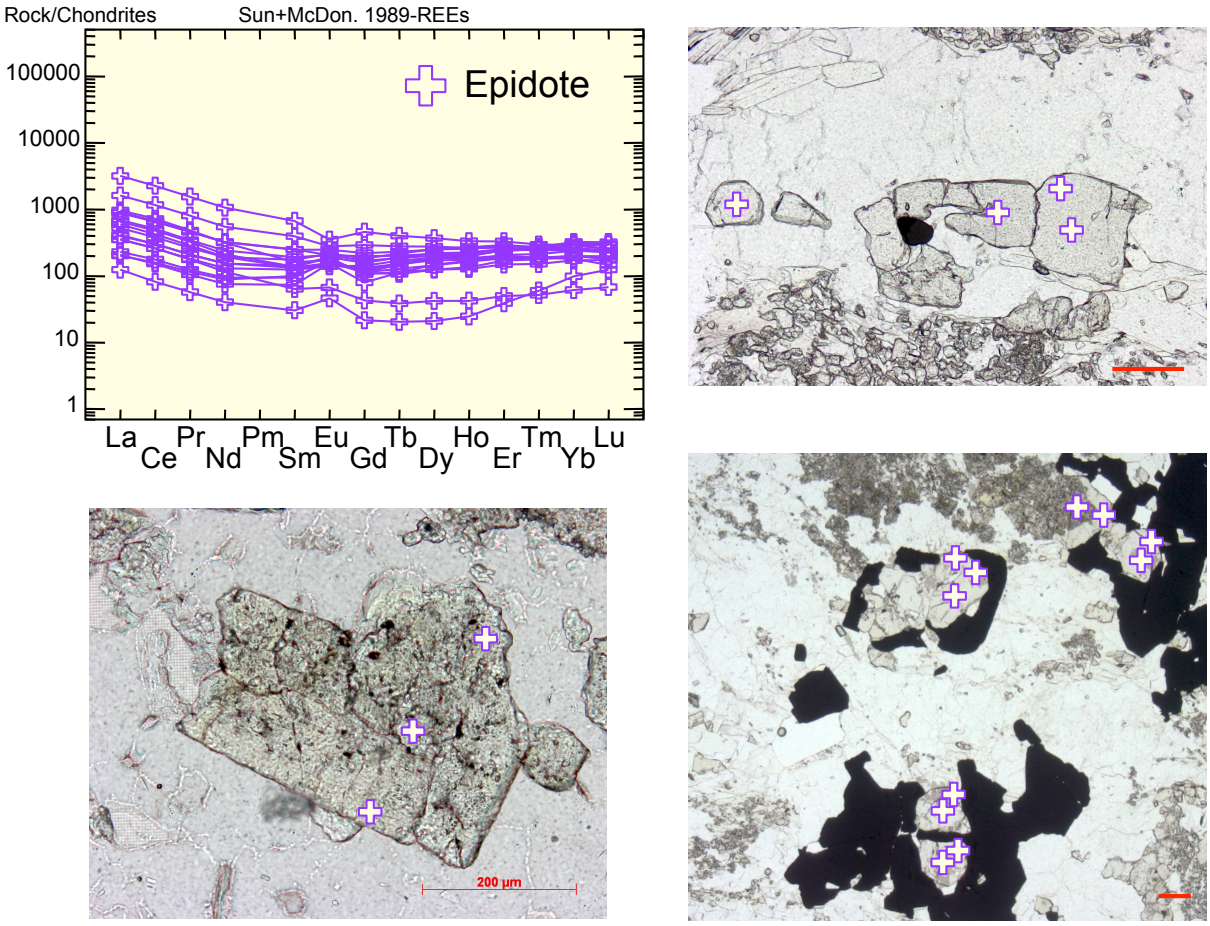

Figure 28: Chondrite-normalized REE patterns of epidote measured by LA-ICP-MS. The epidote from the epidote-rich shear zone ranges between a slightly positive to slightly negative Eu anomalies. Grains are anhedral and fractured. Samples normalized to C1 Chondrite of Sun and McDonough (1989).

The LA-ICP-MS analysis of the epidote from the epidote-rich shear zone show REE patterns with both positive and negative Eu anomalies (Figure 28). The epidote is slightly more enriched in the LREE than the HREE. Measurements on two separate grains show that they all exhibit a positive Eu anomaly, with a semi-basin-shaped REE pattern with a slight increase in the HREEs, and the epidote contain less REEs than the epidote found in the epidote-rich shear zone (Figure 29).

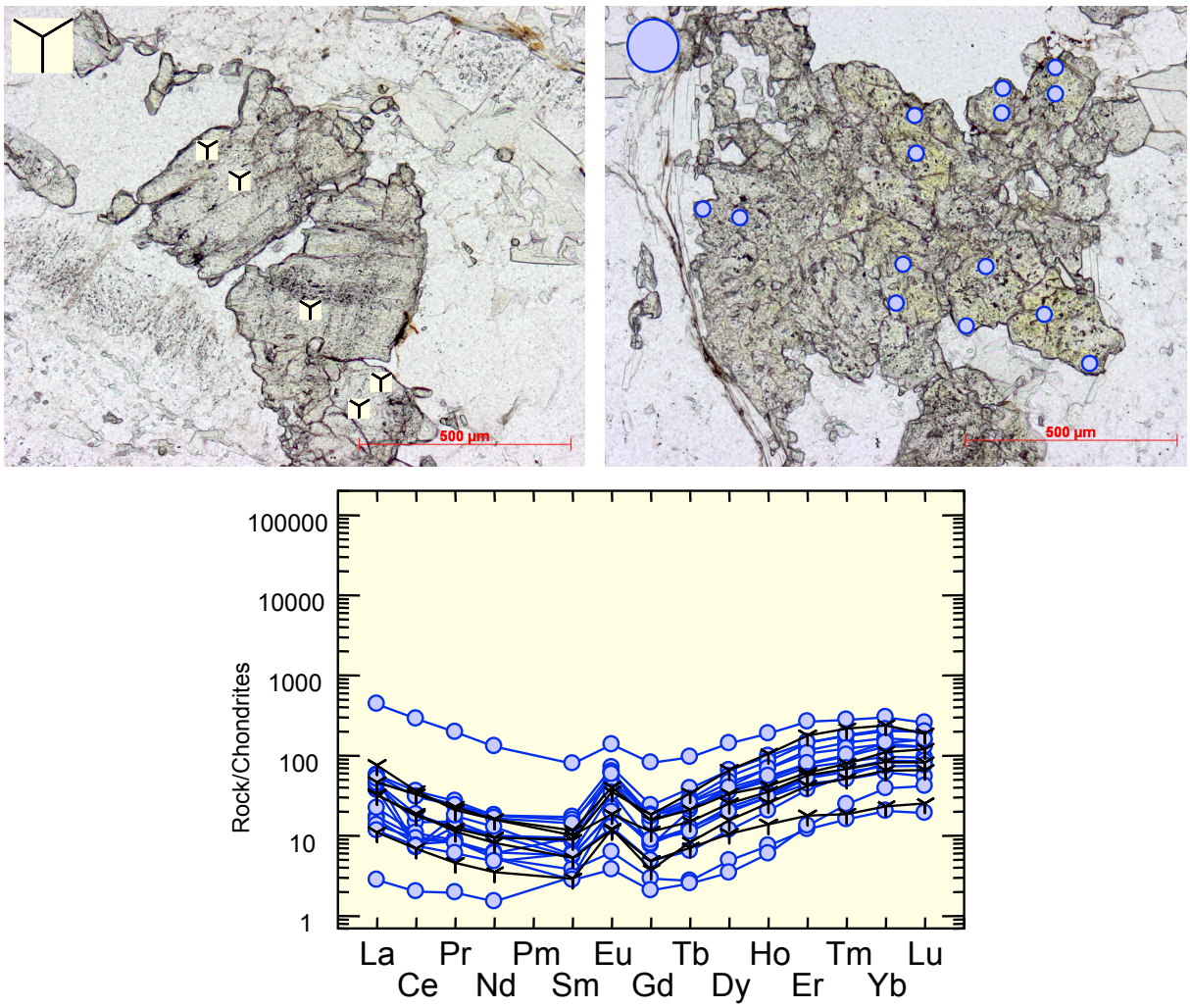

Figure 29: Chondrite-normalized REE patterns of epidote measured by LA-ICP-MS. The epidote shows a positive Eu anomaly, and the enrichment happens in the range 3 to 400 of that of chondrite. Analysed spots on the picture to the right are taken on epidote grains that are located within a cavity. Samples normalized to C1 Chondrite of Sun and McDonough (1989).

Allanite

Anhedral brown pleochroic allanite is rimmed by transparent epidote and opaque pyrite are set as inclusions within the allanite (Figure 30a). The BSE image reveals subhedral, fractured apatite with inclusions of a Th-bearing mineral along with a REE-rich phase located in a

clustering style along with zircon (Figure 31a). Such a comprehensive mineral assemblage is not commonly preserved in these samples, usually only allanite mantled by epidote with occasional titanite are found (e.g. Figure 25). A large allanite surround the grains of fluorapatite, which has a high fracture density. A Th-bearing mineral occur in the fractures in the apatite and an unknown phase that reports 27 wt. % La_2O_3, 25 wt. % Ce_2O_3, 8,5 wt. % Nd_2O_3. The sum of SiO_2, CaO and P_2O_5 is < 3 wt. % is indicating that it is neither a silicate nor a phosphate, though the total given by the microprobe approximates at ~65 demonstrating that essential elements are missing from the analysis. The Th-bearing mineral could only be identified with WDS at the microprobe, because there was no reference standard for Th was available. Both thorite ($(Th,U)SiO_4$) and thorianite (ThO_2) has been reported as a possible product mineral when the apatite-allanite-epidote mineral assemblage has been described (Finger et al., 1998, Budzyń et al., 2010).

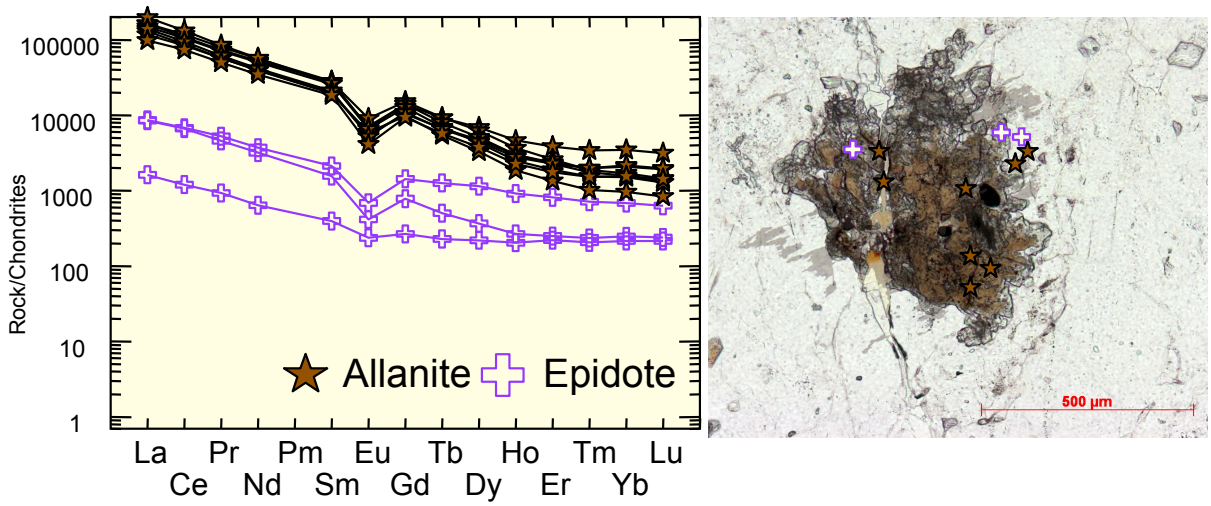

Figure 30: Chondrite-normalized REE patterns of allanite and epidote measured by LA-ICP-MS. The allanite is shows a higher amount of LREE than the epidote occurring along the rim. The HREE content of the epidote reaches nearly to the same level as the allanite. Samples normalized to C1 Chondrite of Sun and McDonough (1989).

The LREE in the allanite is enriched to the factor of 200.000 in that of chondrite, with a slight scattering of the HREE, ranging from 10.000 to 40.000 (Figure 30). The epidote show the same trend as the allanite, with a decreasing content of the LREE, while the enrichment of the HREE nearly reaches the level of the allanite. The BSE image of the assemblage (Figure 31a) shows that the light intensity varies gradually throughout the allanite areas, indicating fluctuations in element concentration.

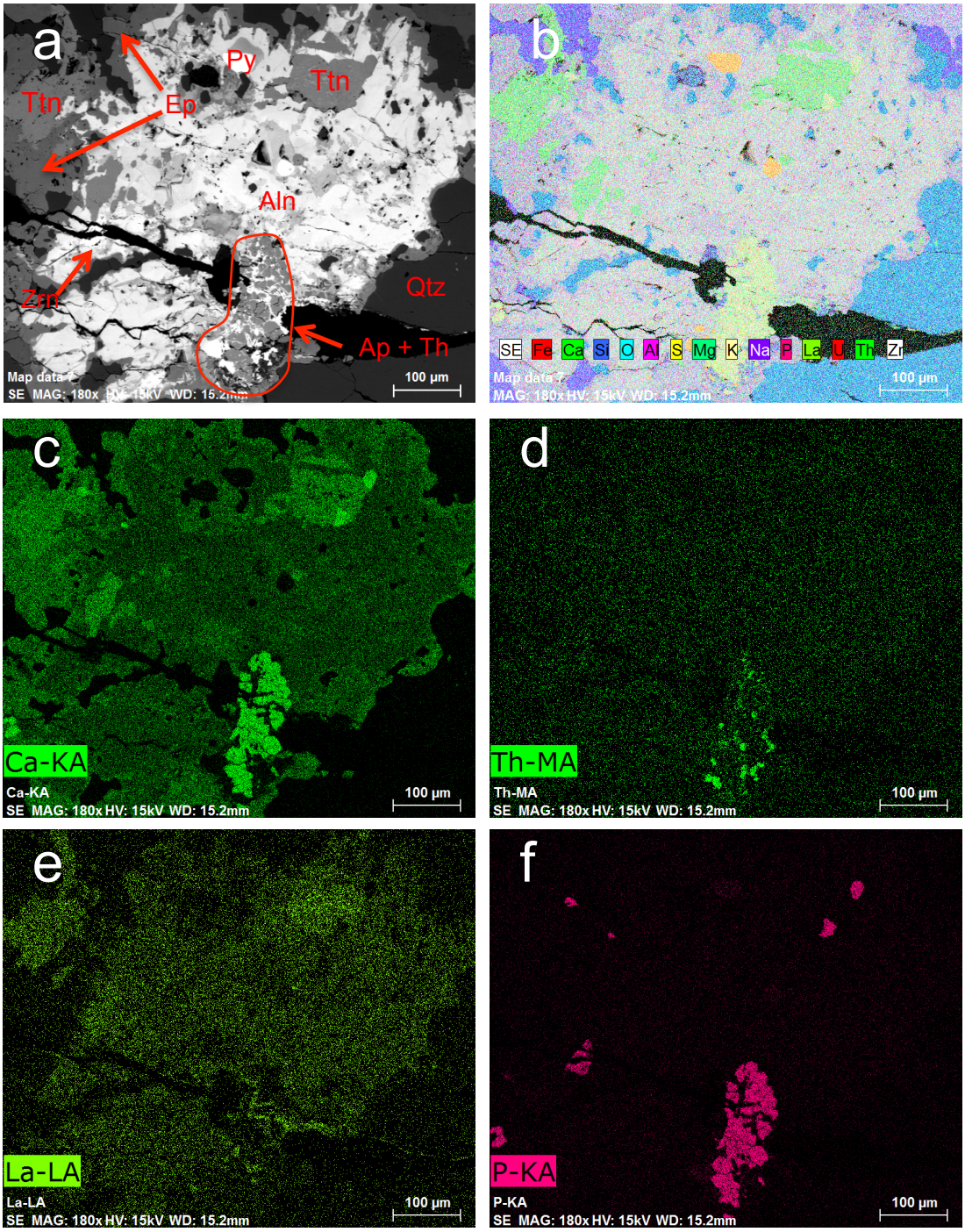

Figure 31: Element maps were made on the brown pleochroic allanite grain in Figure 30. The BSE-image reveal the cluster of minerals located directly above the largest fracture, with apatite holding a Th-rich mineral (bright white phase) phase along with REE-rich phases. a – A high-contrast BSE image, with the apatite grain in the centre at bottom edge. b – Summary map of all the elements recorded during the mapping. c – Calcium map: the concentration of Ca varies throughout the map, with the allanite has the lowest of the Ca-bearing phases. The allanite is rimmed by the epidote, while the Ca-rich in the bottom centre is the apatite. d – Thorium-map: Apatite grains is hosting inclusions of a Th-bearing mineral. e – Lanthanum map: Allanite is rich in La, along with the titanite. f – Phosphorus map: The P phases correlates to the Ca, indicating apatite.

Isocon diagrams

The method of Isocon diagrams will be presented in the following paragraphs, along with a discussion concerning the advantages and drawbacks of the method. This subchapter ends with the result of the Isocon analyses, where the loss or gain each oxide/element is explained by the formation or disappearance of a mineral related to the mineral assemblage. In the discussion chapter, the results of the Isocon analyses will put into a larger context, when trying to explain the element mobility in the rocks.

Gresens (1967) published a general set of equations that dealt with mobilization during metasomatism, which was further developed by Grant (1986) into what is known as *Isocon diagrams*. The Isocon diagrams is a simple way of quantifying changes in mass, volume or concentration by plotting unaltered and altered rock compositions against each other (Grant, 2005). A reference framework is also needed in order to detect the gains and losses in the mass transport, and a plot of immobile elements along a line defines an Isocon, a line of no-mass transfer (Grant, 1986, Grant, 2005). Species plotted above the Isocon has been gained to system, whereas species plotted below has been removed (Grant, 2005).

López-Moro (2012) published a Microsoft Excel spread sheet, EASYGRESGRANT, which simplifies the selection of immobile elements, where he has combined the methods of both Gresens (1967) and Grant (1986). Making the reference framework to be defined by either constant mass, constant volume or immobile elements, where the latter is most often used as evidence of constant mass or volume often cannot be recognized (López-Moro, 2012). He present five ways of determining whether an element is immobile or not: *Clusters of slopes* and *volume factors*, where elements with similar slopes or volume factors are assumed to be immobile. *Composition-volume diagrams* and *the Isocon diagram* are the graphical versions of the comparisons of the clustering of volume factors or slopes, respectively. *Component-ratio diagram*, with plotting element ratios in the unaltered against the altered rocks. If a component appears to be decreasing, it does not necessarily mean that it has been lost. It can also mean that another component has been added and "diluting" the system. The use of a component-ratio diagram will solve this problem and reveal the true nature of the system (Gresens, 1967).

It is not always the case that the assumed immobile elements plot directly on the Isocon line, but rather showing a slight scatter around the line. Mukherjee and Gupta (2008) suggest

several causes for this to happen: (a) Geochemical heterogeneity in the unaltered rocks, creating deviating results compared to the altered rocks, (b) analytical errors or, (c) that no element is completely immobile.

Often in samples, the concentration of different elements varies in orders of magnitude compared to each other and Grant (1986)'s solution was to scale down elements to a comprehensible size and then construct the isocon line, saying that the scaling would not affect the slope of the line. Scaling would not be a problem as long as the isocon line is based on only one element, and therefore giving one unique solution (Mukherjee and Gupta, 2008). However, Baumgartner and Olsen (1995) showed mathematically and argued how scaling would indeed impact the slope of the Isocon line when several immobile elements are chosen. They recommended a more statistical approach, by a weighted least-square method in order to determine the immobile elements within their own range of uncertainties, which takes care of the pitfalls of analytical errors and heterogeneity of any sample.

The Isocon method can be perceived as limiting, as any handling of the data without careful consideration could affect the results. Any decision of the selection of your immobile elements should have support from other sources, such as geochemical and petrological evidence, besides the fact that they lie close to the proposed isocon line (Baumgartner and Olsen, 1995, Mukherjee and Gupta, 2008). When deciding on the immobile elements, it is recommended that several elements are chosen and they are geochemically different, as some species have coupled behaviour making it seem like they are immobile (Grant, 1986). These weaknesses have been taken into consideration in the process, and therefore the results are assumed reliable as it also can be supported petrographically.

The spread sheet EASYGRESGRANT published by López-Moro (2012) was chosen for this study, because it takes many of the weaknesses of the Isocon method pointed out by other authors (e.g. Baumgartner and Olsen, 1995, Mukherjee and Gupta, 2008) into consideration when calculating the diagrams, such as scaling. Immobile elements were selected as the reference framework, as neither constant mass nor volume can be assumed for the samples. Zr and TiO_2 were the choice of immobile elements for the granodiorite and phyllonite calculations. Generally, Zr and TiO_2 are considered to be immobile during greenschist facies metamorphism (Pearce and Cann, 1973, Rollinson, 1993). Major Zr- and Ti-bearing minerals zircon and titanite is found in the granodiorite as well as the phyllonite, suggesting that these

elements has remained immobile during deformation. In the primitive mantle-diagram for the phyllonite (Figure 15c) Nb, Ta, Zr and Ti show a clustering effect, which can be an indication of these elements immobile behaviour during deformation. However, Ta and Nb can have similar geochemical behaviour due to their similarity in size and charge (Rollinson, 1993), and significant amounts of Ta and Nb can substitute for Ti in titanite (Deer et al., 1992).

The robustness of the geochemical data and method was tested by applying extreme values of ± two times the standard deviation (σ) of the values of the average granodiorite (Appendix - Isocon). This had a major implications on the calculation of the isocon line, as the chosen immobile elements Zr and TiO_2 was nearly doubled in the range between – 2σ and +2σ, so the slope of the isocon line also doubled. When this happened, the SiO_2 went from lost and having a negative mass and volume change to be gained in the system with a positive volume and mass change during deformation. The implication is that when applying the Isocon method with average values can yield opposite results, especially when your data suggest small changes in mass or volume. Small variations within your data will possibly give you wrong results. There is also no obvious way to ignore or work around the effect of the SiO_2 as it is the largest single contributor to the geochemical data with an average of 77.6 wt. % in this case. With that taken into consideration, only the paired samples were used in the Isocon analysis, as they represent a local chemical system that is closed.

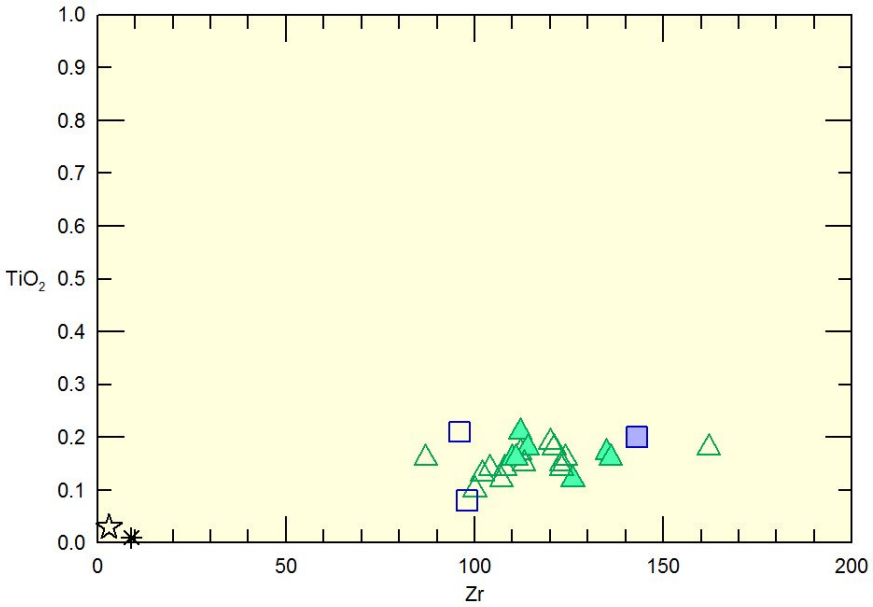

Figure 32: TiO_2 and Zr variation diagram. The correlation between TiO_2 and Zr suggests a limited mobility. The outliers are hydrothermal quartz vein and two massive sulphide samples, therefore are not representative for the granodiorite and phyllonite. A scattered trend would have been an indication of element mobility, though alteration can produce systematic and coupled behaviour (Rollinson, 1993). The hollow green triangles are the granodiorite, filled

green triangles are the phyllonite, the hollow blue squares are a collective class for the hydrothermal quartz, aplite and sulphide-rich samples and the filled blue square is the epidote-rich shear zone.

When plotting the isocon data, the major oxides where listed first as they are compatible and the major controlling factor. The available trace elements were set in a hierarchy, consisting of compatible and incompatible elements, with the incompatible elements were subdivided into large ion lithophile elements (LILE) and high field strength elements (HFSE). The HFSE were split into the non-REE and REEs, and the REEs into the LREE and HREEs. Tl was removed, as the element was not detectable in all the samples, and will thus not yield any results.

The diagram shows the chemical mobility that is observed in quartz-rich granitoid and granodiorite samples vs. phyllonite and the epidote-rich shear zone. Measurements approaching $\Delta C^i/C_o^i \sim 0$ is tough to estimate. The major oxides are the result of that many different minerals can accommodate the same oxides, such as iron in epidote and muscovite, potassium in muscovite and alkali feldspar; aluminium in muscovite, alkali feldspar, plagioclase and epidote.

The first two analyses (P26B-u vs. P26B-d and P18A vs. P18B) (Figure 33a and b) have a striking resemblance. First, both are depleted in most of the major oxides and trace elements. Second, there is a slight increase in Fe_2O_3 and MgO that is likely associated with the formation of pyrite and trace amounts going into muscovite in the phyllonitic shear zones. The P26B-u vs. P26B-d shows an increase in K_2O, while the P18A vs. P18B is depleted and may be due to that the K_2O component does not only account for the muscovite, but also for the alkali feldspar where K is a major structural component. With loss of K_2O in the second sample, but not in the first, might suggest that the loss of alkali feldspar (or K_2O) was greater than the gain contributed by the muscovite. The gain of the Rb is most likely linked to the muscovite formation (Etheridge and Cooper, 1981).

Thirdly, the depletion of CaO can be linked to the disappearance of epidote and the Ca-bearing plagioclase, while the loss of Na_2O and Sr is probably related to the loss of the primary plagioclase and albite in all three samples. The P26B-u vs. P26B-d shows a greater loss of Na_2O than the second sample. Sample P18B is a phyllonite containing more than 25.0 wt. % plagioclase, while there is <1 wt. % plagioclase in the P26B-d sample (Table 2).

There appear to be a significant loss of the P_2O_5, however, this measurement is approaching the lower detection limit and the difference between the samples was a mere 0.01 wt. %. The LILEs, Rb, Cs and Ba, are added to system along with Nb and Ta. The three LILEs can be accommodated by muscovite and possibly Ba in alkali feldspar, while Nb and Ta tend to have a similar behaviour to Ti and can be hosted by Ti-bearing minerals. The REEs appear to be depleted in both samples, with the P26B-d sample showing no significant difference between the LREE and HREE, while the P18B sample show a greater relative loss in the LREE.

The enrichment of Fe_2O_3 in the P31-u vs. P31-d can be attributed to pyrite, but also along with MgO, CaO and trace amounts of MnO and Sr can be accommodated by the epidote. The sample has an overall enrichment of the REE, but mostly by the HREE and a large peak by Y. (For numerical results for all three analyses, see Appendix - Isocon).

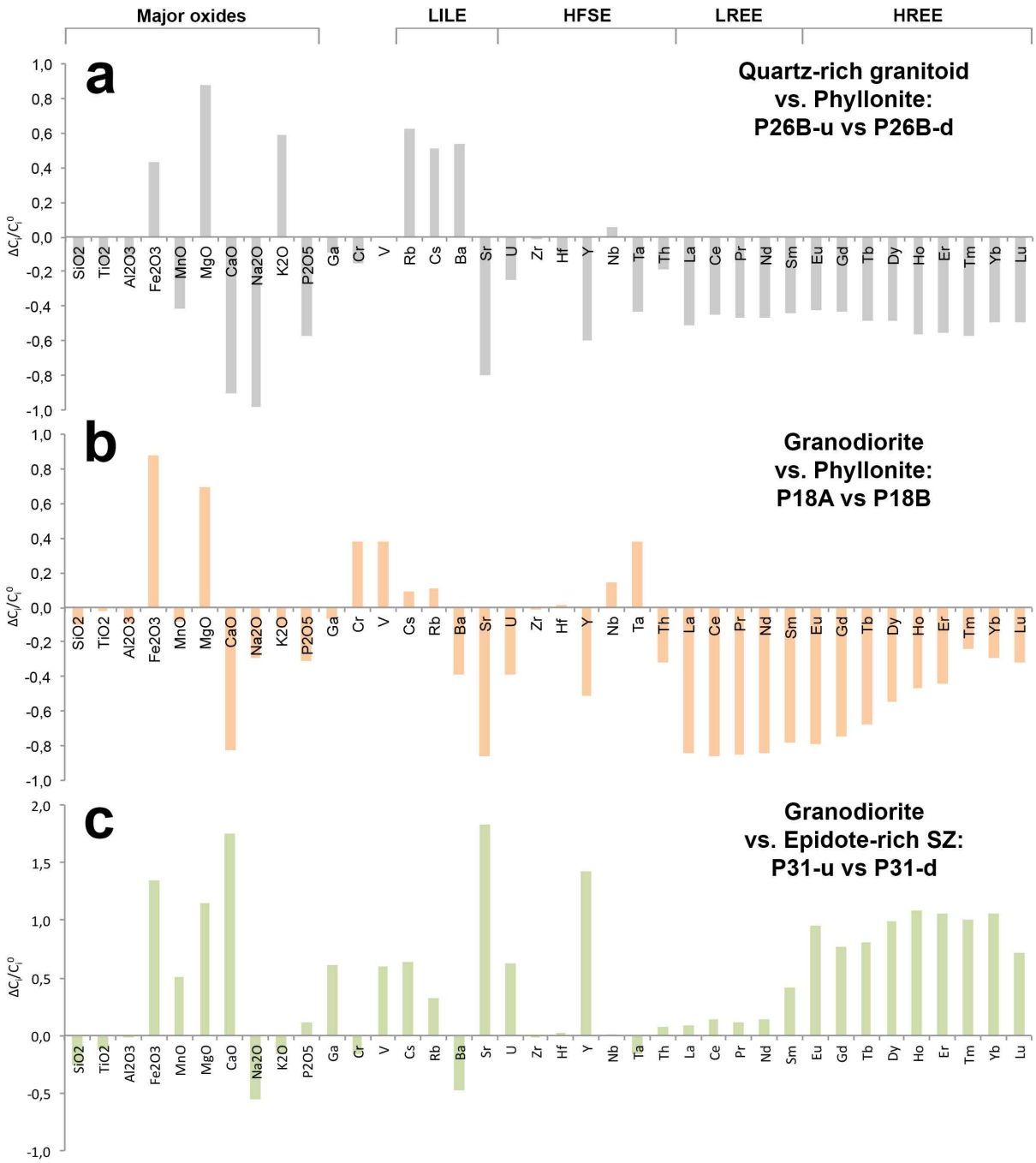

Figure 33: It was assumed that Zr and TiO_2 were immobile during alteration and deformation. The results here are plotted as the relative loss/gain $\Delta C_i/C_o^i$ to the unaltered sample. Note the different scale scales on the Y-axes. The calculations were performed in the spread sheet of López-Moro (2012).

Table 3: Volume and mass changes calculated from the Isocon analysis, based on López-Moro (2012). All samples indicate a mass and volume loss during deformation and alteration.

Samples	Volume change	Mass change
P26B-u vs. P26B-d	-16.67 %	-15.09 %
P18A vs. P18B	-9.84 %	-8.15 %
P31-u vs. P31-d	-21.42 %	-16.10 %

All the samples presented a significant mass and volume loss during the alteration and deformation (Table 3). The bulk density of each sample was calculated based on the modal mineralogy from the XRD and the density of each mineral present. The calculations showed that all the samples had an increase in density during alteration and deformation, which supports the volume loss calculated in the isocon analysis.

Discussion

Granodiorite

Feldspars

The granodiorite samples are texturally well preserved with tabular plagioclase and some crystal faces on quartz (Figure 7). Though, the signs of alteration is evident in all thin sections, by recrystallization of quartz, seritization and saussuritization of the plagioclase, neocrystallization of the perthitic microcline to albite. The accessory minerals occur in aggregates of allanite, epidote and titanite, with most of them connected to muscovite. Throughout the samples, muscovite growth occurred along grain boundaries, especially those of plagioclase. Whether muscovite is part of the igneous mineral assemblage or not is difficult to discern as the alteration is pervasive throughout the granodiorite and muscovite is definitely a part of the secondary alteration assemblage.

The alkali feldspar is replaced by neocrystallized albite, seen as the polygonal albite grains mantling the alkali feldspar (Figure 7a-b), which has commonly been associated with fluid interaction and metasomatism (Engvik et al., 2008). The reaction can be described simply by a base cation exchange (Pirajno, 2009), where Na^+ is introduced into the open system (Equation 2):

$$\underset{Alkali\ feldspar}{KAlSi_3O_8} + Na^+ \longrightarrow \underset{Albite}{NaAlSi_3O_8} + K^+$$

During the exchange, K^+ is released from the alkali feldspar and goes into solution. K is major constituent in sericite, which can form at the expense of the Ca-plagioclase and release Ca^{2+} into the fluid. All plagioclase in the granodiorite samples have small sericite inclusions and larger grained muscovite along its rims (Figure 7a-b). A possible reaction for the alteration of the plagioclase can be written as:

Equation 7: Plagioclase alteration

$$2\ (\underset{Oligoclase}{NaAlSi_3O_8 \cdot CaAl_2Si_2O_8}) + 2\,H^+ + K^+ + \underset{Quartz}{2SiO_2} + Na^+ \rightarrow \underset{Muscovite}{KAl_3Si_3O_{10}(OH)_2} + 3\,\underset{Albite}{NaAlSi_3O_8} + 2\,Ca^{2+}$$

Modified after Orville (1962) and Putnis and Austrheim (2013). The coupled substitution of $Na^{+}+ Si^{4+} = Ca^{2+} + Al^{3+}$ occur during sericitization of the Ca-plagioclase, leaving the residual feldspar as more albite-rich, and the leftover Al^{3+} from the substitution is assigned to the muscovite.

The rim of the plagioclase is occasionally unaffected by the seritization, indicating an albite-rich rim. The rim could have formed during the crystallization of the magma, as a Ca-rich core with Na-rich rim indicate the decrease in temperature during crystallization, or it could have formed later during alteration when Ca^{2+} was released during the seritization. Ca-plagioclase is partially altered to sericite (Equation 7), as it is more prone for hydrothermal alteration and leaving the residual crystal as more Na-rich. This is the most likely scenario as no zoned plagioclase has been observed in the granodiorite samples.

Epidote

Epidote is considered to be a secondary phase in the granodiorite where the alteration of plagioclase contributed with the Ca^{2+} required for the mineral to form. The varying degrees of saussuritization of the plagioclase throughout the samples also suggest a local chemical system. The Ca-component is not stable at lower temperatures and subsequent decomposition of anorthite to a epidote mineral will occur (Franz and Liebscher, 2004), e.g. clinozoisite, along with muscovite:

Equation 8: Epidote formation

$$\underset{Anorthite}{2CaAl_2Si_2O_8} + \underset{Alkali\ feldspar}{2KAlSi_3O_8} + H_2O \rightarrow \underset{Clinozoisite}{Ca_2Al_3Si_3O_{12}(OH)} + \underset{Muscovite}{KAl_3Si_3O_{10}(OH)_2} + \underset{Quartz}{SiO_2} + K^+$$

After Poli and Schmidt (2004). Note: Plagioclase end-member anorthite has been applied for simplicity, though the plagioclase most likely had a significant proportion of albite. Modified version (Equation 7) of the decomposition of Ca-plagioclase to muscovite, where alkali feldspar contributes with K^{+} to the muscovite and the Ca-plagioclase gives the Ca^{2+} to the clinozoisite. Al is redistributed between the clinozoisite and the muscovite, while Si is in excess. Inclusions of epidote are quite hard to distinguish from the sericite when the grain sizes are so small; where as other grains are quite obvious. Some plagioclase grains are completely covered in green epidote, and in other parts, the plagioclase are only showing small inclusions with an anomalous blue interference colour that suggest a clinozoisite (Deer et al., 1992). Ca^{2+} has probably been mobilized to a certain extent and precipitated as epidote

at ideal sites. Some of the plagioclase grains analysed by the EMPA show a range between 2.0 to 2.4 Al c.p.f.u with the rest of the available site occupied by Fe^{3+}, Fe^{2+} and minor Mn (Figure 23). The formation of epidote requires a high f_{O2} and a oxidising environment, which promotes the presence of Fe^{3+} rather than Fe^{2+} (Franz and Liebscher, 2004). The variable composition may be a result of the Fe availability, as epidote and clinozoisite form a solid-solution with Fe^{3+} substituting with Al at the M site and epidote being the iron-rich end-member (Armbruster et al., 2006). At thin section scale, both clinozoisite and epidote may form as epidote can precipitate in Fe-Al-rich domains, while clinozoisite can form in Ca-Al-rich domains (Franz and Liebscher, 2004). The Fe that epidote requires must have a source, e.g. a previously present phase like biotite as it is a very common mineral phase in alumina-saturated granitoid rocks (Clarke, 1981). None of mafic phases that are commonly found in a felsic granitoid is preserved, though a few grains of chloritized biotite have been identified in the aplite (Appendix - Petrography) and Fe-bearing pyrite is disseminated within the granodiorite and is also abundant in the phyllonites, indicating a transport of Fe within the system.

Some epidote analyses showed a distinct positive Eu anomaly and one grain displayed a positive Eu anomaly in the core while the rim showed no anomaly (Figure 27 and Figure 29). In order to form such an anomaly, it requires reducing environments where Eu^{3+} is reduced to Eu^{2+} and thus fractioned from the other trivalent REEs. The possibility of epidote being a magmatic mineral still present in the granodiorite is unsupported. Saussuritization and seritization of the plagioclase along with the neocrystallized albite indicate extensive alteration of the granodiorite, but no secondary alteration of the epidote is observed. A plausible explanation is that Eu^{2+} came from the primary plagioclase that released Ca^{2+} and thus Eu^{2+} during Ca-plagioclase alteration. Analyses of the positive Eu anomalies in Figure 29, (right picture, blue circles) were done on grains straddling the rim of a vug in the granodiorite, indicating a secondary origin of the epidote.

The formation of the epidote as a secondary mineral, and the variable degree of saussuritization of the plagioclase suggest that Ca was easily mobilized during alteration, but the composition was dependent on the local chemical system in the rock e.g. availability of Fe during mineral formation.

Titanite stability

The HREE-enriched titanite occurs always in association with either the epidote, epidote-allanite aggregates or with heavily fractured apatite with Th-inclusions. It often exhibits a rather odd granular tail-shaped habit (Figure 7c) rather than the typical wedge-shaped habit. The mineral is considered to be of secondary origin, but the role of the titanite is unclear besides that under these conditions Ti, Ca and HREE was stable under these conditions so titanite could form. According to Bea (1996) primary titanite always contain at least a couple hundred ppm of Th, so the low amount of Th in the titanite (1 – 25 ppm) suggest that the mineral is not a part of the primary, but rather the secondary mineral assemblage. The immobile nature of Ti and the titanite implies the necessity for a Ti-source nearby, while the Ca is supplied by the decomposition of plagioclase. Possible sources for the Ti are ilmenite, rutile and Ti-bearing biotite. Anhedral titanite has also been described as a common low-grade breakdown of biotite (Tulloch, 1979). Minor amounts of biotite has been found in the north-end boundary of the Fagervika granitoid, in the abandoned quarry down at Munkaunet (Slagstad et al., 2014) and as chloritized biotite in the aplite samples (Appendix - Petrography). This suggests that biotite once was a primary mafic mineral in the granodiorite, though it is only speculative. The presence of titanite in the granodiorite suggests that the mineral could form due to a local Ti saturation. However, the mobility prior to formation cannot be resolved, it is evident that mobility does not occur on a large scale.

Monazite decomposition

During monazite decomposition, fluorapatite nucleated at the pre-existing site where the original PO_4 tetrahedra in the monazite lattice created the foundation for apatite growth, with fluorapatite possibly inheriting a significant proportion of the LREE content of the monazite (Finger et al., 1998, Budzyń et al., 2011). Allanite and epidote analysis done on the rim of the grain (Figure 31) show that a substitution might be taking place where $REE^{3+} + Fe^{2+}$ is exchanged for $Ca^{2+} + Al^{3+}$ (Figure 23). The BSE images of the aggregate show that the epidote-allanite transition is distinct, while the intensity within the allanite area is undulating (Figure 31a), suggesting that the epidote growth along the rim is either controlled by the REE availability from the allanite grain or fluids are externally leaching across the rim of the allanite, though either is hard to differentiate. Leaching of REE at the grain boundary would imply a mobilization of the REE, in the granodiorite, which is doubtful. The most probable scenario is that epidote at the rim formed when availability of REE were low, due to the immobility of REE in the granodiorite. Experimental studies have showed that the Ca and Na

activity is an important factor during metamorphic allanite growth, where high Ca activity promoted the growth of allanite, REE-epidote and fluorapatite, while high Na activity promoted growth of secondary monazite (Budzyń et al., 2011). SEM mapping of the transitional P18B sample between granodiorite and phyllonite show that no epidote is present, while a large proportion of albite is surrounding the quartz (Figure 18). This suggests that at the time of allanite growth, Ca^{2+} were dominating in the fluid in comparison to Na^{+} as it were still detained in the albite. In a peraluminous granite, monazite is the preferential accessory mineral before allanite, due to a higher aluminium and lower CaO content in the system, while allanite, titanite and apatite has affinities to a more metaluminous granite (Bea, 1996). None of the accessory minerals that have been identified at Gråkallen are euhedral or shows any texture indicating a primary origin, except for the zircon that is commonly very resilient towards alteration.

This suggests that the REE mobility were limited to grain scale in the granodiorite, as the allanite and the rest of the assemblage most likely took over REE content of monazite at the previous site. Ca that was required to form apatite, epidote and allanite came from the decomposition of the plagioclase and the Fe could come from breakdown of phase like biotite (Finger et al., 1998).

The epidote-rich shear zone

The undeformed granodiorite surrounding the leached zone and epidote-rich shear zone consists of quartz, plagioclase and alkali feldspar (Appendix - Petrography) is similar to the other granodiorite samples (Table 2). In the leached white zone that surrounds the epidote-rich shear zone, it shows that the alkali feldspar is replaced by the neocrystallized albite, muscovite becomes the main K-bearing phase, and the major mineral phase changes are the same to what is seen in the other granodiorite samples with increasing alteration. SEM mapping of the shear zone shows that the albite is completely leached out and is replaced by epidote, making the mineral assemblage of Ep + Ttn + Ms + Py + Qtz (Figure 20). The enrichment of epidote and titanite is contrasting the mineral assemblage in comparison to the assemblage found in the phyllonite, where there is no epidote present with only minor titanite. The stabilization of epidote and titanite seem to have played a role in the enrichment of the REEs as they can carry these elements. The timing and spatial relation of the epidote-rich shear zone to the granodiorite and phyllonite is unclear and thus making any interpretation rather difficult.

Formation of the phyllonite

The locality at the steep cliff show that the transition between the phyllonite and the granodiorite can occur quite abruptly, indicating that fluid flow was very localized (Figure 13). In order for muscovite to form in the phyllonitic shear zones there must have been a substantial flow of water-rich fluids as water is responsible for approximately 10 % of the total weight in muscovite (Robb, 2005). The increased amount of pyrite in the phyllonite indicates the presence of fluid flow, from which the pyrite precipitated. Fe and Mg in the muscovite, shown by the SEM maps (Figure 19) and the mineral formula calculations, could stem from biotite, which is a common mineral phase in alumina-saturated granitoid rocks (Clarke, 1981). The increase in Rb in the phyllonite (Figure 16) is related to the formation of muscovite as it can incorporate into the muscovite lattice (Deer et al., 1992), while the loss of Sr related to the loss of feldspar and epidote. Quartz behaved ductile during deformation and underwent recrystallization, while alkali feldspar behaved in a brittle manner, being fractured and showing incipient deformation twins. Epidote minerals have shown to be more rigid than feldspar minerals during deformation (Franz and Liebscher, 2004). No epidote is found in the phyllonite or the transitional sample, but if epidote experienced any deformation, it would behave brittle and fractures would have been induced. This would have enabled fluid infiltration into the crystal and allowing a much more effective mineral destabilization.

O'Hara (1988) raises some important questions if whether shear zones are localized due to a higher fluid flow in an area, or did the shear zones act as fluid pathways? And also, did chemical changes occur due to deformation, or did the deformation cause the chemical changes? What exactly triggered the formation of the first phyllonitic shear zone is unknown, but the whole suite of rocks at Gråkallen shows evidence of infiltrating fluid flow occurring over a large scale, evidenced by the presence of the hydrous mineral assemblage of muscovite and epidote. The first shear zones were probably formed where the rocks were the weakest, and after the formation of the first phyllonite the system acted in a positive feedback system, where continuous shearing and fluid flow promoted the formation of more muscovite and thus more phyllonite.

Sample P18B were mapped as a phyllonite in the field, but is believed to be transitional between the granodiorite and the near-feldspar free phyllonite, as it contained specks of white albite. SEM mapping showed large areas of neocrystallized albite that occur at the expense of

the muscovite and quartz, compared to other phyllonites (Figure 18). Albite can be consumed to form muscovite and quartz, after Orville (1962) and O'Hara (1988).

Equation 9: Albite to Muscovite

$$\underset{Albite}{3\,NaAlSi_3O_8} + 2\,H^+ + K^+ \longrightarrow \underset{Muscovite}{KAl_3Si_3O_{10}(OH)_2} + 3\,Na^+ + \underset{Quartz}{6\,SiO_2}$$

The albite available for the reaction is the neocrystallized albite formed from the alkali feldspar and the released K^+ originates from the Na - K substitution forming the same albite. It is thought that the phyllonite acted as a fluid flow pathway, as grain boundary sliding can enable the fluid flow along the grain boundaries and thus increasing the fluid-rock interaction ratio (Rubenach, 2013). The transformation from granodiorite to phyllonite calculated a mass loss of approximately 15% in the Isocon diagram (Table 3), by creating a higher density of the phyllonite than the granodiorite. Such a volume loss and the high-density phase formation could also create a porosity and permeability. If the solubility of the host mineral is greater than the solubility of the product mineral, less new minerals will be precipitated in the same space in comparison to the host mineral. This allows for porosity and permeability to form and thus permitting fluid flow (Putnis and Austrheim, 2010). The fluid circulating in the phyllonite shear zone might be undersaturated with silica at first, shown by the mass calculations of the isocon. Any saturation or oversaturation would have triggered a precipitation of quartz within the shear zones, which would have resulted in strength hardening, rather than a reaction-softening of the rocks (Dixon and Williams, 1983, Wibberley, 1999). By forming new, smaller grains by dynamic recrystallization of quartz and neocrystallization of albite and muscovite, the deformation mechanism change from intracrystalline processes to grain boundary deformation processes, showing that fine-grained rocks are weaker than their coarse-grained equivalents (White and Knipe, 1978, Fitz Gerald and Stünitz, 1993). The breakdown of the feldspars and the increase of quartz and muscovite interconnection allows for extensive fluid access and strain accommodation due to the weakness of muscovite (Tullis, 2002, and references therein). This suggests the possibility of a mineralogical control on the formation of the phyllonite.

Metamorphic conditions recorded

Granitoid rocks are not very useful as P-T estimators in metamorphic petrology, as the main constituents, quartz, alkali feldspar, plagioclase, muscovite, biotite and amphibole, can exist over a wide range of P-T conditions (Bucher and Grapes, 2011). However, P-T conditions can

be broadly constrained by textural observations, especially those in found in quartz. During recrystallization, GBM was the dominant recrystallizing process, which was later overprinted by bulging. With a change in metamorphic conditions, bulging became the controlling process and resulted in protruding grain boundaries of both the larger remnant grains and also the smaller recrystallized grains produced by GBM. This created an amoeboidal appearance of the quartz with long wavelength bulges of the recrystallized grains and subsequent small-scale bulging on the grain boundaries and an inequigranular grain size distribution (Figure 7a and Figure 9a). Rounded albite porphyroclasts are hosted in the muscovite matrix in the phyllonite, and in one sample, a large alkali feldspar porphyroclast has penetrating fractures throughout the grain and along the cleavage planes but also incipient deformation twins, indicating brittle-ductile transition deformation for the feldspars. It is interpreted that the albite porphyroclasts are remnant grains after the primary, but altered plagioclase, and microprobe analyses of the altered plagioclase could confirm this relationship.

Summarizing these textural features, bulging of the ductile quartz and brittle feldspar, could put these recordings in the 300 - 400°C range, ~greenschist facies conditions, though the constraints on the feldspar is inconclusive (Passchier and Trouw, 1996, Tullis, 2002), while the GBM probably initiated at a higher temperature. Experimental studies on granitic rock deformation at these conditions has shown that quartz deform easily, muscovite can glide along grain boundaries and the fracture formation in the feldspar allows for fluid access and thus enabling further deformation (Tullis, 2002).

The occurrence of allanite and epidote corona surrounding the core of fluorapatite along with inclusions of a Th-bearing mineral and REE-phase (Figure 31), has been reported as a replacement of destabilized monazite in metamorphosed granites and granitic gneisses (Finger et al., 1998, Budzyń et al., 2010). Primary monazite appears to be unstable under amphibolite facies conditions in granitoid rocks, though it is highly dependent on the rock composition (Finger et al., 1998, and references therein), and the Fagervika granitoid have previously been set to upper greenschist-lower amphibolite facies conditions (Slagstad et al., 2014), which fits well with field observations.

[Intentionally blank page]

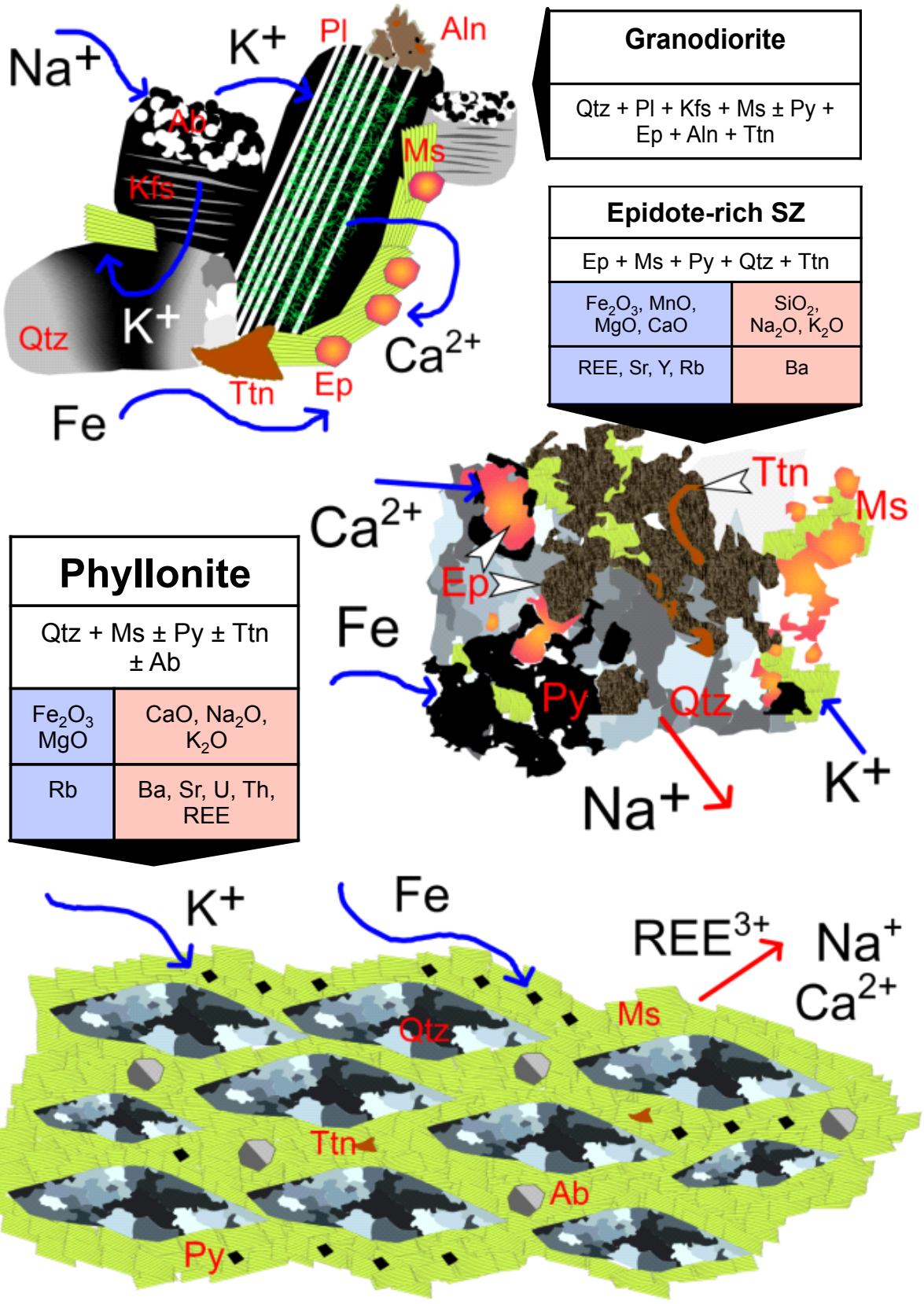
Na+
K+
Pl
Aln
Ab
Ms
Kfs
Qtz
K+
Ca2+
Ttn
Ep
Fe
Granodiorite
Qtz + Pl + Kfs + Ms ± Py + Ep + Aln + Ttn
Epidote-rich SZ
Ep + Ms + Py + Qtz + Ttn
Fe2O3, MnO, MgO, CaO
SiO2, Na2O, K2O
REE, Sr, Y, Rb
Ba
Ca2+
Ttn
Ms
Ep
Fe
Py
Qtz
Na+
K+
Phyllonite
Qtz + Ms ± Py ± Ttn ± Ab
Fe2O3 MgO
CaO, Na2O, K2O
Rb
Ba, Sr, U, Th, REE
K+
Fe
REE3+
Na+
Ca2+
Ms
Qtz
Ttn
Ab
Py

Figure 34: Schematic summary of the different lithologies and associated mineral assemblages. Blue and red columns represent the elements gained and lost in the alteration and deformation during formation of the epidote-rich shear zone and phyllonite, and the data is taken from the Isocon analyses (Figure 33). Similarly, blue arrows indicate the elements that have been gained or redistributed within the system, while red arrows depict the elements that have been lost. Granodiorite: Na is introduced into system, and substitutes with K to form the neocrystallized albite in the alkali feldspar. The K released during the alteration of the alkali feldspar is available to react and alter the primary plagioclase to sericite. Ca is released by plagioclase and becomes richer in albite. Leftover Ca is available to form saussurite, along with epidote, titanite and allanite. Epidote-rich shear zone: Two types of epidote is distinguished in the figure: large euhedral crystals (orange) and dusty, clustering epidote (brown-grey). Fe, Mn, Mg and Ca went to form epidote, but Fe also contributed to the pyrite. The loss of Na is attributed to the complete loss of albite in the shear zone, while K has been redistributed from the alkali feldspar to muscovite, with some loss of the K to the fluid. Gain of Sr is ascribed to the enrichment of epidote, while REE is attributed to the presence of epidote and titanite. Gain of Rb is linked to the muscovite, while the loss of Ba corresponds to the loss of alkali feldspar. Phyllonite: Muscovite has shown to contain a significant amount of Fe and Mg (Equation 5), but the increased amounts of pyrite also contribute to the gain of Fe. The loss of Ca, Na and K is related to the loss of the Ca-bearing minerals along with both feldspars. Muscovite could not incorporate enough K formed from the decomposition of the alkali feldspar, showing that some K has been lost to the fluid, while the gain of Rb is linked to the formation of the muscovite in the phyllonite. The loss of Ba corresponds to loss alkali feldspar, while Sr can be accounted for in the lost epidote and plagioclase. Loss of U, Th and the REEs is linked to the destabilization of the Ca- and REE-bearing mineral, epidote, allanite and some titanite.

Element mobility related to deformation in greenschist facies conditions

It is assumed that the alteration of the granodiorite had progressed to such an extent prior to the phyllonitization that the mineral assemblage represented in the granodiorite today was also present before the phyllonitization. The primary mineral assemblage of the granodiorite at Gråkallen is quartz, with plagioclase and microcline. Upon deformation, the quartz is recrystallized and the plagioclase shows occasional kinked polysynthetic twins. Hydrothermal fluids alter the primary assemblage and transforms microcline to albite; plagioclase to muscovite and epidote; and an allanite-epidote-titanite (Figure 31) assemblage represent the previous presence of accessory monazite, along with precipitated pyrite dispersed in the granodiorite. The formation of epidote and the other secondary minerals can be seen as a redistribution of all the major elements, as nearly all the elements required for the formation of the minerals are found in the local chemical system (Figure 34). However, with the high fluid/rock ratio and deformation during the phyllonitization of the granodiorite significant mineralogical and chemical changes took place. The granodiorite and phyllonite show a completely different mineralogy, indicating metamorphic and metasomatic conditions where both alkali feldspar and plagioclase were not stabile, but instead favoured the formation of muscovite.

In the transition between the granodiorite and the phyllonite, most of the major elements seem to have been mobilized. The alteration of alkali feldspar to albite, and then to muscovite imply that Na^+ was first introduced and then removed from the system while K^+ was gained due to breakdown of the alkali feldspar, as muscovite grew at the expense of the albite (Table 2). K^+ appears to have been lost in the transitional sample during phyllonitization (Figure 33b), but the formation of the epidote (Equation 8) shows that K^+ can be in excess when alkali feldspar is altered and muscovite is formed, suggesting that some of the K^+ available is lost to the fluid. The CaO content is mainly controlled by the presence of epidote. However, no epidote is found in the phyllonites, which is evident from the CaO loss in Figure 33a-b. Even the transitional P18B sample had no detectable amount of epidote in the XRD (Table 2) and the CaO content in P18B is significantly lower than the other granodiorite samples. The CaO content of this sample most likely accounts for the trace amounts of titanite that is found in the phyllonite. Review Figure 34 for detailed explanations of the gains and losses in the granodiorite-phyllonite-epidote-rich shear zone system.

REE distribution between the Ca-bearing mineral phases

The accessory minerals epidote, allanite and titanite has been identified as the main contributors of the REEs to the whole-rock budget in the granodiorite (Figure 15) and the presence of these minerals controls the content of the REEs in the granodiorite (Alderton et al., 1980, Humphris, 1984). In similarity, they are all Ca-bearing minerals and there seem to be a correlation between the gain or loss of CaO and REE content (Pan and Fleet, 1996). The Isocon shows that CaO has been removed from the system, with the alteration and deformation of granodiorite to phyllonite, there has also been a loss of all the REEs (Figure 33a-b). While in the epidote-rich shear zone (Figure 33c), with the addition of the epidote and CaO, there has also been a gain of the REEs as epidote has the capacity to take REE into the crystal lattice by the coupled substitution of either $Ca^{2+} + Al^{3+} = REE^{3+} + Fe^{2+}$ or $Ca^{2+} + Fe^{3+} = REE^{3+} + Fe^{2+}$ (Gieré and Sorensen, 2004).

In the allanite-epidote-titanite aggregate in the granodiorite (Figure 25), the trace element distribution between the minerals show that allanite has the highest content of REE, especially the LREE and epidote is enriched in the LREE to lesser degree, while titanite is depleted in the LREE, but heavily enriched in the HREE up to the same level as the allanite. The REE-bearing epidote and titanite appear to be in equilibrium with each other, suggesting they formed approximately at the same time (Figure 25 and Figure 26). During crystal growth they

appear to have been fighting over the same REEs, seeing that the epidote is enriched in the LREE, while the titanite is enriched in the HREE (Figure 26). Epidote has been ascribed with a preference of incorporating LREE over HREE in the mineral, with primary titanite exhibiting the same preference to LREE where as the HREE part of the pattern is lower and rather flat (Pan and Fleet, 1996, Bea, 1996, fig. 4). Allanite is identified as the main carrier of REE in the assemblage, and the configuration of the REE patterns suggest that REE content of each mineral is dependent on the immediate REE availability during mineral growth, which could reflect preferential incorporation of LREE in allanite and epidote, while titanite is enriched in only the HREEs.

In the epidote-rich shear zone, LA-ICP-MS analyses of the epidote show that it holds REE (Figure 28). The REE pattern is similar to what has been measured for the other epidote in the allanite-epidote-titanite aggregates, but also is similar to what is found in primary epidote in mineral assemblages that also contain REE-bearing accessory phases (Bea, 1996). The high abundance of epidote in the shear zone, but also the presence of titanite explains the enrichment of the REEs (Figure 16). However, the yttrium enrichment is quite conspicuous, as epidote commonly does not include it into its lattice (Figure 16). For the epidote group minerals, it usually held by the allanite (Gieré and Sorensen, 2004), but as no allanite has been found in the shear zone, but the stability of the epidote could suggest that there is a possibility of a coexistence of allanite or another Y-bearing mineral.

Accessory minerals in the phyllonite

In the phyllonites, accessory minerals titanite and zircon have been found, supporting the assumption that Zr and TiO_2 are relatively immobile (Figure 9c). This is also backed up in a vast amount of literature (e.g. Pearce and Cann, 1973, Winchester and Floyd, 1976, Rubin et al., 1993, and references therein). However, the presence of hydrothermal titanite in the AU1 hydrothermal quartz (Figure 12d) raises some questions whether the TiO_2 is truly immobile or not. TiO_2 is commonly regarded as an immobile element in sub-magmatic temperatures, but it can be mobilized in different environments, depending on the solubility of the Ti-oxides in the fluids and temperature in low-medium grade metamorphic conditions (Van Baalen, 1993). A mineral or species can still be regarded as immobile as it is dependent on scale. Yet, since the scale of the mobilization cannot be inferred from the hydrothermal quartz samples other than it exits in a rock that is younger than the granodiorite, any assessment of the immobility of TiO_2 is problematic.

Timing of alteration and deformation

The textural and geochemical evidence do not reveal the chronology of events that cause the alteration and deformation of the granodiorite to form the phyllonite. In this case, there are two possible paths of the primary, unaltered rock: First, the primary, unaltered granitoid only experience the phyllonitization but no alteration, meaning that epidote, allanite and titanite never formed as a part of the secondary assemblage. Second, the granitoid undergoes regional metamorphism and forms epidote, allanite and titanite, which is subsequently deformed during phyllonitization at a later stage. Titanite has been identified in the phyllonite (Figure 9c), and as part of the secondary accessory assemblage stabile with epidote could indicate that epidote also was present in these rocks prior to the phyllonitization. If the epidote or the other secondary minerals did not exist at the time of deformation, at least primary monazite should have been present. As monazite is not found in the phyllonite and the scattering of the REEs in phyllonite spider diagrams (Figure 15c-d) suggest that the REEs have been significantly mobilized regardless of the existence of the secondary accessory minerals during deformation. Formation of the secondary mineral assemblage with epidote, allanite and titanite is ascribed to the regional metamorphism at ~greenschist facies conditions at 420 Ma during the Scandian phase of the Caledonian Orogeny (Hacker et al., 2010, Slagstad et al., 2014). Even with the complete loss of the hypothetical biotite and the alteration of the alkali feldspar suggest that alteration has occurred in the presence of fluid, though the fluid/rock ratio is low in the granodiorite. There also occurs to be different groups of epidote, with epidote formed during plagioclase alteration is separate from the epidote occurring with allanite, and perhaps titanite. This distinction is not fully investigated, and could be focused on in future work.

The preliminary structural investigations done at the Shear zone on the steep cliff at Gråkallen indicate a top-to-the-west transport direction of the phyllonitic shear zones (Figure 13b), which suggest a correlation to the extensional collapse of the Caledonides around 400 – 380 Ma (Hacker et al., 2010). Dating the muscovite formed in the phyllonites could therefore reveal the age of the deformation and constrain the timing of the regional deformation history.

Fluid behaviour

Carbonate, sulphate, chloride and fluoride are considered as important REE-bearing complexes and for enabling REE mobility (Humphris, 1984). REEs are easily accommodated into accessory phases, such as allanite and titanite that can account for 80 to 95 % of the

whole-rock REE budget, but also epidote can contribute significantly (Gromet and Silver, 1983, Bau, 1991). In order to maintain the REE pattern of the bulk-rock during alteration and destabilization of the REE-bearing minerals, the REE has to be accommodated by a secondary mineral phase if not it will be mobilized and leave the system. The fluids flowing through the phyllonite shear zones and pervasively through the granodiorite are probably similar as they are within the same system and in close proximity to each other. The major difference between the granodiorite and the phyllonite is the deformation and fluid-rock ratio, with the phyllonites experiencing a much greater fluid flow. When destabilizing a mineral phase that can host REE and any other trace element, it dissolves and disperses the elements into the fluid; there are two possible pathways. If the fluid-rock ratio is low and because the REEs are incompatible, the will most likely form a new REE-phase. The decomposition of monazite indicate a small-scale mobilization of the REEs, though not very far before it precipitated as apatite, allanite, Th-mineral and epidote *in situ* (Figure 31). The alteration intensity is dependent on the fluid-rock ratio, because it has the major control on whether a reaction will go to completion or not, therefore a high fluid/rock ratio and the presence of complexes in the fluid, it has the ability to reach equilibrium with the surroundings and thus removing the REE-bearing phases (Bau, 1991). Due to the high fluid/rock ratio in the phyllonite, the REE mobility might not be solely dependent on the ligand concentration. No REE-bearing minerals were precipitated in the phyllonites and those that are present are considered to be remains from the granodiorite. This suggests that the REE content never reached a saturation level and was transported out of the system.

Based on the mineral observations, the fluids circulating the suite of rocks at Gråkallen were water-rich, holding Ca^{2+} from the plagioclase, K^{+} from the alkali feldspar along with minor amounts of other ions such as Fe^{2+}/Fe^{3+}, Mg^{2+} and Na^{+}, but it was low in REE, as no new REE-phases have been precipitated in the phyllonites. At some point the fluid carried REE out of the system as the phyllonites is depleted in REEs (Figure 15c-d) while the epidote in the epidote-rich shear zone are enriched in REEs (Figure 28). A sulphur-bearing phase has been present, as pyrite has been precipitated in mainly in the phyllonites, but also in the granodiorite. The amount of ZrO_2 is consistent throughout all the granodiorite and phyllonite samples (Appendix – Whole-rock analyses), suggesting that the fluid were low in effective Zr-carriers such as F^{-}. Calcite occurs interstitially in some of the granodiorite samples, but is also found in the phyllonite (Figure 9e) suggesting the presence of a carbonate carrier in the fluid, e.g. HCO_3^{-} and/or CO_3^{2-}. A high activity CO_2 fluid can decompose Ca-bearing phases,

such as epidote, titanite and actinolite and forming carbonates while mobilizing the REEs, though titanite is only stable if the fraction of CO_2 in the fluid is very low (Henderson, 1984, Miyashiro, 1994). The presence of CO_2 in the fluid would have promoted the formation of a bastnäsite-synchysite phase at the expense of allanite, but as it is not observed suggesting that the fluid phase was low in CO_2 (Budzyń et al., 2010). Summarized, the fluids that flowed through the phyllonites at a fluid-rock ratio appeared to be rich in alkaline elements, but low in REE and important REE-carrying ligands even though the REEs were completely mobilized.

Implications of element mobility

Fluid-rock interaction in the granodiorite at Gråkallen has shown that a number of trace elements have been mobilized; consequently with the possibility of disturbance and complete resetting of the isotopic records of the rocks, e.g. Rb-Sr and Nd-Sm isotopic systems. In the epidote-rich shear zone, there is an enrichment of Sr, Rb, Nd and Sm (Figure 16), with Sr, Nd and Sm most likely hosted by epidote, while Rb has been added to the muscovite. LA-ICP-MS of the epidote in the shear zone show Sr content ranging between 800 to 2000 ppm, with the higher content situated within the euhedral and transparent epidote. Nd and Sm have been mobilized to different extents, where more Sm has been added in comparison to Nd (Figure 33c). The extent of mobility varies within the phyllonites, as Nd and Sm have been equally lost while other samples show a small fractionation between Nd and Sm (Figure 16 and Figure 33a-b). Rb and Sr show complete opposite behaviour with the gain of Rb and loss of Sr, which can be linked to the introduction of muscovite and the disappearance of plagioclase and epidote, respectively (Figure 16 and Figure 33a-b). This shows that in order to correctly use isotopic systems on metasomatic rocks it is crucial to know the full history, so you know how to interpret your results e.g. distinguishing whether you are dating the crystallization or the fluid-interaction event of your rocks.

Conclusion

This study concludes that parts of the Fagervika granitoid have undergone mineralogical changes on the microscopic scale, which locally developed into phyllonitic shear zones. The alteration of the granodiorite distal to the phyllonitic shear zones is indicative of pervasive fluid-flow, but at a low fluid/rock ratio.

Elements in the granodiorite show variable degrees of mobilization. The major phases plagioclase and alkali feldspar have been altered and subsequently Na and K have been mobilized related to the formation and decomposition of feldspar minerals. The variable distribution of epidote suggests mobilization of Ca on thin section scale, while the occurrence of secondary titanite suggest that the source material of titanite must have originated close by due to Ti immobility. The *in situ* replacement of monazite by the apatite-allanite-epidote-titanite-Th-mineral assemblage indicates that mobilization of REE occurs only at grain scale.

The REEs have been redistributed on a small scale between different mineral phases during alteration in the granodiorite. The secondary Ca-bearing minerals, epidote, allanite and titanite are the main REE-bearing minerals, and these minerals are important in order to maintain the trace element budget in the granodiorite, as the integrity of the whole-rock REE pattern has been conserved during metasomatism.

The development of the phyllonites was most likely initiated by mineralogical changes due to deformation, high fluid/rock ratio and fluid composition. Metasomatic alteration weakened the rock by forming new, smaller grains of neocrystallized albite, which formed at the expense of the alkali feldspar. Subsequent destabilization of the neocrystallized albite and formation of muscovite allowed for deformation to be localized in the shear zones and the shear zones acted as a fluid pathway. The chemical and mineralogical changes accompanying the phyllonitization resulted in overall trace element depletion in the phyllonites, as most of the Ca- and REE-bearing phases, allanite, titanite and epidote, were destabilized. Trace element geochemistry suggests that Zr, Ti, Hf, Nb and Ta appear to have been immobile during alteration and deformation, as titanite and zircon occur in all lithologies.

Further work

- Further work should be done on investigating where the mobilized REE has possibly been deposited, as they have not precipitated within the phyllonites. This could be interesting in terms of mineral resources.
- The growth of garnet and muscovite can be utilized in a garnet-phengite thermometer, and thus yield a P-T-estimations for the rocks (Wu and Zhao, 2006).
- LA-ICP-MS on the zircons for dating and trace element distribution as they have the ability to hold REE, especially HREE. LA-ICP-MS and further geochemical analyses concentrating on the epidote resulted from the plagioclase alteration could reveal the relationship it has with the REE-holding epidote occurring along with titanite and allanite, and perhaps it can be separated into different groups/event.
- Fluid inclusion studies focussing on the alteration would put some constraints on the fluid composition and conditions during metasomatism and phyllonitization.
- Continued mapping of the Fagervika granitoid with focus on the structural features of the rocks, along with argon dating of the muscovite will yield the age of the deformation as the muscovite grew during the phyllonitization of the granodiorite. This age can put constraints on the timing of the regional deformation in the area, revealing if it occurred during the obduction of the thrust stacks or during the extensional collapse of Caledonides.

References

ALDERTON, D. H. M., PEARCE, J. A. & POTTS, P. J. 1980. Rare earth element mobility during granite alteration: Evidence from southwest England. *Earth and Planetary Science Letters,* 49**,** 149-165.

ARMBRUSTER, T., BONAZZI, P., AKASAKA, M., BERMANEC, V., CHOPIN, C., GIERÉ, R., HEUSS-ASSBICHLER, S., LIEBSCHER, A., MENCHETTI, S., PAN, Y. & PASERO, M. 2006. Recommended nomenclature of epidote-group minerals. *European Journal of Mineralogy,* 18**,** 551-567.

AUSTRHEIM, H. & GRIFFIN, W. L. 1985. Shear deformation and eclogite formation within granulite-facies anorthosites of the Bergen Arcs, western Norway. *Chemical Geology,* 50**,** 267-281.

BACH, W., JÖNS, N. & KLEIN, F. 2013. Metasomatism Within the Ocean Crust. *Metasomatism and the Chemical Transformation of Rock.* Springer Berlin Heidelberg.

BANKS, D. 1992. Vurdering av mulighetene for grunnvannsforsyning til Forsvarets leir på Lille Gråkallen, Trondheim. Trondheim: Norges Geologiske Undersøkelse (NGU).

BARTON, M. D., ILCHIK, R. P. & MARIKOS, M. A. 1991. Metasomatism. *Reviews in Mineralogy and Geochemistry,* 26**,** 321-349.

BAU, M. 1991. Rare-earth element mobility during hydrothermal and metamorphic fluid-rock interaction and the significance of the oxidation state of europium. *Chemical Geology,* 93**,** 219-230.

BAUMGARTNER, L. P. & OLSEN, S. N. 1995. A least-squares approach to mass transport calculations using the isocon method. *Economic Geology,* 90**,** 1261-1270.

BEA, F. 1996. Residence of REE, Y, Th and U in granites and crustal protoliths; implications for the chemistry of crustal melts. *Journal of Petrology,* 37**,** 521-552.

BEST, M. G. 2009. *Igneous and metamorphic petrology*, John Wiley & Sons.

BUCHER, K. & GRAPES, R. 2011. *Petrogenesis of Metamorphic Rocks,* Berlin, Heidelberg, Springer Berlin Heidelberg.

BUDZYŃ, B., HARLOV, D. E., WILLIAMS, M. L. & JERCINOVIC, M. J. 2011. Experimental determination of stability relations between monazite, fluorapatite, allanite, and REE-epidote as a function of pressure, temperature, and fluid composition. *American Mineralogist,* 96**,** 1547-1567.

BUDZYŃ, B., HETHERINGTON, C., WILLIAMS, M., JERCINOVIC, M. & MICHALIK, M. 2010. Fluid–mineral interactions and constraints on monazite alteration during metamorphism. *Mineralogical Magazine,* 74**,** 659-681.

CEPURITIS, R., GARBOCZI, E. J., FERRARIS, C. F., JACOBSEN, S. & SØRENSEN, B. E. In review. Particle size distribution and specific surface determination of crushed concrete aggregate fines. Submitted to CCC (Cement and Concrete Composites).

CLARKE, D. 1981. The mineralogy of peraluminous granites: a review. *Canadian Mineralogist,* 19**,** 1-17.

CORFU, F., ANDERSEN, T. B. & GASSER, D. 2014. The Scandinavian Caledonides: main features, conceptual advances and critical questions. *Geological Society, London, Special Publications,* 390**,** 9-43.

DEER, W. A., HOWIE, R. A. & ZUSSMAN, J. 1992. *An introduction to the rock-forming minerals*, Longman Scientific & Technical Hong Kong.

DIXON, J. & WILLIAMS, G. 1983. Reaction softening in mylonites from the Arnaboll thrust, Sutherland. *Scottish Journal of Geology,* 19**,** 157-168.

DOSTAL, J., STRONG, D. F. & JAMIESON, R. A. 1980. Trace element mobility in the mylonite zone within the ophiolite aureole, St. Anthony Complex, Newfoundland. *Earth and Planetary Science Letters,* 49**,** 188-192.

DROOP, G. 1987. A general equation for estimating Fe3+ concentrations in ferromagnesian silicates and oxides from microprobe analyses, using stoichiometric criteria. *Mineralogical magazine,* 51**,** 431-435.

EIDE, E. A. & LARDEAUX, J. M. 2002. A relict blueschist in meta-ophiolite from the central Norwegian Caledonides—discovery and consequences. *Lithos,* 60**,** 1-19.

ENGVIK, A. K., PUTNIS, A., GERALD, J. D. F. & AUSTRHEIM, H. 2008. Albitization of granitic rocks: the mechanism of replacement of oligoclase by albite. *The Canadian Mineralogist,* 46**,** 1401-1415.

ETHERIDGE, M. & COOPER, J. 1981. Rb/Sr isotopic and geochemical evolution of a recrystallized shear (mylonite) zone at Broken Hill. *Contributions to Mineralogy and Petrology,* 78**,** 74-84.

FETTES, D., DESMONS, J. & ÁRKAI, P. 2007. *Metamorphic rocks: a classification and glossary of terms : recommendations of the International Union of Geological Sciences Subcommission on the Systematics of Metamorphic Rocks,* Cambridge, Cambridge University Press.

FINGER, F., BROSKA, I., ROBERTS, M. P. & SCHERMAIER, A. 1998. Replacement of primary monazite by apatite-allanite-epidote coronas in an amphibolite facies granite gneiss from the eastern Alps. *American Mineralogist,* 83**,** 248-258.

FITZ GERALD, J. D. & STÜNITZ, H. 1993. Deformation of granitoids at low metamorphic grade. I: Reactions and grain size reduction. *Tectonophysics,* 221**,** 269-297.

FOSSEN, H. 2010. *Structural geology*, Cambridge University Press.

FRANZ, G. & LIEBSCHER, A. 2004. Physical and Chemical Properties of the Epidote Minerals–An Introduction–. *Reviews in mineralogy and geochemistry,* 56**,** 1-81.

GALE, G. H. & ROBERTS, D. 1974. Trace element geochemistry of Norwegian Lower Palaeozoic basic volcanics and its tectonic implications. *Earth and Planetary Science Letters,* 22**,** 380-390.

GEE, D. 1975. A tectonic model for the central part of the Scandinavian Caledonides. *American Journal of Science,* 275**,** 468-515.

GEE, D. & ROBERTS, D. 1983. Timing of deformation in the Scandinavian Caledonides. *Regional trends in the geology of the Appalachian-Caledonian-Hercynian-Mauritanide Orogen.* Springer.

GIERÉ, R. & SORENSEN, S. S. 2004. Allanite and other REE-rich epidote-group minerals. *Reviews in Mineralogy and Geochemistry,* 56**,** 431-493.

GOLDSCHMIDT, V. M. 1937. The principles of distribution of chemical elements in minerals and rocks. The seventh Hugo Müller Lecture, delivered before the Chemical Society on March 17th, 1937. *Journal of the Chemical Society (Resumed)***,** 655-673.

GOLDSTEIN, J., NEWBURY, D. E., JOY, D., LYMAN, C., ECHLIN, P., LIFSHIN, E., SAWYER, L. & MICHAEL, J. 2003. Scanning electron microscopy and x-ray microanalysis. *ISBN,* 306472929**,** 9780306472923.

GRANT, J. A. 1986. The isocon diagram; a simple solution to Gresens' equation for metasomatic alteration. *Economic Geology,* 81**,** 1976-1982.

GRANT, J. A. 2005. Isocon analysis: a brief review of the method and applications. *Physics and Chemistry of the Earth, Parts A/B/C,* 30**,** 997-1004.

GRENNE, T. 1989. Magmatic evolution of the Løkken SSZ Ophiolite, Norwegian Caledonides: Relationships between anomalous lavas and high‐level intrusions. *Geological Journal,* 24**,** 251-274.

GRENNE, T., GRAMMELTVEDT, G. & VOKES, F. Cyprus-type sulphide deposits in the western Trondheim district, central Norwegian Caledonides. Ophiolites. Proceedings of the International Ophiolite Symposium, Cyprus, 1980. 727-743.

GRENNE, T., IHLEN, P. & VOKES, F. 1999. Scandinavian Caledonide metallogeny in a plate tectonic perspective. *Mineralium Deposita,* 34**,** 422-471.
GRESENS, R. L. 1967. Composition-volume relationships of metasomatism. *Chemical geology,* 2**,** 47-65.
GROMET, P. L. & SILVER, L. T. 1983. Rare earth element distributions among minerals in a granodiorite and their petrogenetic implications. *Geochimica et Cosmochimica Acta,* 47**,** 925-939.
HACKER, B. R., ANDERSEN, T. B., JOHNSTON, S., KYLANDER-CLARK, A. R., PETERMAN, E. M., WALSH, E. O. & YOUNG, D. 2010. High-temperature deformation during continental-margin subduction & exhumation: The ultrahigh-pressure Western Gneiss Region of Norway. *Tectonophysics,* 480**,** 149-171.
HARLOV, D. E. & AUSTRHEIM, H. 2013. *Metasomatism and the Chemical Transformation of Rock: Rock-Mineral-Fluid Interaction in Terrestrial and Extraterrestrial Environments*, Springer Berlin Heidelberg.
HARRINGTON, B., GOULD, T. & HURST, N. 2003. Inkscape. 0.48.5 ed.
HEMLEY, J. J. & JONES, W. 1964. Chemical aspects of hydrothermal alteration with emphasis on hydrogen metasomatism. *Economic Geology,* 59**,** 538-569.
HENDERSON, P. 1984. *Rare earth element geochemistry*, Elsevier.
HOLLAND, H. D. 1972. Granites, solutions, and base metal deposits. *Economic Geology,* 67**,** 281-301.
HOLLOCHER, K., ROBINSON, P., KENNEDY, C. & WALSH, E. 2014. Metamorphosed cumulate gabbros from the Støren Group of the Upper Allochthon, northern Western Gneiss Region, Norway: petrology and metamorphic record. *Norwegian Journal of Geology,* 94**,** 21.
HOLLOCHER, K., ROBINSON, P., WALSH, E. & ROBERTS, D. 2012. Geochemistry of amphibolite-facies volcanics and gabbros of the Støren Nappe in extensions west and southwest of Trondheim, Western Gneiss Region, Norway: a key to correlations and paleotectonic settings. *American Journal of Science,* 312**,** 357-416.
HUMPHRIS, S. E. 1984. The mobility of the rare earth elements in the crust. *In:* HENDERSON, P. (ed.) *Rare earth element geochemistry.* Elsevier Amsterdam.
HØYEN, A. B. In Prep. *Umbukta Gabbro.* Master Thesis, Norwegian University of Science and Technology.
JAMTVEIT, B., BUCHER-NURMINEN, K. & AUSTRHEIM, H. 1990. Fluid controlled eclogitization of granulites in deep crustal shear zones, Bergen arcs, Western Norway. *Contributions to Mineralogy and Petrology,* 104**,** 184-193.
JENSEN, B. B. 1973. Patterns of trace element partitioning. *Geochimica et Cosmochimica Acta,* 37**,** 2227-2242.
KORZHINSKII, D. 1959. Physicochemical basis of the analysis of the paragenesis of minerals= Fiziko-khimicheskie osnovy analiza paragenezisov mineralov.
LE MAITRE, R. W., BATEMAN, P., DUDEK, A., KELLER, J., LAMEYRE, J., LE BAS, M., SABINE, P., SCHMID, R., SORENSEN, H. & STRECKEISEN, A. 2002. *A classification of igneous rocks and glossary of terms: Recommendations of the International Union of Geological Sciences Subcommission on the Systematics of Igneous Rocks*, Blackwell Oxford.
LÓPEZ-MORO, F. J. 2012. EASYGRESGRANT—A Microsoft Excel spreadsheet to quantify volume changes and to perform mass-balance modeling in metasomatic systems. *Computers & Geosciences,* 39**,** 191-196.
MIYASHIRO, A. 1994. *Metamorphic petrology*, CRC Press.

MUKHERJEE, P. & GUPTA, P. 2008. Arbitrary scaling in ISOCON method of geochemical mass balance: An evaluation of the graphical approach. *Geochemical Journal,* 42**,** 247-253.

O'HARA, K. 1988. Fluid flow and volume loss during mylonitization: an origin for phyllonite in an overthrust setting, North Carolina USA. *Tectonophysics,* 156**,** 21-36.

ONUMA, N., HIGUCHI, H., WAKITA, H. & NAGASAWA, H. 1968. Trace element partition between two pyroxenes and the host lava. *Earth and Planetary Science Letters,* 5**,** 47-51.

ORVILLE, P. M. 1962. Alkali metasomatism and feldspars. *Norsk Geologisk Tidsskrift,* 42**,** e316.

PAN, Y. & FLEET, M. E. 1996. Intrinsic and external controls on the incorporation of rare-earth elements in calc-silicate minerals. *The Canadian Mineralogist,* 34**,** 147-159.

PASSCHIER, C. W. & TROUW, R. A. 1996. *Microtectonics*, Springer.

PEARCE, J. A. 1983. Role of the subcontinental lithosphere in magma genesis at active continental margins.

PEARCE, J. A. & CANN, J. 1973. Tectonic setting of basic volcanic rocks determined using trace element analyses. *Earth and planetary science letters,* 19**,** 290-300.

PETRÍK, I., BROSKA, I., LIPKA, J. & SIMAN, P. 1995. Granitoid allanite-(Ce): substitution relations, redox conditions and REE distributions (on an example of I-type granitoids, Western Carpathians, Slovakia). *Geologica Carpathica,* 46**,** 79-94.

PIRAJNO, F. 2009. *Hydrothermal Processes and Mineral Systems,* Dordrecht, Springer Science + Business Media B.V.

PIRAJNO, F. 2013. Effects of metasomatism on mineral systems and their host rocks: alkali metasomatism, skarns, greisens, tourmalinites, rodingites, black-wall alteration and listvenites. *Metasomatism and the Chemical Transformation of Rock.* Springer.

POLI, S. & SCHMIDT, M. W. 2004. Experimental subsolidus studies on epidote minerals. *Reviews in mineralogy and geochemistry,* 56**,** 171-195.

PUTNIS, A. 2002. Mineral replacement reactions: from macroscopic observations to microscopic mechanisms. *Mineralogical Magazine,* 66**,** 689-708.

PUTNIS, A. & AUSTRHEIM, H. 2010. Fluid-induced processes: metasomatism and metamorphism. *Geofluids,* 10**,** 254-269.

PUTNIS, A. & AUSTRHEIM, H. 2013. Mechanisms of Metasomatism and Metamorphism on the Local Mineral Scale: The Role of Dissolution-Reprecipitation During Mineral Re-equilibration. *Metasomatism and the Chemical Transformation of Rock.* Springer Berlin Heidelberg.

REED, M. H. 1997. Hydrothermal alteration and its relationship to ore fluid composition. *Geochemistry of hydrothermal ore deposits,* 3**,** 303-365.

REED, S. J. B. 2005. *Electron microprobe analysis and scanning electron microscopy in geology,* Cambridge, Cambridge University Press.

ROBB, L. 2005. *Introduction to ore-forming processes*, John Wiley & Sons.

ROBERTS, D. & GEE, D. 1985. An introduction to the structure of the Scandinavian Caledonides. *The Caledonide orogen–Scandinavia and related areas,* 1**,** 55-68.

ROBERTS, D., MELEZHIK, V. & HELDAL, T. 2002a. Carbonate formations and early NW-directed thrusting in the highest allochthons of the Norwegian Caledonides: evidence of a Laurentian ancestry. *Journal of the Geological Society,* 159**,** 117-120.

ROBERTS, D. & STURT, B. 1980. Caledonian deformation in Norway. *Journal of the Geological Society,* 137**,** 241-250.

ROBERTS, D., WALKER, N., SLAGSTAD, T., SOLLI, A. & KRILL, A. 2002b. U-Pb zircon ages from the Bymarka ophiolite, near Trondheim, central Norwegian Caledonides, and regional implications. *Norsk Geologisk Tidsskrift,* 82**,** 19-30.

ROBINSON, P., ROBERTS, D., GEE, D. G. & SOLLI, A. 2014. A major synmetamorphic Early Devonian thrust and extensional fault system in the Mid Norway Caledonides: relevance to exhumation of HP and UHP rocks. *Geological Society, London, Special Publications,* 390**,** 241-270.

ROLLINSON, H. R. 1993. *Using geochemical data: evaluation, presentation, interpretation*, Routledge.

RUBENACH, M. 2013. Structural Controls of Metasomatism on a Regional Scale. *Metasomatism and the Chemical Transformation of Rock.* Springer.

RUBIN, J. N., HENRY, C. D. & PRICE, J. G. 1993. The mobility of zirconium and other "immobile" elements during hydrothermal alteration. *Chemical Geology,* 110**,** 29-47.

RØ, G. & MIDTSIAN, A. 1995. *Bymarka: geologi og gruvedrift i byens utmark,* Trondheim, Trondheim Amatørgeologiske Forening.

SANDER, B. 1911. X. Über Zusammenhänge zwischen Teilbewegung und Gefüge in Gesteinen. *Zeitschrift für Kristallographie, Mineralogie und Petrographie,* 30**,** 281-314.

SHELLEY, D. 1993. *Igneous and metamorphic rocks under the microscope: classification, textures, microstructures and mineral preferred-orientations*, Chapman & Hall London.

SLAGSTAD, T. 1998. *High-K2O plagiogranite and greenstones in ophiolitic rocks of Bymarka, Trondheim.* Diploma, Norwegian University of Science and Technology (NTNU).

SLAGSTAD, T. 2003. Geochemistry of trondhjemites and mafic rocks in the Bymarka ophiolite fragment, Trondheim, Norway: Petrogenesis and tectonic implications. *Norwegian Journal of Geology,* 83**,** 167-185.

SLAGSTAD, T., PIN, C., ROBERTS, D., KIRKLAND, C. L., GRENNE, T., DUNNING, G., SAUER, S. & ANDERSEN, T. 2014. Tectonomagmatic evolution of the Early Ordovician suprasubduction-zone ophiolites of the Trondheim Region, Mid-Norwegian Caledonides. *Geological Society, London, Special Publications,* 390**,** 541-561.

STEPHENS, M., GUSTAVSON, M., RAMBERG, I. & ZACHRISSON, E. 1985. The Caledonides of central-north Scandinavia—a tectonostratigraphic overview. *The Caledonide orogen–Scandinavia and related areas***,** 135-162.

STRECKEISEN, A. 1976. To each plutonic rock its proper name. *Earth-Science Reviews,* 12**,** 1-33.

STØRSETH, L. R. pers. comment.

SUN, S.-S. & MCDONOUGH, W. 1989. Chemical and isotopic systematics of oceanic basalts: implications for mantle composition and processes. *Geological Society, London, Special Publications,* 42**,** 313-345.

SØRENSEN, B. E. & GRANSETH, A. U. 2014. Detailed mapping using aerial photos and automatic rendering of outcrops. 31st Nordic Geological Winter Meeting, 8-10 January 2014, Lund University: Svenska Geologiska Foreningen.

TORSVIK, T., SMETHURST, M., MEERT, J. G., VAN DER VOO, R., MCKERROW, W., BRASIER, M., STURT, B. & WALDERHAUG, H. 1996. Continental break-up and collision in the Neoproterozoic and Palaeozoic—a tale of Baltica and Laurentia. *Earth-Science Reviews,* 40**,** 229-258.

TORSVIK, T. H. & COCKS, L. R. M. 2005. Norway in space and time: a centennial cavalcade. *Norwegian Journal of Geology,* 85**,** 73-86.

TULLIS, J. 2002. Deformation of granitic rocks: experimental studies and natural examples. *Reviews in Mineralogy and Geochemistry,* 51**,** 51-95.

TULLOCH, A. J. 1979. Secondary Ca-Al silicates as low-grade alteration products of granitoid biotite. *Contributions to Mineralogy and Petrology,* 69**,** 105-117.

VAN BAALEN, M. R. 1993. Titanium mobility in metamorphic systems: a review. *Chemical Geology,* 110**,** 233-249.

VEDELER, S. 2013. *Structural and Petrological Study of the Klemetsaunet Plagiogranite, Trondheim, Norway.* Master, Norwegian University of Science and Technology (NTNU).

VERNON, R. H. & CLARKE, G. L. 2008. *Principles of metamorphic petrology*, Cambridge University Press.

WATNE, T. A. K. 1991. *Utkast til foreløpig berggrunnsgeologisk kart 1621 IV Trondheim, M 1:50 000 med bekrivelse.* Hovedoppgave, Universitetet i Trondheim, Norges Tekniske Høgskole.

WHITE, S. & KNIPE, R. 1978. Transformation-and reaction-enhanced ductility in rocks. *Journal of the Geological Society,* 135**,** 513-516.

WIBBERLEY, C. 1999. Are feldspar-to-mica reactions necessarily reaction-softening processes in fault zones? *Journal of Structural Geology,* 21**,** 1219-1227.

WILL, G. 2006. *Powder Diffraction: The Rietveld Method and the Two Stage Method to Determine and Refine Crystal Structures from Powder Diffraction Data,* Berlin, Heidelberg, Springer-Verlag Berlin Heidelberg.

WINCHESTER, J. & FLOYD, P. 1976. Geochemical magma type discrimination: application to altered and metamorphosed basic igneous rocks. *Earth and Planetary Science Letters,* 28**,** 459-469.

WINTER, J. D. 2010. *Principles of igneous and metamorphic petrology*, Prentice Hall New York.

WOOD, S. & SAMSON, I. 1998. Solubility of ore minerals and complexation of ore metals in hydrothermal solutions. *Rev. Econ. Geol,* 10**,** 33-80.

WU, C.-M. & ZHAO, G. 2006. Recalibration of the garnet–muscovite (GM) geothermometer and the garnet–muscovite–plagioclase–quartz (GMPQ) geobarometer for metapelitic assemblages. *Journal of Petrology,* 47**,** 2357-2368.

YARDLEY, B. W. 1989. *An introduction to metamorphic petrology*, Longman Scientific & Technical "[u.a.]".

YARDLEY, B. W. 2005. 100th Anniversary Special Paper: metal concentrations in crustal fluids and their relationship to ore formation. *Economic Geology,* 100**,** 613-632.

YARDLEY, B. W. 2009. The role of water in the evolution of the continental crust. *Journal of the Geological Society,* 166**,** 585-600.

YARDLEY, B. W. 2013. The chemical composition of metasomatic fluids in the crust. *Metasomatism and the Chemical Transformation of Rock.* Springer.

ZHARIKOV, V., PERTSEV, N., RUSINOV, V., CALLEGARI, E. & FETTES, D. 2007. Metasomatism and metasomatic rocks.

Appendix

Appendix A – Sample Coordinates

Appendix B – Detailed Geological Field Maps

Appendix C – Petrography

Appendix D – XRD Spectra

Appendix E – Whole-rock analyses

Appendix F – Isocon

Appendix G – Joint Assembly GAC-MAC Poster

Appendix A – Sample Coordinates

Sample	North	East
P01	7032946.86	562469.47
P02	7032945.99	562465.04
P03	7032945.16	562451.12
P04	7033063.41	562416.75
P05	7032924.83	562858.40
P06	7033563.20	563021.10
P07	7033259.08	563181.28
P08	7033266.81	563177.03
P09	7033851.59	563013.27
P10	7033175.02	562442.09
P11	7033137.15	562374.82
P12	7033140.26	562373.86
P13	7033042.04	562583.15
P14	7032922.33	562855.66
P15	7032920.95	562858.73
P17	7032929.01	562855.72
P18A P18B	7032925.72	562863.68
P19	7032926.05	562863.52
P20	7033044.66	562449.68
P21	7033086.06	562475.18
P22-T	*Tunnel*	*Tunnel*
P23A-T	*Tunnel*	*Tunnel*
P23B-T	*Tunnel*	*Tunnel*
P24-T	*Tunnel*	*Tunnel*
P25A-T	*Tunnel*	*Tunnel*
P25B-T	*Tunnel*	*Tunnel*
P26A	7033240.27	562513.37
P26B	7033240.27	562513.37
P27	7033055.13	562495.36
P28	7033139.88	562480.27
P29	7033180.91	562538.34
P30	7033175.33	562554.78
P31	7032922.71	562858.29
P32	7032939.34	562449.89
AU1	7032240.41	562436.72
AU2	7032239.51	562425.34

Appendix B – Detailed Geological Field Maps

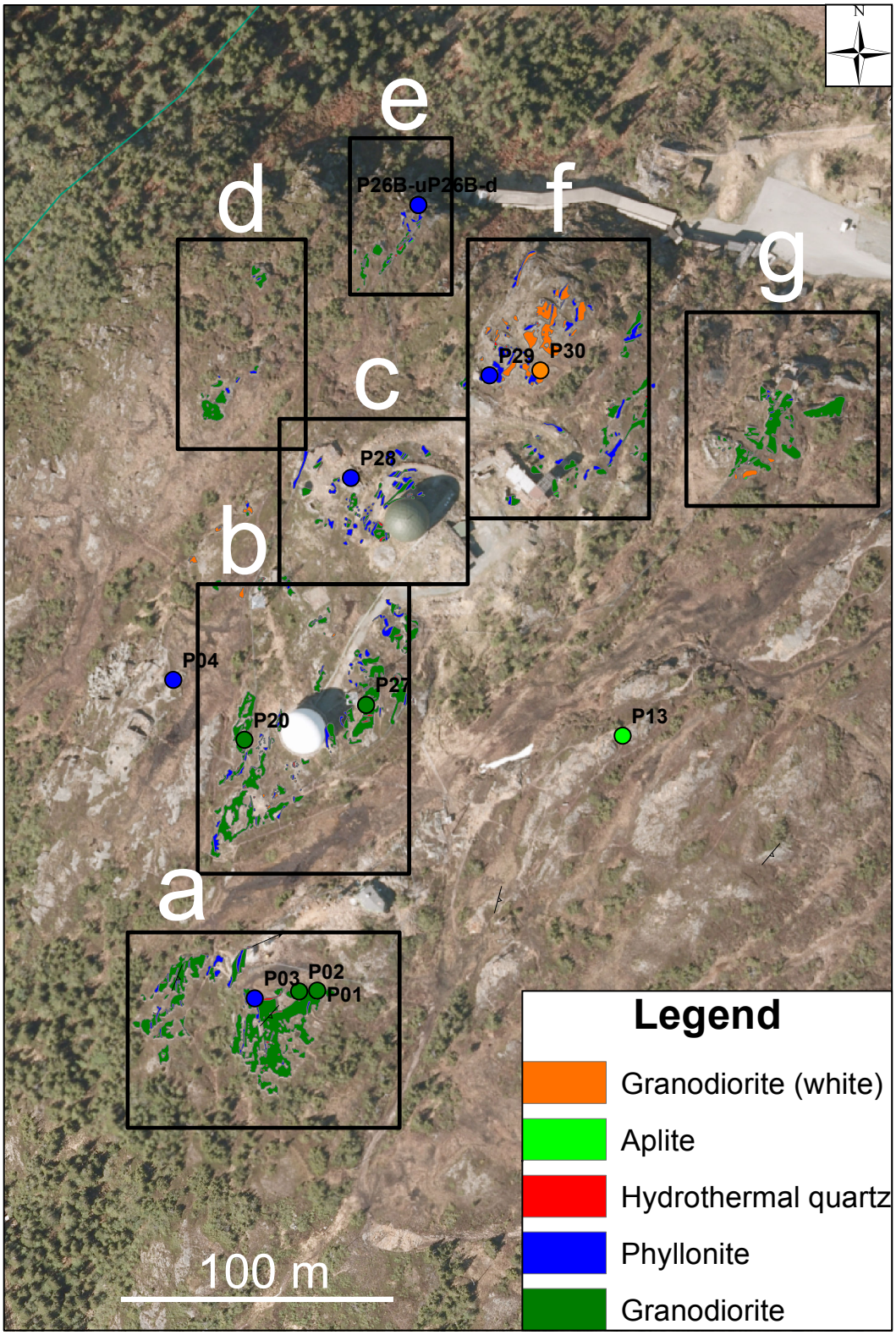

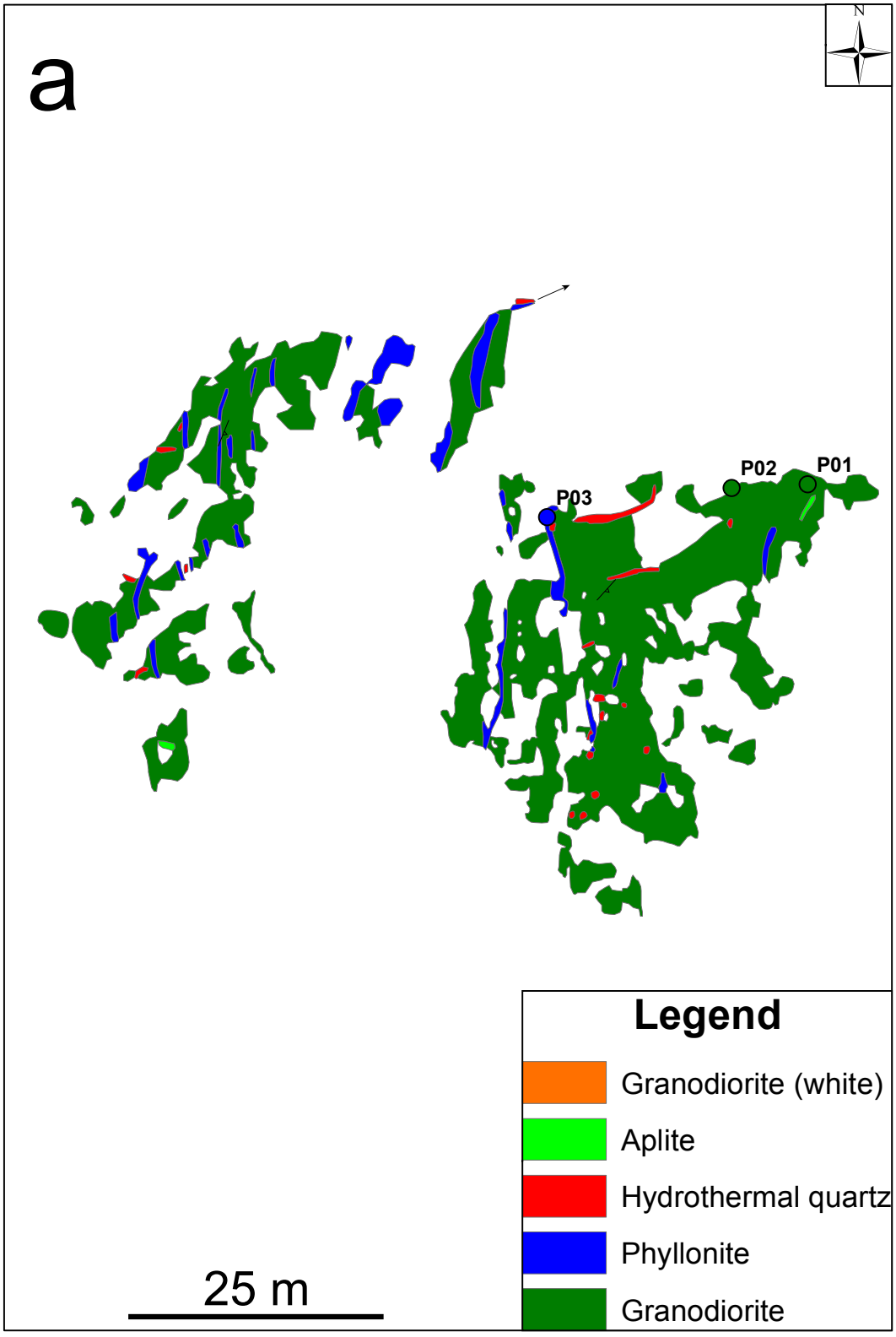
a
N
P03
P02
P01
Legend
Granodiorite (white)
Aplite
Hydrothermal quartz
Phyllonite
Granodiorite
25 m

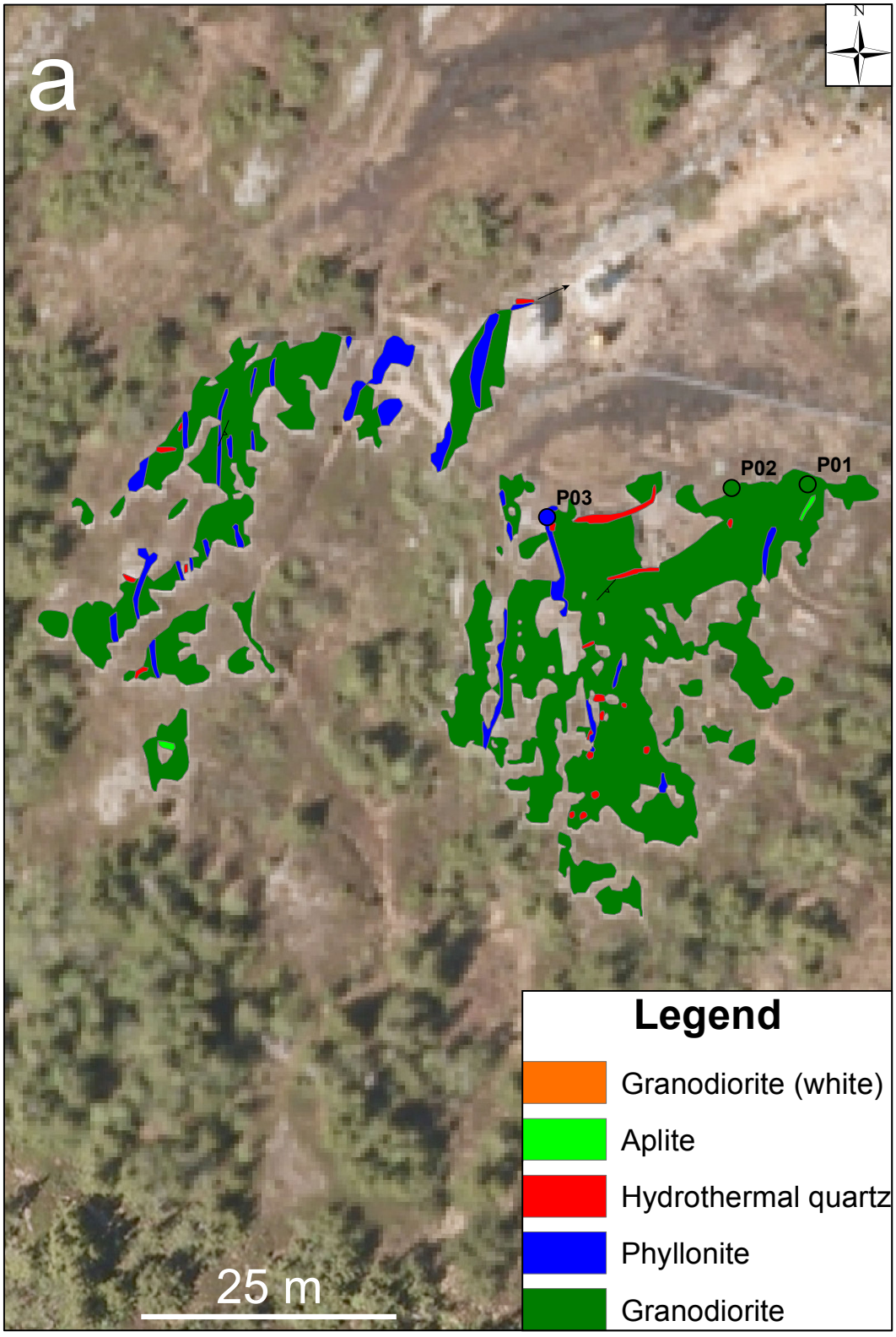
a
N
P03
P02
P01
Legend
Granodiorite (white)
Aplite
Hydrothermal quartz
Phyllonite
Granodiorite
25 m

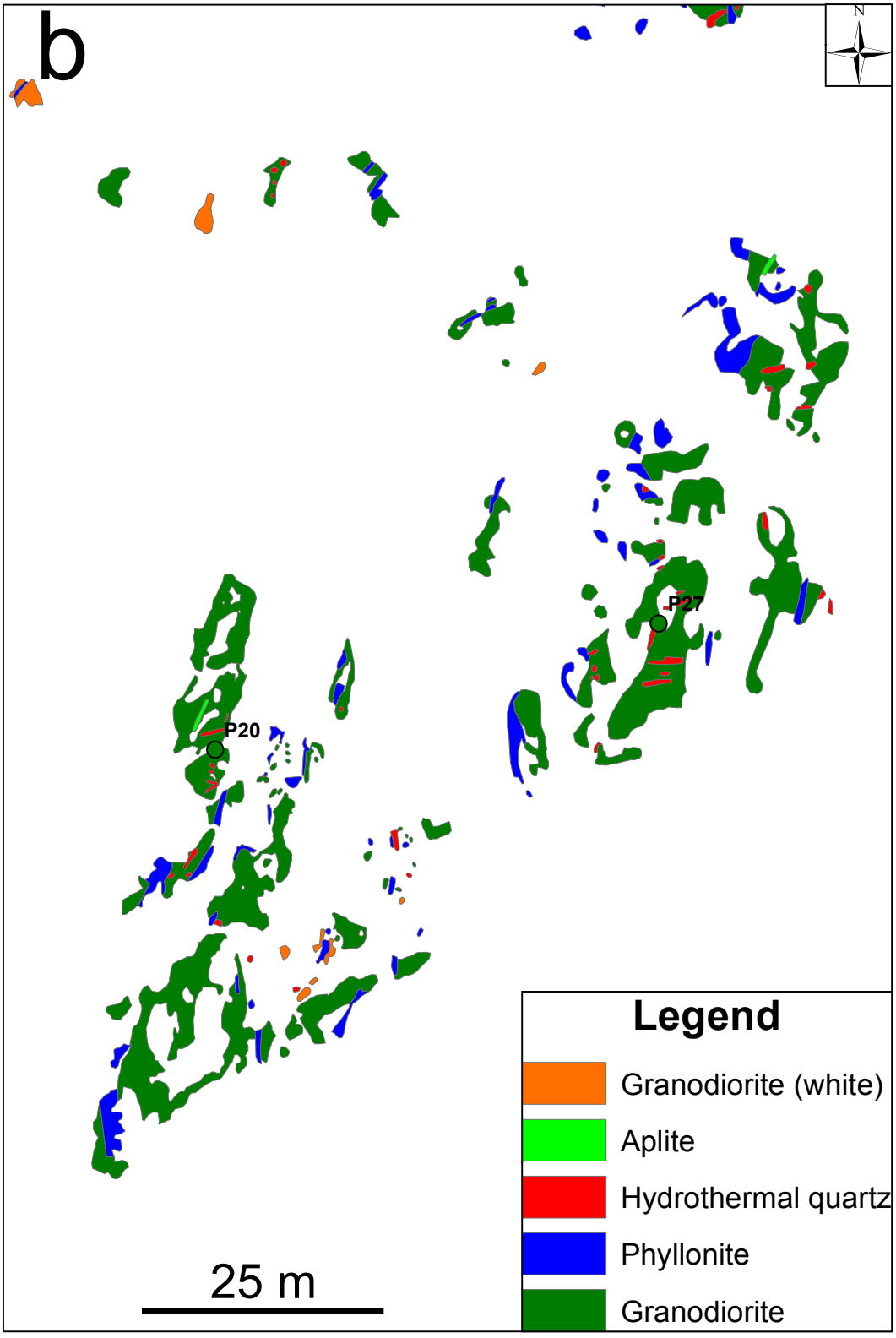
b
N
P27
P20
25 m
Legend
Granodiorite (white)
Aplite
Hydrothermal quartz
Phyllonite
Granodiorite

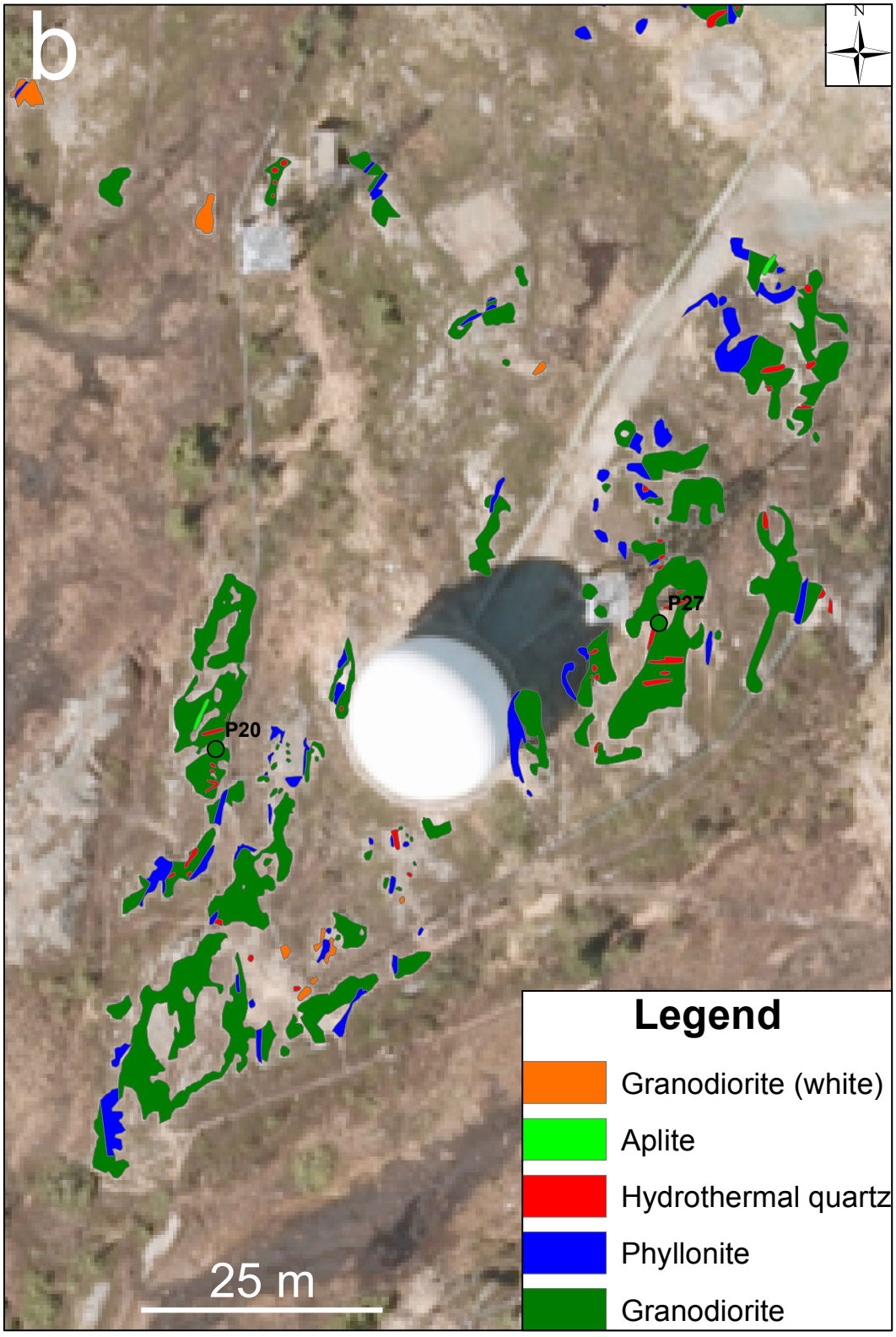
b
N
P27
P20
25 m
Legend
Granodiorite (white)
Aplite
Hydrothermal quartz
Phyllonite
Granodiorite

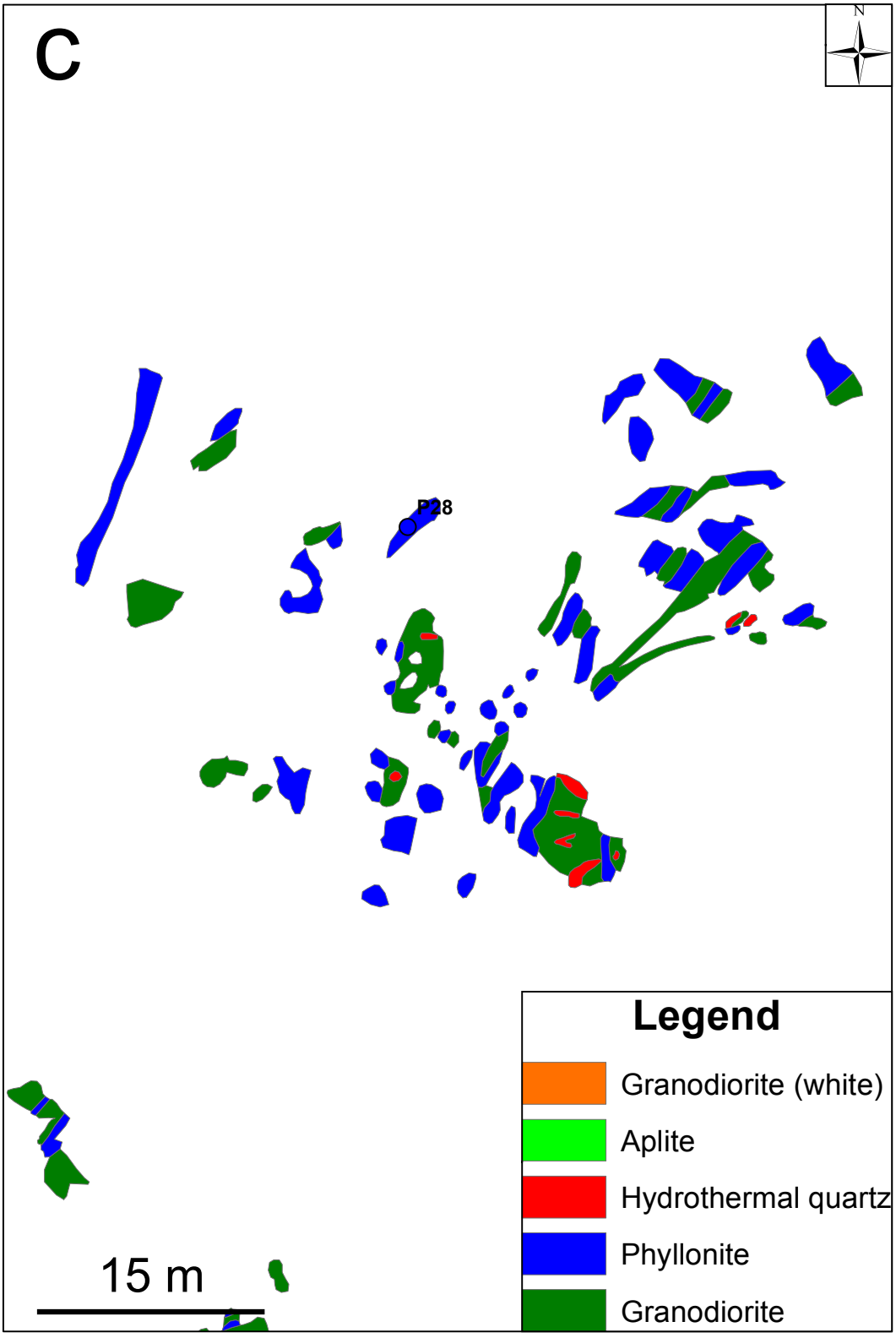
C
N
P28
15 m
Legend
Granodiorite (white)
Aplite
Hydrothermal quartz
Phyllonite
Granodiorite

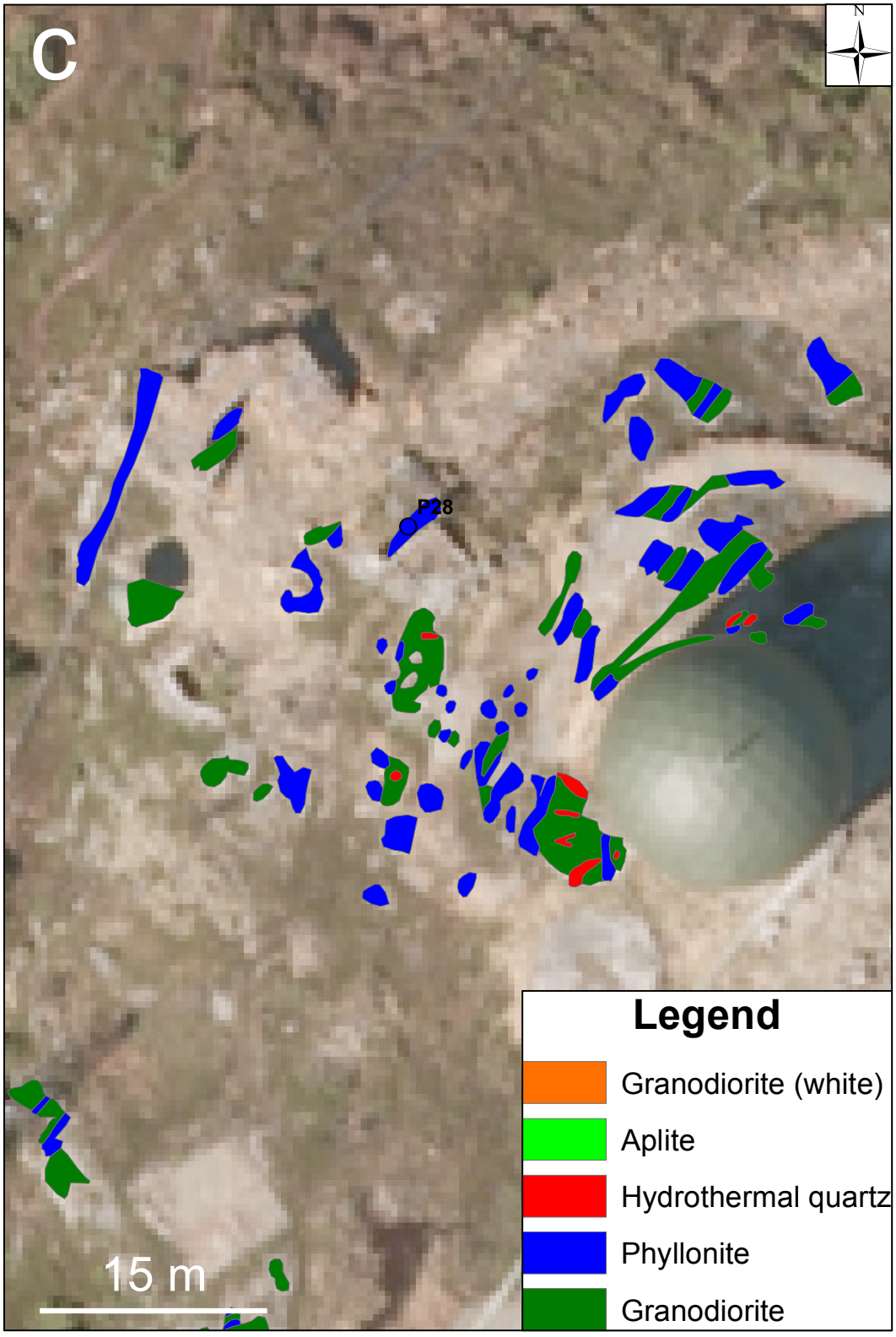
C
N
P28
15 m
Legend
Granodiorite (white)
Aplite
Hydrothermal quartz
Phyllonite
Granodiorite

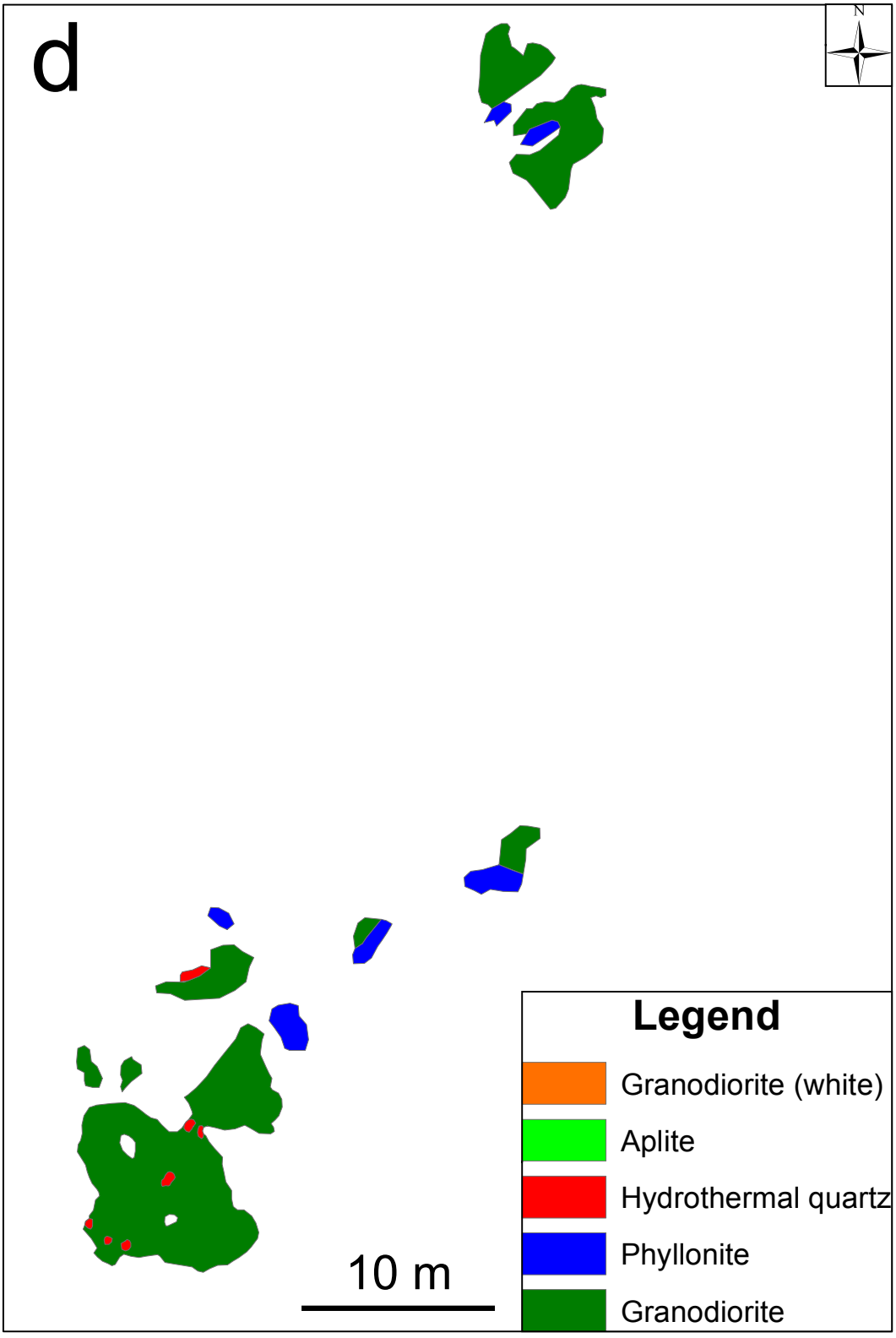
d
N
10 m
Legend
Granodiorite (white)
Aplite
Hydrothermal quartz
Phyllonite
Granodiorite

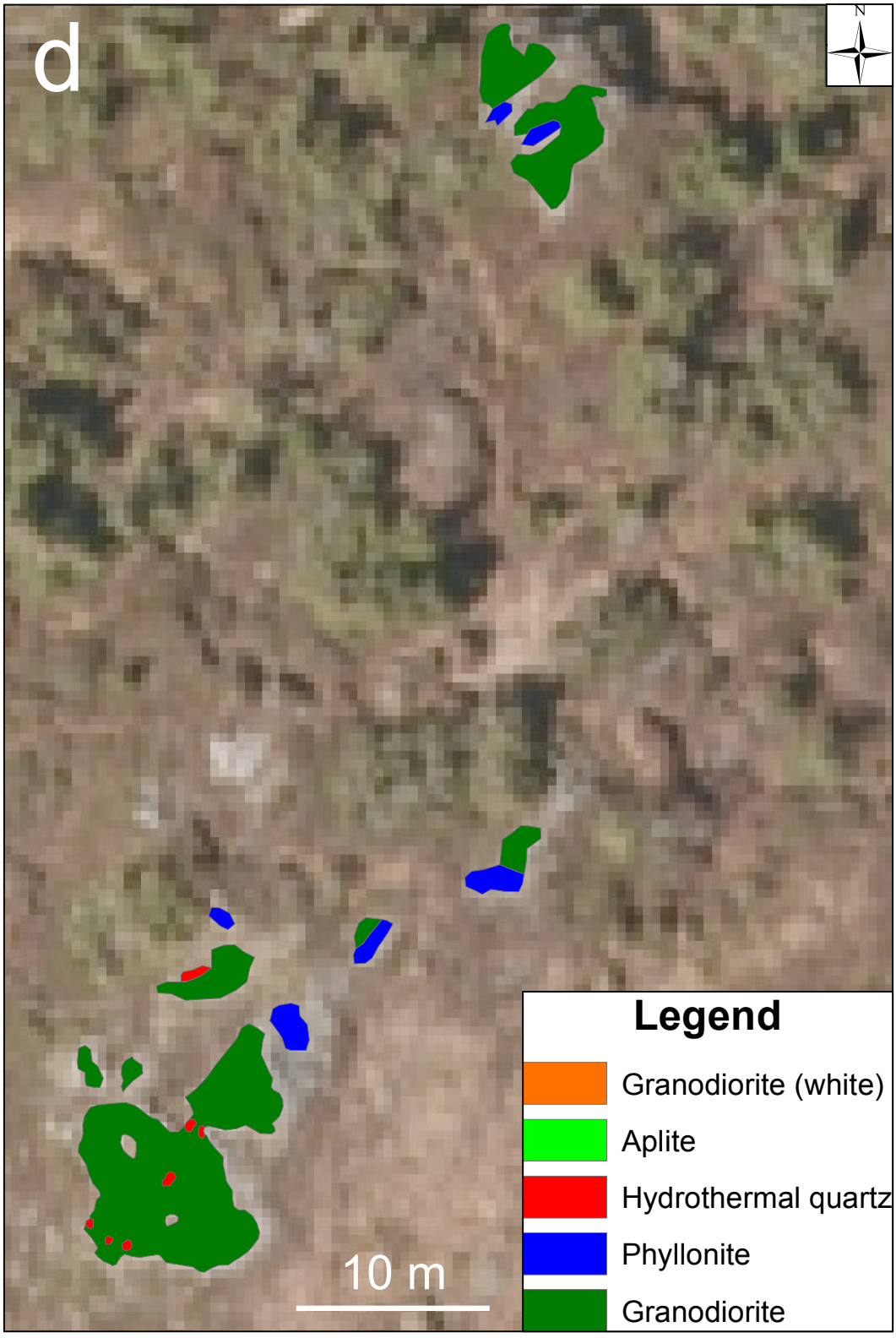
d
N
Legend
Granodiorite (white)
Aplite
Hydrothermal quartz
Phyllonite
Granodiorite
10 m

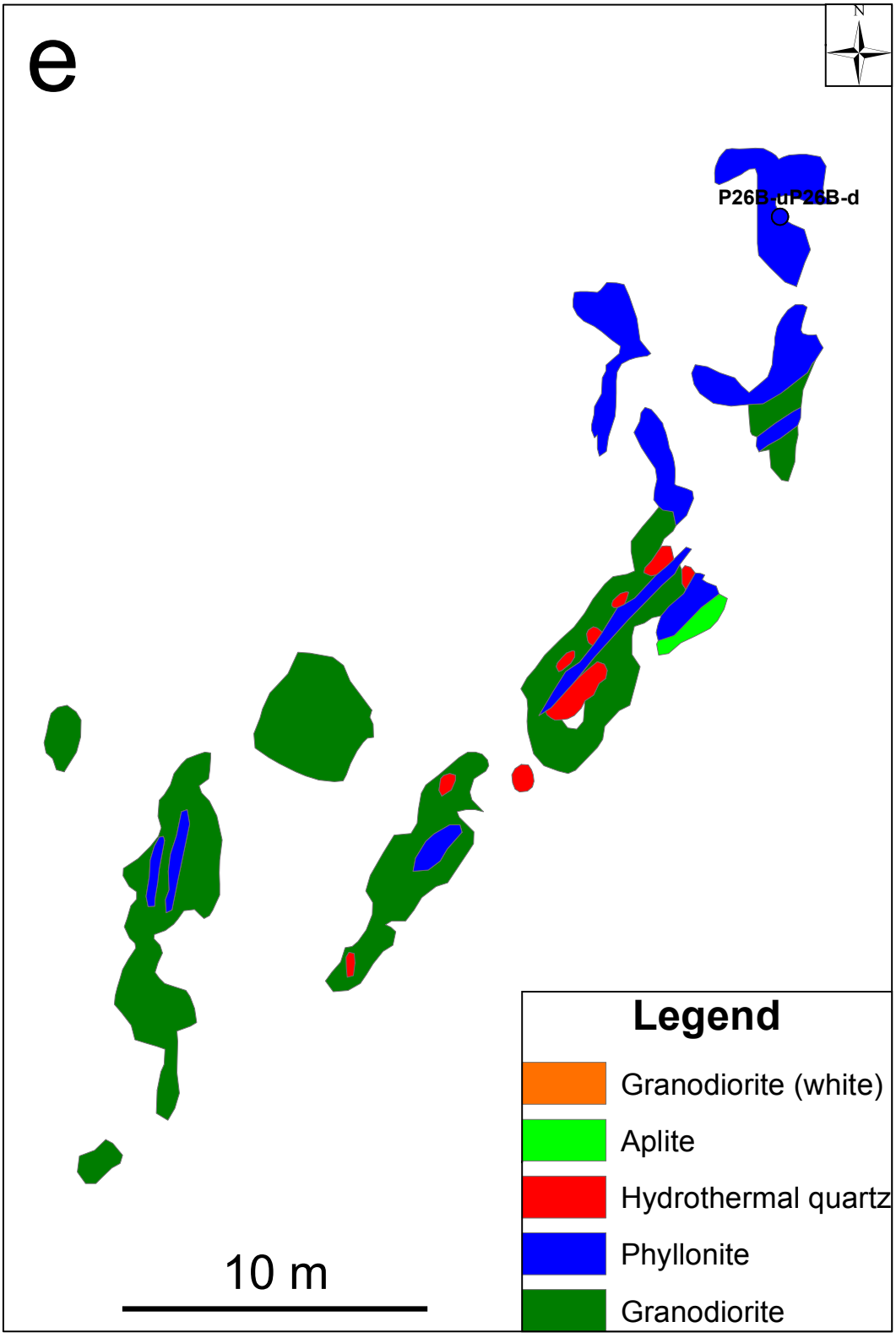
e
N
P26B-uP26B-d
10 m
Legend
Granodiorite (white)
Aplite
Hydrothermal quartz
Phyllonite
Granodiorite

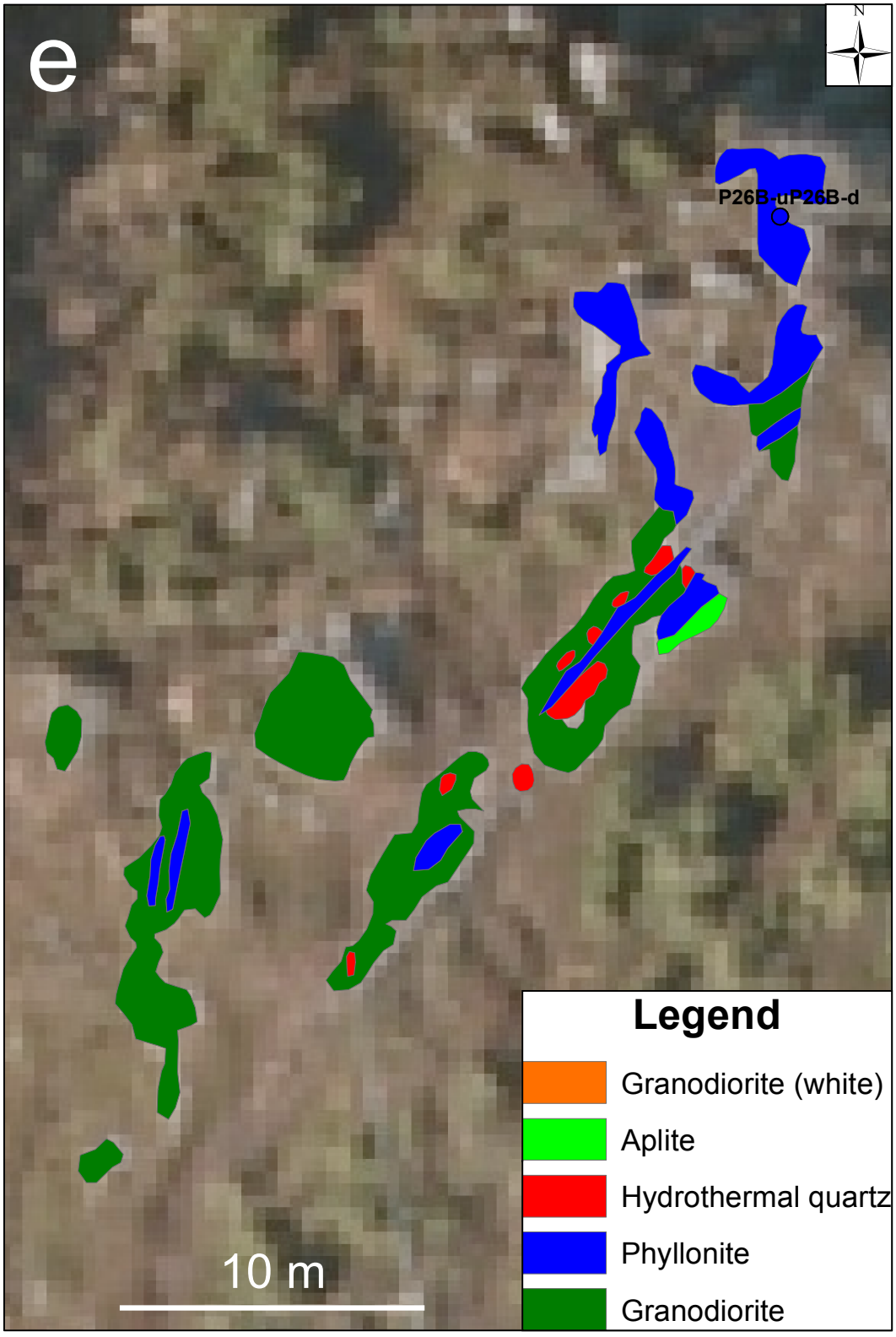
e
N
P26B-uP26B-d
Legend
Granodiorite (white)
Aplite
Hydrothermal quartz
Phyllonite
Granodiorite
10 m

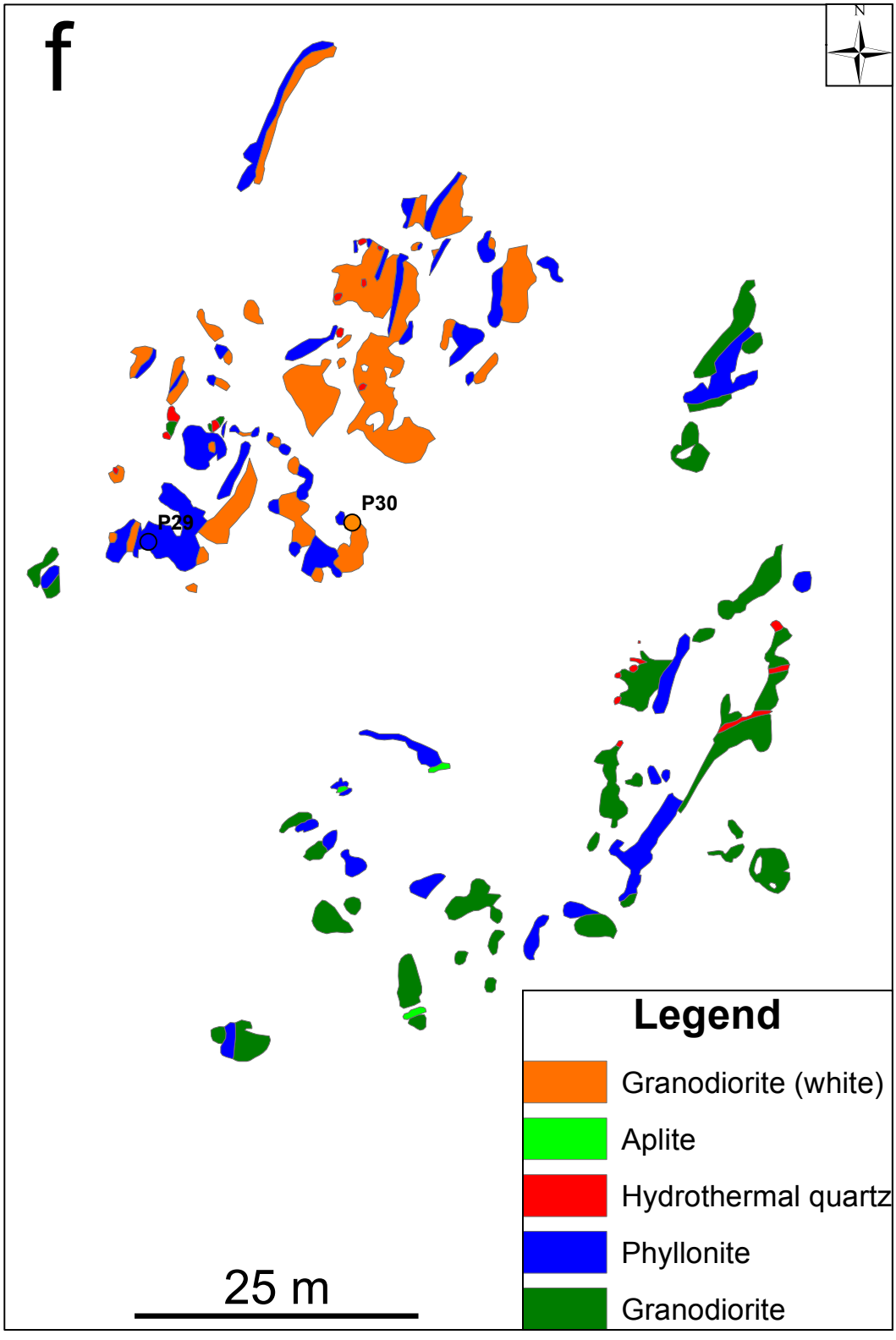
f
N
P29
P30
25 m
Legend
Granodiorite (white)
Aplite
Hydrothermal quartz
Phyllonite
Granodiorite

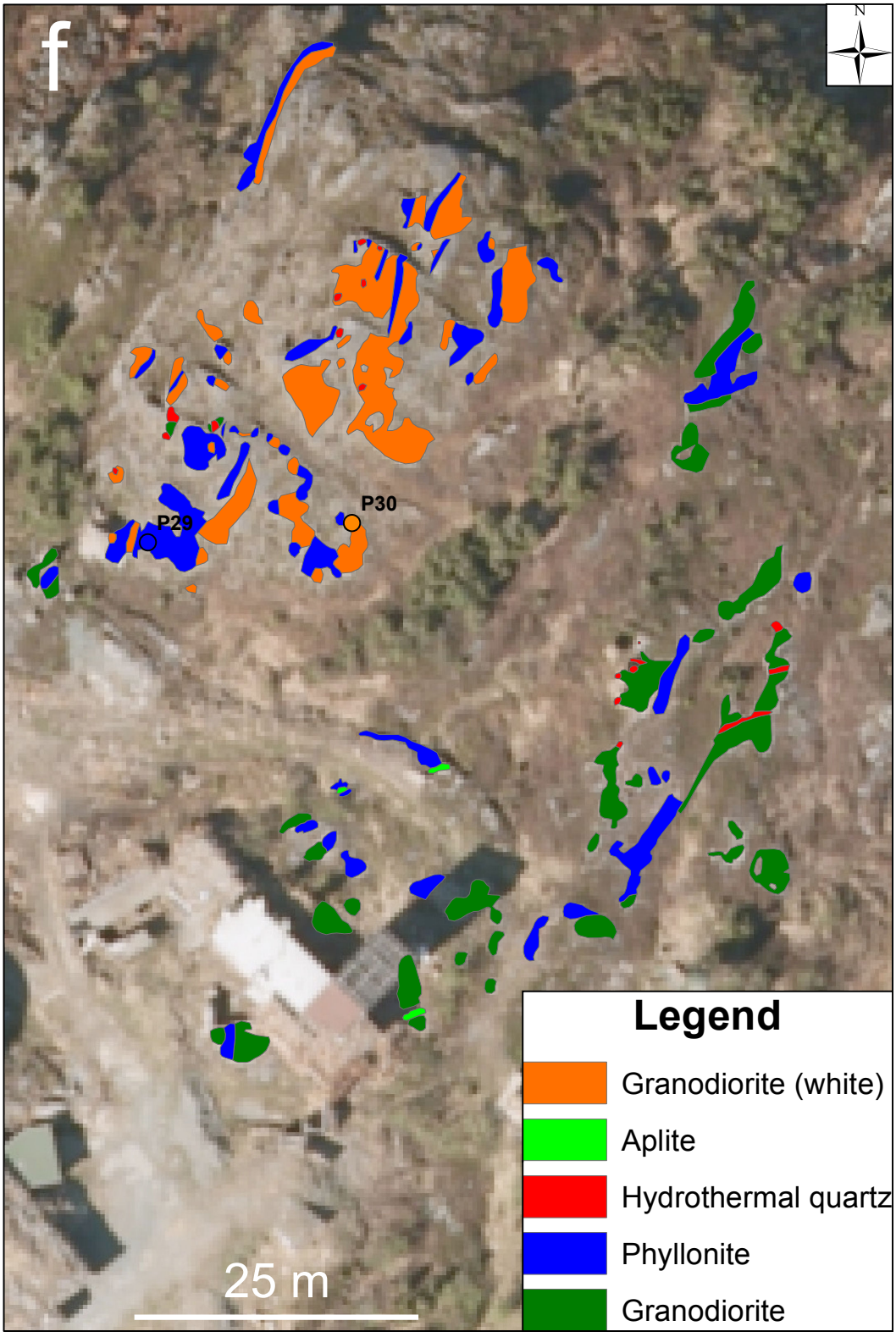
f
N
P29
P30
25 m
Legend
Granodiorite (white)
Aplite
Hydrothermal quartz
Phyllonite
Granodiorite

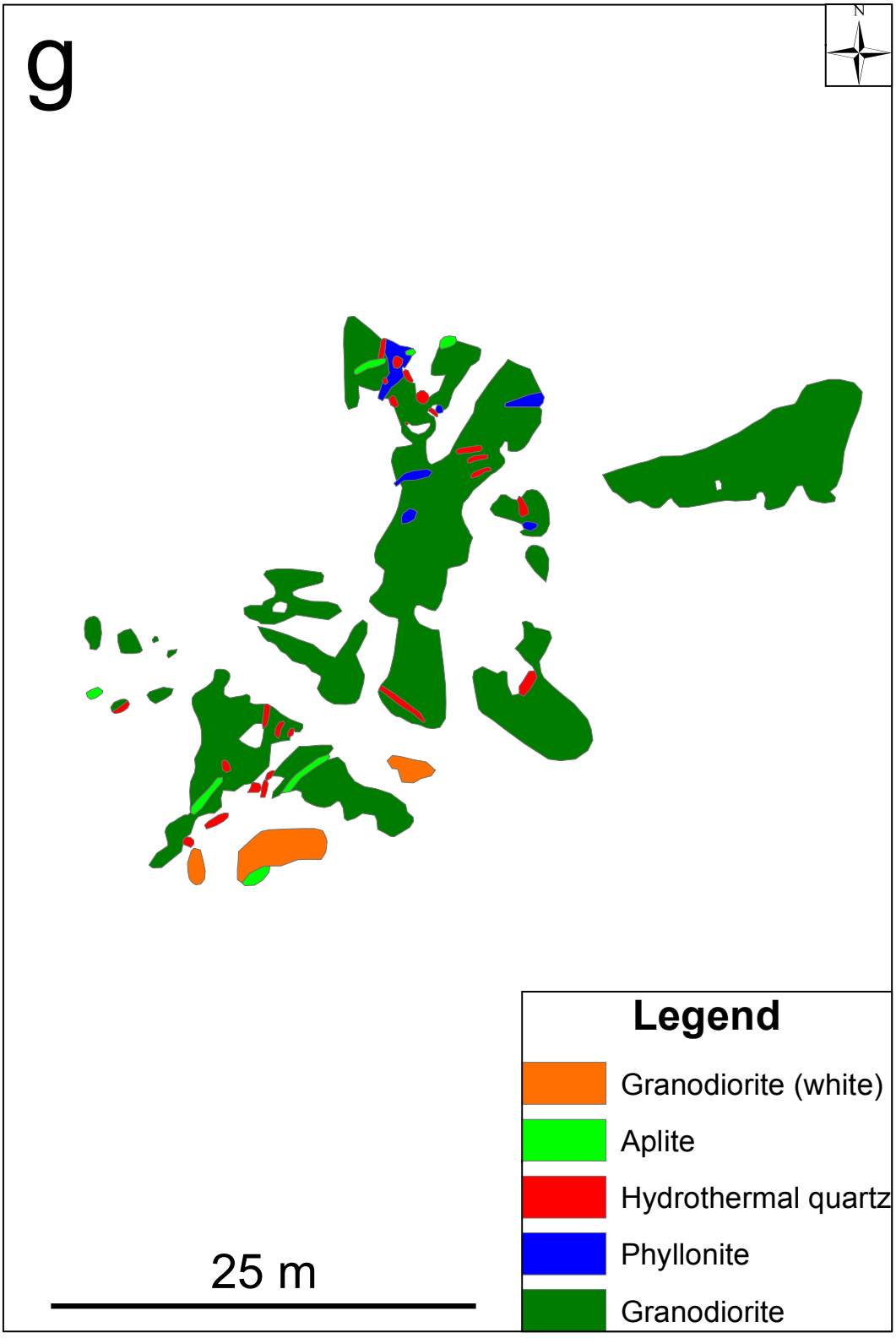
g
N
Legend
Granodiorite (white)
Aplite
Hydrothermal quartz
Phyllonite
Granodiorite
25 m

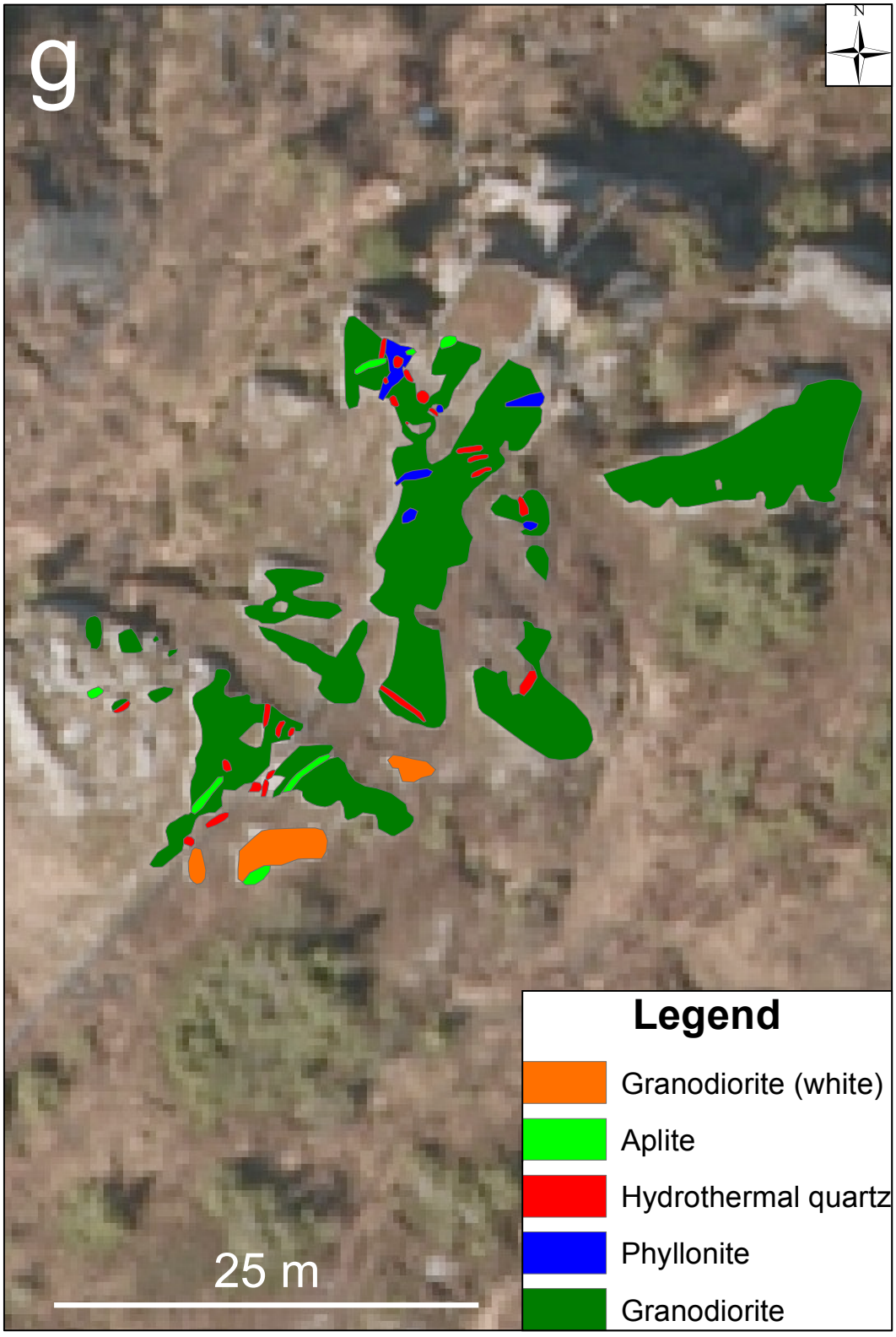
g
N
25 m
Legend
Granodiorite (white)
Aplite
Hydrothermal quartz
Phyllonite
Granodiorite

Appendix C - Petrography

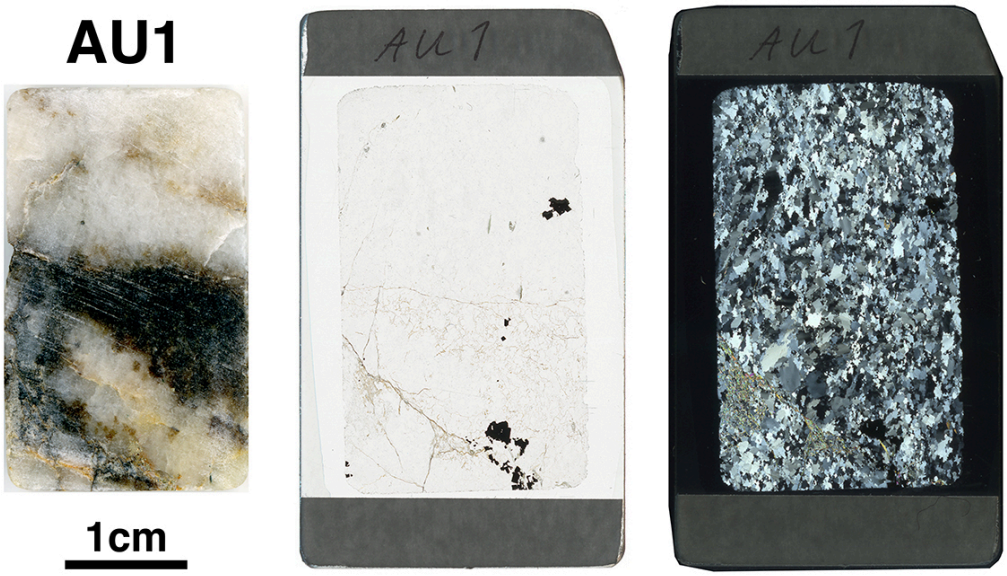

Hand specimen
Massive leucocratic hydrothermal quartz. Mainly white in colour with patches of stained dark quartz hosting acicular green chlorite and epidote, along with dispersed cubic pyrite.

Minerals
Quartz, Muscovite, Epidote, Titanite, Chlorite, Pyrite

Petrographic description
Massive quartz is inequigranular with seriate grain size distribution and patchy extinction. Platy muscovite occurs along fractures in the quartz, forming aggregates along with sub- to euhedral epidote occurring both as single grains and as crystal clusters. The epidote showing patchy interference colours and some grains show zoning. Cubic pyrite measuring up to 2 mm, with sporadic green chlorite and subhedral titanite occurs both as isolated crystal aggregates and along with epidote.

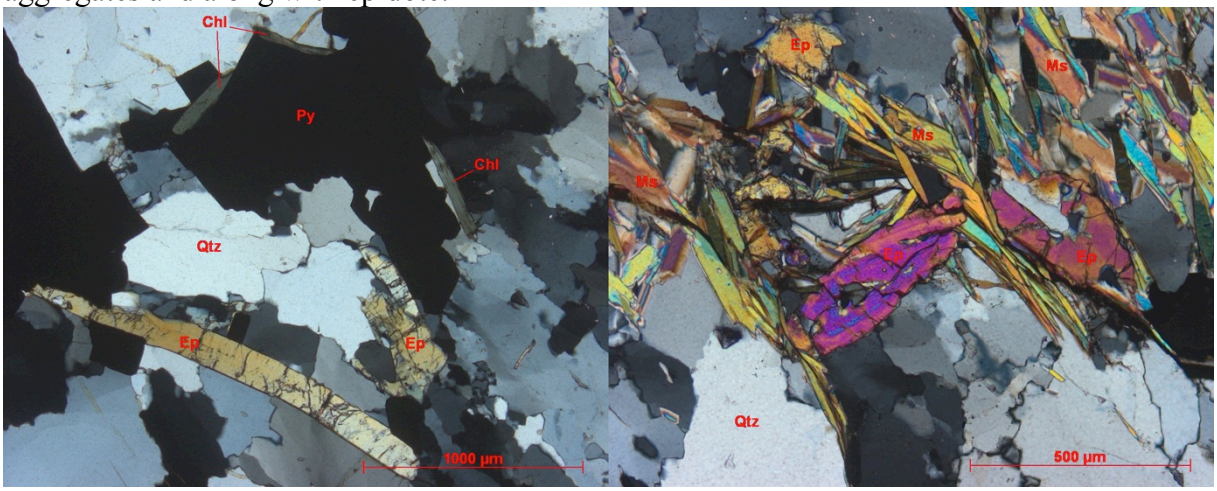

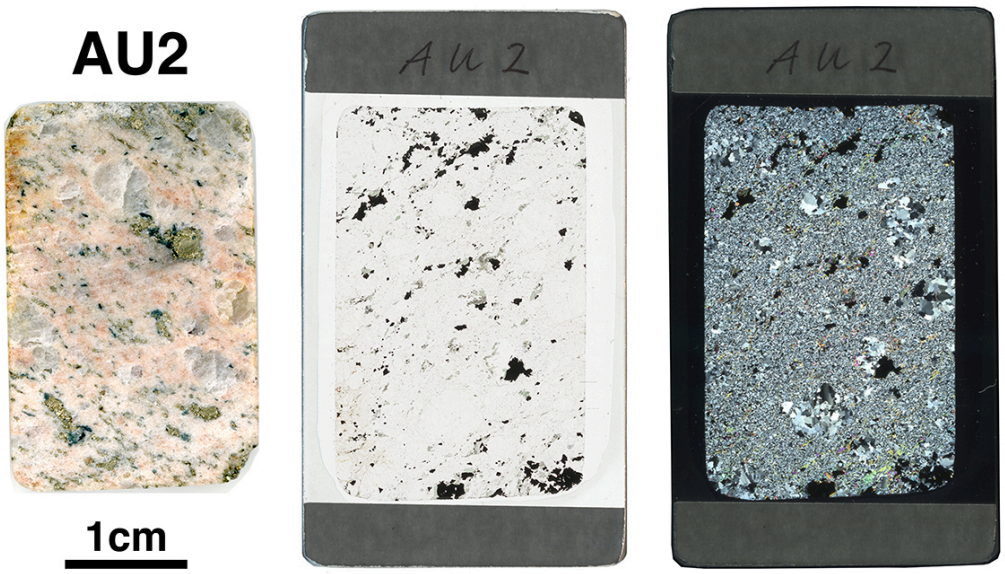

Hand specimen
Porphyric, pink-coloured aplite with grey phenocrysts of quartz, dull white and pink feldspar matrix; cubic pyrite and with muscovite defining a weak foliation.

Minerals
Quartz, Albite, Muscovite, Epidote, Pyrite, Chalcopyrite, Titanite, Chlorite, Biotite

Petrographic description
Porphyritic, recrystallized quartz phenocrysts up to 5 mm are dispersed throughout in a fine-grained albite-muscovite matrix. Subhedral to euhedral epidote with maximum grain size up to 0.9 mm. Some grains show weakly zoned birefringence from core to rim, sector zoning and twinning. The titanite is anhedral, and is associated with epidote. Subhedral pyrite, with inclusions of chalcopyrite (10-20 μm), associated with the epidote and chlorite; some grains show typical cubic of the triangular corners. Subhedral fans of chlorite with pleochroic halos, with undulose extinction; also found as an alteration product of a few grains of biotite. Epidote, titanite, pyrite and chlorite occur together in aggregates occasionally with muscovite. The muscovite occurs as plates, both as individual grains and aggregates and show crenulation cleavage locally.

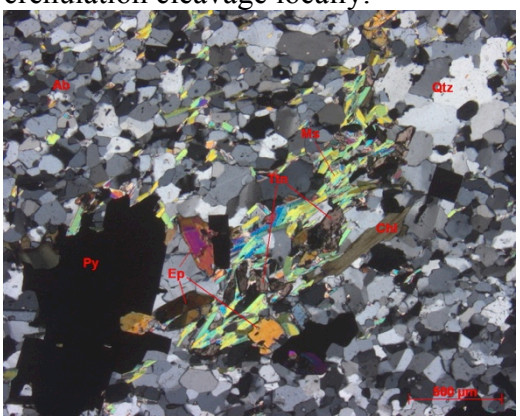

Hand specimen
Coarse-grained leucocratic granodiorite. The rock is homogenous, coarse-grained and composed of subhedral grey quartz, white and pink feldspar, with green-looking mica defining faint foliation. A brown mineral is present, probably titanite. The sample shows a weak brown weathering surface.

Minerals
Quartz (45.8 %), Plagioclase (32.6 %), Alkali feldspar (13.5 %), Muscovite (5.3 %), Epidote (2.6 %), Titanite (0.2 %), + Pyrite, Chlorite

Petrographic description
Inequigranular quartz show dynamic recrystallization with remnants of large unrecrystallized grains. The quartz is amoeboid with jagged grain boundaries, due to bulging overprinting on the grain boundary migration. The alkali feldspar is anhedral to subhedral, inequigranular and showing albite exsolution lamellae and tartan twinning. Polygonal albite grains are mantling and crosscutting the alkali feldspar. Subhedral plagioclase showing polysynthetic twins, some are also kinked, with deformation twins. Heavily altered by mainly sericitization and saussuritization, giving a dusty appearance and inclusions of sericite. Semi-decussate muscovite also occurs along the grain boundaries of the altered plagioclase. Small-grained epidote and epidote with orange-brown allanite core occur randomly, commonly associated with the muscovite. Accessory chlorite seen as an alteration of muscovite; anhedral titanite is oddly tail-shaped commonly occurs with the epidote and muscovite.

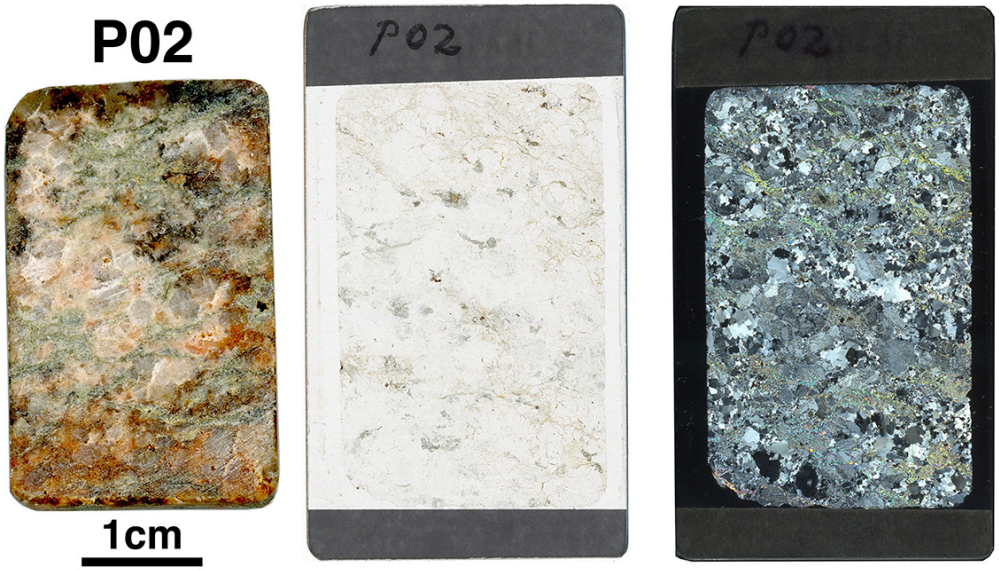

Hand specimen
Hypidiomorphic, coarse-grained and leucocratic granodiorite composed of grey/white quartz, with dull white plagioclase and pink alkali feldspar. The green minerals are muscovite defining a weak foliation along with epidote, which is permeating the rock. Weathering and red-looking rust is penetrating from the surface and into the sample, but the exposed surface looks relatively unaffected.

Minerals
Quartz (44.1%), Plagioclase (32 %), Alkali feldspar (14.4 %), Muscovite (7.7 %), Epidote (1.8 %), Titanite, Pyrite remnants

Petrographic description
Inequigranular quartz showing patchy extinction and sutured grain boundaries. Anhedral plagioclase with polysynthetic twins, with some kinked grains. The plagioclase is heavily affected by sericitization ± saussuritization, shown by sericite inclusions and/or epidote bordering or residing within the plagioclase. Subhedral epidote with occasional twinning occurs in aggregates along with randomly oriented muscovite and anhedral titanite, sometimes set within the polygonal albite. Epidote grains size up to 0.45 mm; however, most grains are less than 70 microns. Many of the epidote grains appear to have a distinct boundary between the rim and core, with no or slight difference in the birefringence. Anhedral microcline shows perthitic exsolution lamellae and tartan twinning. It is less affected by alteration than plagioclase. Polygonal albite grains are crosscutting and/or bordering the microcline. Some pyrite is left, but most is lost due to weathering. Three conspicuous clusters with euhedral epidote are radiating out from a brown-yellow clustered core. Two of them are associated with tail-shaped titanite.

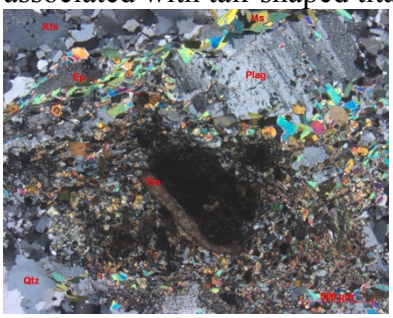

Hand specimen
Porphyric and leucocratic phyllonite, with elongated white-grey quartz grains set in a yellow-green muscovite matrix, which defines the foliation. The surface exhibits signs of rust and protruding quartz grains, while the mica seems to be the less resistant.

Minerals
Quartz (61.7 %), Muscovite (37.6 %), Zircon, Pyrite (+ Plagioclase 0.7 %)

Petrographic description
Anhedral quartz phenocrysts occur as fine-grained aggregates in between the muscovite. The muscovite is anhedral and inequigranular and forming sub-horizontal foliation. A few euhedral zircons are found within the foliation, with size less than 90 microns. Anhedral pyrite is found as small inclusions in the quartz and muscovite, with maximum grain size at 50 microns.

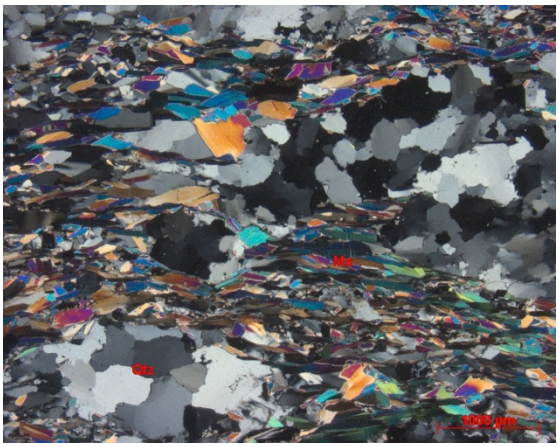

Hand specimen
Porphyric, leucocratic phyllonite having elongated and protruding grey-white quartz grains in a light-coloured yellow-green muscovite matrix, which defines the foliation. Cubic pyrite is unevenly distributed throughout the rock. The surface shows patches of rust and the sample has small cavities that are probably are remnant after weathered pyrite.

Minerals
Quartz (71.6 %), Muscovite (26.1 %), Pyrite (1.5 %), Alkali feldspar, (+ Plagioclase 0.9 %)

Petrographic description
Anhedral and inequigranular quartz phenocrysts showing patchy undulose extinction and wavy grain boundaries. The grain size of quartz is smaller in areas where muscovite dominates. Muscovite is anhedral and defining the foliation, with some grains occurring at an angle to the foliation. The muscovite pins the quartz. A few grains of anhedral alkali feldspar show three distinct cleavages/fracture directions, probably due to a grain orientation effect. Subhedral pyrite is dispersed in the muscovite foliation.

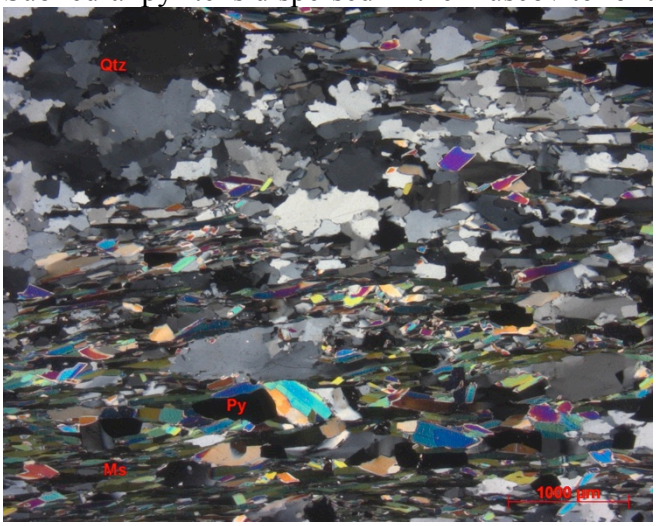

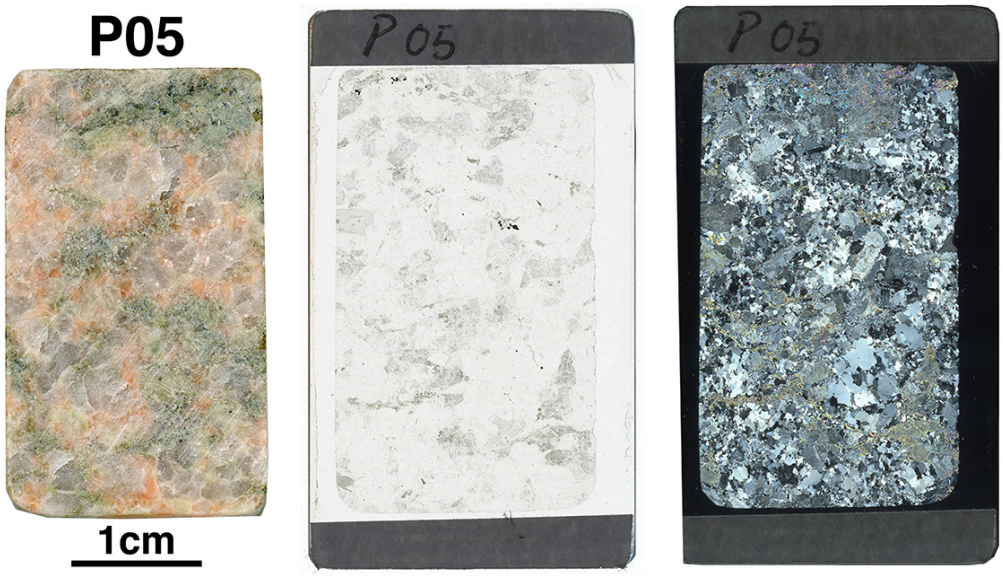

Hand specimen
Coarse-grained leucocratic granodiorite that is homogeneous composed of grey quartz (1-5mm), pink feldspar (1-2mm), green saussurittized plagioclase and green muscovite defining a weak foliation, plus sporadic cubic pyrite. The surface shows weak weathering.

Minerals
Quartz (46.2 %), Plagioclase (29.5 %), Alkali feldspar (14.4 %), Muscovite (5.1 %), Epidote (3.7 %), Pyrite (0.3 %), Titanite (0.5 %), Calcite

Petrographic description
Anhedral quartz with inequigranular size distribution. Anhedral alkali feldspar shows albite exsolution lamellae and occasional microcline twinning; dusty with fine alteration. Small-grained clusters of albite crosscut and border the alkali feldspar. Subhedral plagioclase shows polysynthetic twinning and is heavily affected by sericitization ± saussuritization. Some grains are more affected by the saussuritization than other. Decussate muscovite forming mineral aggregates along with epidote and anhedral titanite, in close proximity to the altered plagioclase. Subhedral to euhedral epidote found as together as clusters of fine-grained reaction product by saussuritization or coarser grained on pyrite; with distinct patchy birefringence. Anhedral calcite appears interstitially to quartz and feldspar.

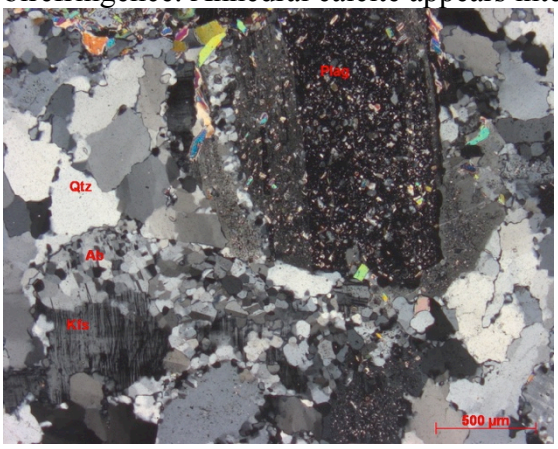

Hand specimen
Porphyric and leucocratic aplite with individual phenocrysts of quartz, plagioclase and alkali feldspar set in a fine-grained pink saccharoidal matrix with irregular patches of green epidote and rust.

Minerals
Quartz (43.7 %), Plagioclase (34.7 %), Alkali feldspar (15.4 %), Muscovite (6 %), Epidote (0.1 %), Pyrite, Titanite, Allanite (+ Calcite 0.1 %)

Petrographic description
Phenocrysts of quartz, plagioclase and alkali feldspar set in matrix consisting of quartz, plagioclase, alkali feldspar, muscovite and epidote. Titanite, allanite and pyrite occur as accessory phases. The quartz phenocrysts show wavy grain boundaries and patchy extinction. The quartz in the matrix is equigranular and rounded. The plagioclase phenocrysts exhibit tabular habit, with polysynthetic twinning. Sericitization and saussuritization penetrates both the phenocrysts and the plagioclase in the matrix. The alkali feldspar phenocrysts are averagely smaller than the plagioclase and quartz. The alkali feldspar shows microcline twinning and albite exsolution lamellae. Albite grains borders and crosscuts the alkali feldspar. Decussate muscovite occurs both as alteration product of the plagioclase and interstitially in the matrix, along with euhedral epidote that shows zonation. A few occurrences of titanite; one grain of allanite, revealed by its brown pleochroism and low birefringence; and a pyrite grain, highly altered along its rim.

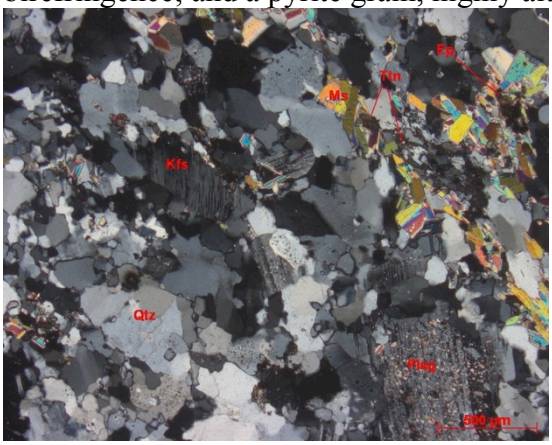

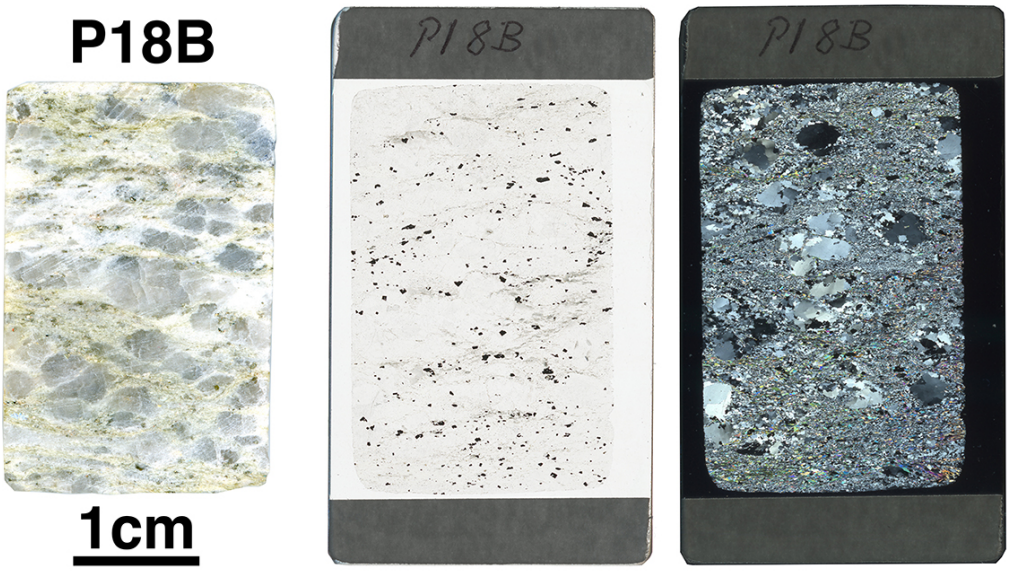

Hand specimen
Leucocratic and porphyric phyllonite, with elongated quartz phenocrysts set in a matrix consisting of fine-grained white albite and white-green muscovite, which is defining a weak foliation. Pyrite is dispersed throughout the muscovite foliation.

Minerals
Quartz (51.5 %), Albite (26.6 %), Muscovite (17.6 %), Pyrite (2.6 %), Epidote, Titanite, (+kfs 1.7 %) + Unknown

Petrographic description
Inequigranular quartz phenocrysts set in an albite-muscovite matrix. Euhedral muscovite forms a sub-horizontal foliation. Equigranular anhedral titanite and subhedral epidote shows high birefringence and relief and is distributed in the muscovite foliation along with subhedral pyrite. Unknown brown material shows no pleochroism and speckled low birefringence.

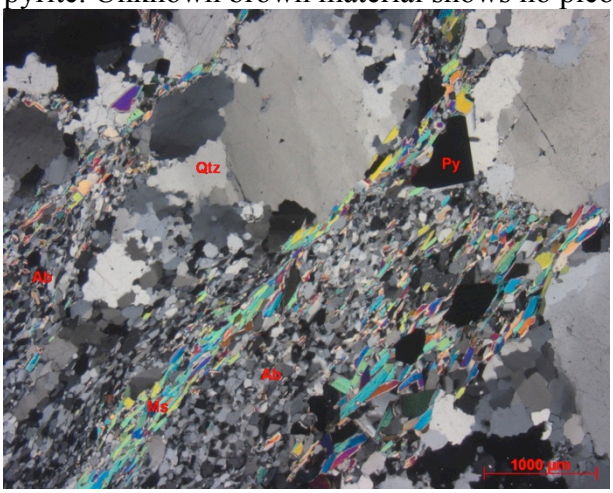

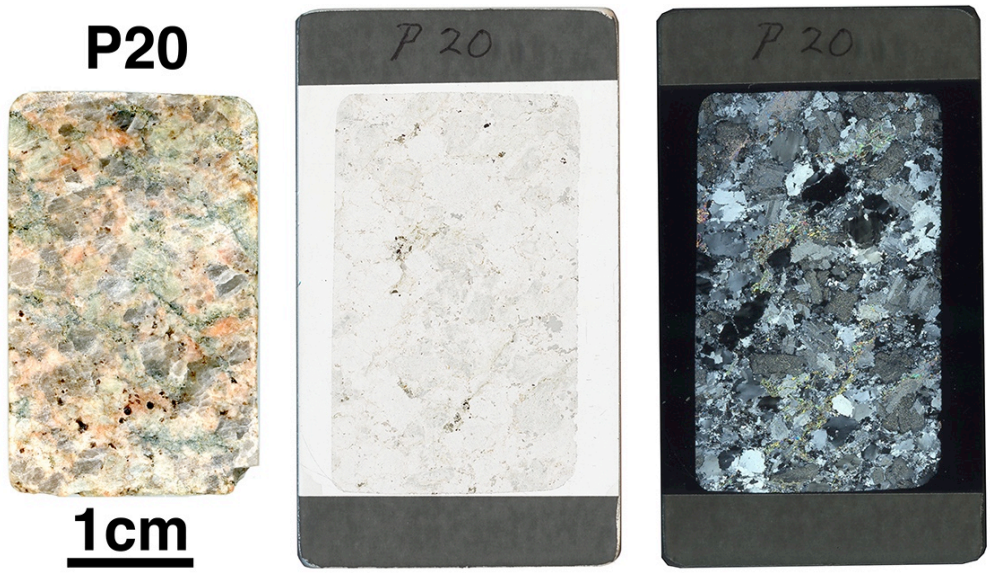

Hand specimen

Coarse-grained, leucocratic, hypidiomorphic granodiorite. The grains are interlocked and composed of grey quartz, white and pink feldspar, speckled with green muscovite and/or epidote, defining a weak foliation.

Minerals

Quartz (43.7 %), Plagioclase (35.8 %), Alkali feldspar (14.1 %), Muscovite (4.7 %), Epidote (1.6 %), Titanite (0.1 %), Pyrite, Chlorite, Allanite (+ Calcite 0.1 %)

Petrographic description

Anhedral to subhedral and seriate quartz with locally preserved grain size, shown by the presence of semi-hexagonal quartz grain that shows bulging along the grain boundary. Elsewhere the quartz is recrystallized into individual grains and subgrains. Subhedral plagioclase with polysynthetic twinning that is heavily affected by sericitization and saussuritization. Anhedral alkali feldspar shows albite exsolution lamellae and microcline twinning with incipient replacement of alkali feldspar by albite, shown by small-grained clusters of albite crosscutting or bordering the alkali feldspar. Decussate, subhedral muscovite associated with subhedral epidote and anhedral titanite, and cubic remnant after pyrite. One grain of allanite found in the muscovite foliation and chlorite has been found as alteration product of the muscovite.

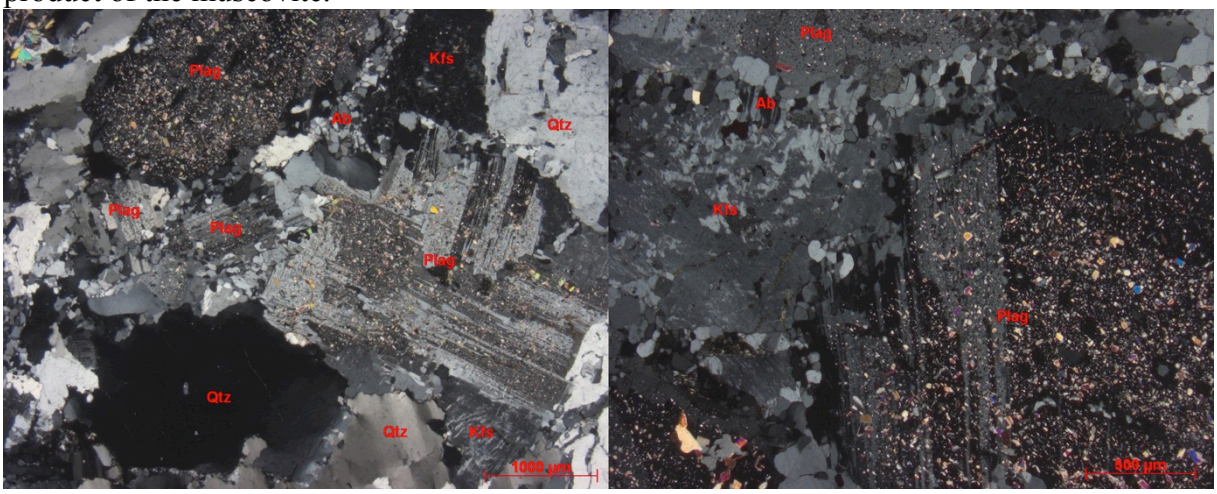

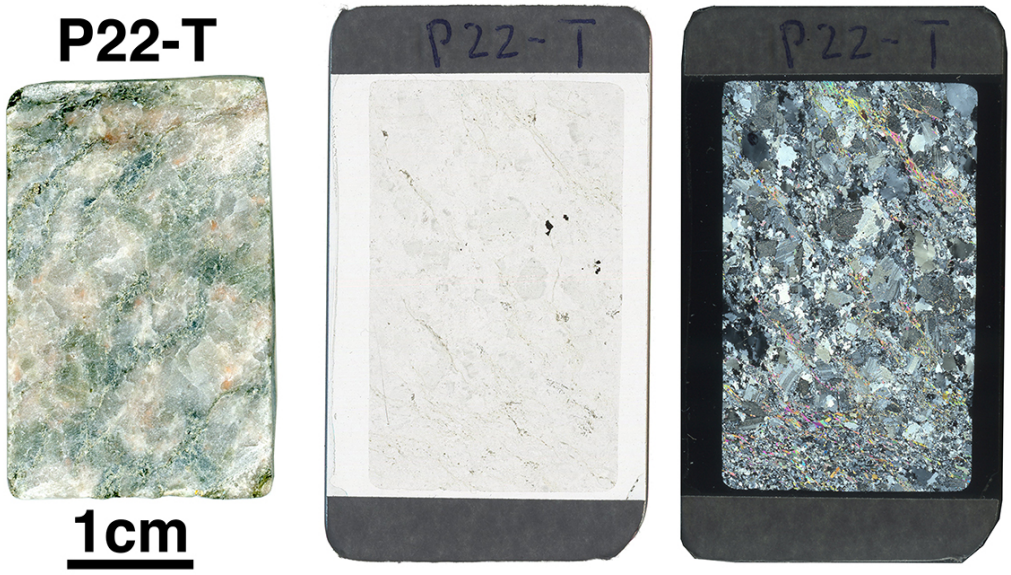

Hand specimen
Coarse-grained, mesocratic granodiorite composed of grey quartz, pink alkali feldspar and white plagioclase, with green muscovite defining a faint foliation.

Minerals
Quartz (45.6 %), Plagioclase (35.5 %), Alkali feldspar (9.3 %), Muscovite (6.6 %), Calcite (2.1 %), Epidote (0.5 %), Titanite (0.3 %), Zircon, Allanite

Petrographic description
Anhedral inequigranular quartz showing patchy undulose extinction. Subhedral alkali feldspar shows albite exsolution lamellae and microcline twinning. Small-grained clusters of albite crosscut and border the alkali feldspar. Subhedral plagioclase exhibit polysynthetic twinning; sericitization and saussuritization alteration dominates the plagioclase. Bands of subhedral muscovite define a weak foliation from the upper left to the lower right corner of the thin section. The foliation is associated with euhedral epidote with zoning; a few occurrences of anhedral allanite ± epidote ± titanite clusters; one grain of zircon is found within the muscovite foliation, revealed by a weak pleochroic halo. Anhedral calcite appears interstitially and randomly throughout the sample.

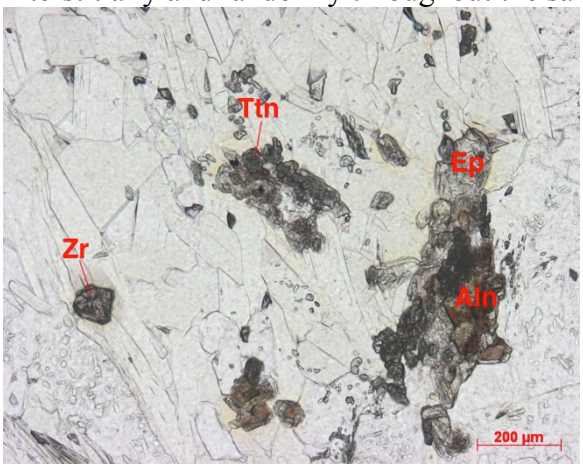

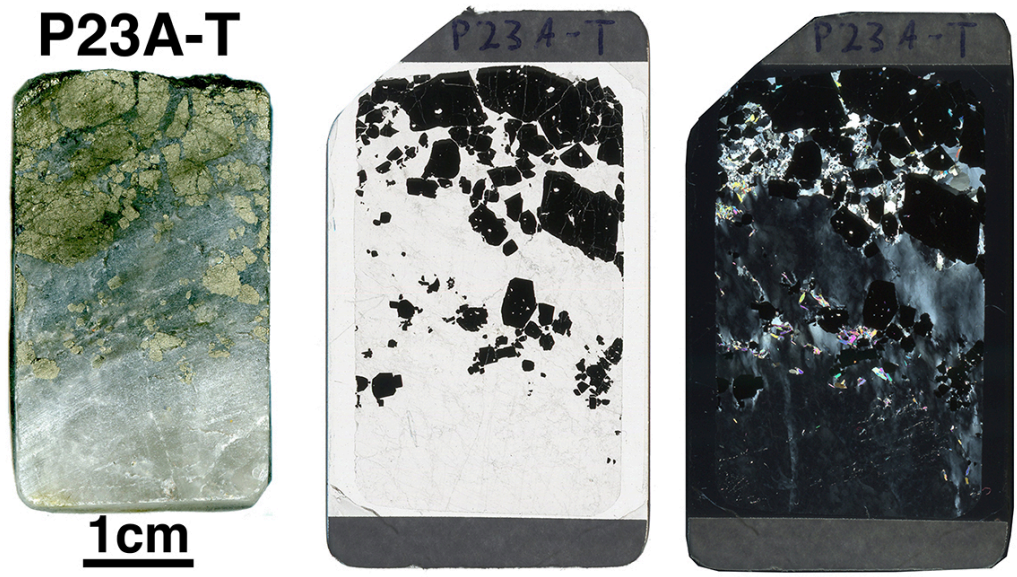

Hand specimen
Massive hydrothermal grey-white quartz hosting coarse-grained cubic pyrite (up to 1 cm) along with fine-grained muscovite.

Minerals
Quartz, Muscovite, Pyrite

Petrographic description
Massive, anhedral quartz exhibits deformation lamellae with fluid inclusion trails and undulose extinction and subgrains. The quartz in the pyrite domain shows both primary quartz growth extending from pyrite grains (lower right picture) and amoeboidal quartz and subgrains therein (lower left picture). The quartz is acting as a host for the muscovite that is decussate in between cubic euhedral pyrite and shows both straight and undulose extinction.

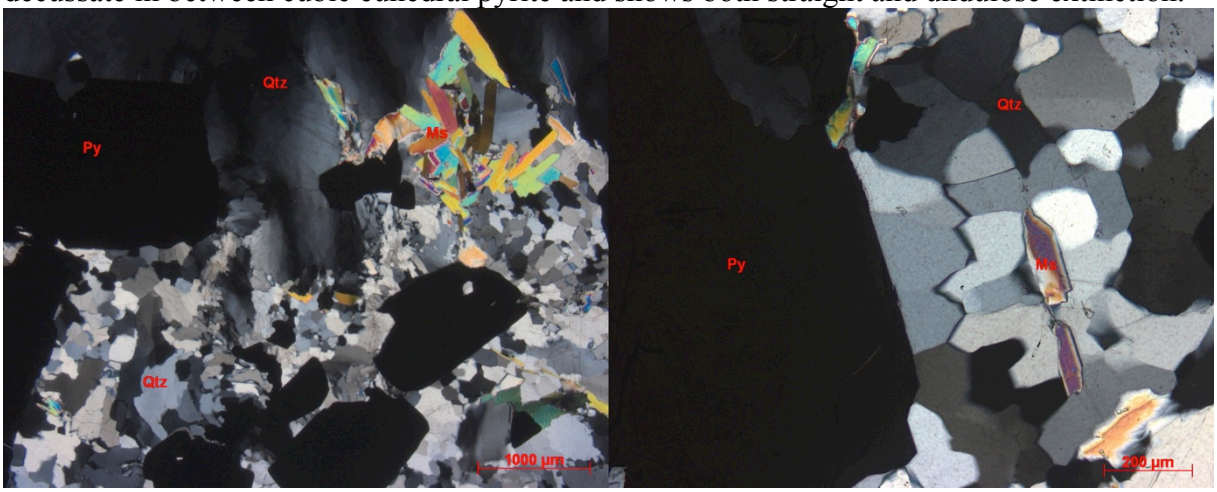

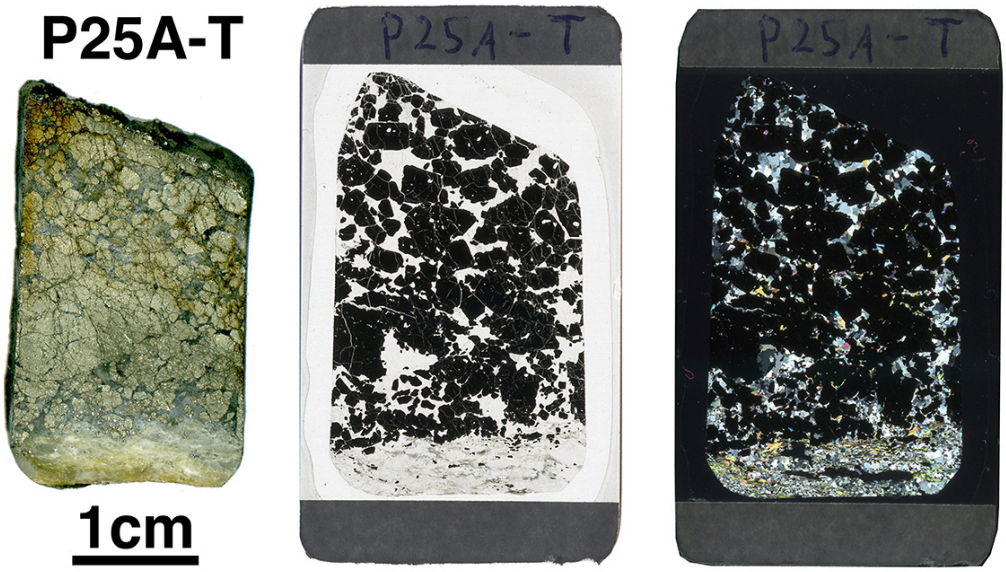

Hand specimen
Melanocratic rock with large subhedral pyrite grains hosted by grey quartz. Bottom end show layers of muscovite, which borders to phyllonite (Sample P25B-T). Sulphide sample taken from a preserved sulphide vein inside the tunnels at Gråkallen.

Minerals
Quartz, Unknown: Alkali feldspar, Muscovite, Pyrite

Petrographic description
Large, subhedral pyrite phenocrysts, with a few chalcopyrite inclusions up 0.5 mm. Quartz are set interstitially with the pyrite, showing bulging, formation of subgrains and straight grain boundaries with triple junctions; and in the phyllonite domain exhibiting signs of bulging. The muscovite within the pyrite domain are decussate and in direct contact with the pyrite. In the phyllonite domain the muscovite defines the foliation. Unknown mineral is present in the phyllonite: Anhedral, low birefringence and all grains exhibit first order grey, with several fractures. It appears to have a lower refractive index than quartz, so a possible identification could be alkali feldspar.

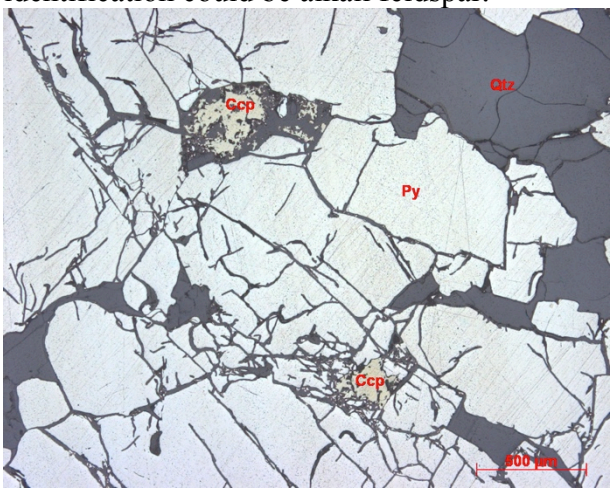

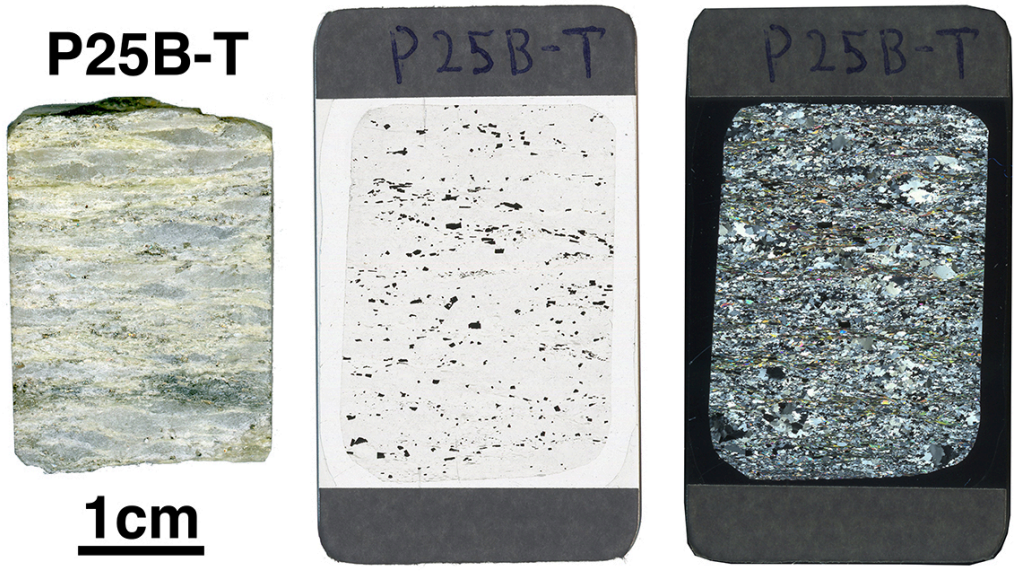

Hand specimen
Porphyric leucocratic phyllonite with quartz phenocrysts elongated in a yellow-green muscovite matrix defining a foliation. Subhedral pyrite is distributed within the muscovite foliation.

Minerals
Quartz (64.1 %), Muscovite (21.5 %), Albite porphyroclasts (5.6 %), Pyrite (5.1 %), Titanite (+ Kfs 3.7 %)

Petrographic description
Inequigranular amoeboid quartz exhibits bulging at the grain boundaries and subgrains within. Platy, subhedral muscovite defines the foliation, with subhedral pyrite is evenly distributed throughout. Anhedral titanite are clustered along with pyrite within the muscovite foliation, revealed by the high relief, brown colour and extreme birefringence. Equant albite porphyroclasts enclosed by the muscovite foliation with a few grains that show Carlsbad twinning and inclusions of quartz. An unknown anhedral feldspar display tapered deformation twins, most likely alkali feldspar.

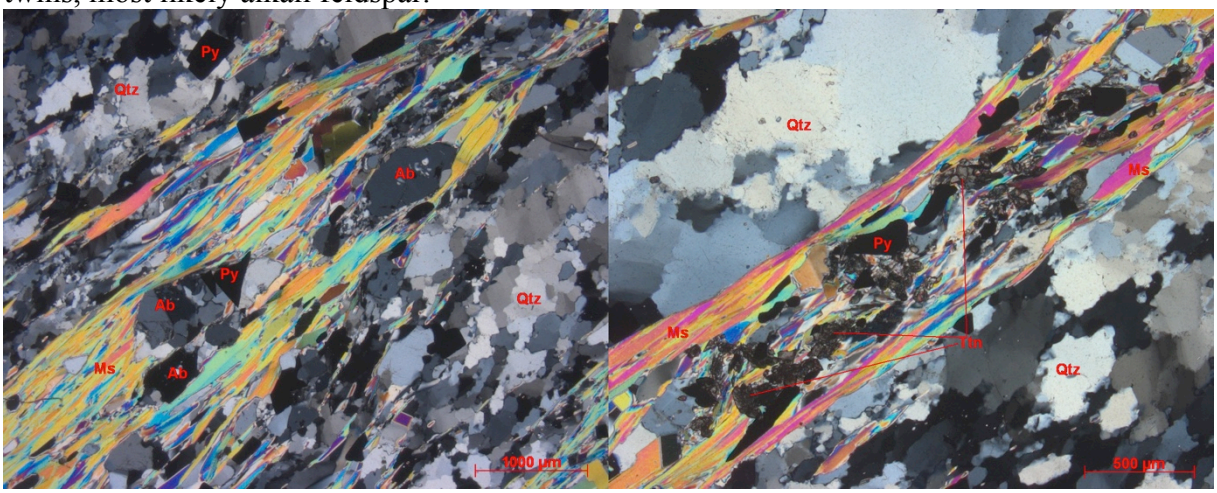

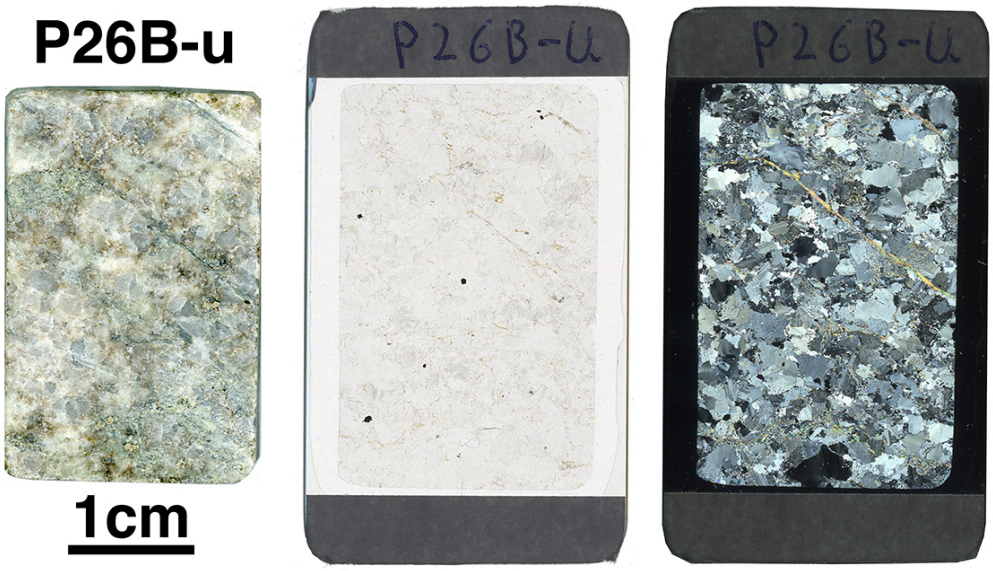

Hand specimen
The phyllonitic P26B-d is paired with the less deformed P26B-u. Mesocratic and phaneritic granodiorite composed of grey quartz grains and white feldspar, and a thin shear band of consisting of a green muscovite. The sample has brown stains of unknown material. The structural evidence at this location shows a top-to-NW movement, where shear bands curves towards the shear zone.

Minerals
Quartz (53.3 %), Plagioclase (26.1 %), Muscovite (11.2 %), Alkali feldspar (8 %), Pyrite, Calcite (0.9 %), Titanite (0.2 %) (+ Epidote 0.4 %)

Petrographic description
Anhedral and inequigranular, amoeboidal quartz with patchy undulose extinction. Inequigranular alkali feldspar with albite exsolution lamellae and weakly altered by sericitization, along with inclusions of calcite. Small-grained clusters of albite crosscut and border the alkali feldspar. Anhedral plagioclase show polysynthetic twins and sericitization, the inclusions follow the polysynthetic twins. Inequigranular decussate muscovite occurs as alteration product of feldspar and as part as shear band through the rock, dominating in the feldspar-rich parts. Euhedral titanite is found within the muscovite shear band and anhedral calcite and pyrite occurs interstitially.

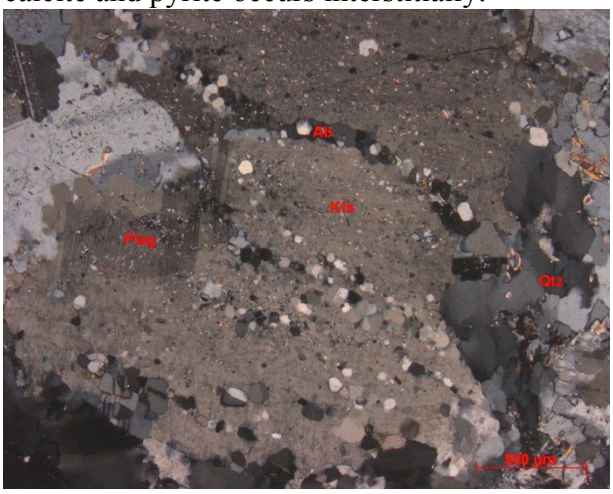

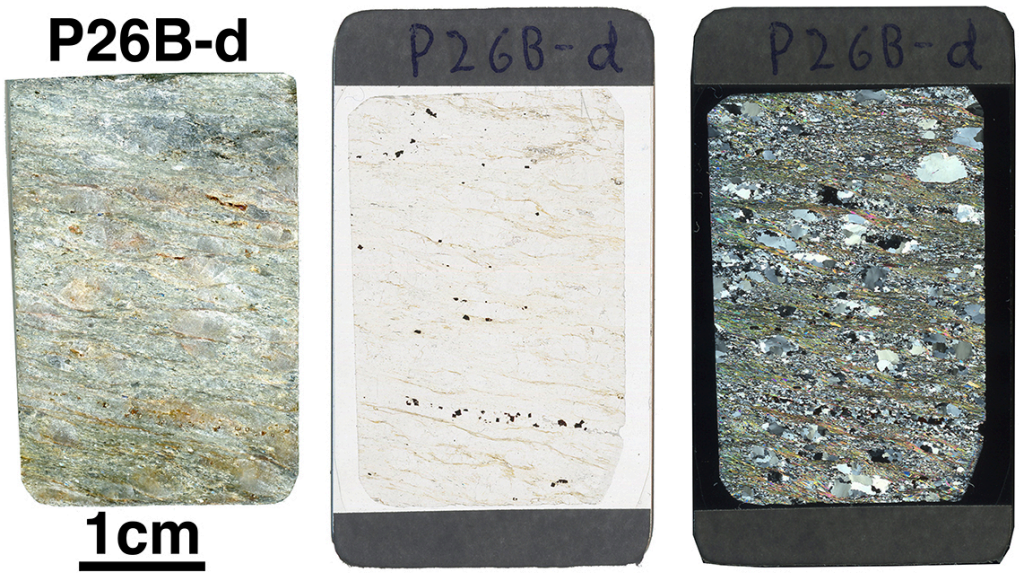

Hand specimen

The phyllonitic P26B-d is paired with the less deformed P26B-u. Mesocratic phaneritic phyllonite composed of elongated quartz grains in a green fine-grained muscovite matrix, along with pyrite. The sample has stains of a brown material, which is unknown. The structural evidence shows a top-to-west movement, where shear bands curves towards the shear zone and sigma-type porphyroclasts of quartz within the shear zone.

Minerals

Quartz (64.9 %), Muscovite (33.9 %), Calcite (0.3 %), Pyrite (0.2 %), (+ Pl/Ab 0.9 %)

Petrographic description

Anhedral and inequigranular quartz shows dynamic recrystallization. Some quartz porphyroclasts are preserved and only show subgrains within the crystal, where as others show subgrains within the recrystallized porphyroclasts and bulging along the grain boundaries of the recrystallized grains. Areas between the porphyroclasts show layering of fine-grained quartz and muscovite. The muscovite is highly inequigranular and defining the foliation, showing long and platy crystals with finer-grained muscovite in between. A few grains intersect at an angle to the foliation (lower left picture). Subhedral pyrite is distributed within the muscovite and anhedral calcite showing lamellar twinning and fractures.

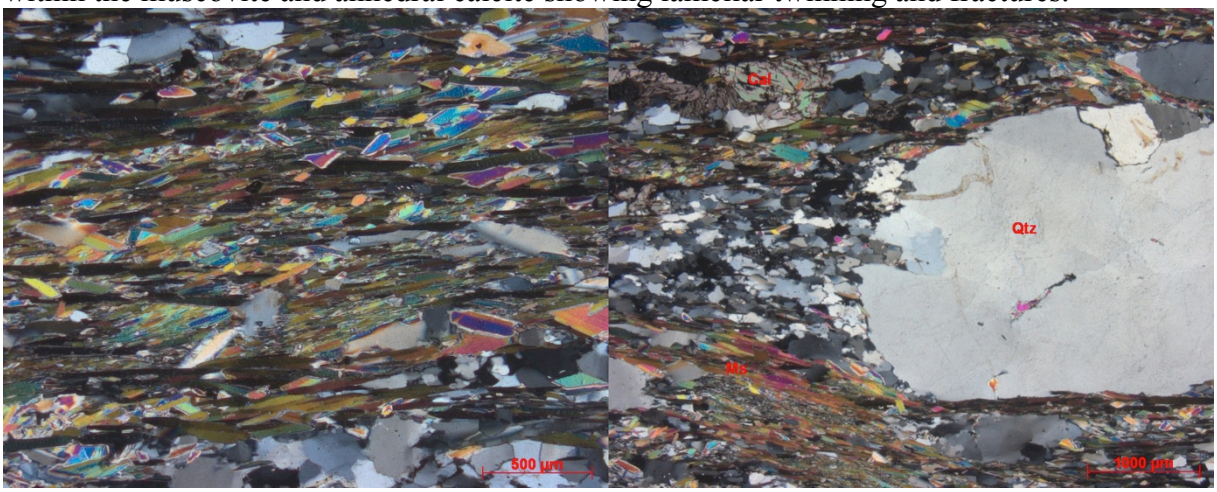

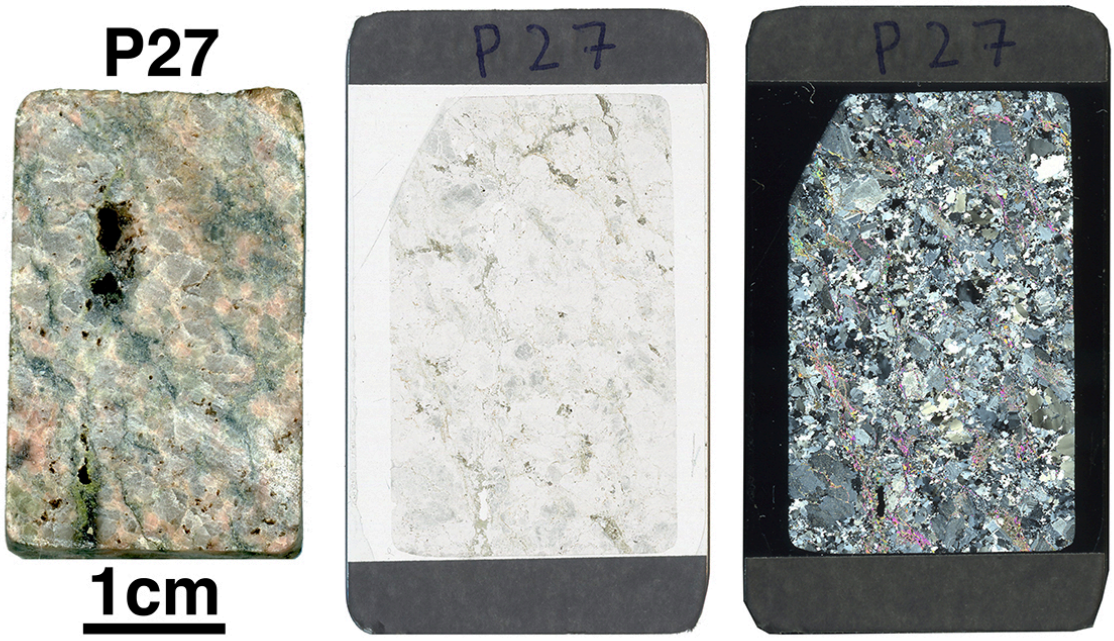

Hand specimen
Leucocratic and phaneritic granodiorite composed of milky white quartz (~2-4mm), pink and white feldspar. A weak green muscovite foliation is evident throughout the sample. Subhedral pyrite and fine-grained subhedral epidote occurs as accessory phases.

Minerals
Quartz (46.8 %), Plagioclase (31.1 %), Alkali feldspar (13.5 %), Muscovite (5.8 %), Epidote (2.5 %), Titanite (0.3 %), Pyrite

Petrographic description
Inequigranular quartz showing dynamic recrystallization while not all grains is completely recrystallized. Some large grains remains, showing undulose extinction. Anhedral alkali feldspar shows albite exsolution lamellae and tartan twinning. Anhedral to subhedral plagioclase showing polysynthetic twinning and is heavily altered by sericitization. Muscovite is seen as the sericite inclusions within the plagioclase, but also as a large-grained variety along the feldspar grain boundaries. Accessory chlorite is seen as alteration of the muscovite. Inequigranular epidote cluster associated with anhedral titanite along with muscovite. Several of the epidote shows a brown allanite core. Yellow-green pleochroic epidote also occurs along the cavities and jugs within the sample.

Hand specimen
Leucocratic and porphyric phyllonite. The rock is homogenous and composed of elongated light grey quartz grains in a yellow-white muscovite matrix that defines the foliation in the rock, with clusters of pyrite in the matrix and irregular patches of albite. Shows some rust towards the exposed surface.

Minerals
Quartz (67.6 %), Muscovite (29.3 %), Albite (2.6 %), Pyrite (0.5 %), Epidote (?)

Petrographic description
Anhedral quartz and inequigranular with fine-grained amoeboidal quartz with a few partially preserved porphyroclasts. Anhedral platy muscovite defines an oscillatory foliation that wraps around the quartz-rich domains. Subhedral pyrite is dispersed in the muscovite foliation, along with albite porphyroclasts showing Carlsbad twinning and fractures (picture below). A few grains of anhedral epidote show zonation and patchy birefringence, with grain size up to 140 microns.

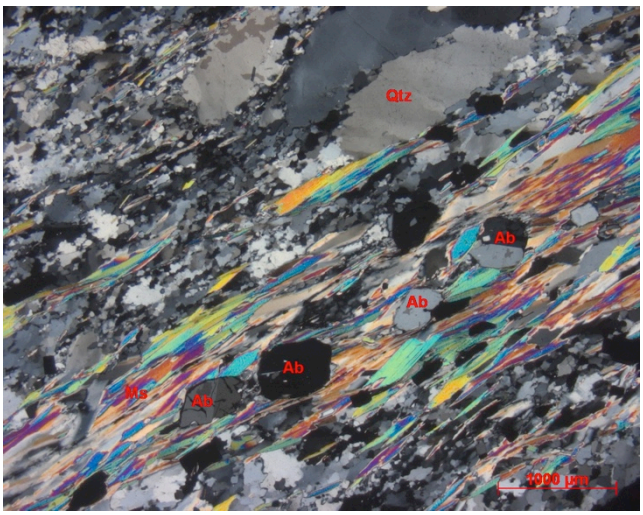

Hand specimen
Porphyric and leucocratic phyllonite, composed of elongated grey-white quartz grains in a white-yellow muscovite matrix defining the foliation, with randomly distributed occurrences of cubic pyrite and irregular patches of white albite.

Minerals
Quartz (69.5 %), Muscovite (26.6 %), Pyrite (2.3 %), Albite (1.7 %), Alkali feldspar

Petrographic description
Anhedral and amoeboid, inequigranular quartz porphyroclasts. Muscovite defines the foliation, with occasional grains crosscutting. The foliation wraps around the quartz domains. Subhedral pyrite is dispersed throughout the muscovite foliation, along with anhedral albite porphyroclasts. The albite is equigranular and often cracked, with occasional quartz inclusions and Carlsbad twins. An aggregate of unknown anhedral feldspars are found, exhibiting fractures, undulose extinction and deformation twins (picture below).

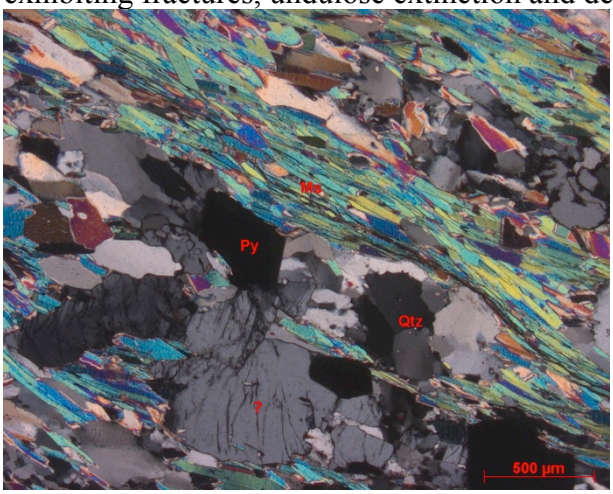

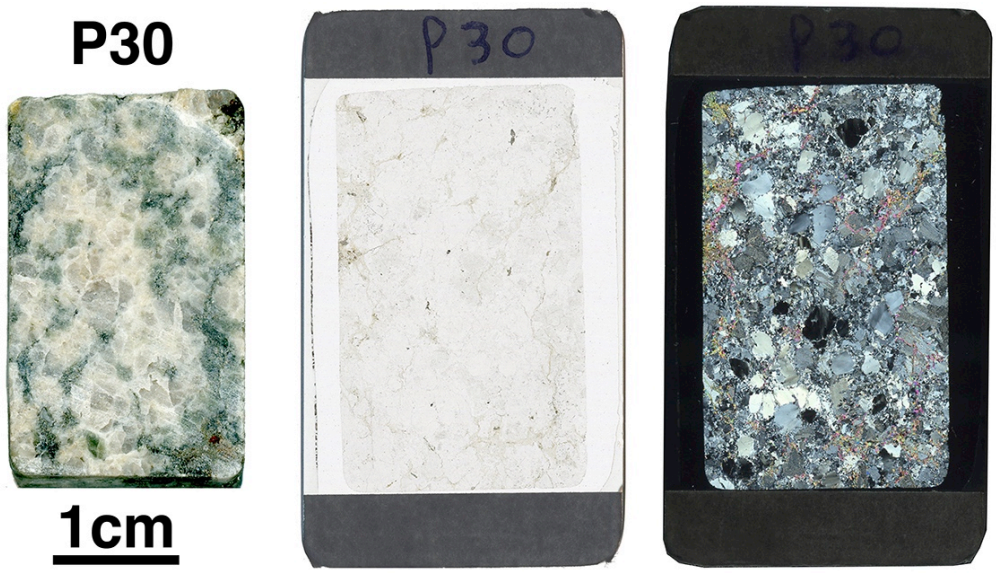

Hand specimen
Leucocratic, phaneritic granodiorite composed of transparent/white quartz and white feldspar, with dark green muscovite penetrating the granodiorite.

Minerals
Quartz (45.2 %), Plagioclase (31.5 %), Alkali feldspar (16.8 %), Muscovite (5.4 %), Calcite (1 %), (+ Epidote, Chlorite, Garnet (0.1 %), Zircon)

Petrographic description
Anhedral, inequigranular quartz shows development of subgrains within the larger relics and bulging along the grain boundary. The alkali feldspar shows exsolution lamellae of albite and occasional microcline twinning and small inclusions. Small-grained clusters of albite crosscut and border the alkali feldspar. The albite-rich domains of the alkali feldspar are more prone to sericitization, compared to alkali feldspar-domains. Subhedral plagioclase shows polysynthetic twinning, heavily affected by alteration, shown by its many inclusions of sericite. Decussate muscovite occurs in areas dominated with altered plagioclase and along their grain boundaries, occasionally accompanied by anhedral titanite. Anhedral calcite occurs interstitially throughout with no particular affinity. Two grains of zircon is found within the muscovite foliation, revealed by a weak pleochroic halo. Two euhedral garnets found with quartz inclusions, enclosed by muscovite (lower right picture). Patches of anhedral chlorite found as alteration product of muscovite and as individual grains (lower left picture). One subhedral grain of epidote shows weak pleochroism and cleavage.

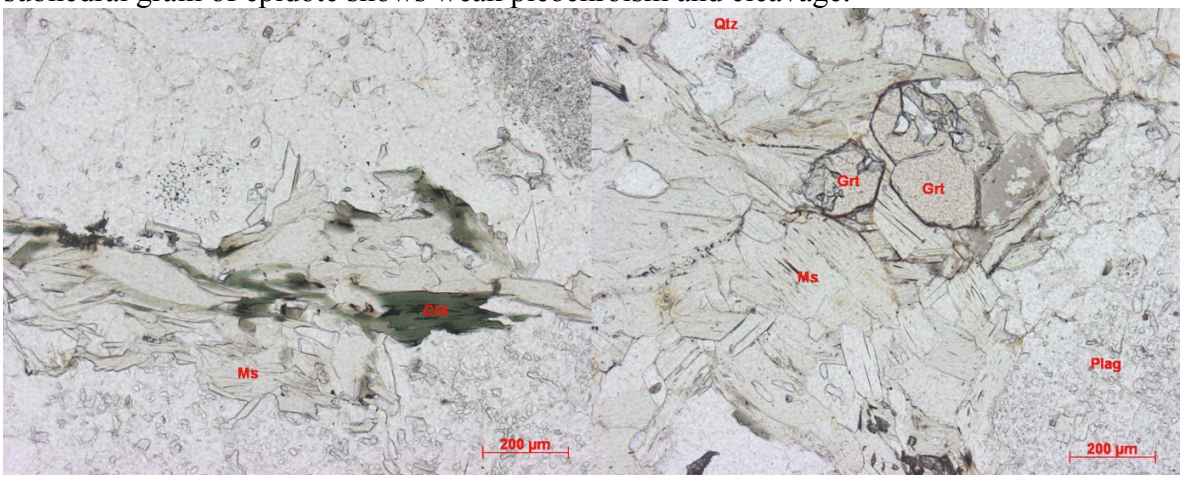

Hand specimen
Coarse-grained leucocratic phaneritic granodiorite composed of grey quartz, pink alkali feldspar and white-green saussurittized plagioclase and a green muscovite and epidote, along with sporadic cubic pyrite. The surface shows weak weathering.

Minerals
Quartz (45 %), Alkali feldspar (13.9 %), Plagioclase (32.9 %), Muscovite (5.1 %), Epidote (2.5 %), Pyrite (0.4 %), Titanite (0.3 %), Calcite (0.1 %)

Petrographic description
Inequigranular quartz exhibits dynamic recrystallization. The quartz is amoeboidal, undulose/patchy extinction seen as subgrains within the larger grains. Bulging is seen on both the larger remnant grains and the smaller set of grains. Anhedral alkali feldspar exhibits albite exsolution lamellae and tartan twinning, with polygonal albite mantling and/or crosscutting the alkali feldspar. Subhedral plagioclase shows polysynthetic twinning/deformation twins. It is heavily altered by sericitization and/or saussuritization giving a dusty appearance. Decussate muscovite is well represented in the plagioclase-dominated areas, both as fine-grained sericite inclusions within the plagioclase, but also as larger-grained variety along grain boundaries. Subhedral epidote occurs as alteration of the plagioclase, associated with the muscovite. It is revealed as a higher relief in PPL compared to the plagioclase altered exclusively to sericite. Epidote is also associated with titanite and pyrite and as a rim component with a brown pleochroic allanite core.

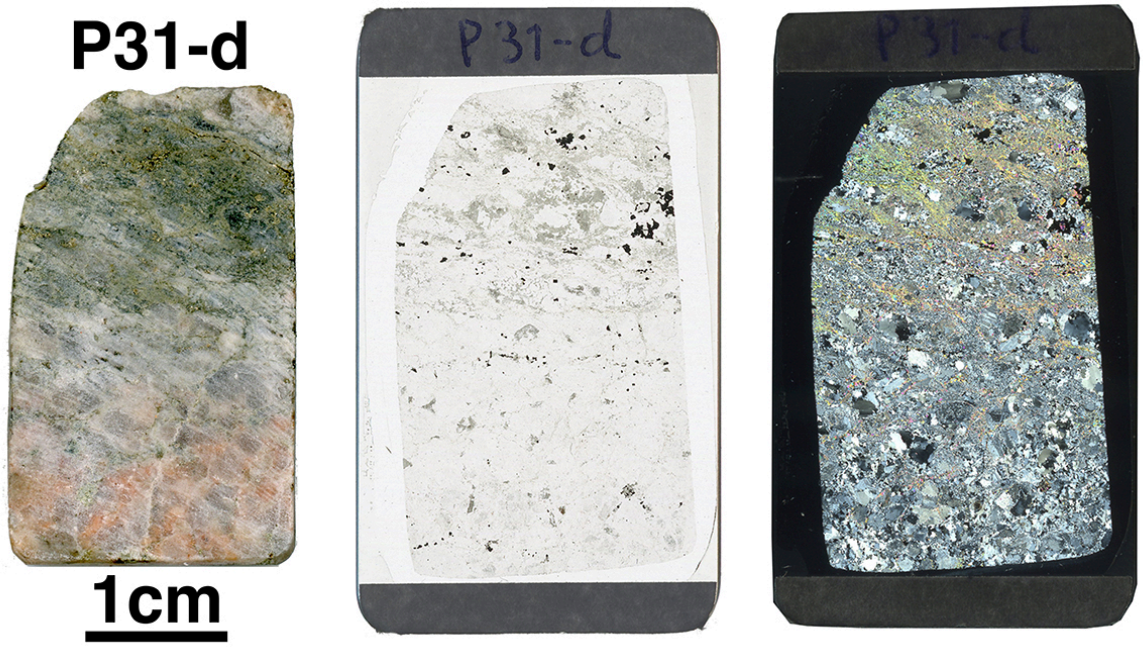

Hand specimen
This sample can be divided into three sections, from top to bottom:
Section one: ~2cm thick shear zone composed of grey quartz grains, green muscovite and epidote, titanite and cubic pyrite; section two: Coarse-grained leached zone, composed of grey quartz and white feldspar, similar to section one; section three: coarse-grained granodiorite, composed of grey quartz, pink alkali feldspar and white plagioclase and is distinguished by its pink, white and green colours.

Minerals in section one:
Quartz (42.4 %), Alkali feldspar (1.4 %), Plagioclase (21.3 %), Muscovite (19 %), Epidote (13.6 %), Pyrite (1.7 %), Titanite (0.6 %)
Minerals in section two:
Quartz, Albite (intermediate to section one and three. (No individual XRD analysis.)
Minerals in section three:
Quartz (45 %), Alkali feldspar (13.9 %), Plagioclase (32.9 %), Muscovite (5.1 %), Epidote (2.5 %), Pyrite (0.4 %), Calcite (0,1 %), Titanite (0.3 %),

Petrographic description (Section one and two only, see P31-u for section three)
Section one: Large subhedral-euhedral epidote with patchy interference colours and large fine-grained aggregates is associated with skeletal-looking pyrite, which increases in amount and grain size towards the shear zone and occasional anhedral titanite. Inequigranular, anhedral quartz with variable degree of recrystallization and with platy muscovite forming a sub-horizontal foliation dispersed within the shear zone.
Section two: Small-grained amoeboidal recrystallized quartz and polygonal albite matrix corresponds to the white leached zone. Epidote and muscovite is distributed within the leached zone. No alkali feldspar is found within this zone.

Appendix D – XRD spectra

Journal number	Sample
140672	AU1
140673	AU2
140649	P01
140650	P02
140651	P03
140652	P04
140653	P05
140654	P09
140655	P13
140656	P17
140657	P18A
140658	P18B
140659	P20
140660	P22-T
	P23A-T
140661	P23B-T
140662	P25A-T
140663	P25B-T
140664	P26B-u
140665	P26B-d
140666	P27
140667	P28
140668	P29
140669	P30
140670	P31-u
140671	P31-d

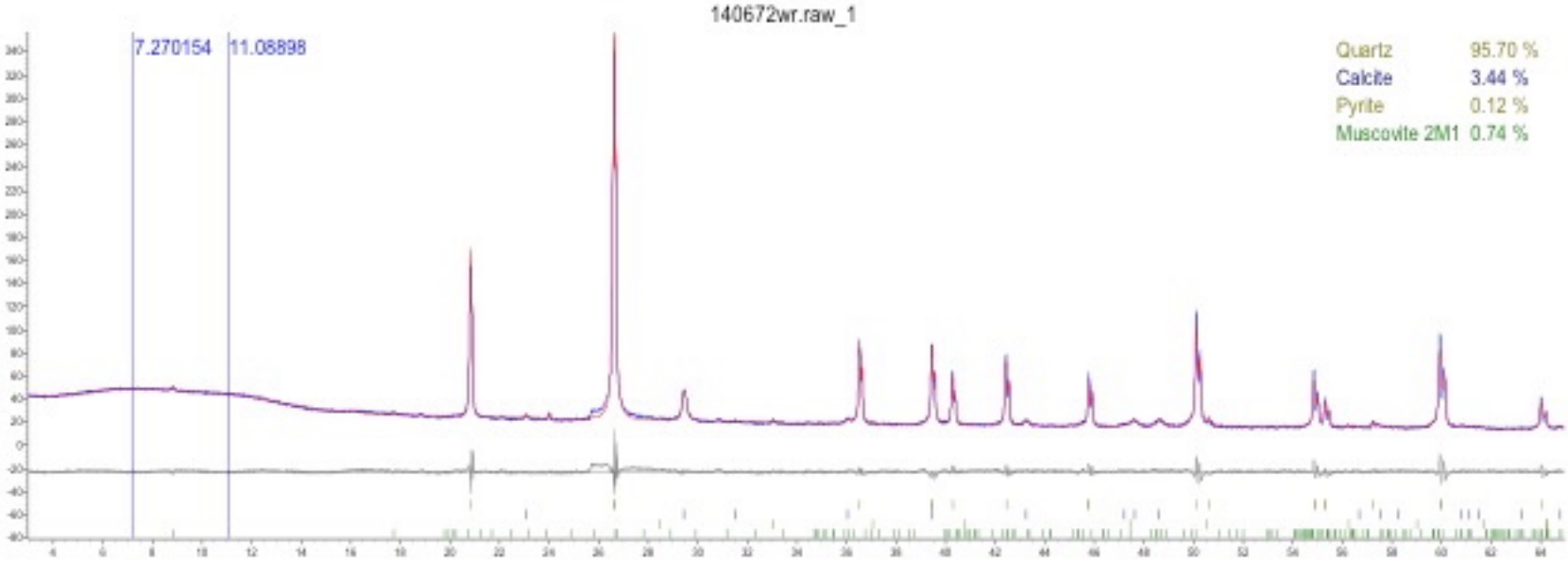
140672wr.raw_1
7.270154
11.08898
Quartz 95.70 %
Calcite 3.44 %
Pyrite 0.12 %
Muscovite 2M1 0.74 %

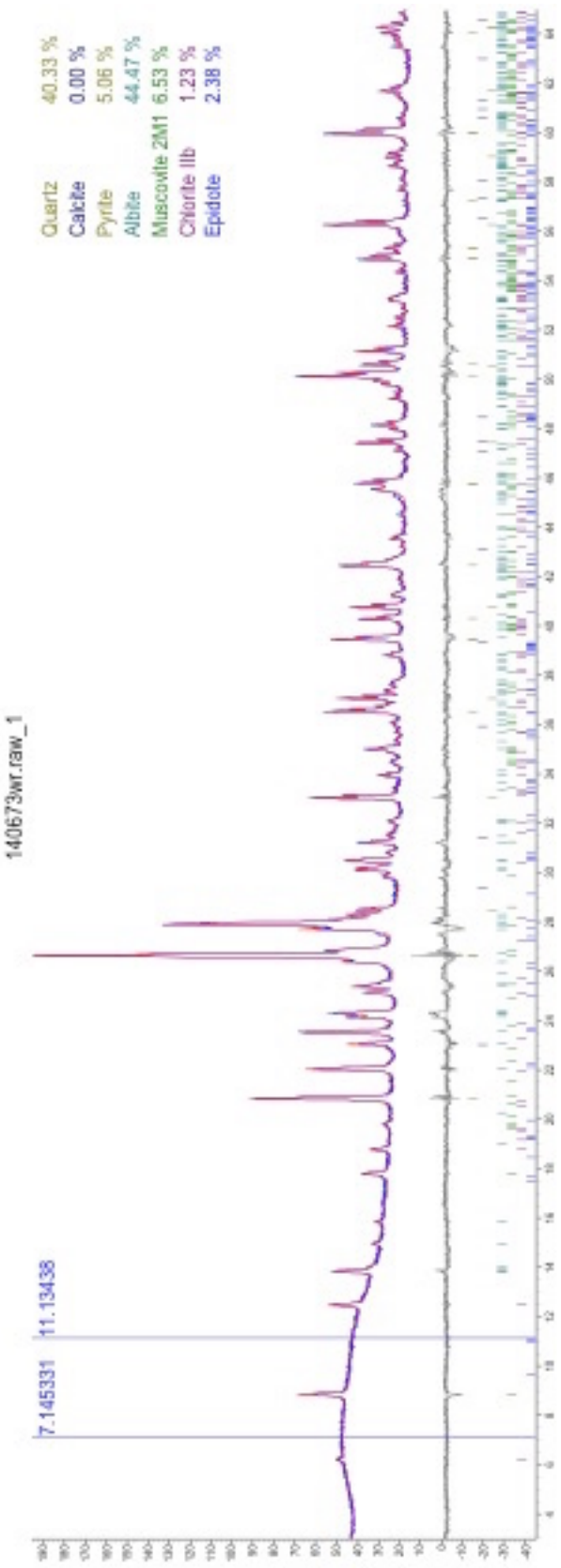
140673wr.raw_1
7.145331
11.13438
Quartz 40.33 %
Calcite 0.00 %
Pyrite 5.06 %
Albite 44.47 %
Muscovite 2M1 6.53 %
Chlorite IIb 1.23 %
Epidote 2.38 %

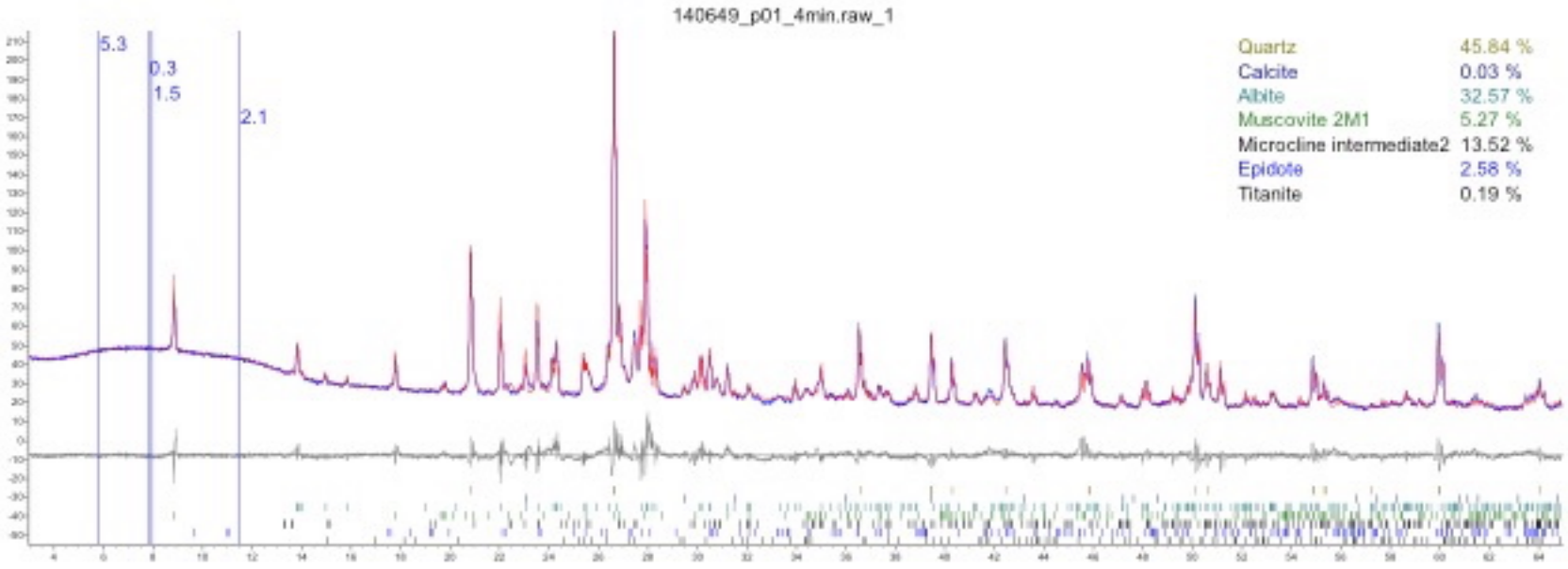
140649_p01_4min.raw_1
5.3
0.3
1.5
2.1
Quartz 45.84 %
Calcite 0.03 %
Albite 32.57 %
Muscovite 2M1 5.27 %
Microcline intermediate2 13.52 %
Epidote 2.58 %
Titanite 0.19 %

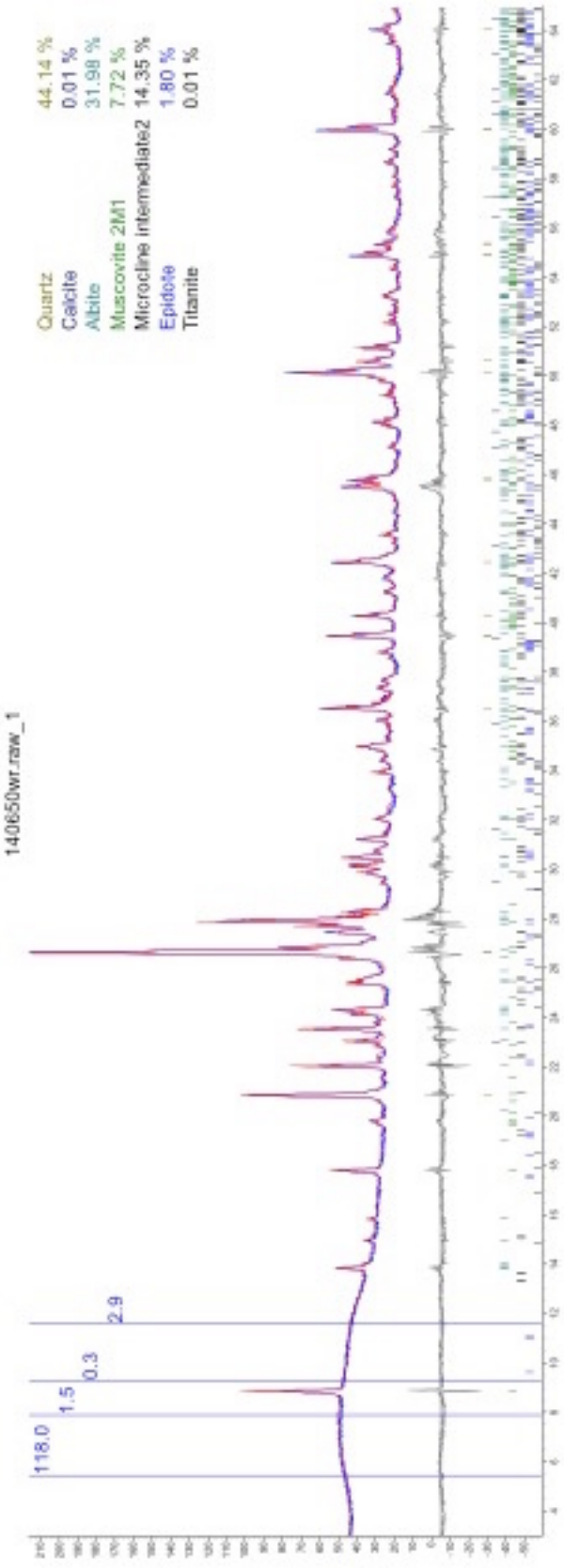
140650wr.raw_1
Quartz 44.14 %
Calcite 0.01 %
Albite 31.98 %
Muscovite 2M1 7.72 %
Microcline intermediate2 14.35 %
Epidote 1.80 %
Titanite 0.01 %
118.0
1.5
0.3
2.9

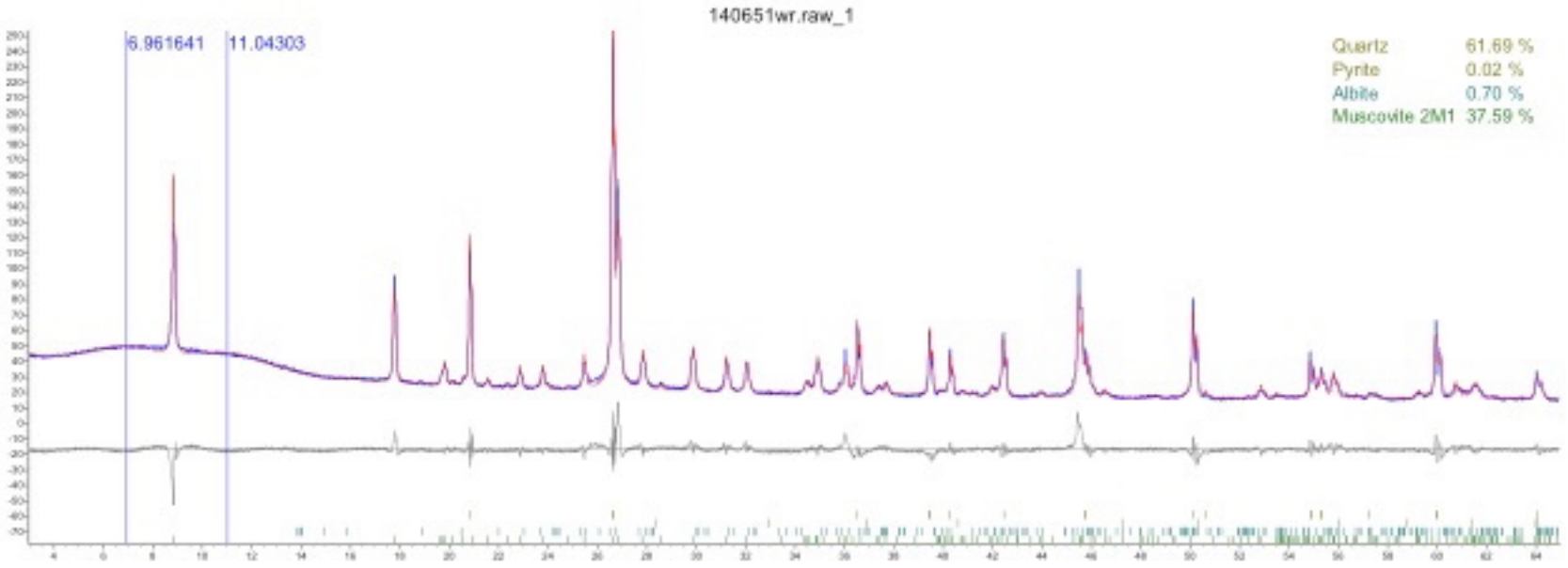
140651wr.raw_1
6.961641
11.04303
Quartz 61.69 %
Pyrite 0.02 %
Albite 0.70 %
Muscovite 2M1 37.59 %

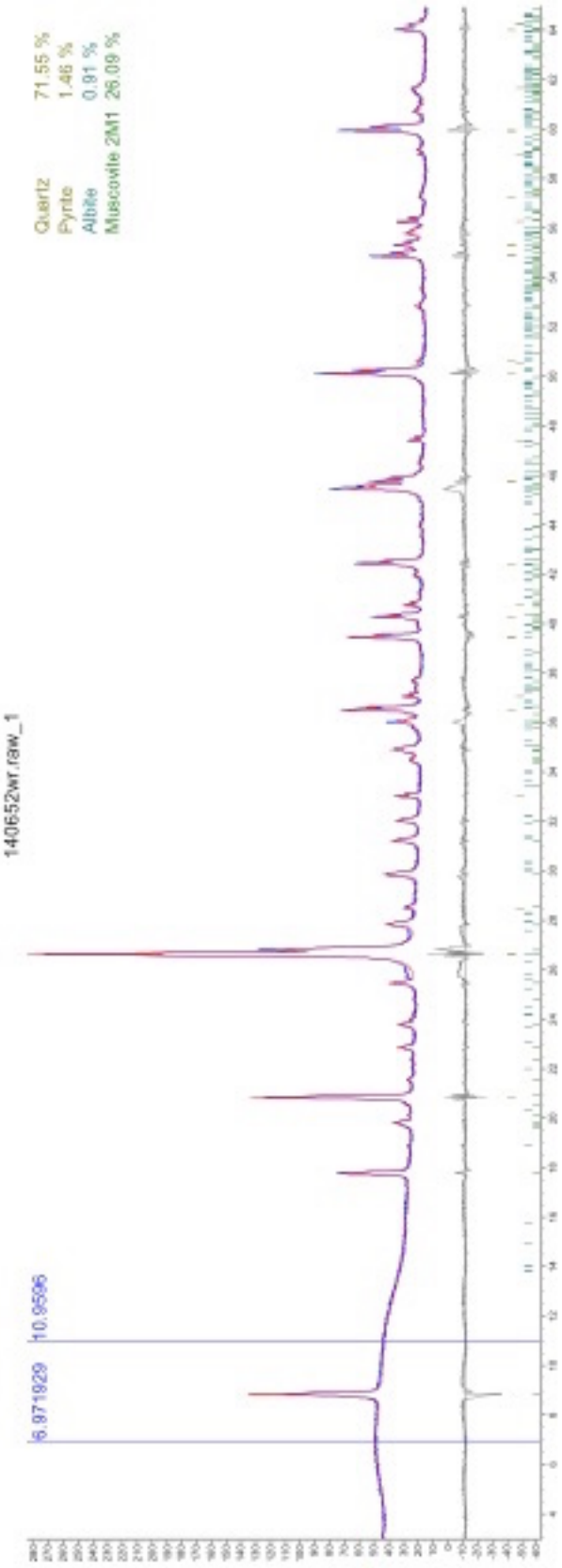
140652wr.raw_1
Quartz 71.55 %
Pyrite 1.46 %
Albite 0.91 %
Muscovite 2M1 26.09 %
6.971929
10.9596

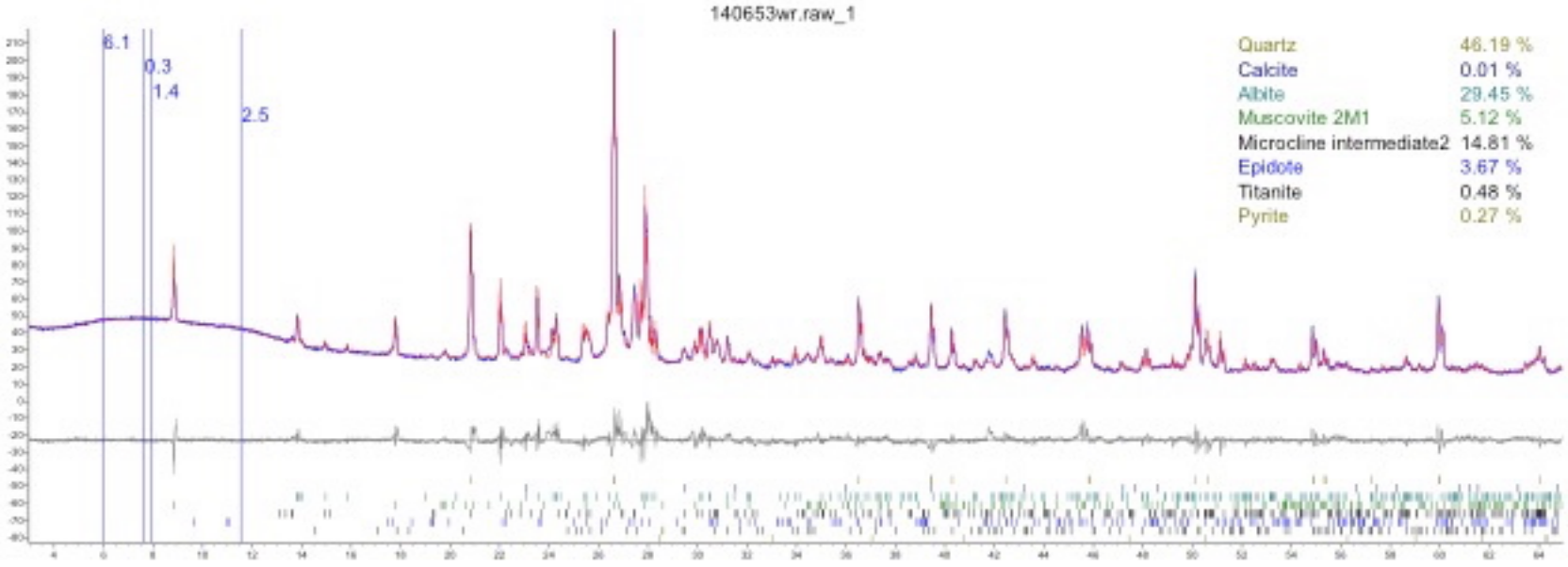
140653wr.raw_1
6.1
0.3
1.4
2.5
Quartz 46.19 %
Calcite 0.01 %
Albite 29.45 %
Muscovite 2M1 5.12 %
Microcline intermediate2 14.81 %
Epidote 3.67 %
Titanite 0.48 %
Pyrite 0.27 %

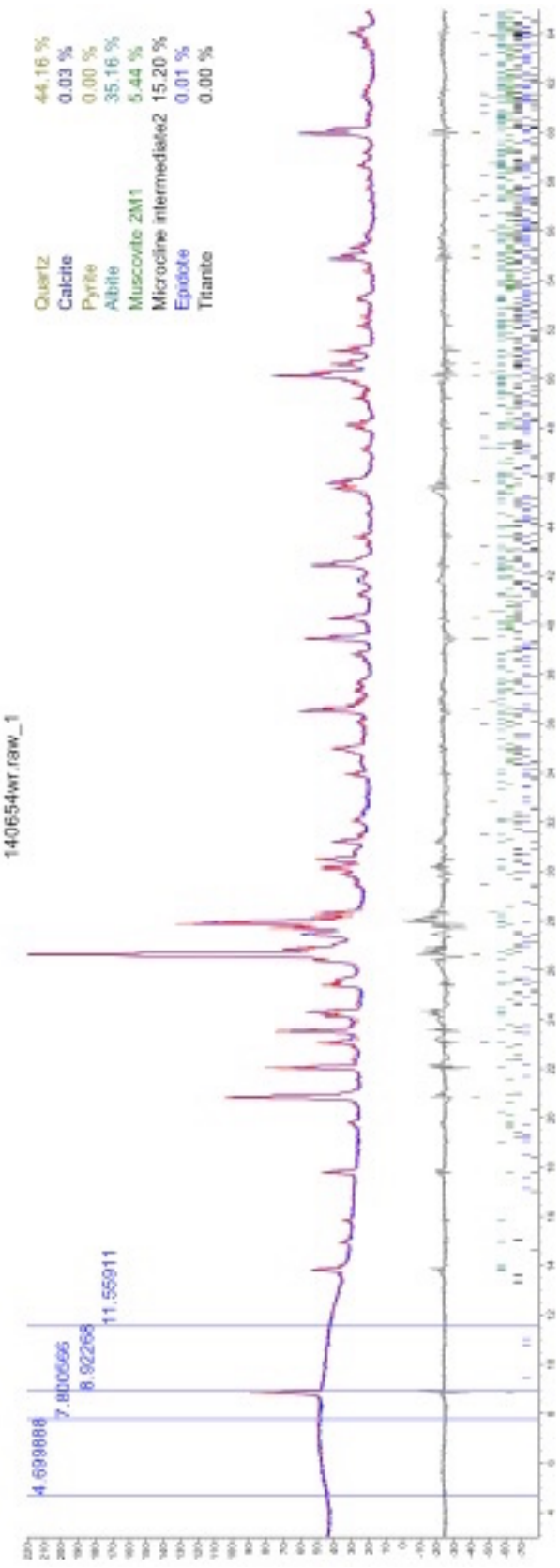
140654wr.raw_1
Quartz 44.16 %
Calcite 0.03 %
Pyrite 0.00 %
Albite 35.16 %
Muscovite 2M1 5.44 %
Microcline intermediate2 15.20 %
Epidote 0.01 %
Titanite 0.00 %
4.699888
7.800666
8.92268
11.55911

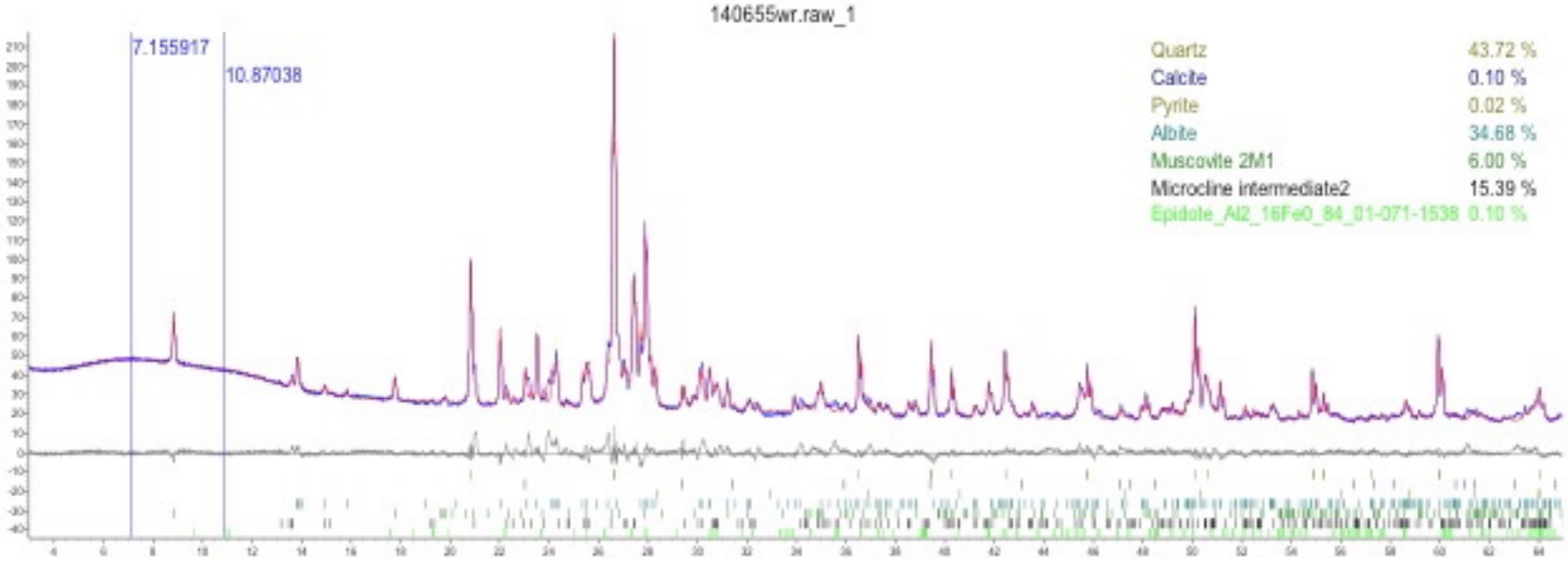
140655wr.raw_1
7.155917
10.87038
Quartz 43.72 %
Calcite 0.10 %
Pyrite 0.02 %
Albite 34.68 %
Muscovite 2M1 6.00 %
Microcline intermediate2 15.39 %
Epidote_Al2_16Fe0_84_01-071-1538 0.10 %

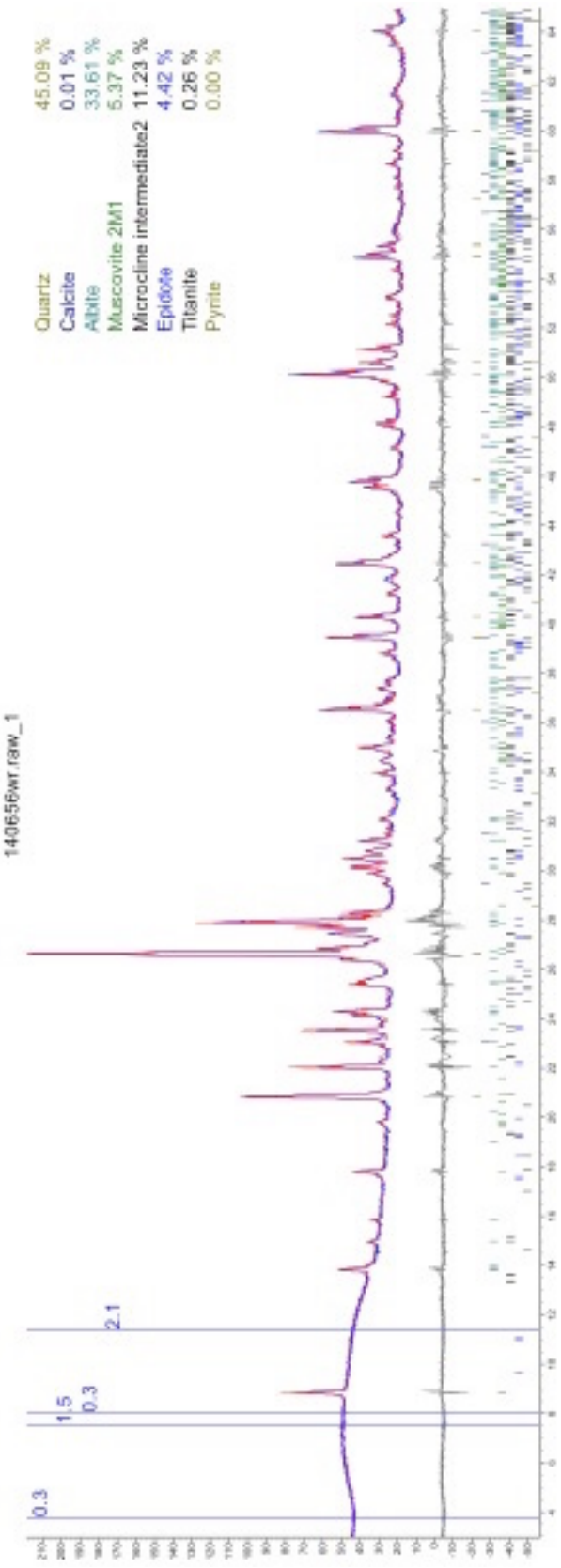
140656wr.raw_1
Quartz 45.09 %
Calcite 0.01 %
Albite 33.61 %
Muscovite 2M1 5.37 %
Microcline intermediate2 11.23 %
Epidote 4.42 %
Titanite 0.26 %
Pyrite 0.00 %
0.3
1.5
0.3
2.1

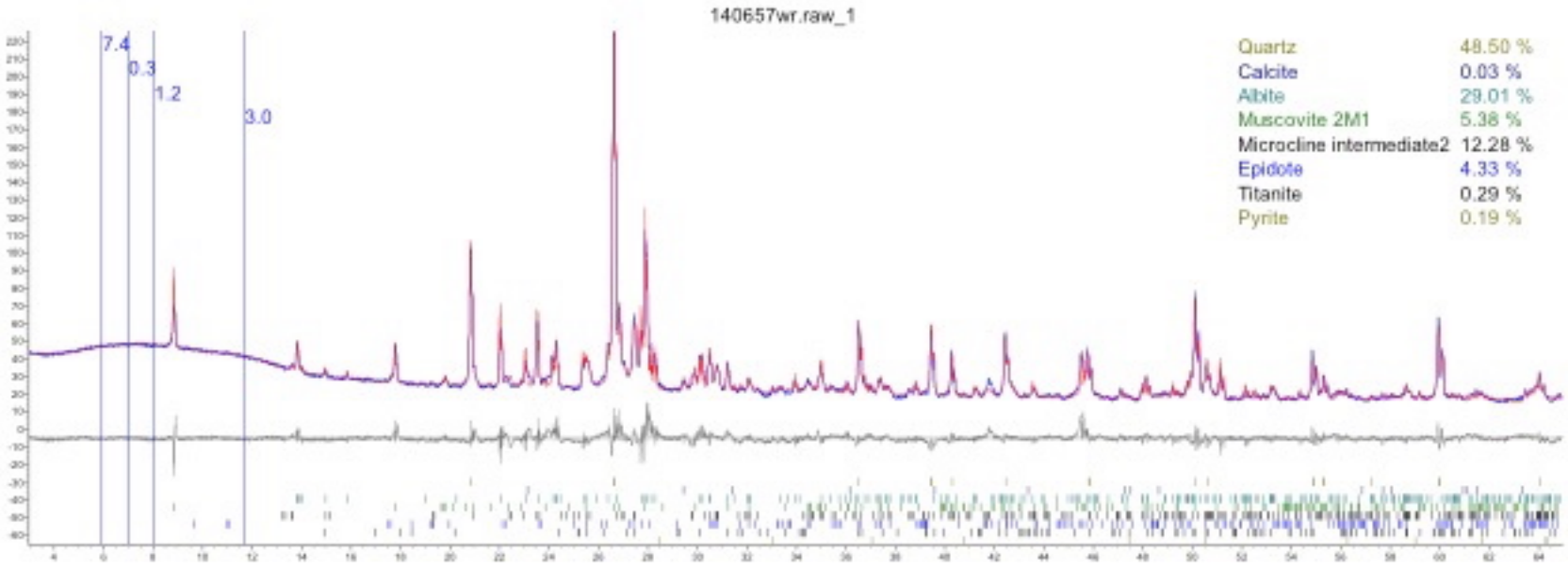
140657wr.raw_1
7.4
0.3
1.2
3.0
Quartz 48.50 %
Calcite 0.03 %
Albite 29.01 %
Muscovite 2M1 5.38 %
Microcline intermediate2 12.28 %
Epidote 4.33 %
Titanite 0.29 %
Pyrite 0.19 %

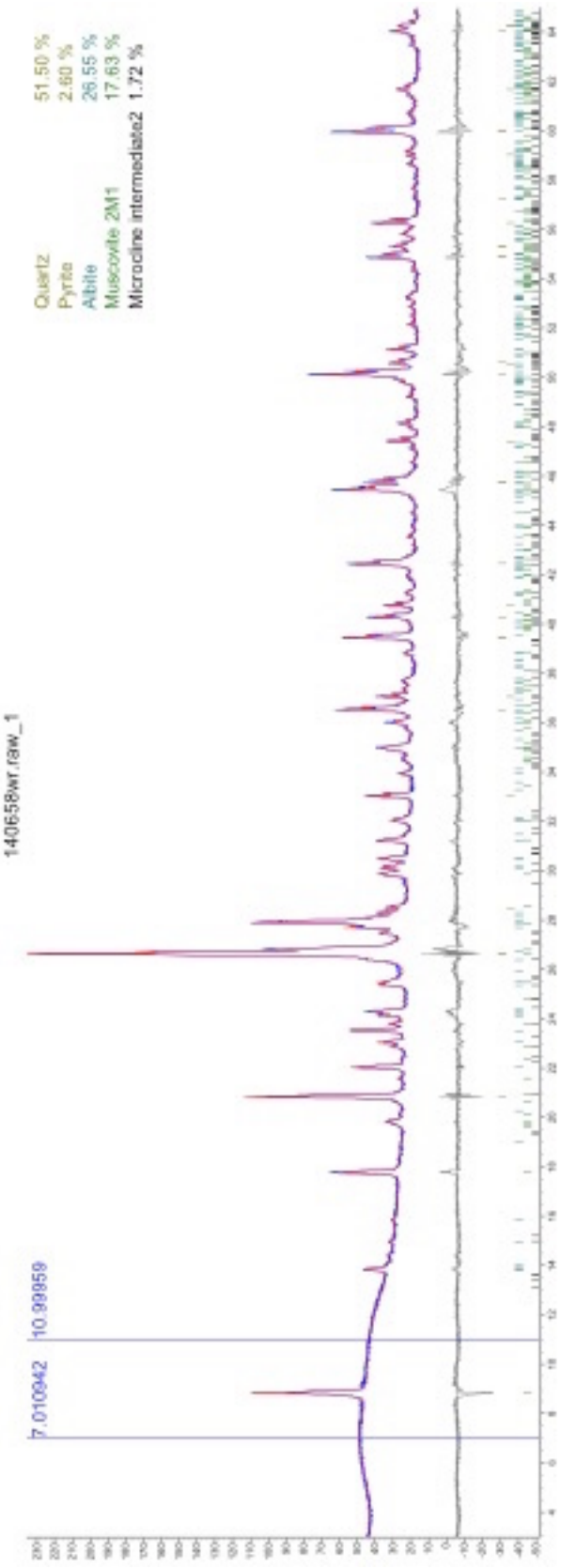
140658wr.raw_1
Quartz 51.50 %
Pyrite 2.60 %
Albite 26.55 %
Muscovite 2M1 17.63 %
Microcline intermediate2 1.72 %
7.010942
10.99859

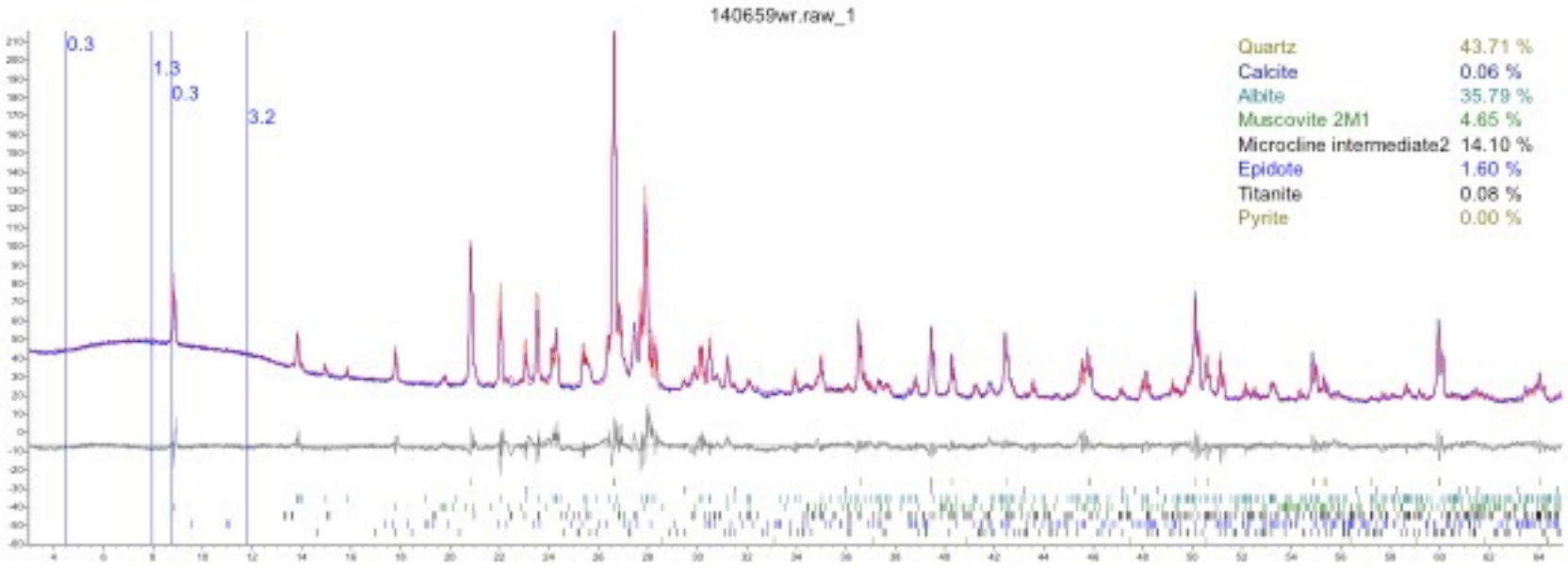
140659wr.raw_1
0.3
1.3
0.3
3.2
Quartz 43.71 %
Calcite 0.06 %
Albite 35.79 %
Muscovite 2M1 4.65 %
Microcline intermediate2 14.10 %
Epidote 1.60 %
Titanite 0.08 %
Pyrite 0.00 %

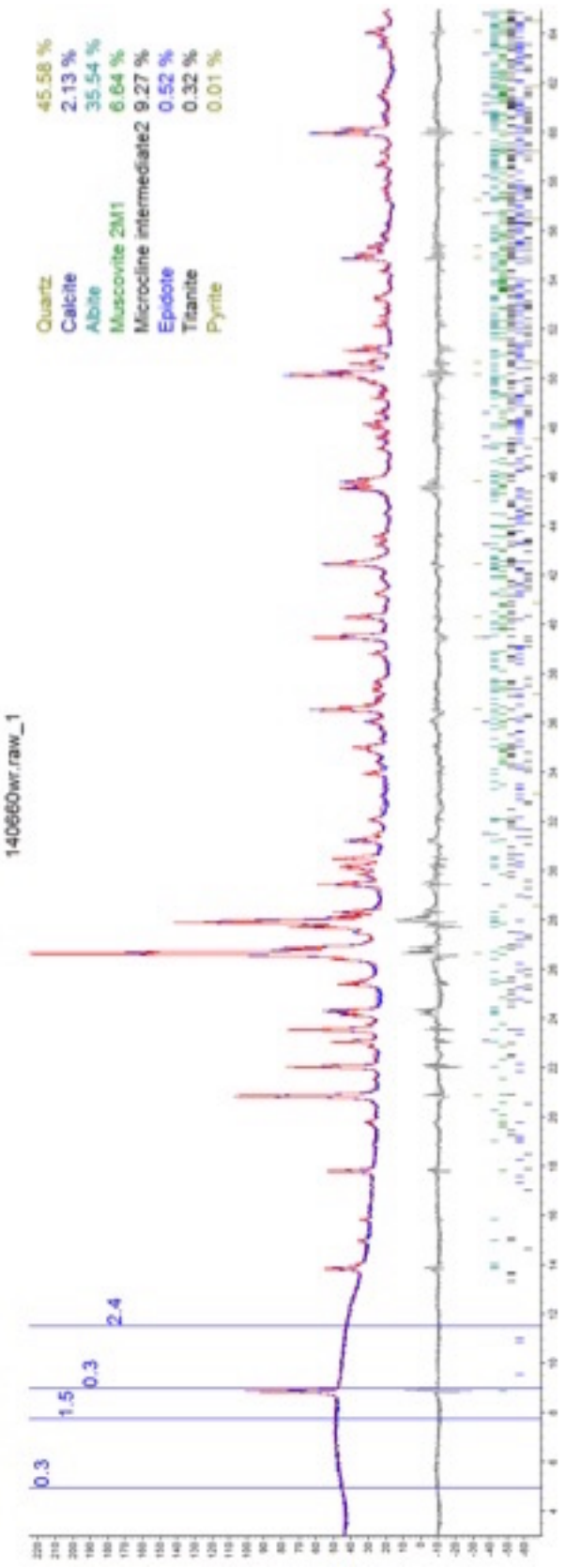
140660wr.raw_1
Quartz 45.58 %
Calcite 2.13 %
Albite 35.54 %
Muscovite 2M1 6.64 %
Microcline intermediate2 9.27 %
Epidote 0.52 %
Titanite 0.32 %
Pyrite 0.01 %
0.3
1.5
0.3
2.4

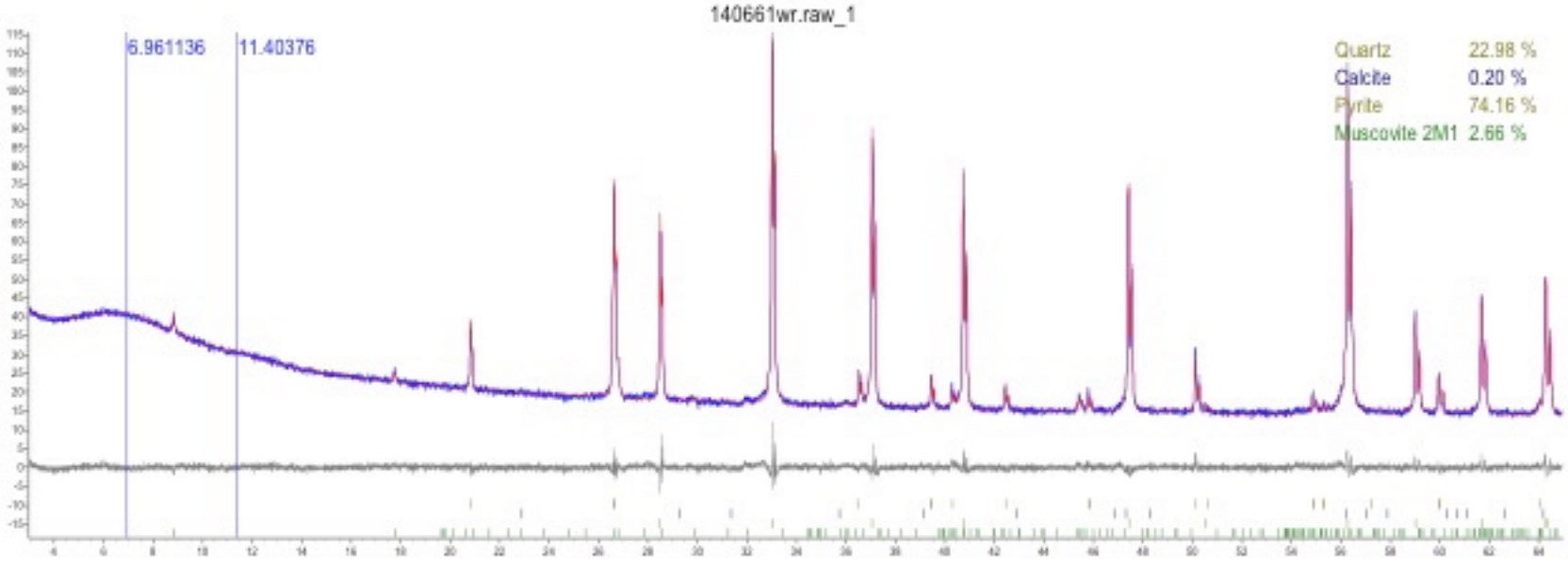
140661wr.raw_1
6.961136
11.40376
Quartz 22.98 %
Calcite 0.20 %
Pyrite 74.16 %
Muscovite 2M1 2.66 %

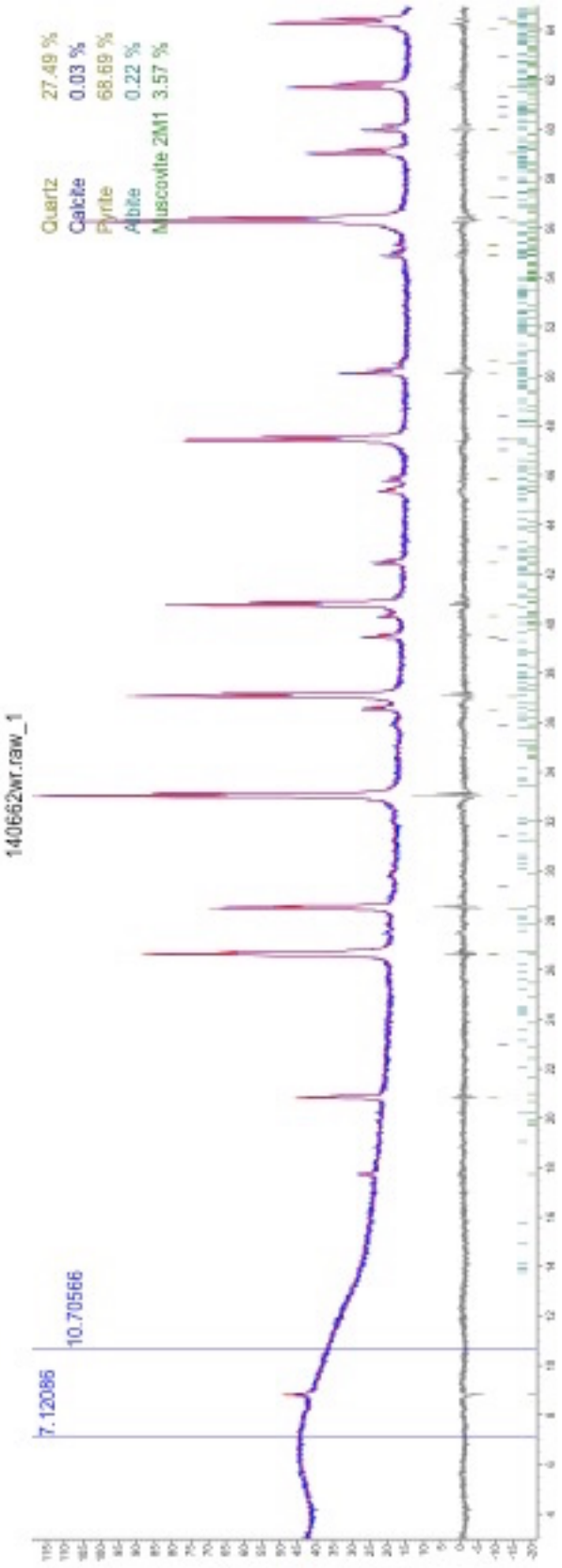
140662wr.raw_1
Quartz 27.49 %
Calcite 0.03 %
Pyrite 68.69 %
Albite 0.22 %
Muscovite 2M1 3.57 %
7.12086
10.70566

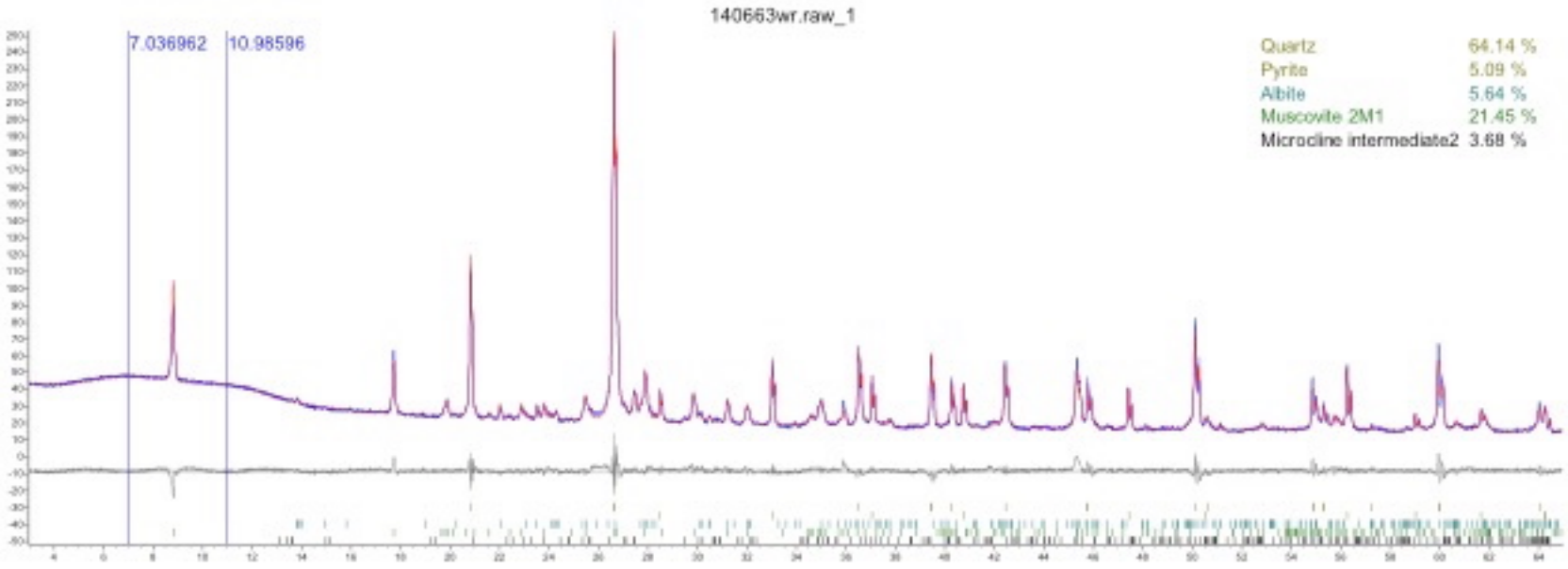
140663wr.raw_1
7.036962
10.98596
Quartz 64.14 %
Pyrite 5.09 %
Albite 5.64 %
Muscovite 2M1 21.45 %
Microcline intermediate2 3.68 %

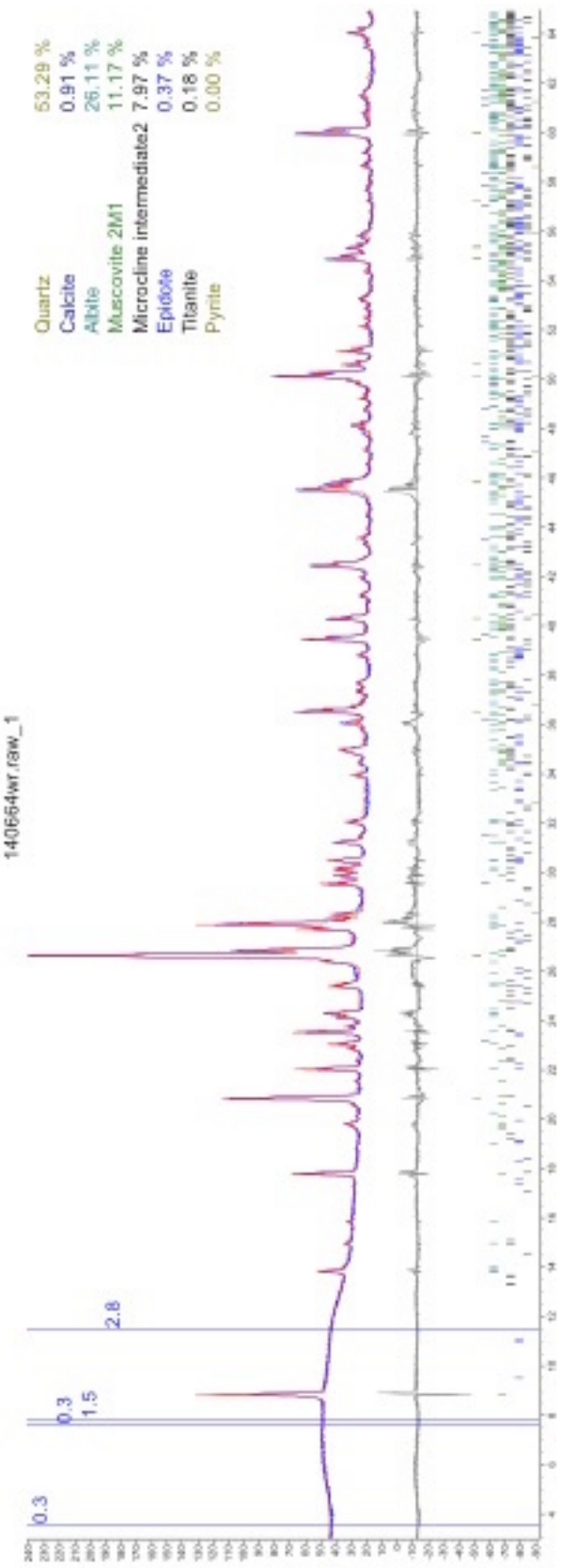
140664wr.raw_1
Quartz 53.29 %
Calcite 0.91 %
Albite 26.11 %
Muscovite 2M1 11.17 %
Microcline intermediate2 7.97 %
Epidote 0.37 %
Titanite 0.18 %
Pyrite 0.00 %
0.3
0.3
1.5
2.8

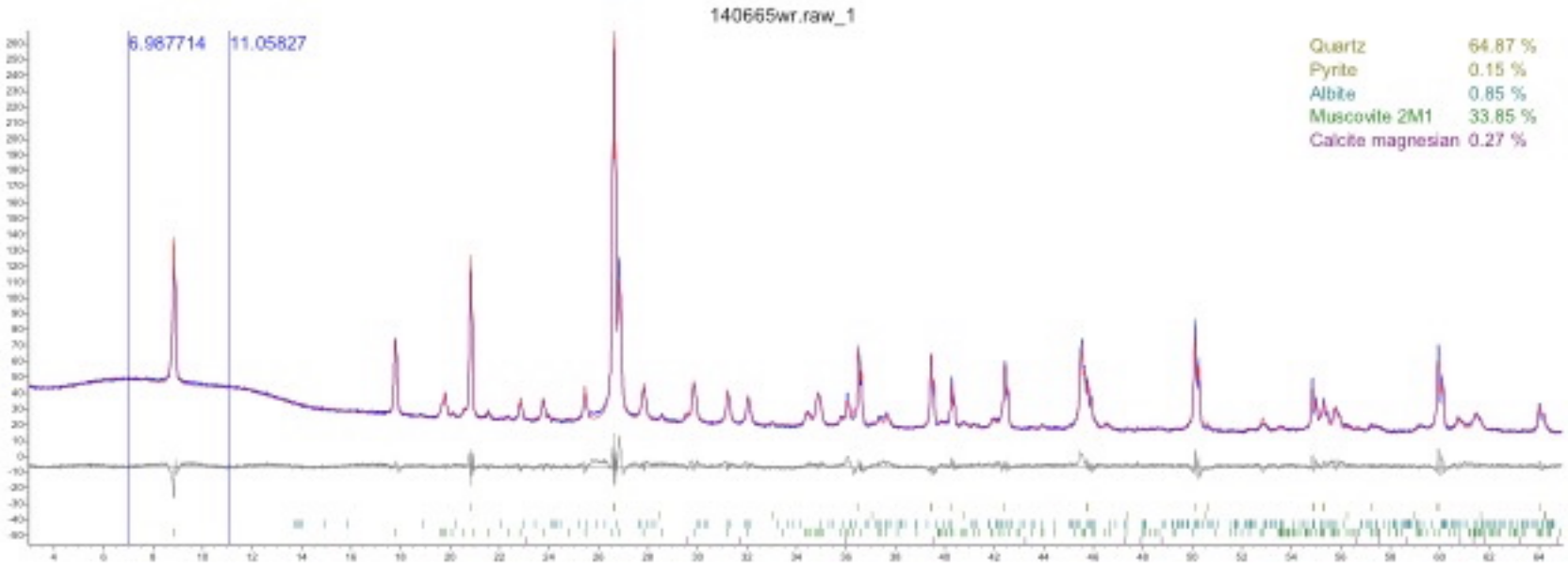
140665wr.raw_1
6.987714
11.05827
Quartz 64.87 %
Pyrite 0.15 %
Albite 0.85 %
Muscovite 2M1 33.85 %
Calcite magnesian 0.27 %

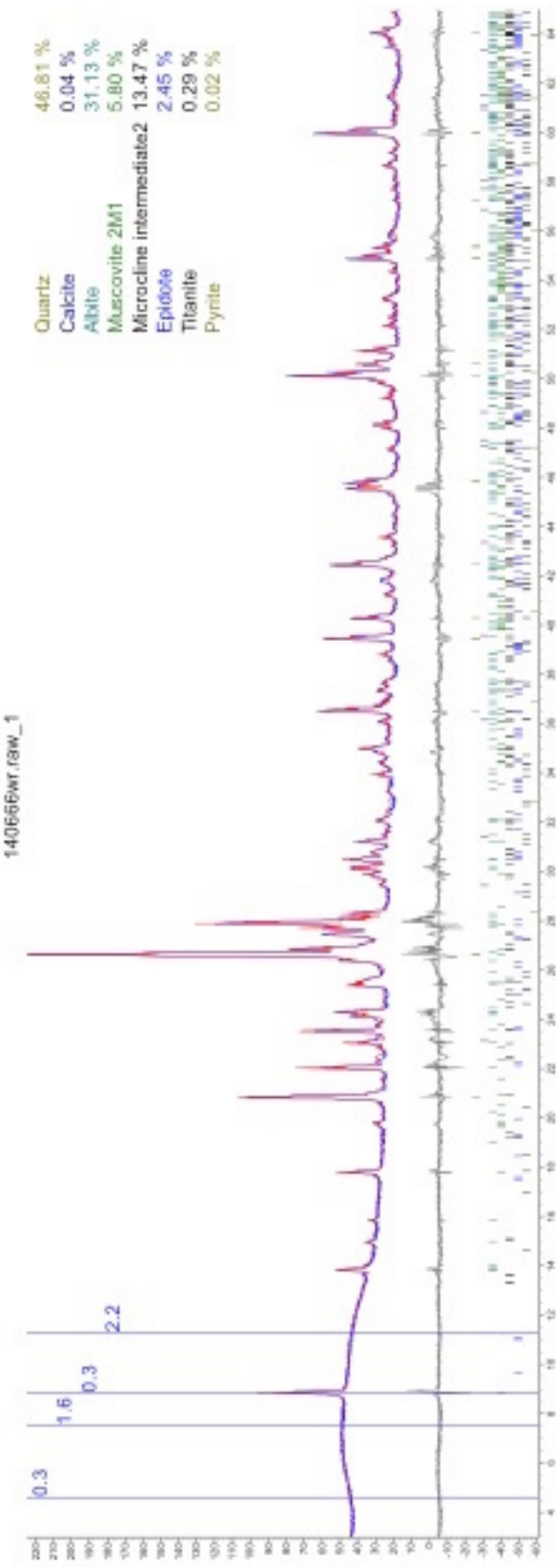
140656wr.raw_1
Quartz 46.81 %
Calcite 0.04 %
Albite 31.13 %
Muscovite 2M1 5.80 %
Microcline intermediate2 13.47 %
Epidote 2.45 %
Titanite 0.29 %
Pyrite 0.02 %
0.3
1.6
0.3
2.2

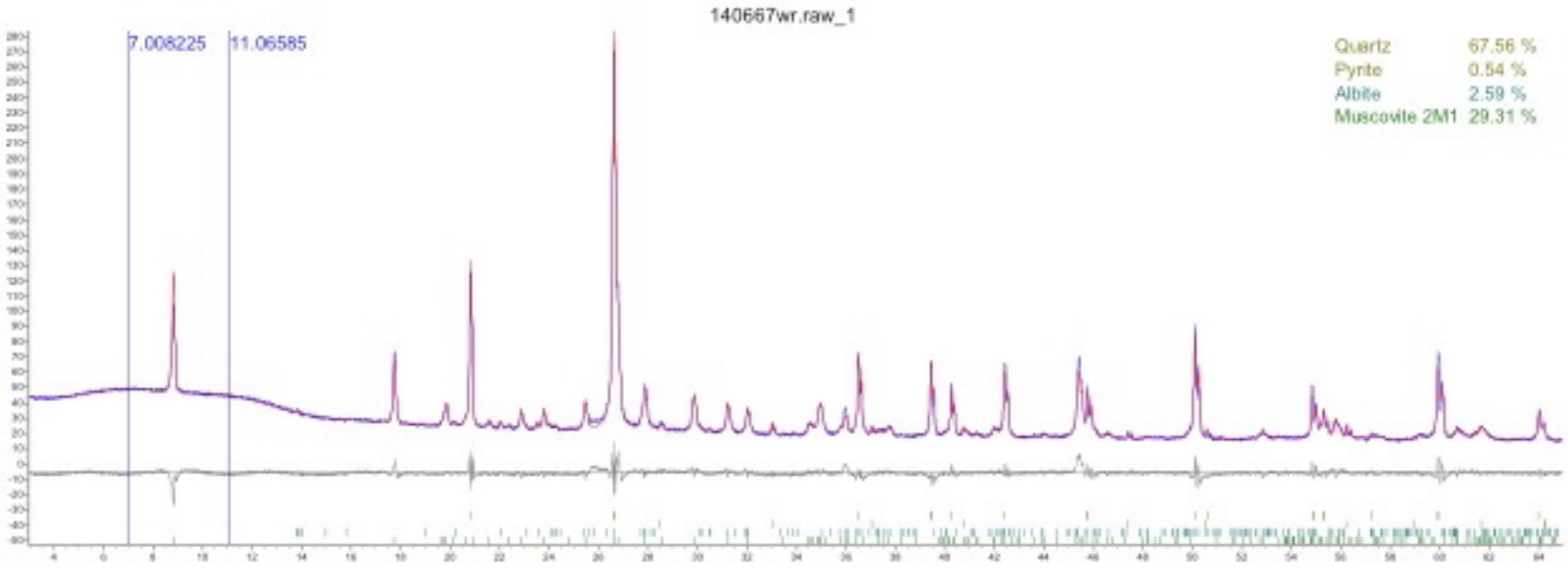
140667wr.raw_1
7.008225
11.06585
Quartz 67.56 %
Pyrite 0.54 %
Albite 2.59 %
Muscovite 2M1 29.31 %

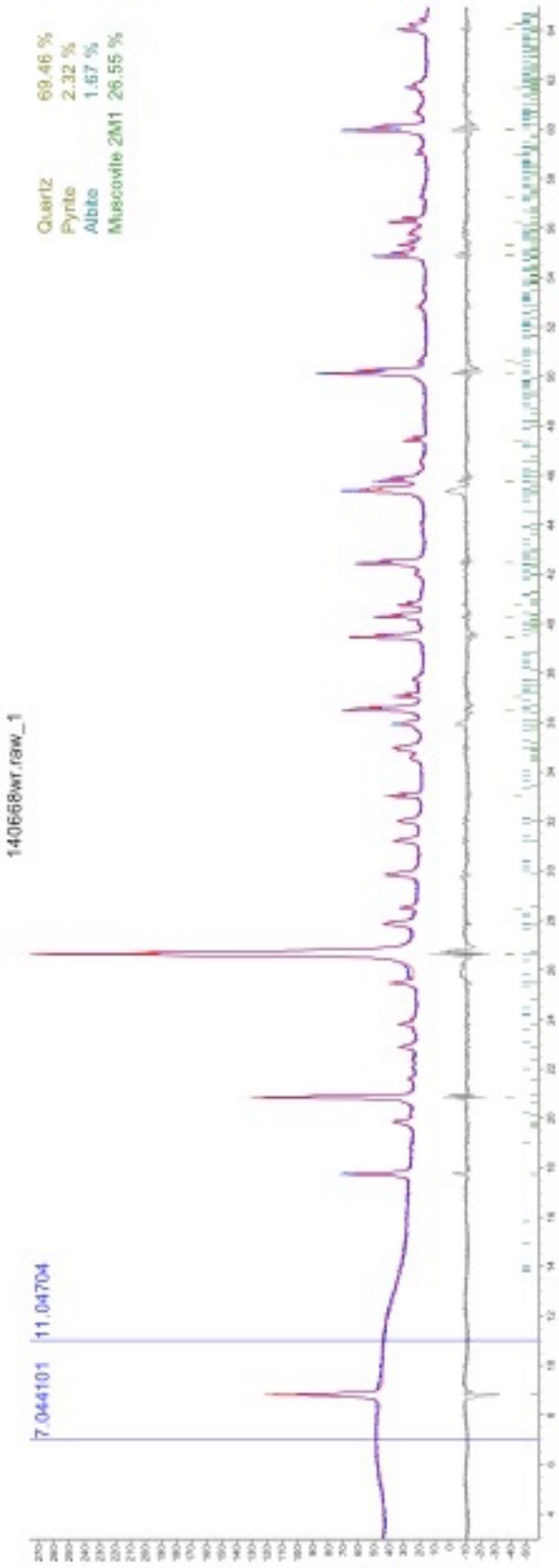
140668wr.raw_1
Quartz 69.46 %
Pyrite 2.32 %
Albite 1.67 %
Muscovite 2M1 26.55 %
7.044101
11.04704

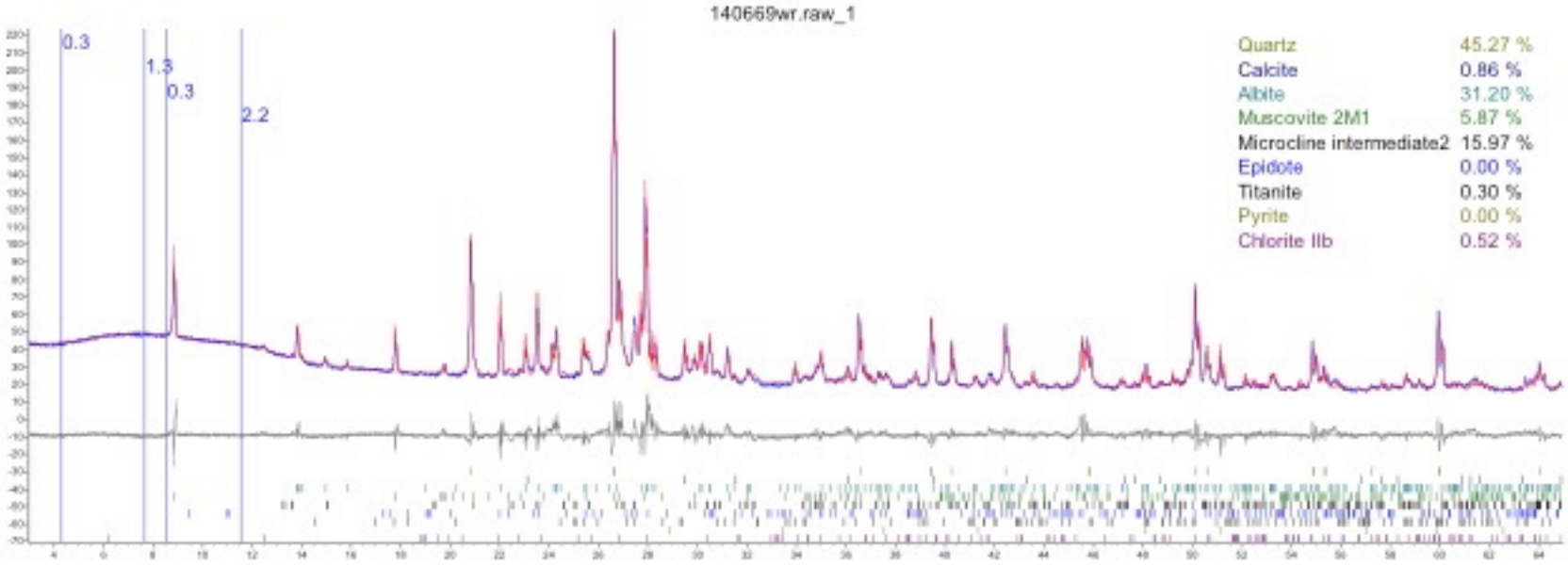
140669wr.raw_1
0.3
1.3
0.3
2.2
Quartz 45.27 %
Calcite 0.86 %
Albite 31.20 %
Muscovite 2M1 5.87 %
Microcline intermediate2 15.97 %
Epidote 0.00 %
Titanite 0.30 %
Pyrite 0.00 %
Chlorite IIb 0.52 %

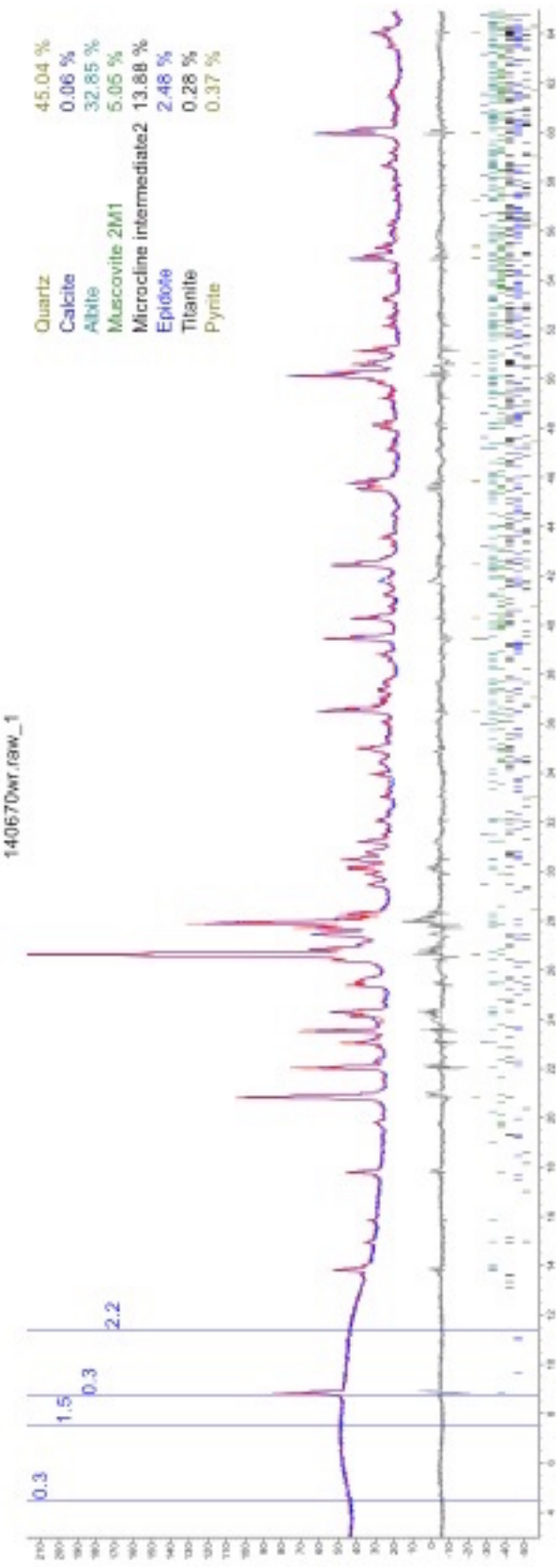
140670wr.raw_1
Quartz 45.04 %
Calcite 0.06 %
Albite 32.85 %
Muscovite 2M1 5.05 %
Microcline intermediate2 13.88 %
Epidote 2.48 %
Titanite 0.28 %
Pyrite 0.37 %
0.3
1.5
0.3
2.2

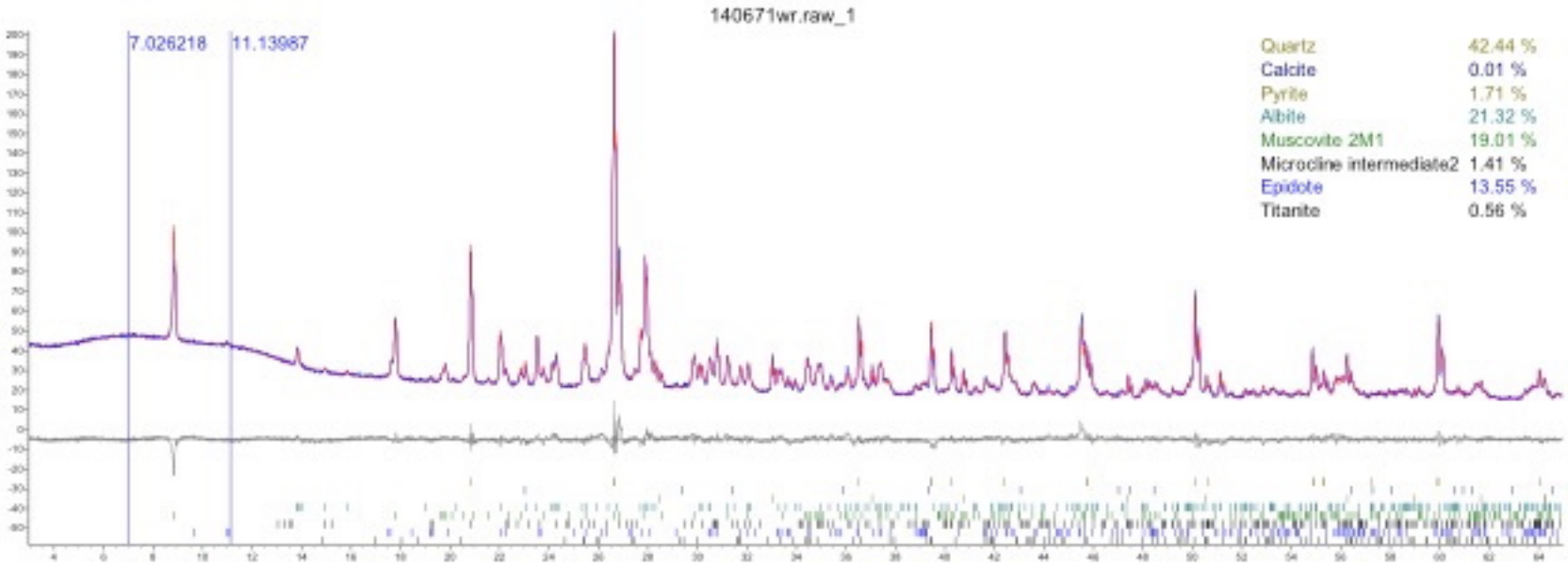
140671wr.raw_1
7.026218
11.13987
Quartz 42.44 %
Calcite 0.01 %
Pyrite 1.71 %
Albite 21.32 %
Muscovite 2M1 19.01 %
Microcline intermediate2 1.41 %
Epidote 13.55 %
Titanite 0.56 %

Appendix E – Whole-rock analyses

	Granodiorite											
Sample	**P01**	**P02**	**P05**	**P09**	**P17**	**P18A**	**P20**	**P22-T**	**P26B-u**	**P27**	**P30**	**P31-u**
SiO_2 (wt. %)	76,70	76,50	77,30	78,40	77,40	77,50	79,10	76,80	78,00	78,60	78,60	78,20
TiO_2	0,16	0,17	0,18	0,10	0,15	0,16	0,14	0,15	0,12	0,18	0,14	0,19
Al_2O_3	11,95	12,35	12,50	11,85	12,35	12,15	11,75	11,55	12,05	12,20	11,95	12,15
Fe_2O_3	1,43	1,50	1,41	1,06	1,65	1,57	1,37	1,58	1,49	1,97	1,65	1,65
MnO	0,02	0,02	0,04	0,03	0,05	0,03	0,04	0,06	0,13	0,03	0,07	0,05
MgO	0,29	0,27	0,31	0,26	0,26	0,26	0,21	0,24	0,42	0,25	0,24	0,25
CaO	0,90	0,70	1,54	0,03	1,39	1,29	0,52	1,87	1,20	0,90	0,86	1,16
Na_2O	3,96	3,97	4,08	4,25	3,77	3,51	4,32	4,37	3,29	3,65	3,79	3,84
K_2O	2,65	2,71	3,02	2,64	2,36	2,88	2,33	1,81	2,49	2,72	2,75	2,76
P_2O_5	0,04	0,03	0,03	0,01	0,04	0,04	0,02	0,02	0,02	0,02	0,03	0,03
Cr_2O_3	0,01	0,01	0,01	b.d.	b.d.	b.d.	b.d.	b.d.	b.d.	b.d.	b.d.	b.d.
SrO	b.d.	b.d.	b.d.	b.d.	0,01	0,01	b.d.	b.d.	b.d.	0,01	b.d.	b.d.
BaO	0,12	0,12	0,13	0,11	0,10	0,11	0,10	0,09	0,06	0,12	0,13	0,13
LOI	0,90	1,12	1,16	0,82	0,74	1,00	0,88	1,99	2,29	1,11	1,56	1,34
Total	99,13	99,47	101,71	99,56	100,27	100,51	100,78	100,53	101,56	101,76	101,77	101,75
Au	n.a.	n.a.	n.a.	b.d.	b.d.	b.d.	b.d.	b.d.	b.d.	b.d.	b.d.	b.d.
A/CNK	1,17	1,22	1,10	1,20	1,23	1,21	1,16	1,06	1,31	1,25	1,20	1,17
Cs (ppm)	0,40	0,37	0,36	0,37	0,27	0,31	0,35	0,42	0,46	0,33	0,32	0,23
Ba	1140	1100	1245	1100	932	1050	989	881	573	1105	1230	1095
Rb	66,80	68,00	74,30	77,00	62,70	78,70	66,40	63,60	102,00	76,10	84,50	65,70
Sr	102,50	85,20	131,50	32,30	133,00	133,50	91,80	101,00	58,10	148,50	103,00	98,30
Y	23,00	24,40	31,80	35,50	31,80	31,10	26,50	35,10	42,00	34,10	35,10	35,40
Zr	87	112	162	100	123	124	108	113	107	121	123	120
Nb	3,50	3,90	3,80	3,30	3,70	3,70	3,90	4,10	2,80	4,70	3,50	3,80
Th	19,75	20,30	24,60	22,20	23,80	20,90	20,90	21,40	22,40	25,30	22,00	22,60
V	15	13	16	b.d.	10	12	9	11	5	11	12	11
Cr	30	10	10	20	20	20	20	30	20	20	20	10
Hf	3,00	3,90	5,00	3,60	3,60	3,90	3,60	3,40	3,70	4,30	4,00	3,70
Ta	0,70	0,70	0,70	0,30	0,30	0,20	0,40	0,30	0,60	0,30	0,30	0,40
U	3,97	3,60	5,20	2,64	4,68	4,51	3,46	4,88	3,29	4,70	3,81	5,16
Sn	2	1	1	1	1	1	1	1	1	2	1	1
W	1	2	3	1	2	2	2	3	4	3	3	1
Ga	12,50	11,70	13,60	12,70	13,50	13,30	12,10	12,40	13,00	13,40	12,60	11,70
Tl	b.d.	b.d.	b.d.	b.d.	b.d.	b.d.	b.d.	b.d.	0,50	b.d.	0,60	b.d.
La	35,60	26,00	51,30	39,70	48,00	41,90	37,00	49,10	46,90	41,30	49,70	56,20
Ce	71,50	63,90	93,80	75,00	85,80	74,00	73,00	87,60	82,60	80,70	84,70	91,20
Pr	7,14	4,87	9,70	8,21	9,31	7,79	7,26	9,01	8,69	7,69	9,08	10,00
Nd	22,30	17,10	32,20	26,80	29,80	25,50	23,10	29,60	29,20	25,80	29,30	33,10
Sm	3,89	3,39	5,46	4,91	5,54	4,69	4,14	5,38	5,25	4,62	5,25	5,88
Eu	0,85	0,66	1,09	0,71	1,00	0,84	0,76	0,89	0,87	0,81	0,77	0,99
Gd	3,12	2,50	4,38	4,37	4,56	4,10	3,38	4,78	4,29	3,95	4,79	4,82
Tb	0,63	0,53	0,78	0,76	0,77	0,73	0,59	0,76	0,84	0,66	0,74	0,85
Dy	3,39	3,41	4,83	5,03	4,52	4,61	3,58	4,87	5,20	5,04	4,59	5,00
Ho	0,80	0,84	1,08	1,19	1,02	1,03	0,86	1,12	1,26	1,22	1,07	1,13
Er	2,39	2,72	3,56	3,80	3,10	3,35	2,64	3,48	4,27	3,64	3,69	3,66
Tm	0,42	0,45	0,50	0,58	0,53	0,46	0,42	0,55	0,69	0,61	0,55	0,58
Yb	2,87	2,90	3,66	4,36	3,81	3,47	3,37	4,13	4,91	4,21	4,03	3,98
Lu	0,51	0,53	0,70	0,70	0,65	0,59	0,56	0,71	0,83	0,71	0,64	0,74

	Phyllonite							Epidote-rich SZ	Quartz	Aplite		Quartz-sulphides	
Sample	**P03**	**P04**	**P18B**	**P25B-T**	**P26B-d**	**P28**	**P29**	**P31-d**	**AU1**	**AU2**	**P13**	**P23B-T**	**P25A-T**
SiO_2 (wt. %)	72,70	75,30	75,80	74,50	78,10	79,30	77,00	69,50	97,30	71,60	78,30	13,50	18,05
TiO_2	0,21	0,18	0,17	0,16	0,12	0,16	0,16	0,20	0,03	0,21	0,08	0,01	0,01
Al_2O_3	15,25	11,85	12,00	11,55	12,35	12,25	12,35	14,20	0,47	11,00	11,80	0,55	1,25
Fe_2O_3	1,83	3,01	3,21	6,38	2,51	1,84	3,91	4,60	0,78	6,15	0,86	51,00	47,80
MnO	0,03	0,05	0,03	0,04	0,09	0,04	0,05	0,09	0,04	0,06	0,01	0,02	0,02
MgO	1,17	0,56	0,48	0,20	0,93	0,37	0,28	0,64	0,09	0,53	0,04	0,03	0,03
CaO	0,04	0,04	0,25	0,10	0,14	0,02	0,01	3,80	1,49	0,86	0,28	0,02	0,02
Na_2O	0,08	0,06	2,69	0,61	0,07	0,33	0,15	2,04	0,01	4,82	3,57	0,02	0,03
K_2O	5,52	4,17	2,76	3,61	4,67	3,76	3,91	2,77	0,10	0,75	4,02	0,22	0,50
P_2O_5	0,02	b.d.	0,03	b.d.	0,01	0,01	b.d.	0,04	b.d.	0,03	b.d.	0,01	b.d.
Cr_2O_3	0,01	0,01	b.d.	b.d.	b.d.	b.d.	0,01	b.d.	b.d.	b.d.	b.d.	b.d.	b.d.
SrO	b.d.	b.d.	b.d.	b.d.	b.d.	b.d.	b.d.	0,03	b.d.	b.d.	b.d.	b.d.	b.d.
BaO	0,14	0,14	0,07	0,10	0,11	0,09	0,09	0,08	b.d.	0,01	0,05	b.d.	0,02
LOI	2,62	2,75	2,61	4,50	2,35	2,44	3,57	2,72	1,50	3,70	0,60	29,50	27,50
Total	99,62	98,12	100,10	101,75	101,45	100,61	101,49	100,71	101,81	99,72	99,61	94,88	95,23
Au	n.a.	n.a.	b.d.	0,005	0,002	b.d.	b.d.	b.d.	b.d.	0,002	b.d.	0,033	0,016
A/CNK										1,16	1,13		
Cs (ppm)	0,70	0,45	0,37	0,32	0,82	0,44	0,26	0,45	0,08	0,16	0,25	0,08	0,05
Ba	1230	1315	695	1005	1040	879	817	686	15,2	128	470	42,7	199
Rb	171,00	122,00	94,90	101,00	195,50	110,00	118,00	104,00	4,00	35,30	95,20	6,40	12,50
Sr	5,80	10,60	20,20	41,80	14,10	43,20	14,20	332,00	33,30	86,90	70,10	1,90	10,70
Y	1,10	4,90	16,60	24,80	19,90	1,80	2,80	102,50	3,30	45,20	30,00	1,80	1,30
Zr	112	114	135	136	126	110	111	143	3	96	98	9	9
Nb	3,60	4,20	4,60	4,10	3,50	4,20	3,90	4,60	b.d.	5,10	9,40	b.d.	b.d.
Th	1,14	2,68	15,45	2,52	21,40	1,79	3,10	29,00	0,65	16,95	18,75	1,75	0,43
V	47	15	18	12	b.d.	14	12	21	b.d.	21	b.d.	b.d.	b.d.
Cr	10	10	30	20	20	20	30	10	20	30	20	20	20
Hf	4,00	3,50	4,30	4,10	3,90	3,90	3,80	4,50	b.d.	3,00	4,90	0,30	0,30
Ta	0,60	0,70	0,30	0,60	0,40	0,40	0,40	0,40	0,30	0,30	0,90	b.d.	0,20
U	0,35	1,01	3,00	0,94	2,92	0,47	0,96	10,00	0,48	3,58	4,16	0,46	0,38
Sn	7	6	8	7	2	10	6	3	12	12	2	1	1
W	8	4	3	5	9	4	3	4	1	2	2	1	1
Ga	19,30	17,40	13,50	11,30	13,90	17,70	13,90	22,40	1,10	11,60	13,70	0,90	1,40
Tl	0,60	0,80	b.d.	0,50	1,20	0,60	0,70	0,50	b.d.	b.d.	0,50	b.d.	b.d.
La	0,80	1,20	7,10	6,20	27,20	3,00	1,40	73,20	2,10	18,80	8,50	2,80	1,50
Ce	0,80	1,30	11,50	11,20	53,40	5,00	1,60	123,50	2,50	32,80	17,30	3,90	1,50
Pr	0,07	0,13	1,29	1,25	5,46	0,54	0,17	13,25	0,28	3,65	2,05	0,38	0,17
Nd	0,10	0,50	4,50	4,50	18,40	1,60	0,60	44,80	1,10	12,40	7,20	1,20	0,40
Sm	0,05	0,21	1,14	1,43	3,44	0,33	0,15	9,94	0,23	2,55	1,72	0,27	0,08
Eu	b.d.	b.d.	0,19	0,27	0,59	0,06	b.d.	2,30	0,05	0,52	0,16	0,06	0,04
Gd	0,07	0,19	1,15	1,61	2,89	0,20	0,13	10,20	0,45	3,18	1,93	0,26	0,12
Tb	0,02	0,06	0,26	0,41	0,51	0,03	0,05	1,83	0,06	0,69	0,48	0,04	0,02
Dy	0,12	0,60	2,27	3,24	3,17	0,23	0,31	11,90	0,46	4,98	3,34	0,22	0,19
Ho	0,04	0,15	0,60	0,83	0,65	0,07	0,09	2,81	0,11	1,31	0,90	0,08	0,04
Er	0,12	0,63	2,04	2,86	2,23	0,19	0,42	8,96	0,29	4,98	3,17	0,26	0,15
Tm	0,02	0,10	0,38	0,53	0,35	0,03	0,05	1,39	0,06	0,94	0,64	0,05	0,03
Yb	0,33	0,89	2,69	3,69	2,93	0,41	0,51	9,78	0,46	6,71	4,91	0,29	0,22
Lu	0,07	0,15	0,44	0,59	0,50	0,08	0,11	1,52	0,08	1,13	0,85	0,03	0,02

Appendix F – ISOCON results and diagrams

-2σ

Mass change: -28.86%
Volume change: -30.17%
Slope: 1.41

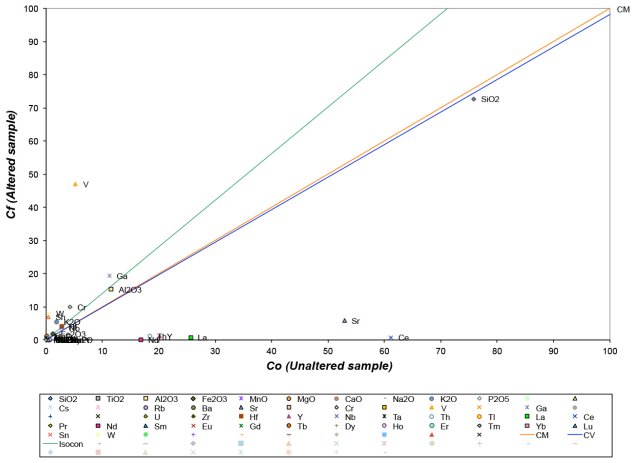

Average granodiorite

Mass change: 5.09%
Volume change: 3.15%
Slope: 0.95

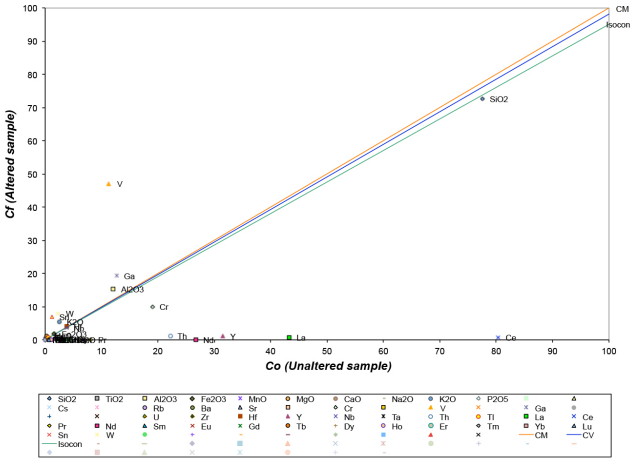

+2σ

Mass change: 39.03%
Volume change: 36.74%
Slope: 0.72

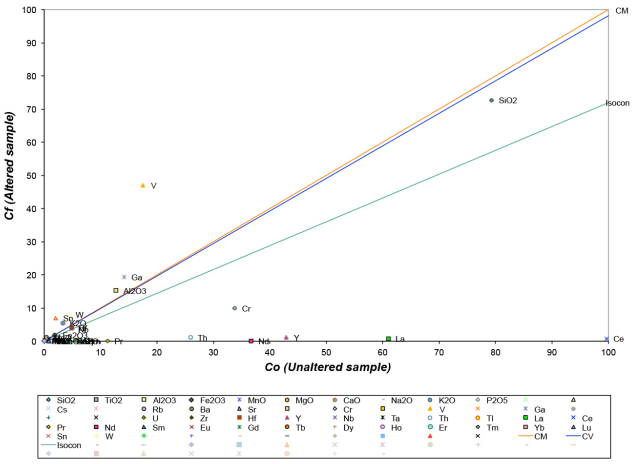

P26B-u vs. P26B-u

Overall volume	-16,67
Overall mass ch	-15,09
Slope	1,18

Table 1 Results

Sample	Unaltered P26B-u	Altered P26B-d	Gain/Loss relative to C_i^0 $\Delta C_i/C_i^0$	Gain/Loss in wt.% or ppm ΔC_i
SiO2	78,00	78,10	-0,15	-11,69
TiO2	0,12	0,12	-0,15	-0,02
Al2O3	12,05	12,35	-0,13	-1,56
Fe2O3	1,49	2,51	0,43	0,64
MnO	0,13	0,09	-0,41	-0,05
MgO	0,42	0,93	0,88	0,37
CaO	1,20	0,14	-0,90	-1,08
Na2O	3,29	0,07	-0,98	-3,23
K2O	2,49	4,67	0,59	1,48
P2O5	0,02	0,01	-0,58	-0,01
Ga	13,00	13,90	-0,09	-1,20
Cr	20,00	20,00	-0,15	-3,02
V				
Rb	102,00	195,50	0,63	63,99
Cs	0,46	0,82	0,51	0,24
Ba	573,00	1040,00	0,54	310,03
Sr	58,10	14,10	-0,79	-46,13
U	3,29	2,92	-0,25	-0,81
Zr	107,00	126,00	0,00	-0,02
Hf	3,70	3,90	-0,11	-0,39
Y	42,00	19,90	-0,60	-25,10
Nb	2,80	3,50	0,06	0,17
Ta	0,60	0,40	-0,43	-0,26
Th	22,40	21,40	-0,19	-4,23
La	46,90	27,20	-0,51	-23,81
Ce	82,60	53,40	-0,45	-37,26
Pr	8,69	5,46	-0,47	-4,05
Nd	29,20	18,40	-0,46	-13,58
Sm	5,25	3,44	-0,44	-2,33
Eu	0,87	0,59	-0,42	-0,37
Gd	4,29	2,89	-0,43	-1,84
Tb	0,84	0,51	-0,48	-0,41
Dy	5,20	3,17	-0,48	-2,51
Ho	1,26	0,65	-0,56	-0,71
Er	4,27	2,23	-0,56	-2,38
Tm	0,69	0,35	-0,57	-0,39
Yb	4,91	2,93	-0,49	-2,42
Lu	0,83	0,50	-0,49	-0,41

P18A vs. P18B

Table 1 Results

Overall volume c	-9,84
Overall mass cha	-8,15
Slope	1,09

Sample	Unaltered P18A	Altered P18B	Gain/Loss relative to C_i^0 $\Delta C_i/C_i^0$	Gain/Loss in wt.% or ppm ΔC_i
SiO2	77,50	75,80	-0,10	-7,88
TiO2	0,16	0,17	-0,02	0,00
Al2O3	12,15	12,00	-0,09	-1,13
Fe2O3	1,57	3,21	0,88	1,38
MnO	0,03	0,03	-0,08	0,00
MgO	0,26	0,48	0,70	0,18
CaO	1,29	0,25	-0,82	-1,06
Na2O	3,51	2,69	-0,30	-1,04
K2O	2,88	2,76	-0,12	-0,34
P2O5	0,04	0,03	-0,31	-0,01
Ga	13,30	13,50	-0,07	-0,90
Cr	20,00	30,00	0,38	7,55
V	12,00	18,00	0,38	4,53
Cs	0,31	0,37	0,10	0,03
Rb	78,70	94,90	0,11	8,46
Ba	1050,00	695,00	-0,39	-411,65
Sr	133,50	20,20	-0,86	-114,95
U	4,51	3,00	-0,39	-1,75
Zr	124,00	135,00	0,00	0,00
Hf	3,90	4,30	0,01	0,05
Y	31,10	16,60	-0,51	-15,85
Nb	3,70	4,60	0,14	0,53
Ta	0,20	0,30	0,38	0,08
Th	20,90	15,45	-0,32	-6,71
La	41,90	7,10	-0,84	-35,38
Ce	74,00	11,50	-0,86	-63,44
Pr	7,79	1,29	-0,85	-6,61
Nd	25,50	4,50	-0,84	-21,37
Sm	4,69	1,14	-0,78	-3,64
Eu	0,84	0,19	-0,79	-0,67
Gd	4,10	1,15	-0,74	-3,04
Tb	0,73	0,26	-0,67	-0,49
Dy	4,61	2,27	-0,55	-2,53
Ho	1,03	0,60	-0,46	-0,48
Er	3,35	2,04	-0,44	-1,48
Tm	0,46	0,38	-0,24	-0,11
Yb	3,47	2,69	-0,29	-1,00
Lu	0,59	0,44	-0,32	-0,19

P31-u vs. P31-d

Overall volume	-21,42
Overall mass ch	-16,10
Slope	1,19

Table 1 Results

Sample	Unaltered P31-u	Altered P31-d	Gain/Loss relative to C_i^0 $\Delta C_i/C_i^0$	Gain/Loss in wt.% or ppm ΔC_i
SiO2	78,20	69,50	-0,25	-19,89
TiO2	0,19	0,20	-0,12	-0,02
Al2O3	12,15	14,20	-0,02	-0,24
Fe2O3	1,65	4,60	1,34	2,21
MnO	0,05	0,09	0,51	0,03
MgO	0,25	0,64	1,15	0,29
CaO	1,16	3,80	1,75	2,03
Na2O	3,84	2,04	-0,55	-2,13
K2O	2,76	2,77	-0,16	-0,44
P2O5	0,03	0,04	0,12	0,00
Ga	11,70	22,40	0,61	7,09
Cr	10,00	10,00	-0,16	-1,61
V	11,00	21,00	0,60	6,62
Cs	0,23	0,45	0,64	0,15
Rb	65,70	104,00	0,33	21,56
Ba	1095,00	686,00	-0,47	-519,44
Sr	98,30	332,00	1,83	180,25
U	5,16	10,00	0,63	3,23
Zr	120,00	143,00	0,00	-0,02
Hf	3,70	4,50	0,02	0,08
Y	35,40	102,50	1,43	50,60
Nb	3,80	4,60	0,02	0,06
Ta	0,40	0,40	-0,16	-0,06
Th	22,60	29,00	0,08	1,73
La	56,20	73,20	0,09	5,22
Ce	91,20	123,50	0,14	12,42
Pr	10,00	13,25	0,11	1,12
Nd	33,10	44,80	0,14	4,49
Sm	5,88	9,94	0,42	2,46
Eu	0,99	2,30	0,95	0,94
Gd	4,82	10,20	0,78	3,74
Tb	0,85	1,83	0,81	0,69
Dy	5,00	11,90	1,00	4,98
Ho	1,13	2,81	1,09	1,23
Er	3,66	8,96	1,05	3,86
Tm	0,58	1,39	1,01	0,59
Yb	3,98	9,78	1,06	4,23
Lu	0,74	1,52	0,72	0,54

Appendix G – Joint Assembly GAC-MAC Poster

NTNU – Trondheim
Norwegian University of Science and Technology

Deformation, Phyllonitization and Associated Element Mobilization of Granitoid Rocks

GEOLOGICAL SURVEY OF NORWAY · NGU ·

Anette U. Granseth[1], Nolwenn Coint[2], Trond Slagstad[2], Bjørn E. Sørensen[1].
1. Department of Geological and Mineral Resources Engineering (IGB), NTNU, N-7491 Trondheim. anetteut@stud.ntnu.no, bjorn.sorensen@ntnu.no.
2. The Geological Survey of Norway, 7491 Trondheim, nolwenn.coint@ngu.no, trond.slagstad@ngu.no

The Problem

- The Fagervika granitoid underwent greenschist facies metamorphism during the Caledonian Orogeny.
- The alteration was pervasive, whereas the deformation was localized in phyllonitic shear zones.
- This study documents extensive element mobility related to the deformation.

Epidote-rich SZ → **Granodiorite** → **Phyllonite**

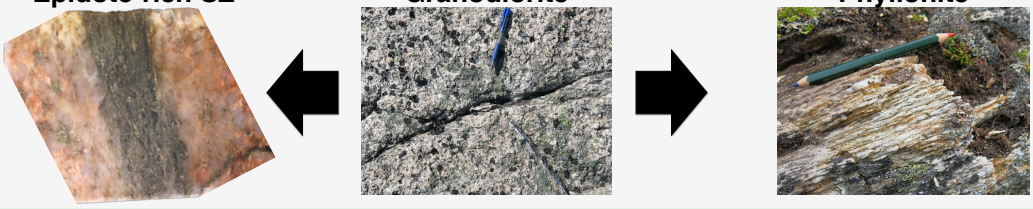

Mineralogy

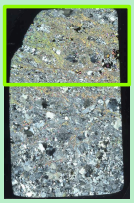

- Epidote-rich, with Ms + Py + Qtz + Acc. Ttn
- Gain of Ca-bearing epidote + titanite → REE gain

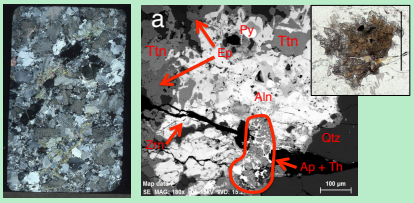

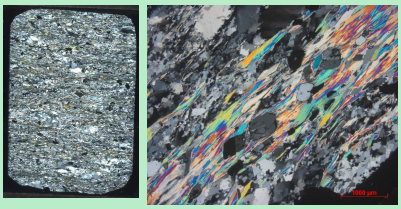

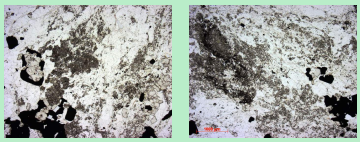

- Qtz + Kfs + Pl + Ms + Py + Acc. Aln + Ttn + Ep
- Alkali feldspar is neocrystallized to albite, plagioclase is seritized/sausurittized
- Allanite, epidote and titanite – main REE carriers
- Secondary allanite, epidote, titanite, apatite + Th-mineral = Monazite decompostion?

- Qtz + Ms + Py ± Ab ± Acc. Ttn
- Only sporadic titanite remains
- Epidote loss → REE loss

Whole-rock chemistry

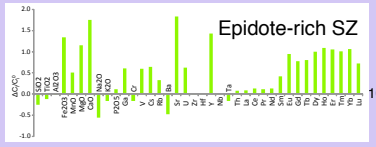

- Plagioclase and Alkali feldspar loss
- Muscovite gain; Epidote gain → REE gain

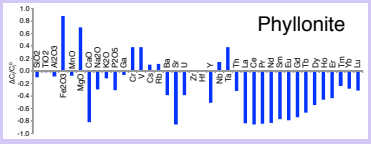

- Muscovite gain; Epidote loss→ REE loss
- Plagioclase and Alkali feldspar loss → Na, K, Ba, Sr

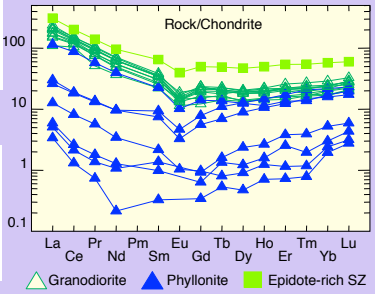

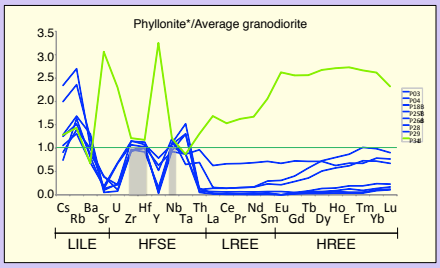

- Epidote-rich SZ: Epidote ← Sr + REE: Titanite ← REE
- Phyllonite: Muscovite ← Rb; Epidote loss → REE loss

Mineral chemistry…

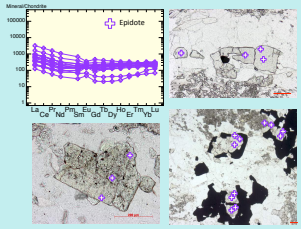

… in the epidote-rich SZ
Flat REE pattern, positive and negative Eu anomaly

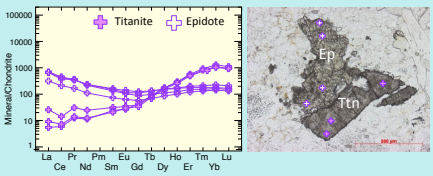

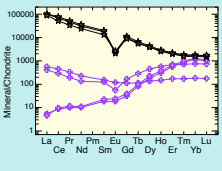

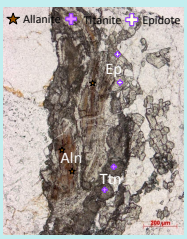

… in the granodiorite

- Allanite and, to a lesser degree, epidote are enriched in the LREE, whereas titanite has a LREE-depleted pattern

→ could reflect preferential incorporation of LREE in allanite and epidote

Conclusion

Mobilization of K and Na, related to the stability of the major phases. REE related to Ca-bearing epidote, titanite and allanite, with small-scale mobility of REE within the granodiorite. Instability of major and minor phases in the phyllonites, with the loss of REE-bearing phases allowed for mobilization of commonly assumed immobile elements.